A strong gravitational lensing view on the dynamical properties of high-redshift star-forming galaxies

Francesca Rizzo

München 2020

A strong gravitational lensing view on the dynamical properties of high-redshift star-forming galaxies

Francesca Rizzo

Dissertation
an der Fakultät für Physik
der Ludwig–Maximilians–Universität
München

vorgelegt von
Francesca Rizzo
aus Casarano, Italien

München, den 25 August 2020

Erstgutachter: Prof. Dr. Simon White
Zweitgutachter: Prof. Dr. Eiichiro Komatsu
Tag der mündlichen Prüfung: 8 Oktober 2020

"Don't be afraid of hard work. Nothing worthwhile comes easily. Don't let others discourage you or tell you that you can't do it. In my day I was told women didn't go into chemistry. I saw no reason why we couldn't."
Gertrude B. Elion

Contents

List of Figures

List of Tables

List of Abbreviations

AGN	Active Galactic Nuclei
ALMA	Atacama Large Millimeter/Submillimeter Array
AO	Adaptive optic
CASA	Common Astronomy Software Applications package
CDM	Cold Dark Matter
cSFG	Compact Star-Forming Galaxy
DSFG	Dusty Star-Forming Galaxy
ELT	Extremely Large Telescope
ETG	Early Type Galaxy
FIR	Far InfraRed
FoV	Field of View
FWHM	Full Width at Half Maximum
HST	Hubble Space Telescope
IFU	Integral Field Unit
IGM	Intergalactic Medium
IMF	Initial Mass Function
ISM	Interstellar Medium
JWST	James Webb Space Telescope
KMOS	K-band Multi-Object Spectrograph
MIR	Mid InfraRed
MS	Main Sequence
NFW	Navarro-Frenk-White
NIR	Near InfraRed
PSF	Point-Spread Function
SFR	Star Formation Rate
SNR	Signal-to-Noise Ratio
SPT	South Pole Telescope
UV	Ultraviolet
VLT	Very Large Telescope

This thesis is my own work. I chose to use the pronoun “we” to conform with the typical writing style in our field.

Zusammenfassung

Aktuellen Modellen zur Entstehung und Entwicklung von Galaxien zufolge war das Gas in Galaxien in den frühen kosmischen Epochen aufgrund starker Gas Akkretion, Galaxienverschmelzungen, Rückkopplungen durch Sternentstehung und Supernova-Explosionen sehr turbulent. Aus diesem Grund wird erwartet, dass junge Galaxien strukturelle und dynamische Eigenschaften aufweisen, die stark von diesen Phänomenen beeinflusst werden, und sich deshalb von den beobachteten Eigenschaften naher Galaxien unterscheiden. Bis zu diesem Zeitpunkt haben jedoch verschiedene Herausforderungen in der Beobachtung von jungen Galaxien die Möglichkeit eingeschränkt, diese theoretischen Vorhersagen zu testen. Die geringe räumliche Auflösung und das Signal-Rausch-Verhältnis (SNR, für engl. signal-to-noise) von Beobachtungen schränken die Untersuchung der Dynamik junger Galaxien erheblich ein. Ein möglicher Weg diese Einschränkungen zu überwinden ist es Galaxien zu betrachteten, welche durch den starken Gravitationslinseneffekt abgebildet werden. Die Vergrößerung durch den Gravitationslinseneffekt erhöht sowohl den Raumwinkel der Hintergrundlichtquelle als auch den beobachteten Lichtfluss. Infolgedessen können entfernte Objekte mit erhöhter Winkelauflösung und besseren SNR beobachtet werden. Dies hat jedoch seinen Preis: Der Linseneffekt verzerrt die entfernten Lichtquellen und es ist nicht trivial, ihre intrinsischen physikalischen Eigenschaften ohne systematische Fehler abzuleiten.

Diese Doktorarbeit konzentriert sich auf die Untersuchung der kinematischen und dynamischen Eigenschaften von Galaxien, die durch den Gravitationslinseneffekt abgebildet werden, bei Rotverschiebungen von $z \gtrsim 3$, als das Universum nicht mehr als einige Milliarden Jahre alt war. Wir stellen hier eine Methode vor, welche die Rekonstruktion und Modellierung der Kinematik von Galaxien, die durch den Gravitationslinseneffekt abgebildet werden, aus Beobachtungen von räumlich aufgelösten Emissionslinien ermöglicht. Die größte Innovation unserer Methode besteht darin, dass sie gleichzeitig die Massenverteilung der Linse und die Kinematik der Lichtquelle direkt aus dem ursprünglichen dreidimensionalen (3D) Datenraum rekonstruieren kann. Wir haben die Robustheit dieser Technik anhand mehrerer künstlicher Beobachtungen unterschiedlicher Datenqualität von sternbildenden Galaxien getestet, welche durch eine Vielzahl von kinematischen und geometrischen Eigenschaften gekennzeichnet sind. Wir haben festgestellt, dass die Rekonstruktionsgenauigkeit in den meisten Fällen innerhalb weniger Prozent liegt. Diese Technik stellt eine signifikante Verbesserung gegenüber den bisher verwendeten Methoden dar, weil die Kinematik der Lichtquelle nicht von den Unsicherheiten in der Fehlerfortpflanzung und der effektiven Auflösung der Lichtquelle beeinflusst wird. Außerdem erlaubt diese neue Methodologie das Studium sämtlicher Entartungen

zwischen den Parametern der Linse und den kinematischen Parametern, und schätzt damit die Unsicherheiten auf eine konsistente Weise ab.

Beobachtungen mit dem Atacama Large Millimeter/Submillimeter Array (ALMA) von Galaxien, die durch den Gravitationslinseneffekt abgebildet werden, sind besonders nützlich um räumliche Details bei $z \gtrsim 3$ zu untersuchen, die sonst nur für Galaxien im lokalen Universum beobachtbar sind. In dieser Arbeit konzentrierten wir uns auf ALMA-Beobachtungen der [CII] -Emissionslinie von SPT0418-47, einer staubigen sternebildenden Galaxie (DSFG, für engl. Dusty star-forming galaxy) bei $z = 4.2$. Basierend auf unserer kinematischen Analyse haben wir festgestellt, dass SPT0418-47 ähnliche dynamische Eigenschaften wie lokale Spiralgalaxien aufzeigt: SPT0418-47 ist rotationsgestüzt und weist eine geringe Turbulenz auf, das heißt sie ist dynamisch kalt. Dies weist unerwarteterweiße darauf hin, dass der gemessene Gasanteil und die hohe Sternentstehungsrate für diese DSFG keine hohen turbulenten Bewegungen antreiben und die Stabilität der Galaxie beeinträchtigen.

Mit Hilfe einer Studie von sechs durch den Gravitationslinseneffekt abgebildeten DSFGs mit Rotverschiebungen zwischen 3 und 5 zeigen wir, dass SPT0418-47 kein seltenes Objekt ist und weisen eine größere Präsenz dynamisch kalter Galaxien im frühen Universum nach. ALMA-Beobachtungen ihrer [CII] - Emissionslinien ermöglichen die Berechnung ihrer Rotationskurven und Geschwindigkeitsdispersionsprofile auf Sub-kpc-Skalen und liefern damit die bislang größte Stichprobe von $z \sim 4$ -Galaxien mit systematischen kinematischen Messungen. Insgesamt zeigt unsere Analyse, dass Galaxien mit hohen Rotverschiebungen nur schwach von extremen physikalischen Prozessen betroffen sind, was im Widerspruch zu Vorhersagen aus aktuellen theoretischen Modellen steht. Durch eine dynamische Dekomposition ihrer Rotationskurven untersuchen wir auch den evolutionären Zusammenhang zwischen diesen DSFGs und ihren plausibelsten Nachkommen, den lokalen elliptischen Galaxien (ETGs, für engl. Early-type galaxies). Wir fanden, dass einige der DSFGs bereits kugelförmige Massenkomponenten entwickelt haben und alle eine ähnliche Menge an baryonischer Masse wie lokale ETGs angesammelt haben. Diese Ergebnisse grenzen die Anzahl der Galaxienverschmelzungen und die Menge des angesammelten Materials stark ein, welches die sukzessive Umwandlung der DSFG-Population in massive lokale ETGs über einen Zeitraum von 12 Milliarden Jahren bewirkt.

Abstract

According to current galaxy formation and evolution models, in the early cosmic epochs, the gas within galaxies was highly turbulent due to vigorous gas accretion, mergers, feedback from star formation and supernova explosions. For this reason, it is expected that young galaxies have structural and dynamical properties strongly affected by these phenomena and distinct from those observed in nearby galaxies. Nevertheless, before now, observational challenges have hampered the possibility to test these theoretical predictions. The low angular resolutions and signal-to-noise ratio (SNR) of the observations significantly limit the study of the dynamics of such young galaxies. One way to overcome these limitations is to target strongly gravitationally lensed galaxies. The magnification provided by gravitational lensing increases the solid angle of background sources and hence their observed flux. As a result, distant objects can be observed with increased spatial resolutions and SNRs. This phenomenon, however, comes at a price: the effect of lensing distorts the distant sources, and it is not trivial to derive their intrinsic physical properties without introducing systematic errors.

This thesis focuses on the study of the kinematic and dynamical properties of gravitationally lensed galaxies at redshifts $z \gtrsim 3$ when the Universe was a few billion years old. We start by presenting a methodology that allows the reconstruction of lensed galaxies from spatially-resolved emission-line observations. The main novelty of our technique is that it simultaneously recovers the lens-mass distribution and the source kinematics directly in the native three-dimensional (3D) space of the data. We tested the robustness of this technique on mock observations of star-forming galaxies characterized by a variety of both kinematic and geometrical properties and data quality, finding that the accuracy of the model parameters stays within a few percent in most cases. This technique represents a significant improvement over the methods used until now, as the source kinematics is not affected by the uncertainties in the error propagation and the effective resolution on the source plane. Furthermore, this new methodology allows the study of any degeneracies between the lens and kinematic parameters and estimates their uncertainties consistently.

Observations of strongly lensed galaxies with the Atacama Large Millimeter/Submillimeter Array (ALMA) are especially useful for studying galaxies at $z \gtrsim 3$ with spatial details achievable otherwise only for galaxies in the local Universe. In this thesis, we focused on ALMA observations of the [CII] emission line from SPT0418-47, a dusty star-forming galaxy (DSFG) at $z = 4.2$. Based on our kinematic analysis, we found that SPT0418-47 has dynamical properties similar to those of local spiral galaxies: it is rotationally supported and has a low level of

turbulence, that is, it is dynamically cold. These features indicate that, unexpectedly, the high star-formation rate and the gas fraction measured for this DSFG do not drive high turbulent motions and affect the stability of the galaxy.

With a study of six lensed DSFGs at z between 3 and 5, we show that SPT0418-47 is not a rare object and reveal the wider presence of dynamically cold galaxies in the early Universe. ALMA observations of their [CII] emission line allow the derivation of the rotation curves and velocity dispersion profiles on sub-kpc scales, providing the largest sample of $z \sim 4$ galaxies with systematic kinematic measurements, so far. Overall, our analysis indicates that high-z galaxies are only weakly affected by extreme physical processes, challenging any predictions from state-of-the-art theoretical models. Through a dynamical decomposition of their rotation curves, we also investigate the evolutionary connection between these high-z DSFGs and their most plausible descendants, the local early-type galaxies (ETGs). We found that some of the DSFGs have already developed a spheroidal mass component, and all of them have assembled a similar amount of baryonic mass as the local ETGs. These results provide strong constraints on the number of mergers and the amount of accreted material that cause the successive transformation of the DSFG population into the massive local ETGs over a period of 12 billion years.

Chapter 1

Introduction

The focus of this thesis is the study of the kinematic and dynamical properties of star-forming galaxies at important cosmological epochs. Our research is devoted to improving current constraints on galaxy formation models through detailed studies of strongly gravitationally lensed galaxies in the early Universe. To fully exploit the significant advantages given by strong gravitational lensing, we developed a new code that accurately determines the distortions caused by the foreground gravitational lens and reconstructs the kinematics of the background source. The application of this code on high-quality data obtained through state-of-the-art sub-mm/mm interferometers allows us to robustly determine the dynamics of galaxies on scales as small as those achievable only for nearby galaxies. Thanks to this unprecedented view, this thesis brings new insights on the central mechanisms shaping galaxies when the Universe was just $\sim$ 1 - 2 Gyr old.

The purpose of this chapter is to give the reader the necessary background information to interpret the results and evaluate the methods presented in this thesis. In Section 1.1, we briefly summarize the theoretical framework of galaxy formation and evolution in a cosmological context and underline the main challenges of current numerical simulations. The evolution of the star formation and morphological properties of galaxies are summarized in Sections 1.2 and 1.3, respectively. In Sections 1.4 and 1.5, we give an overview of the current status of knowledge on the evolution of galaxy dynamics and describe the challenges of observational studies. The basics of gravitational lensing are described in Section 1.6. Finally, Section 1.7 presents the outline of the thesis and the scientific questions that it addresses.

1.1 Galaxy formation in the ΛCDM cosmology

According to the current paradigm of structure formation in the Cold Dark Matter (CDM) cosmological framework, galaxies form from the collapse of dark-matter overdensities and grow through the accretion of both baryons and dark matter (see review by Benson 2010). In the classical picture of galaxy formation (Rees & Ostriker 1977, White & Rees 1978), after falling into the dark matter halo, the gas from the intergalactic medium (IGM) shock-heats

to the virial temperature of the halo, then cools and condensates into the halo center. In the successive epochs, galaxies accrete new gas in a stochastic and rapid way through mergers.

In the last two decades, numerical simulations (e.g., Kereš et al. 2005, Dekel et al. 2009a, Nelson et al. 2015) have shown that the accretion of gas is significantly more complex. In particular, gas accretion from the IGM can occur in two different modes, cold and hot. In the first case, filamentary structures from the IGM enter the galaxy along cold streams without being heated. In the hot-mode accretion, the infalling gas is shock heated, and it is available as a reservoir for later star formation on timescales set by the cooling time. Simulations (Dekel et al. 2009a, van de Voort et al. 2011) suggest that the mass of the dark matter halo determines the dominant accretion mode: at $z \sim 0$, above a critical mass of $\sim 10^{12}\ M_{\odot}$ the gas is accreted in the hot mode. Cold-mode accretion dominates, instead, at high redshift (z) and in low mass galaxies at low-z. The physical properties of the accreting gas, such as density and temperature, and angular momentum, affect the morphology and features of the end-product galaxies (Lagos et al. 2017).

On the other hand, the growth of galaxies through accretion and mergers is partly prevented by the expulsion and heating of gas driven by active-galactic-nuclei (AGN) or stellar feedbacks. While the evolution of dark matter structures is driven only by gravity, proper treatment of the evolution of baryonic structures must, therefore, include all these complex physical processes, e.g., gas heating and cooling, AGN and stellar feedback, chemical enrichment, gas accretion. For example, in state-of-the-art cosmological simulations, stellar and AGN feedbacks are essential ingredients to reproduce some of the observed galaxy properties (Nelson et al. 2019). However, these processes operate on physical scales that are not resolved by current simulations and are usually parametrized using simple sub-resolution prescriptions (Kim & Ostriker 2018, Nelson et al. 2019). The results of cosmological simulations are thus strongly dependent on the different implementations of these sub-resolution models and may not be able to capture the detailed physical mechanisms at work (Naab & Ostriker 2017, Vogelsberger et al. 2020).

1.2 Interstellar medium and star formation

Hydrogen is the most abundant element in the Universe, and it is located both in the IGM and in the interstellar medium (ISM). In particular, in the ISM, hydrogen can be present in different thermal phase components (Tielens 2005, Cimatti et al. 2019):

- molecular, with a temperature $T \sim 10$ K. In local galaxies, the molecular gas can be found mainly in so-called giant molecular clouds, and it constitutes the reservoir for the formation of stars;
- neutral, with a typical T in the range between 30 and 120 K;
- neutral and ionized, with typical T of 8000 K and 10^4 K, respectively. Ultraviolet (UV) photons from young massive stars are the main source of the photoionization or heating of the neutral gas;

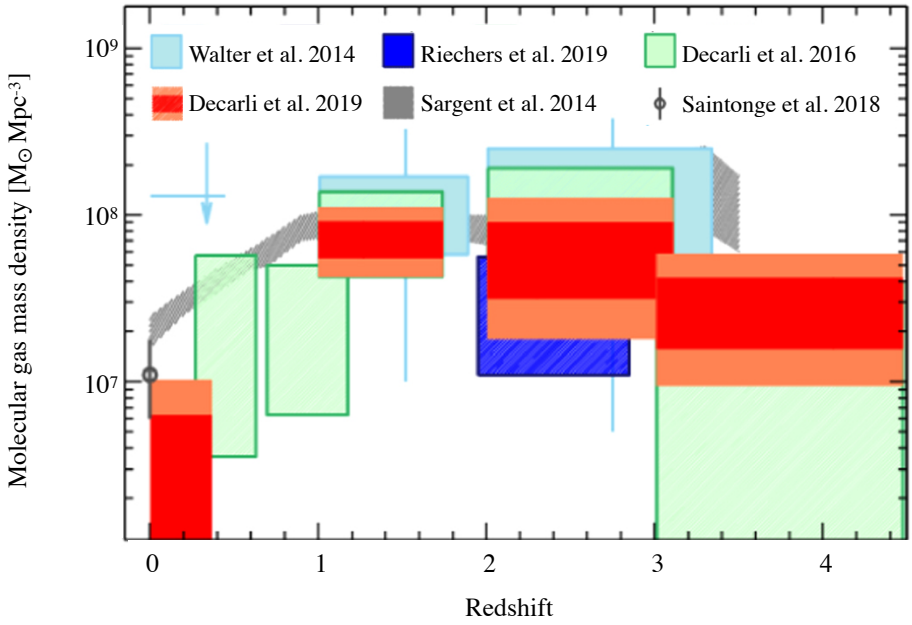

Figure 1.1: **Cosmic evolution of the molecular mass.** Observational estimates of the total molecular mass density per comoving volumes at different redshifts. The cyan, blue, green and red boxes show the measurements from Walter et al. (2014), Riechers et al. (2019), Decarli et al. (2016) and Decarli et al. (2019), respectively. The gray circle is a measurement for nearby galaxies from Saintonge et al. (2018). The gray area shows an empirical prediction of cosmic molecular density evolution (Sargent et al. 2014). This figure is adapted from Decarli et al. (2019).

- ionized and hot, with $T \gtrsim 10^6$. In this case, the gas is very diffuse and possibly generated by supernova explosions.

The evolution of galaxy properties across cosmic time is closely linked to the continuous exchange of gas from one thermal phase to another via different heating and cooling processes.

Recent studies (Decarli et al. 2016, 2019, Walter et al. 2016, Riechers et al. 2019) have shown that the amount of molecular gas within galaxies increases with redshift and has a peak at $z \sim 2$ (see Figure 1.1). This result is not surprising: molecular gas is the fuel of star formation, and its evolution matches the star formation history of our Universe. Multiwavelength observations over the last years have shown, indeed, that the cosmic star formation rate (SFR) density has a peak at $z \sim 1$ - 3 and then declines by a factor of 10 - 15 at the present epoch (Madau & Dickinson 2014, see Figure 1.2).

In the Local Universe, most of the cosmic star formation occurs in galaxies that lie in the so-called main sequence (MS), a tight almost linear relation between the SFR and the stellar mass (Brinchmann et al. 2004, Noeske et al. 2007, Speagle 2019). The MS holds up to $z \sim 6$ with a normalization that increases at earlier epochs, indicating that at a fixed stellar mass,

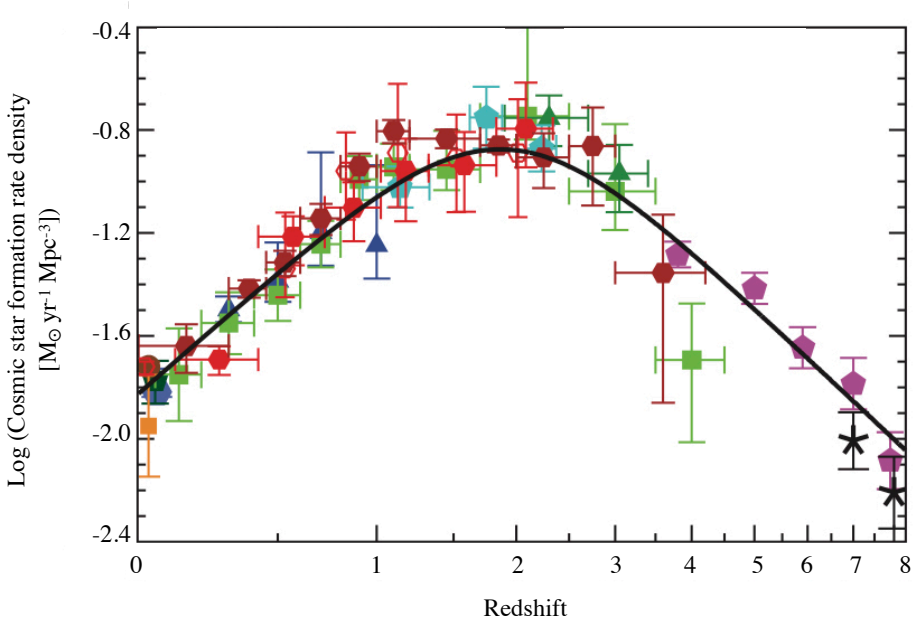

Figure 1.2: **Star-formation history of the Universe.** The cosmic star-formation rate density from UV and infrared observations as a function of redshift. This figure is adapted from Madau & Dickinson (2014).

a galaxy on the MS at high-z has a higher SFR than its local counterpart (Speagle 2019, Whitaker et al. 2012). The small scatter of the MS at all redshifts has been used to argue that smooth processes, e.g., gas accretion, rather than mergers and interactions (Schreiber et al. 2015, Rodighiero et al. 2015) dominate the growth of galaxies.
Starbursts are a distinct class of galaxies that are forming stars at a rate which is typically two orders of magnitude larger than the MS, and are likely the end-product of gas-rich major mergers, at least at $z \sim 0$ (Casey et al. 2014). Until recently another group of galaxies, that of dusty star-forming galaxies (DSFGs, see Section 1.4.3 for further details) at high-z, was believed to be a class of objects analogues to local starbursts (Casey et al. 2014). Recent studies (e.g. Michałowski et al. 2014, Koprowski et al. 2016, Michałowski et al. 2017, Hodge & da Cunha 2020), however, have shown that these are a heterogeneous population made up of both starbursts and normal MS galaxies.

Massive galaxies, lying below the MS because of their low star-formation activity, have been observed at $z \lesssim 3$ (Cappellari et al. 2013b, Lang et al. 2014, Belli et al. 2017, Glazebrook et al. 2017). In this passive population, a quenching mechanism has prevented the cooling of gas and the subsequent formation of new stars. At present, it is not yet clear whether the quenching processes causing the transition of galaxies from the MS to the passive population depend on the mass of the dark matter halos (i.e., hot-mode accretion, see Section 1.1) or processes internal to the galaxies (Man & Belli 2018), such as AGN feedback that causes the expulsion or heating of the cold gas (see recent review by Harrison 2017) and morphological quenching, where a stellar spheroidal component, i.e., a bulge, stabilizes the gas disk against

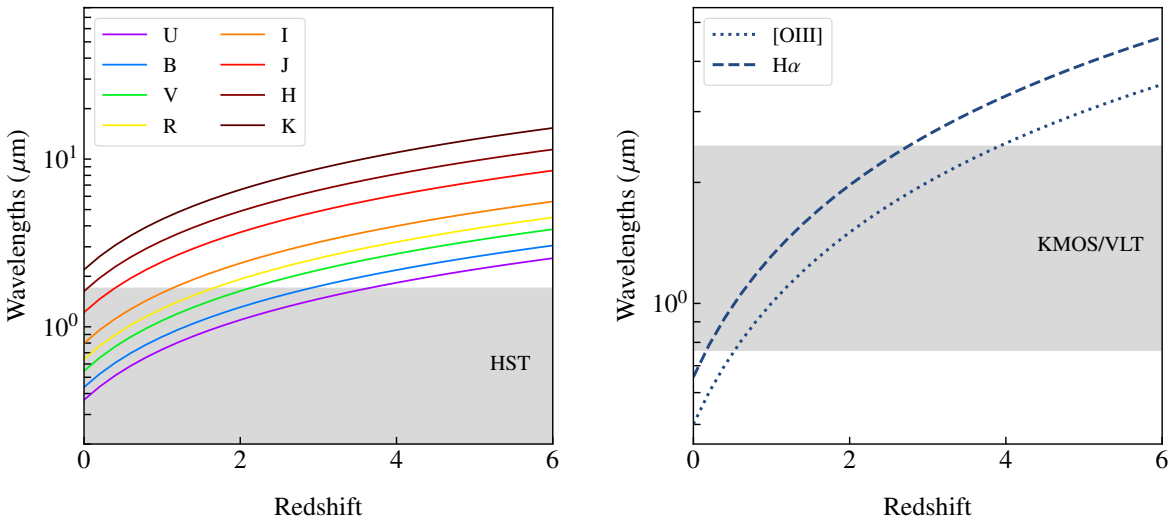

Figure 1.3: **Redshifted wavelengths.** Left panel: redshifted effective wavelengths of the optical (U, B, V, R, I) and NIR (J, H, K) bands in the Johnson-Cousins system (Bessell 2005). The shaded area shows the wavelength range covered by the Hubble Space Telescope (HST), the only space telescope able to spatially resolved the optical continuum emission from galaxies at high-z, nowadays. Right panel: redshifted emission lines, usually used as kinematic tracers at $1 \lesssim z \lesssim 3$. The shaded area shows the wavelength range covered by KMOS, a state-of-the-art IFU instrument on the VLT.

fragmentation (Martig et al. 2009).

1.3 Galaxy morphology across cosmic time

The study of the morphology and structure of galaxies requires rest-frame optical/near-infrared (NIR) observations. In these spectral ranges, the emission is dominated by low-mass stars that contribute to the bulk of the galaxy stellar mass. Observations at wavelengths $\lesssim$ 4000 Å are, instead, dominated by the emission of young stars and can thus be wrongly biased towards clumpy and irregular morphologies (Carilli & Walter 2013, Chen et al. 2015). Due to the lack of telescopes able to spatially resolve the rest-frame optical and NIR at $z \gtrsim 2$, to date, we have been able to study galaxy structures up to $z \sim 2$ (see left panel in Figure 1.3).

The star-formation properties of galaxies are very strongly correlated with their morphologies both in the local (Morselli et al. 2017, Cook et al. 2020) and in the most distant Universe (Lang et al. 2014). At low-z, galaxies in the MS have prominent disks and show a trend of increasing bulge-to-total stellar mass ratio (B/T, Cook et al. 2020) as a function of stellar mass. Low-mass galaxies with stellar masses $M_{\rm star}$ of $\sim 10^9$ - $10^{10} M_\odot$ are nearly pure disks, while high-mass galaxies with $M_{\rm star}$ of $\sim 10^{11} M_\odot$ have typical B/T of $\sim$ 0.4 (Cook et al. 2020). At all stellar masses, galaxies below the MS are, on average, more bulge dominated

(Morselli et al. 2017) than those on or above it. In particular, the massive quiescent galaxies, also called early-type galaxies (ETGs), have typical B/T $\gtrsim 0.5$ (Krajnović et al. 2013).

Studies on the morphology of galaxies (van der Wel et al. 2014, Lang et al. 2014) at the peak epoch of star-formation show that the structures observed in nearby galaxies were already in place at $z \sim 2$ (Lang et al. 2014). Galaxies on the MS are, on average, disk dominated also at these epochs, with typical B/T $\lesssim 0.5$ (Lang et al. 2014). At a given total stellar mass, even at these high redshifts, quenched galaxies have B/T larger than star-forming systems.

1.3.1 Evolutionary connection between low- and high-z galaxies

It is now well established that galaxy-formation follow the so-called downsizing scenario: more massive galaxies have assembled earlier and on shorter timescales (Thomas et al. 2010). Stellar population studies of local ETGs have shown, indeed, that more than half of the stars in the most massive galaxies were formed at $z \gtrsim 2$ (McDermid et al. 2015). Furthermore, recent studies have found a spectroscopically-confirmed population of massive, quiescent galaxies that are a few Gyr old already at $z \sim 2$ (Belli et al. 2017, Glazebrook et al. 2017). The properties of the quiescent populations both at low and intermediate redshifts suggest that their progenitors should belong to the star-forming population at $z \gtrsim 3$ (Belli et al. 2017, Hodge & da Cunha 2020). The matching number densities, stellar masses and sizes of the massive star-forming at $z \sim 4$ and quiescent populations at $z \lesssim 2$ seem to support this picture (Toft et al. 2012, Valentino et al. 2020). Observations of the DSFGs and the high-stellar mass galaxies at $z \gtrsim 4$ in the MS allow one to gain insights into the formation of the massive quiescent galaxies at intermediate and low redshifts.

1.4 Galaxy dynamics across cosmic time

The study of galactic kinematics and dynamics plays a key role in our understanding of galaxy evolution and structure formation. In particular, measurements of galactic rotation curves, describing the variation of the circular velocity as a function of the galactocentric radius, are a powerful tool to constrain the distribution and the composition of mass in galaxies across cosmic time (e.g., Sofue & Rubin 2001, Lelli et al. 2016, Genzel et al. 2017, Tiley et al. 2019). For example, in the 1970s and 1980s, the flat rotation curves of spiral galaxies became one of the main pieces of evidence of the presence of dark matter (e.g., Rubin et al. 1978, Bosma 1981, van Albada et al. 1985). In particular, the discrepancy between the expected rotation curves, as derived from the visible matter (stars and gas) and the flatness of the observed rotation curves were later used to estimate the radial profile of the dark matter haloes (e.g. van den Bosch & Swaters 2001, de Blok et al. 2001, Walker & Peñarrubia 2011).

The gas velocity dispersions, $\sigma_{\rm gas}$, measured through the broadening of the emission lines, is the second key observable to gain insights into the dynamics of galaxies, and in particular on the level of turbulent motions. The line width is the result of thermal broadening,

characterized by a velocity dispersion $\sigma_{\rm th}$, and turbulence within the gas, characterized by a velocity dispersion $\sigma_{\rm turb}$ (Utomo et al. 2019, Cimatti et al. 2019). The intrinsic gas velocity dispersions, $\sigma_{\rm gas}$ is thus the sum in quadrature of these two contributions, $\sigma^2_{\rm gas} = \sigma^2_{\rm th} + \sigma^2_{\rm turb}$. Random motions of the particles within the fluid contribute to the thermal broadening, in a way that is dependent on their temperature T. The thermal velocity dispersion contribution is thus given by $\sigma_{\rm th} = \sqrt{k_{\rm B}T/(\widetilde{m}m_{\rm p})}$, where $k_{\rm B}$ is the Boltzmann constant, $\widetilde{m}$ is the mean average mass of the particle in the fluid in units of the proton mass, while $m_{\rm p}$ is the mass of the proton. For the multiphase gas composing the ISM of star-forming galaxies $\sigma_{\rm th}$ has typical values of 0.1, 8, 10 km s^{-1} for the molecular, neutral and ionized medium, respectively (Tielens 2005, Cimatti et al. 2019)[1]. For each gas phase, observed velocity dispersions $\sigma_{\rm gas}$ larger than their corresponding $\sigma_{\rm th}$ can be attributed to turbulent motions (see Section 1.4.1).

A common way to describe the dynamical status of a galaxy is through the ratio of rotational velocity ($V_{\rm rot}$) to velocity dispersion, i.e., the V/σ ratio. This measure quantifies the relative contribution of ordered and turbulent motions (see Figure 1.6).

1.4.1 Low-z galaxies

Studies of nearby star-forming galaxies have used the 21 cm emission line from the atomic hydrogen (HI) as one of the best kinematic tracers of the gravitational potential: its extension beyond the stellar component, allows one to trace the gravitational potential up to 10s kpc, where the dark matter is expected to dominate (Walter et al. 2008, Lelli et al. 2016, Kleiner et al. 2019, see Figure 1.4). The inner regions of the rotation curves of nearby galaxies are, instead, characterized by a variety of shapes that mainly reflect their stellar distributions. In particular, we can distinguish three main classes of rotation curves (Cimatti et al. 2019):

- rotation curves that steeply rise and then decline before flattening at large radii. These curves are typical of massive spiral galaxies with large stellar bulges, i.e., central spheroidal component (Figure 1.5, panel a);
- the typical present-day disk galaxy has a rotation curve with an inner rise and then a flattening out to the outermost measured value (Figure 1.5, panel b);
- slowly rising rotation curves are typical of dwarf galaxies (Figure 1.5, panel c).

In the inner regions of most local star-forming galaxies, the observed velocity dispersion $\sigma_{\rm gas}$ typically exceeds the expected values and is of the order of 3 - 6 km s^{-1} for the molecular gas observed through the CO lines (Mogotsi et al. 2016, Bacchini et al. 2019, 2020), 15 - 20 km s^{-1} for the neutral gas traced by the HI line (Mogotsi et al. 2016, Iorio et al. 2017), and 15 - 30 km s^{-1} for the ionized medium observed through the recombination line Hα at 6563 Å (Moiseev et al. 2015, Varidel et al. 2020). The discrepancy between the observed and the

[1]We used $\widetilde{m} \approx 2.3$ and $T = 10$ K for the molecular medium, $\widetilde{m} \approx 1.3$ and $T = 8000$ K for a neutral gas of hydrogen, helium and metals, $\widetilde{m} = 0.6$ and $T = 10^4$ K for the ionized gas (Tielens 2005, Cimatti et al. 2019).

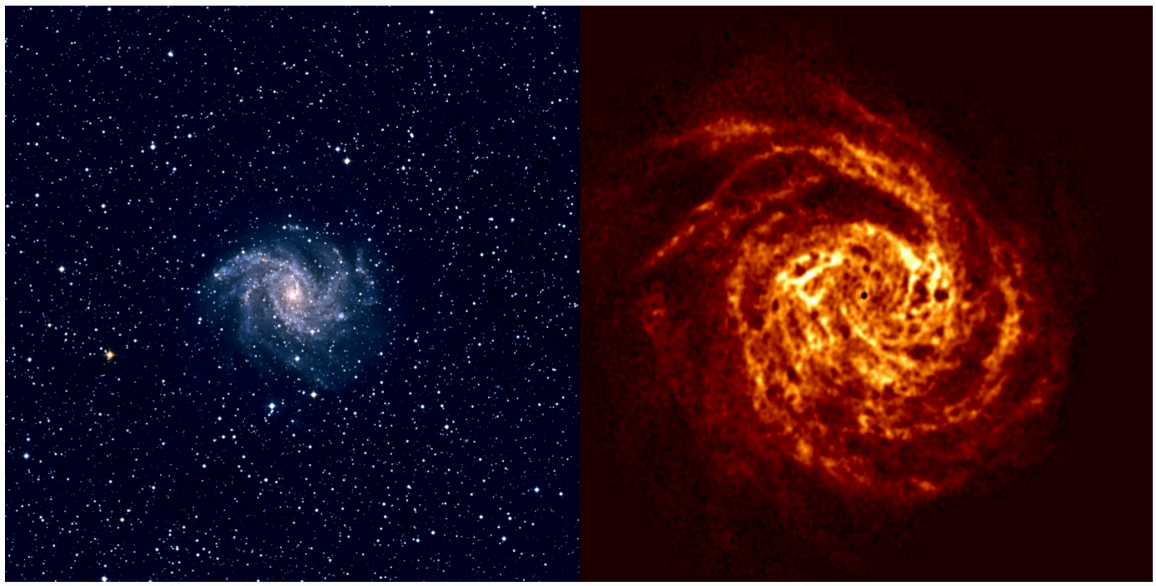

Figure 1.4: **NGC 6946 at different wavelengths.** Optical (left panel) and HI (right panel) emission from the nearby spiral galaxy NGC 6496. The two images are on the same scale, showing how the HI emission is much more extended than the stellar component. Image Credit: Boomsma et al. (2008)

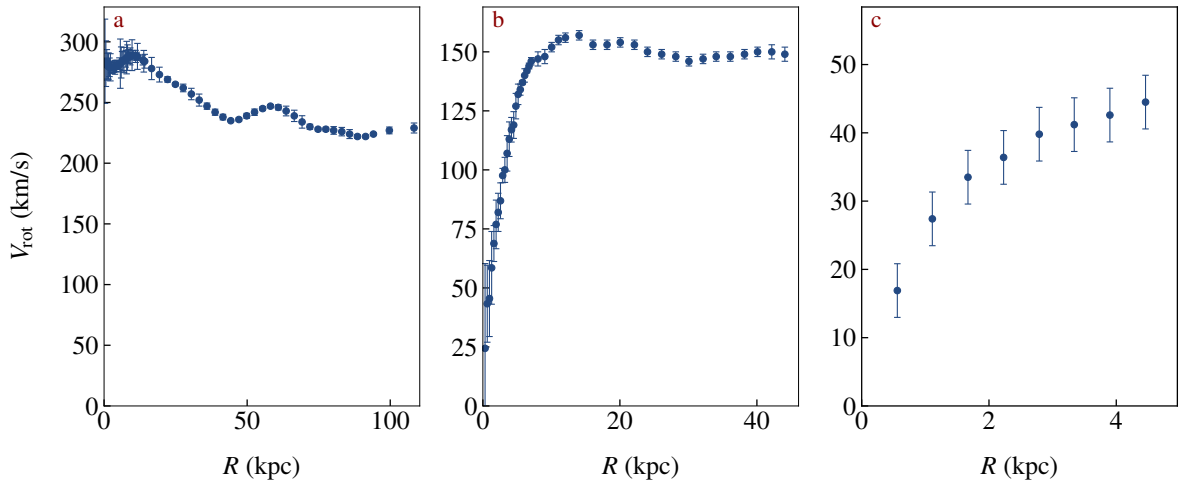

Figure 1.5: **Different shapes of the local rotation curves.** Rotation curves for the massive spiral galaxy UGC 9133 (panel a), for the typical disk galaxy NGC 3198 (panel b) and for the dwarf irregular UGC 5918 (panel c). The rotation velocities are taken from Lelli et al. (2016).

thermal broadening of the line is usually ascribed to the presence of turbulent motions. Given that turbulence dissipates on a short timescale ($\sim 10^7$ yr, Mac Low et al. 1998, Stone et al. 1998), a continuous energy source able to feed the observed non-thermal motions is required

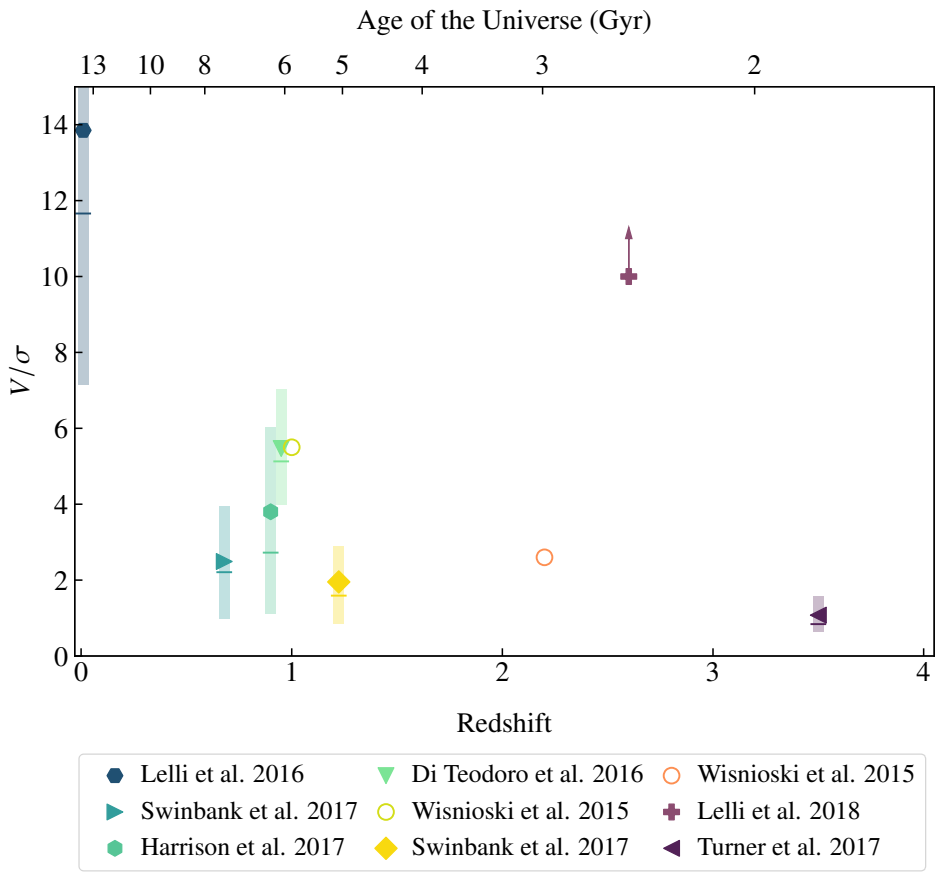

Figure 1.6: **Observed V/σ versus z.** Mean ratios of the rotational to random motion versus redshift for the samples of observed star-forming galaxies indicated in the legend. The gas tracers are: HI (Lelli et al. 2016), Hα (Swinbank et al. 2017, Harrison et al. 2017, Di Teodoro & Fraternali 2015, Wisnioski et al. 2015), [OII] (Swinbank et al. 2017), [OIII] (Turner et al. 2017) and [CI] (Lelli et al. 2018). The shaded regions show the area between the 16th and 84th percentiles of the sample distributions, and the horizontal bars show the median values (where available). The violet cross is a lower limit for a single galaxy.

(e.g. Stilp et al. 2013, Utomo et al. 2019). The most plausible drivers of turbulence are stellar feedback from massive stars and supernova explosions (Joung & Mac Low 2006, Bacchini et al. 2020), gravitational instabilities (Krumholz & Burkhart 2016, Krumholz et al. 2018) and magneto-rotational instabilities (Dziourkevitch et al. 2004).

Overall, the kinematics of most local star-forming galaxies is dominated by circular motions, with typical $V_{\rm rot}$ from 100 to 300 km s^{-1} and average values of the HI velocity dispersion of 10 km s^{-1} (Lelli et al. 2016), resulting in $V/\sigma \gtrsim 10$ (see Figure 1.6).

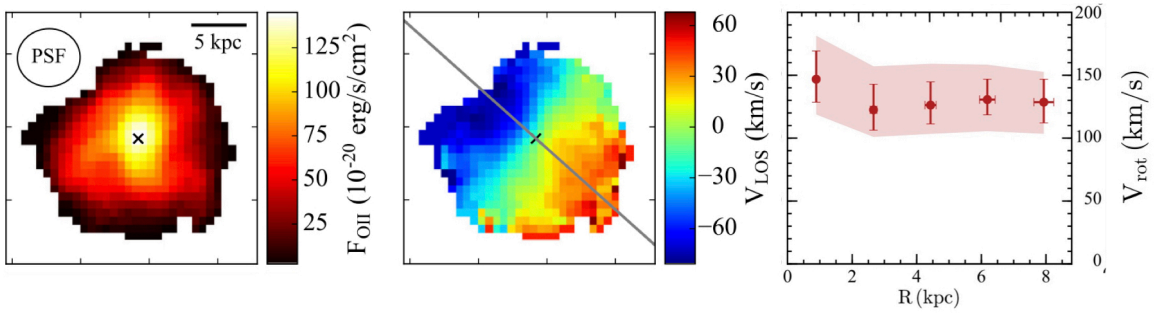

Figure 1.7: **Kinematic observations at $z \sim 1.5$.** From left to right: [OII] intensity maps, velocity fields and rotation curve for Sp1149, a star-forming galaxy at $z = 1.49$. The ellipse in the intensity map shows the point-spread function for this observation, while the bar shows the angular scale corresponding to 5 kpc. In the velocity field map, the image is color-coded according to the observed line-of-sight velocities as indicated in the color bar. The red circles in the right panel show the five resolution elements that sample the rotation curve. This figure is adapted from Di Teodoro et al. (2018).

1.4.2 Galaxies at $1 \lesssim z \lesssim 3$

At $z \gtrsim 0.5$, galaxy kinematics can not be studied using the HI line, due to the limited sensitivities of current radio telescopes. This lack of HI observations prevents the study of their kinematics at large radii, where the dark matter should give the largest contribution to the galaxy gravitational potential. In the last decade, studies of the molecular gas content for a few hundred galaxies were published (e.g., a recent review is given by Tacconi et al. 2020). However, to date, only a handful of galaxies (e.g., Übler et al. 2018, Girard et al. 2018) have spatially resolved observations with a signal-to-noise (SNR) high enough to allow one to investigate their kinematic properties through the CO emission lines.
The easiest way to study the kinematics of galaxies at the peak epoch of star formation is, therefore, to observe their optical recombination (e.g., Hα for galaxies at $z \approx 1$ - 2) or forbidden (e.g., [OIII] at 5007 Å for galaxies at $z \approx 3$) emission lines tracing the ionized gas component through Integral Field Unit (IFU) observations (see right panel in Figure 1.3). In particular, a few hundreds galaxies at $1 \lesssim z \lesssim 3$ were observed (Förster Schreiber et al. 2006, Wisnioski et al. 2015, Turner et al. 2017, Jones et al. 2010b) with the latest generation IFU instruments, e.g., the K-band Multi-Object Spectrograph (KMOS, Sharples et al. 2013) on the Very Large Telescope (VLT). However, only a small fraction has high-quality observations. The small intrinsic sizes of high-z galaxies combined with seeing-limited observations result, indeed, in barely spatially resolved data (i.e., the rotation curve is sampled by a few resolution elements, see Figure 1.7) or observations in adaptive-optic (AO) mode are characterized by low SNR (see Chapters 2).

On average, galaxies at the peak epoch of star formation show a large variety of kinematics properties. Several studies (e.g. Swinbank et al. 2017, Turner et al. 2017, Wisnioski et al.

2019) have attempted to classify these galaxies in different kinematic categories: rotating disks, dispersion dominated systems, irregular rotators, merger-like systems. However, the actual fraction of each kinematic class is debated. For example, the fraction of rotating disks seems to rise as the quality of the observations improves, moving from an initial value of $\sim$ 30 percent (Förster Schreiber et al. 2006, Swinbank et al. 2017) to more than $\sim$ 80 percent (Wisnioski et al. 2015, 2019), suggesting that these classifications are strongly biased by observational limitations, in particular by the so-called "beam smearing" effect (see Section 1.5).

While in the Local Universe the flatness of the rotation curves and the matter content of star-forming galaxies is a well-established fact, at high-z it is currently a matter of debate. For example, declining rotation curves were found by Lang et al. (2017) and Genzel et al. (2017) and explained as an indication of baryon dominated systems, with a negligible fraction of dark matter. These two studies raise questions of whether or not such a result is consistent with the current cosmological framework (Genzel et al. 2017, Teklu et al. 2018). On the other hand, Tiley et al. (2019) showed that the findings of Lang et al. (2014) and Genzel et al. (2017) depend on their specific assumptions used to derive the rotation curves, concluding that rotation curves at these intermediate redshifts are approximately flat, as also found by, e.g., Mason et al. (2017), Di Teodoro et al. (2016) and Lelli et al. (2018).

The velocity dispersions of high-z star-forming galaxies are higher by a factor of $\sim$ 2 - 5 compared to local star-forming galaxies (Wisnioski et al. 2019, Übler et al. 2019). If these high values of velocity dispersion are intrinsic and not affected by instrumental artifacts, they imply that the physical mechanisms considered the main drivers of turbulence at low-z (Section 1.4.1) have a more significant effect in the high-z Universe (Krumholz et al. 2018, Johnson et al. 2018, Übler et al. 2019). However, note also that, by using a direct forward technique to derive the kinematics (Di Teodoro et al. 2016), some studies (Di Teodoro & Fraternali 2015, Di Teodoro et al. 2018, Lelli et al. 2018) have found that galaxies up to $z = 2.6$ have a velocity dispersion typical of low-z disks.

Overall, at the peak epoch of star-formation, a significant fraction of star-forming galaxies is a rotating disk, with typical values of $V/\sigma \lesssim 10$ (see Figure 1.6). Such values of V/σ are smaller than those measured for local galaxies, indicating an evolution of the dynamical properties with redshift. Whether this evolution is real or a result of observational limitations (see Section 1.5), is something that we will be able to investigate only with the next-generation telescopes (see Chapter 5).

1.4.3 Galaxies at $z \gtrsim 4$

Up to date, a few observations (e.g., De Breuck et al. 2014, Litke et al. 2019, Johnson et al. 2018, Smit et al. 2018) of galaxy kinematics at $z \gtrsim 4$ have been reported in the literature. While there is an indication that also at these high-z, some galaxies are rotating disks (De Breuck et al. 2014, Smit et al. 2018, Johnson et al. 2018), the strong uncertainties on the measured velocity dispersion hamper robust estimates of their dynamical status and their V/σ

ratios.

The study of galaxies at $z \gtrsim 4$ is challenging due to limitations of the currently available telescopes (see Figure 1.3). For a galaxy at $z \sim 4$, the continuum optical/NIR emission, tracing the stellar component, and the optical emission lines, tracing the ionized gas component, are redshifted into the mid-infrared (MIR) wavelength range. This spectral window can not be observed with ground-based telescopes due to the opacity of the Earth's atmosphere at these wavelengths (Casey et al. 2014). At the same time, because of the coarse angular resolutions of the currently available space telescopes in the MIR, e.g., $\gtrsim 2$ arcsec for Spitzer, (Werner et al. 2004), spatially-resolved rest-frame optical studies of the kinematics and structures of galaxies will be feasible only with the next-generation telescopes (see Chapter 5).

One of the way to study galaxies at $z \gtrsim 4$ is to look at their rest-frame emission in the far-infrared (FIR) that is redshifted into the sub-mm wavelength range. The sub-mm spectral window can be probed efficiently with the Atacama Large Millimeter/Submillimeter Array, ALMA, e.g., (Wootten & Thompson 2009). In the last years, ALMA studies have revealed that observations of the fine-structure transition from the ionized carbon (i.e., [CII]; see Chapter 3 for details) are a promising tool for the investigation of the kinematics of galaxies at these epochs. However, due to the long integration times needed to observe typical unlensed galaxies (see Section 1.6), detailed dynamical studies at $z \gtrsim 4$ are still limited to a handful of sources. Besides, even with the superb angular resolution of ALMA, [CII] observations at these high-z have poor spatial resolutions (≈ 1 kpc), so that kinematic studies suffer from the same uncertainties described in Section 1.4.2.

Overall, the easiest way to study galaxy kinematics at $z \gtrsim 3.5$ is to target DSFGs. As mentioned in Section 1.2, DSFGs are objects with SFR $\gtrsim 100$ $M_{\odot}$/yr, high dust content and, as a consequence, very bright FIR luminosities (e.g., Casey et al. 2014, Hodge & da Cunha 2020). The UV radiation, emitted by young, massive stars, is, indeed, absorbed by the dust grains and re-emitted in the FIR range. Furthermore, thanks to the so-called negative K-correction (Cimatti et al. 2019), DSFGs have constant brightness in the sub-mm/mm range from $z \sim 1$ up to $z \sim 10$ (Casey et al. 2014). The peak of the dust emission at $\sim 100\mu$m is, indeed, redshifted in the sub-mm/mm, countering the dimming due to the increased cosmological distances.

1.5 The beam-smearing effect

Nowadays, the majority of kinematic studies of high-z galaxies covers the redshift range between 1 and 3, where the emission lines tracing the ionized gas can be easily observed using IFU instruments on ground-based telescopes (see right panel in Figure 1.3). Typical IFU observations without AO have angular resolutions of ~ 0.5 - 1 arcsec, meaning that a $z \sim 2$ galaxy with a size of 2 arcsec, can be observed with less than four resolution elements. Under these conditions, the beam-smearing effect can strongly affect the derivation of the

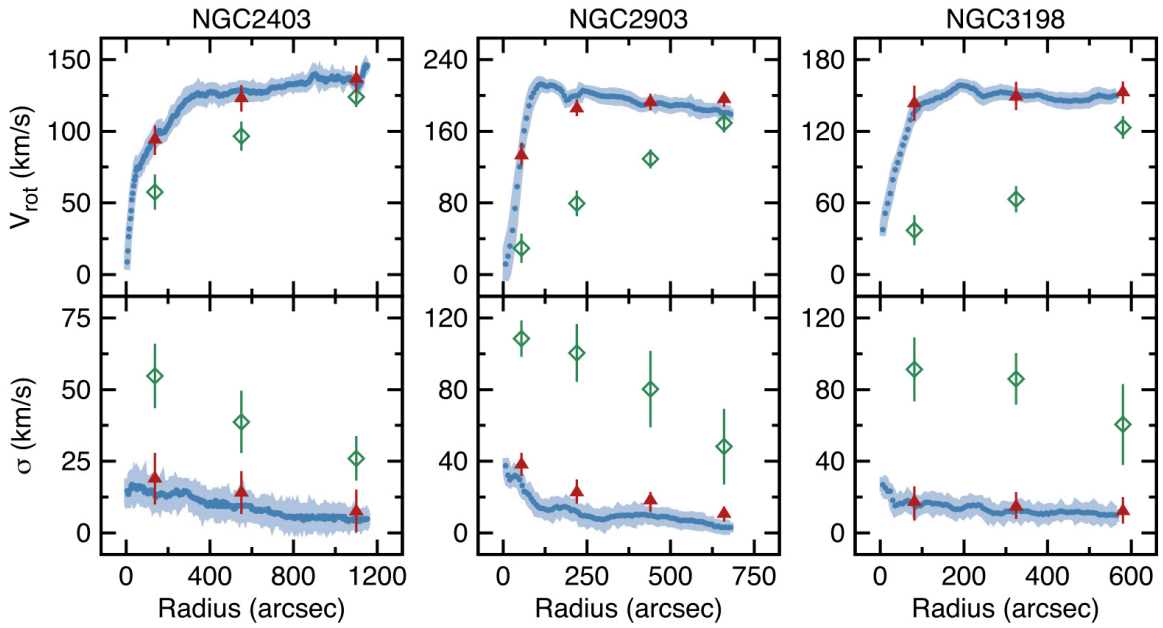

Figure 1.8: **The effect of beam-smearing on the kinematics.** Rotation velocity (top panels) and velocity dispersion (bottom panels) for three local spiral galaxies. The blue dots were derived using high spatial resolution observations. The green diamonds and the red triangles were derived using low spatial resolution observations. The green diamonds were obtained without a beam-smearing correction. To derive the red triangles, instead, a direct forward modeling (Di Teodoro & Fraternali 2015) was applied to correct for the beam-smearing effect. This figure is adapted from Di Teodoro & Fraternali (2015).

kinematics of galaxies. Because the point-spread-function (PSF) of the observations has a finite size the emission line at a given point in the galaxy is smeared onto the adjacent regions (Bosma 1978, Begeman 1987). As a consequence, the peak of the observed line profile (i.e., the line-of-sight velocity) is the flux-weighted average of the velocities from an area of the size of the PSF, while the width of the line profile becomes broader due to the contribution from different velocities coming from different part of the galaxy. The result of the beam-smearing effect is that the gradients in the velocity fields may become shallower and there is a consecutive increase of the observed velocity dispersions (see Figure 1.8).

To date, a variety of approaches have been used to derive the intrinsic kinematic parameters of galaxies, while attempting to correct for the beam-smearing effect. Here, we summarize the most popular techniques employed in the literature, discussing their corresponding weaknesses and strengths:

- direct forward modeling technique (Di Teodoro & Fraternali 2015, Bouché et al. 2015). In this case, the data are fitted directly in their native three-dimensional (3D) space. A 3D kinematic model is convolved with the PSF and then compared directly with the data. While this approach guarantees the derivation of the intrinsic rotation velocity and

velocity dispersion even at low spatial resolutions, it requires high SNR observations, meaning that so far it could only be applied to small samples of galaxies.

- Forward modeling technique and 1D kinematic extraction (Wuyts et al. 2016, Übler et al. 2019). The fitting algorithm creates a 3D kinematic model convolved with the PSF and it then compares the 1D rotation velocity and velocity dispersion profiles of the data and the model, extracted along the major axis of the corresponding 2D maps. This method allows one to derive kinematic measurements even from low SNR observations, but it might result in biased values of both the rotation velocity and velocity dispersions (Davies et al. 2011).

- 2D modeling and beam-smearing correction map (Turner et al. 2017). In this case, only the velocity field is fitted with the corresponding 2D model map, while the observed velocity dispersion map is corrected using a "beam-smearing correction map". To obtain these model maps, one first creates a 3D kinematic model with a fixed and spatially constant velocity dispersion, then convolves the model with the observed PSF and finally produces the beam-smeared 2D velocity and velocity dispersion maps. The first is directly compared with the observed velocity fields, while the second is used to create the beam-smearing correction map. In particular, the difference between the beam-smeared velocity dispersion map of the model and the assumed constant velocity dispersion is applied to the observed velocity dispersion map. Due to the strong degeneracy between the rotation velocity and velocity dispersion, this method is not self-consistent. In particular, the derived values of the rotation velocity may depend on the assumed value of the velocity dispersion.

- A posteriori correction (Burkert et al. 2016, Harrison et al. 2017, Wisnioski et al. 2019). The rotation velocity and velocity dispersion are extracted from the major axis of the corresponding 2D maps. Empirical relations depending on the galaxy sizes, masses and the sizes of the PSF are then employed to correct both the rotation velocities and the velocity dispersions. Since this approach is time-inexpensive, it has been used on large samples of galaxies. However, it may largely suffer from residual contamination from the beam-smearing effect.

- Exclusion of inner regions Wisnioski et al. (2015). The velocity dispersions are measured from the outer regions of the galaxies, that in principle should be less affected by the beam-smearing effect. However, due to the sensitivities of the observations and the intrinsic sizes of high-z galaxies, the effect of beam-smearing can be significant even at the outermost measured values (see Figure 1.8). This method, therefore, results in strongly biased values of the derived kinematic parameters, towards low values for the rotation velocities and high values for the velocity dispersions.

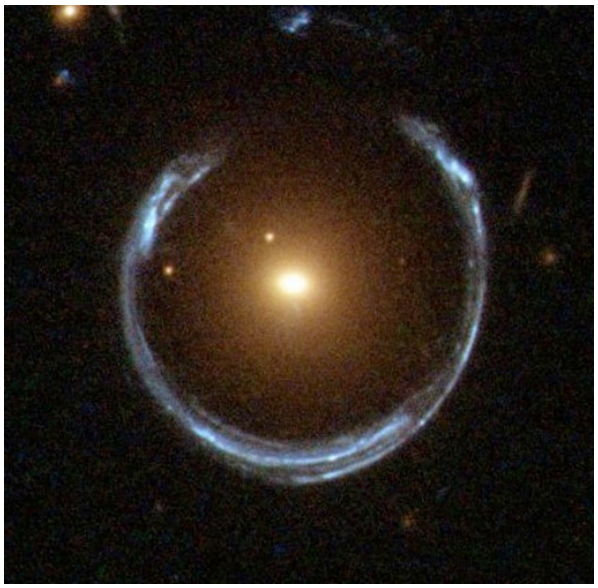

Figure 1.9: **Example of a strong gravitational lens system.** This figure shows the famous lens system known as the Cosmic Horseshoe. The foreground galaxy at the center of the figure is a massive ETG at $z = 0.45$, acting as a lens. The arc shows the lensed images of the background source at $z = 2.38$. Image credit: ESA/Hubble, NASA.

1.6 Strong gravitational lensing

In the previous section, we discussed how low spatial resolutions and SNR hinder observations of high-z galaxies and the study of their dynamical properties. In this thesis, we partly overcome these observational limitations by targeting strongly gravitationally lensed galaxies. Strong gravitational lensing occurs when the light emitted by a distant object (the source), e.g., a galaxy, encounters a massive object (the lens), e.g., a galaxy or a cluster of galaxies, along the line of sight to the observer. As the lens modifies the space-time geometry, the source will appear to the observer in the form of multiple, distorted and magnified images. In Figure 1.9, we show an example of a strong gravitational lens system where both the source and the lens are galaxies (galaxy-galaxy strong lensing). In Figure 1.10, we present a schematic view of the lensing phenomenon and refer the reader to Schneider (2006) for an extensive review of the theory of gravitational lensing in all of its forms.

To describe the lens system, for this thesis, we can assume that the gravitational field is weak[2], so that the gravitational effects can be linearized, and the thin-lens approximation is valid[3]. In

[2]The strength of the radiation field can be characterized through the dimensionless ratio between the gravitational potential of the deflector ψ and the square of the speed of light c, ψ/c^2. In the galaxy-galaxy lensing scenario, if the lens galaxy is in virial equilibrium and has a circular velocity v, then $\psi \sim v^2$. Considering a typical $v \sim 200$ km s^{-1}, we thus obtain $\psi^2/c^2 \lesssim 10^{-6} \ll 1$.

[3]A mass distribution for which the extent of the deflecting mass along the line-of-sight is much smaller than

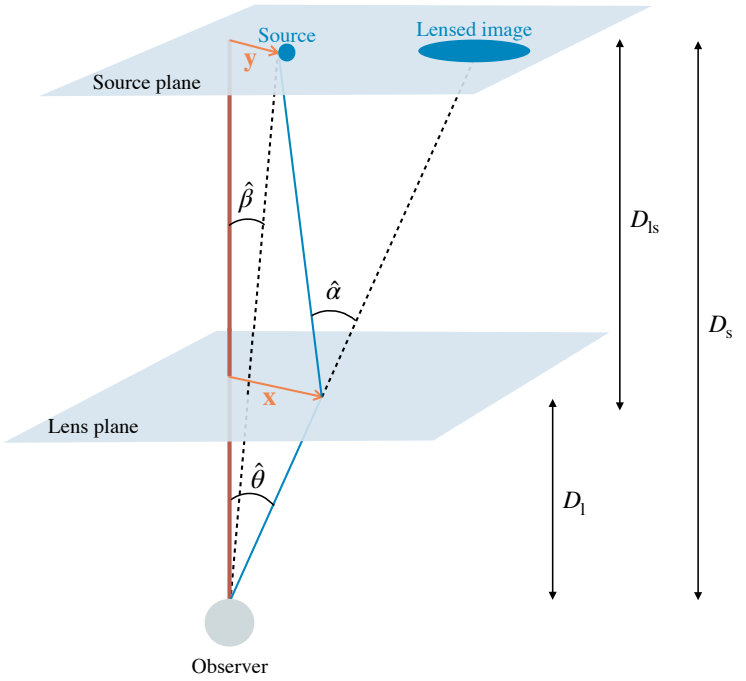

Figure 1.10: **Schematic representation of the gravitational lens geometry.** The blue lines shows the path of a light ray from the source to the observer in the presence of a massive object (e.g., a galaxy or a cluster of galaxy) that acts as a deflector.

Figure 1.10, the lens and the source planes are defined as the plane perpendicular to the line connecting the observer to the lens and the source, respectively. We define $\mathbf{y}$ the position of the source on the source plane, $\hat{\beta}$ the corresponding angular position, i.e., the angular position at which it would be observed in the absence of light deflection, while D_s is the angular diameter distance between the source and the observer. The position in the lens plane of a light ray coming from the source is denoted by $\mathbf{x}$ and $\hat{\theta}$ is its angular position, with coordinates (θ_1, θ_2). D_l and D_{ls} are the angular diameter distances between the lens and the observer and the lens and the source, respectively. Under the thin-lens approximation, the deflection angle $\hat{\alpha}(\mathbf{x})$ of a lens with a surface mass density distribution $\Sigma(\mathbf{x})$ is given by

$$\hat{\alpha}(\mathbf{x}) = \frac{4G}{c^2} \int d^2\mathbf{x}' \, \Sigma(\mathbf{x}') \frac{\mathbf{x} - \mathbf{x}'}{|\mathbf{x} - \mathbf{x}'|^2}, \tag{1.1}$$

where G is the gravitational constant and c is the speed of light.
Considering the geometry shown in Figure 1.10, the lens equation takes the form:

$$\hat{\beta} = \hat{\theta} - \frac{D_{ls}}{D_s} \hat{\alpha}(D_l \hat{\theta}) = \hat{\theta} - \vec{\alpha}(\hat{\theta}), \tag{1.2}$$

the distance between the observer and the lens and the distance between the lens and the source is called a geometrically thins lens.

where we have defined $\vec{\alpha} = \frac{D_{ls}}{D_s}\hat{\alpha}(D_l\hat{\theta})$. The condition for the formation of multiple images is thus that for a fixed $\hat{\beta}$, equation (1.2) has more than one solution for $\hat{\theta}$.
The deflection angle $\vec{\alpha}$ is usually written as a function of the dimensionless surface mass density or convergence, κ,

$$\vec{\alpha}(\hat{\theta}) = \frac{1}{\pi}\int d^2\hat{\theta}'\,\kappa(\hat{\theta}')\frac{\hat{\theta}-\hat{\theta}'}{|\hat{\theta}-\hat{\theta}'|^2}. \tag{1.3}$$

The explicit expression for the convergence κ is

$$\kappa(\theta) = \frac{\Sigma(D_l\hat{\theta})}{\Sigma_{cr}}, \text{ with } \Sigma_{cr} = \frac{c^2}{4\pi G}\frac{D_s}{D_l D_{ls}}. \tag{1.4}$$

It can be shown that the gravitational potential of the lens galaxy ψ is related to the convergence κ through the Poisson equation

$$\nabla^2\psi = 2\kappa. \tag{1.5}$$

It is clear from equations (1.2), (1.4), (1.5) that strong gravitational lensing observations can be used to measure the total mass distribution of the lens. Since the light is deflected independently of the nature and the state of the deflecting matter, gravitational lensing is equally sensitive to both baryonic and dark matter (e.g. Caminha et al. 2019, Rescigno et al. 2020). At the same time, strong gravitational lensing provides a magnified view of the source galaxy, and therefore it allows one to investigate the physical properties of distant source galaxies with a much higher SNR and angular resolution than otherwise possible. This, however, comes at a price: the shapes of the background galaxy are distorted, appearing as complete rings or arcs in the lens plane (see Figure 1.9). Hence, dedicated and sophisticated lens modeling codes are required to simultaneously infer the mass distribution of the lens and the intrinsic properties of the source (see Chapter 2). For sources smaller than the scales of the lens, the distortion of the images can be described by the Jacobian matrix $\mathbf{J}$ defined as $\mathbf{J} = \partial\hat{\beta}/\partial\hat{\theta}$. Under this assumption, the lensing equation can be linearized, so that $\hat{\beta}(\theta) = \hat{\beta}_0 + \mathbf{J}(\hat{\theta}_0)(\hat{\theta}-\hat{\theta}_0)$, where $\hat{\theta}_0$ is a point in the lens plane corresponding to the point $\hat{\beta}(\hat{\theta}_0)$ on the source plane. By defining the shear component γ as a combination of the second derivatives of the lensing potential, ψ, $\gamma = \sqrt{\gamma_1^2+\gamma_2^2}$, with

$$\gamma_1 = \frac{1}{2}\left(\frac{\partial^2\psi}{\partial\theta_1^2} - \frac{\partial^2\psi}{\partial\theta_2^2}\right),\ \gamma_2 = \frac{\partial^2\psi}{\partial\theta_1\theta_2}, \tag{1.6}$$

the Jacobian matrix $\mathbf{J}$ can be written explicitly as

$$\mathbf{J} = \begin{pmatrix}1-\kappa & 0\\ 0 & 1-\kappa\end{pmatrix} - \begin{pmatrix}\gamma_1 & \gamma_2\\ \gamma_2 & -\gamma_1\end{pmatrix}. \tag{1.7}$$

As can be seen from equation (1.7), the shear is responsible for stretching the intrinsic shape of the source, while the convergence κ induces an isotropic distortion.

The key feature of gravitational lensing is that it conserves the source surface brightness but changes the solid angle under which the source is seen, implying that the flux received from a distant source is magnified. In particular, the magnification μ is given by the determinant of the matrix $\mathbf{J}^{-1}$. The positions on the lens plane for which formally μ diverges, i.e., $\det(\mathbf{J}) \rightarrow 0$, are defined as the critical curves, while their mapping in the source plane define the caustic curves. Since real source galaxies have finite sizes, the magnification is always finite. Nevertheless, the lensed images corresponding to sources located close to the caustics are highly magnified near the corresponding critical curves.

1.7 This thesis

Despite the significant progress made in the last decade on the characterization of distant galaxies, detailed studies at the highest redshifts ($z \gtrsim 4$) have been rare because of observational limitations. This thesis aims to shed new light on the dynamical properties of DSFGs at $z \gtrsim 4$. By targeting strong gravitational lensed DSFGs, we probe the effects of baryonic physics on $\sim$ 100s parsecs scales, setting new constraints on galaxy formation models in the early Universe. In particular, we exploit the superb spatial resolutions obtained by combining ALMA and strong gravitational lensing to address the following questions:

- *Is there any observational signature of the extreme physical processes that are assumed to be the main drivers of galaxy evolution in the early Universe?* Galaxy formation models predict that young galaxies are much less settled in rotationally supported disks and much more perturbed by star-formation feedback and mergers than intermediate and low-z galaxies (Pillepich et al. 2019, Dekel & Burkert 2014, Zolotov et al. 2015).

- *When and how do the morphological and structural properties of the local ETGs form and evolve?* The formation of the spheroidal and disk components and their connection to the star-formation properties remain one of the outstanding puzzles in extragalactic astrophysics (Papovich et al. 2015, Tacchella et al. 2016, 2019). It is still unclear, for example, whether a morphological transformation from a star-forming disk to a quiescent spheroidal is a by-product of quenching, in the sense that the mechanisms responsible for halting the star formation, also lead to the build-up of a massive bulge, or not.

In this thesis, we address these questions with a robust kinematic analysis that allows us to measure the rotation velocity and the velocity dispersion profile of lensed DSFGs. The study of the rotational-to-random ratios allows us to test whether or not the interplay between increasing gas accretion, SFR and stellar feedback are responsible for boosting the random motions in these galaxies. Moreover, by focusing on DSFGs, the most plausible progenitors of the massive ETGs, we can also investigate the formation of the quiescent galaxy population and the emergence of their structural properties.

To robustly reconstruct the intrinsic properties of strongly lensed DSFGs, we develop the first Bayesian kinematic-lens modeling technique that allows the simultaneous fitting of the lens-mass distribution and the source kinematics. The methodology and the main fitting algorithm are presented in Chapter 2. By using mock IFU observations of galaxies with a variety of kinematic properties and different SNR, in the same chapter, we test the robustness and limitations of our technique in recovering reliable kinematic and lens parameters.
In Chapter 3, we present the first application of our kinematic-lens modeling technique to real ALMA observations of the [CII] emission line from a typical DSFG, SPT0418-47, at $z = 4.2$. The rare almost perfect alignment between the foreground and the background galaxy results in a high magnification of the lensed images, allowing for the investigation of the source physical properties on 60 pc scales. By comparing the dynamical properties of SPT0418-47 with predictions from theoretical studies, we pose a significant challenge to galaxy formation models and the effects of their ingredients at early epochs. Furthermore, this analysis shows the significant advantages of our approach over traditional techniques in measuring galaxy kinematics at high-z, also revealing the importance of high-quality data for reliable and robust results.
Chapter 4 deals with the extension of our dynamical analysis to six other gravitationally lensed DSFGs in the redshift range $3 \lesssim z \lesssim 5$. Up to date, this is the largest sample of galaxies at this redshift with a systematic kinematic measurement. Our dynamical analysis, combined with the SFR measurements on the galaxies of the sample, provides us with insights on the effects of stellar feedback processes in driving turbulence within young galaxies. Furthermore, by comparing the structural and physical properties of our sample with those of local ETGs, we set strong constraints on the mechanisms expected to transform these DSFGs into a quiescent population. In Chapter 5, we provide a summary of the main findings of this thesis, along with a discussion on current and future prospects.

Chapter 2

A novel 3D technique to study the kinematics of lensed galaxies

The content of this chapter is based on the work originally published as ***Rizzo, F.****, Vegetti, S., Fraternali, F., Di Teodoro, E., 2018, MNRAS, 481, 5606*

The structural and kinematic properties of high-z star-forming galaxies are still poorly constrained. Low-quality data is the leading cause behind this lack of knowledge, and the different methods used to overcome observational limitations have often lead to diverging results (see Section 1.4 for further details). In particular, the study of the kinematics is mainly hampered by two factors: low spatial resolutions and low SNR. To date, most kinematic studies of $z \sim 1$ - 3 galaxies have used IFU observations in seeing-limited mode, with typical spatial resolutions of 5 kpc (e.g., Förster Schreiber et al. 2009, Swinbank et al. 2017), while only a handful of adaptive optics (AO) observations have achieved higher resolutions of ∼1 - 1.6 kpc (Molina et al. 2017, Förster Schreiber et al. 2018). Furthermore, because of cosmological surface-brightness dimming, only the bright central regions of galaxies can be observed, especially with AO. Although AO observations are characterized by a better spatial resolution with respect to seeing-limited observations, they have a worse sensitivity and a data binning is often required to increase the SNR. As extensively described in Section 1.5, one of the main consequences of limited spatial resolution is to cause a strong degeneracy between the rotation velocity and the velocity dispersion (e.g. Wright et al. 2009, Newman et al. 2013, Di Teodoro & Fraternali 2015), via the beam-smearing effect.

The observational limitations imposed by low resolution and SNR can be successfully overcome by targeting strongly gravitationally lensed galaxies (see Section 1.6). Strong gravitational lensing offers the opportunity to study high-z galaxies at a much higher physical resolution and SNR in the source plane (e.g. Nesvadba et al. 2006, Swinbank et al. 2007). Furthermore, the magnifying power of gravitational lensing opens the possibility to study galaxies in the low stellar-mass range ($\lesssim 10^{10} M_{\odot}$, e.g., Jones et al. 2010b, Leethochawalit et al. 2016, Mason et al. 2017), which is instead not easily achievable by surveys targeting

unlensed galaxies (e.g. Förster Schreiber et al. 2006, Swinbank et al. 2012b).

It was only in recent years that the potential of gravitational lensing has started to be exploited: for example, Stark et al. (2008) studied the kinematics of a lensed galaxy at a resolution of 120 pc at $z = 3.07$. The analysis of two larger samples then followed this study: Jones et al. (2010b) analyzed six lensed galaxies in the redshift range 1.7 - 3.1, and Livermore et al. (2015) further extended this sample to seventeen targets with redshift from 1 to 3. Leethochawalit et al. (2016) analyzed fifteen lensed galaxies at z $\sim$ 2. These kinematic analyses of lensed sources from the rest-frame optical emission lines have been characterized by the following features:

1. the lens mass model is derived from high-spatial-resolution-imaging data (e.g., from HST images, Stark et al. 2008, Jones et al. 2010a, 2013, Shirazi et al. 2014, Leethochawalit et al. 2016, Livermore et al. 2015, Yuan et al. 2017);

2. the kinematic modeling is done either by delensing the 3D IFU data (e.g. Jones et al. 2013, Livermore et al. 2015) and deriving the velocity and dispersion maps with a Gaussian fit to the emission lines in the source plane, or by deriving the moment maps in the image plane and then delensing these maps to the source plane (e.g. Jones et al. 2010a, Leethochawalit et al. 2016). In both cases, the lens model is kept fixed.

3. A functional form, usually an arctangent function, is used to fit the delensed velocity field and derive the rotation curve.

Recent studies based on molecular line observations have used a similar approach (e.g. Dye et al. 2015, Rybak et al. 2015, Swinbank et al. 2015). One first derives the lens mass distribution from the radio continuum, observed in the same bands as the molecular lines. Then, this model is used to reconstruct the source and calculate the corresponding moment maps. Finally, kinematic parameters are derived either by applying the kinemetry method (Krajnović et al. 2006) to both the first and second-moment maps (Rybak et al. 2015) or by applying a dynamical model to the first-moment map (Dye et al. 2015, Swinbank et al. 2015).

All these approaches are suboptimal mainly for two reasons: first, if the lens model is kept fixed, it is not possible to quantify any degeneracy between the lens mass parameters and the source kinematic properties. Second, the kinematic fitting is done on the reconstructed source rather than on the data. However, on the source plane, pixels are correlated, the noise properties not fully characterized, and the effective resolution changes with position according to the lensing magnification. As a consequence, one introduces systematic errors in the derivation of the kinematic properties of the source, which may be difficult to quantify.
Recently, Patrício et al. (2018) have applied a forward modeling approach which partly overcomes some of the above issues by deriving the velocity map directly on the image plane through a Gaussian fitting to the emission lines. However, similarly to the techniques described above, this method is not ideal, as it relies on a fixed lens model derived from a separate HST observation and it performs a kinematic modeling of the 2D velocity map,

instead of the full 3D data cube.
Finally, other studies have been focusing on sources that are not significantly lensed (i.e., only weakly distorted), so that the kinematic analysis can be done directly on the image plane without having to reconstruct the unlensed emission (e.g. Mason et al. 2017, Girard et al. 2018, Di Teodoro et al. 2018). However, even small distortions of the observed axis ratio, due to lensing, could affect the capability to recover the kinematic parameters accurately. Mason et al. (2017) have tried to correct for this effect using a global value for the magnification factor.

In this chapter, we present a novel Bayesian 3D and pixelated approach, which, applied either to IFU or interferometric data, enables us to simultaneously reconstruct both the lensing mass distribution and the kinematics of the source. Our method represents a significant improvement over those described above as it is not affected by differential magnification nor poor understanding of the errors and resolution properties of the reconstructed unlensed plane. Our technique, indeed, does not require the use of high-resolution imaging data for the derivation of the lens parameters, as these are derived from the same 3D data used for the modeling of the kinematics of the background galaxy. Since the lens parameters and the source are inferred simultaneously from the same dataset, our method is not affected by differential magnification. Moreover, the kinematics of the background galaxy is not obtained by fitting on the source plane, but directly the lensed data in a hierarchical Bayesian fashion, where the kinematics on the source plane is essentially a hyper-parameter (i.e., a parameter defining the prior) of the model. The main novelty of our procedure is that a modified tilted-ring kinematic model is an extra constraint for a pixelated source reconstruction. Furthermore, the derivation of the lens mass model and the source kinematics is done simultaneously, allowing us to quantify possible degeneracies and to estimate the errors on all model parameters using a Bayesian approach. Finally, our 3D approach enables us to describe the kinematics of the source minimizing the influence of the beam smearing effect.
This chapter is organized as follows. In Section 2.1, we describe in details the method used for the lens modeling and the derivation of the kinematics. In Section 2.2, we present the IFU simulated datasets. In Section 2.3 we describe the modeling strategy and the assumptions applied to model the simulated datasets, which are then used in Section 2.4 to test our method under different observational set-ups. The robustness and the limits of the technique are summarized in Section 2.5, where we also list future developments and applications. Finally, Section 2.6 contains some supplementary material.

2.1 Method description

This section describes the core features of our method, which is an extension of the technique developed by Vegetti & Koopmans (2009) to the 3D domain. In particular, we present the statistical framework that allows us to reconstruct the background source, its kinematics and the lens mass distribution. The lens-mass parametrization is described in Section 2.1.2, while the details of the kinematic model used to describe the lensed source are given in Section

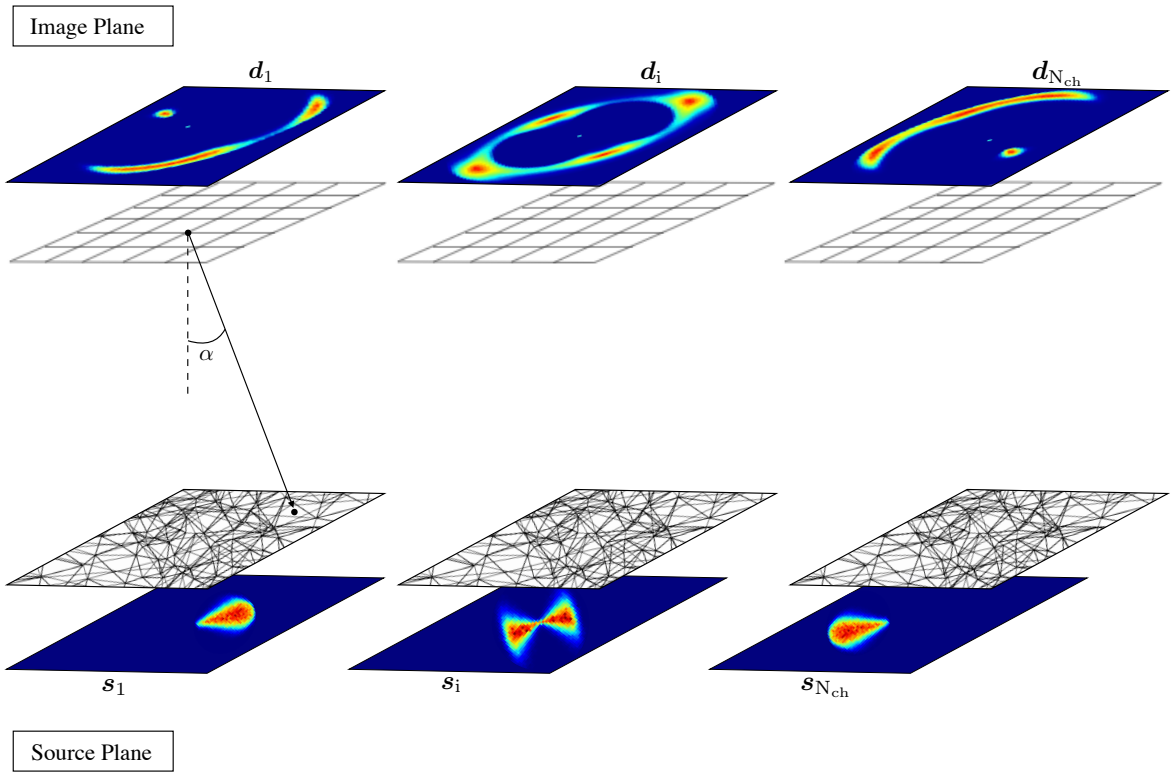

Figure 2.1: **A schematic view of the source and lens planes.** On the upper panel, the lensed data for three representative spectral channels and the respective regular grid on the image plane. For each spectral channel, the position $\vec{x}$ of a subset of N_s pixels in the image plane corresponds to a position $\vec{y}$ on the source plane (lower panel), through the lens equation $\vec{y} = \vec{x} - \vec{\alpha}(\vec{x})$ (see Section 1.6). The points $\vec{y}$ are the vertices of a triangular adaptive grid on the source plane.

2.1.3.

2.1.1 Source reconstruction

In the following, we indicate with **s** and **d** the 3D pixelated surface brightness distribution of the source and the data in the image plane, respectively. We refer the reader to Figure 2.1 for a schematic representation of the source and image planes.

Given a set of N_{ch} observed spectral channels, the source and data vectors, **s** and **d**, have a total of N_{ch} components, $s_{i..N_{ch}}$ and $d_{i..N_{ch}}$ respectively, each representing the surface brightness distribution in one channel i:

$$\mathbf{s} = \{s_1, ..., s_i, ..., s_{N_{ch}}\}, \tag{2.1}$$

$$\mathbf{d} = \{d_1, ..., d_{\rm i}, ..., d_{\rm N_{ch}}\}. \tag{2.2}$$

For each ith spectral channel, the surface brightness distribution of the lensed cube $d_{\rm i}$, its noise $n_{\rm i}$ and the relative unknown source surface brightness distribution $s_{\rm i}$ are related to each other by the following set of linear equation:

$$\mathbf{M}\,(\boldsymbol{\psi})\; s_{\rm i} + n_{\rm i} = d_{\rm i}, \tag{2.3}$$

where $\mathbf{M = B\,L}$ is the response operator which depends on the lensing operator $\mathbf{L}$ and the PSF operator $\mathbf{B}$ (for interferometric data, $\mathbf{B}$ is the Fourier transfer operator, see Appendix A.2). The lensing operator $\mathbf{L}$, is a non-linear function of the lens mass-density distribution parameters $\boldsymbol{\eta}_{\mathbf{lens}}$ (see Section 2.1.2 for their definition) via the lensing potential $\psi\,(\boldsymbol{\eta}_{\mathbf{lens}})$.
The method used for the source reconstruction is grid-based in the sense that the background-source surface-brightness distribution is reconstructed on a triangular adaptive grid defined by a Delaunay tessellation. The source grid automatically adapts with the lensing magnification, so that there is a high pixel-density in the high-magnification regions close to the caustics. The vertices of the triangular grid are obtained by casting back to the source plane a subset $\rm N_s$ of the $\rm N_d$ image-plane pixels via the lens equation (1.2). We determine the surface brightness at each source-plane pixel by interpolating between the values at the vertices of the triangles. We reconstruct each channel on the same triangulation.
As both $\boldsymbol{\eta}_{\mathbf{lens}}$ and the source $s_{\rm i}$ are unknown, equation (2.3) is ill-defined and cannot be simply inverted. Therefore, we derive a penalty function defined in the context of three levels of Bayesian inference, which are described below.

First level of inference - Linear optimization

Using Bayes' rule, the most probable a posteriori source, $\mathbf{s_{MP}}$, given the data and a lens mass model, is derived by maximizing the following posterior probability (Suyu et al. 2006, Vegetti & Koopmans 2009):

$$P\,(\mathbf{s}|\mathbf{d}, \lambda, \boldsymbol{\eta}_{\mathbf{lens}}, \boldsymbol{\eta}_{\mathbf{kin}}, \mathbf{R}) = \frac{P\,(\mathbf{d}|\mathbf{s}, \boldsymbol{\eta}_{\mathbf{lens}})\; P\,(\mathbf{s}|\lambda, \boldsymbol{\eta}_{\mathbf{kin}}, \mathbf{R})}{P\,(\mathbf{d}|\lambda, \boldsymbol{\eta}_{\mathbf{lens}}, \boldsymbol{\eta}_{\mathbf{kin}}, \mathbf{R})}. \tag{2.4}$$

Here, the matrix $\mathbf{R}$ is the source regularization form (variance, gradient or curvature), with a strength set by the regularization level vector λ (see Koopmans 2005, Vegetti & Koopmans 2009, for further details). The regularization level vector λ has $\rm N_{ch}$ components, so that the user can choose whether the level of regularization is constant across the spectral channels or not. For simplicity, all equations below and above assume a constant value of λ as a function of frequency. $\boldsymbol{\eta}_{\mathbf{kin}}$ in equation (2.4) are the source kinematic parameters, as defined in Section 2.1.3. The remaining terms in equation (2.4) are the likelihood function $P\,(\mathbf{d}|\mathbf{s}, \boldsymbol{\eta}_{\mathbf{lens}})$, the prior on the source surface brightness distribution $P\,(\mathbf{s}|\lambda, \boldsymbol{\eta}_{\mathbf{kin}}, \mathbf{R})$, and the evidence $P\,(\mathbf{d}|\lambda, \boldsymbol{\eta}_{\mathbf{lens}}, \boldsymbol{\eta}_{\mathbf{kin}}, \mathbf{R})$, which is irrelevant for the maximization of the posterior, but plays an

important role at the third level of inference (see Section 2.1.4). Under the assumption of Gaussian noise, the likelihood can be expressed as follows

$$P\left(\mathbf{d}|\mathbf{s},\boldsymbol{\eta}_{\mathbf{lens}}\right)=\frac{\exp\left[-E_{\mathrm{D}}\left(\mathbf{d}|\mathbf{s},\boldsymbol{\eta}_{\mathbf{lens}}\right)\right]}{Z_{\mathrm{D}}}, \tag{2.5}$$

where Z_{D} is the normalization, and E_{D} is given by

$$E_{\mathrm{D}}\left(\mathbf{d}|\mathbf{s},\boldsymbol{\eta}_{\mathbf{lens}}\right)=\frac{1}{2}\sum_{\mathrm{i}=1}^{\mathrm{Nch}}\left(\mathbf{M}s_{\mathrm{i}}-d_{\mathrm{i}}\right)^{\mathsf{T}}\mathbf{C}_{\mathrm{d\,i}}^{-1}\left(\mathbf{M}s_{\mathrm{i}}-d_{\mathrm{i}}\right). \tag{2.6}$$

Above, $\mathbf{C}_{\mathrm{d\,i}}$ is the covariance matrix of the data for the ith spectral channel. Since the noise is assumed to be uncorrelated, it is a diagonal matrix.
In our implementation, the source prior assumes a quadratic form, which peaks at a source kinematic model, $\mathbf{s}_{\mathrm{kin}}\left(\boldsymbol{\eta}_{\mathbf{kin}}\right)$. The prior probability distribution is, therefore, expressed as

$$P\left(\mathbf{s}|\lambda,\boldsymbol{\eta}_{\mathbf{kin}},\mathbf{R}\right)=\frac{\exp\left[-\lambda E_{\mathrm{R}}\left(\mathbf{s}|\boldsymbol{\eta}_{\mathbf{kin}},\mathbf{R}\right)\right]}{Z_{\mathrm{R}}}, \tag{2.7}$$

where the quadratic functional E_{R} and the normalization Z_{R} are given respectively by

$$E_{\mathrm{R}}\left(\mathbf{s}\right)=\sum_{\mathrm{i}=1}^{\mathrm{Nch}}\left[E_{\mathrm{R}}\left(s_{\mathrm{kin\,i}}\right)+\frac{1}{2}\left(s_{\mathrm{i}}-s_{\mathrm{kin\,i}}\right)^{\mathsf{T}}\mathbf{H}_{\mathrm{R,i}}\left(s_{\mathrm{i}}-s_{\mathrm{kin\,i}}\right)\right] \tag{2.8}$$

and

$$Z_{\mathrm{R}}\left(\lambda\right)=\int d^{N_s}\mathbf{s}\,e^{-E_{\mathrm{R}}(\mathbf{s})}=e^{-E_{\mathrm{R}}(\mathbf{s}_{\mathbf{kin}})}\left(\frac{2\pi}{\lambda}\right)^{\frac{\mathrm{N_s N_{ch}}}{2}}\left(\det\mathbf{H}_{\mathrm{R}}\right)^{-\mathrm{N_{ch}}/2}. \tag{2.9}$$

$\mathbf{H}_{\mathrm{R}}$ in the above equation is a block matrix made up of the $\mathrm{N_{ch}}$ matrices $\mathbf{H}_{\mathrm{R,i}}$, see equation (2.8), and it is defined as the Hessian of E_{R}, $\mathbf{H}_{\mathrm{R}}=\nabla\nabla E_{\mathrm{R}}=\mathbf{R}^{\mathsf{T}}\mathbf{R}$. The most probable surface brightness is obtained by maximizing the posterior probability in equation (2.4), i.e., by solving the following set of linear equations:

$$\left[\mathbf{M}^{\mathsf{T}}\mathbf{C}_{\mathrm{d\,i}}^{-1}\mathbf{M}+\lambda\mathbf{H}_{\mathrm{R}}\right]s_i=\mathbf{M}^{\mathsf{T}}\mathbf{C}_{\mathrm{d\,i}}^{-1}d_{\mathrm{i}}+\lambda\mathbf{H}_{\mathrm{R}}s_{\mathrm{kin\,i}}. \tag{2.10}$$

The form of these equations differs from those derived in Vegetti & Koopmans (2009) in the last term on the right-hand side, $\lambda\mathbf{H}_{\mathrm{Ri}}s_{\mathrm{kin\,i}}$. This term is due to a different assumption about the peak of the source prior, which is equal to zero in Vegetti & Koopmans (2009) and $\mathbf{s}_{\mathbf{kin}}$ here.

Second level of inference - Non-linear optimization

To infer the kinematic parameters $\boldsymbol{\eta}_{\mathbf{kin}}$, the lens parameters $\boldsymbol{\eta}_{\mathbf{lens}}$ and the optimal level of regularization λ we maximize the following posterior probability

$$P\left(\lambda,\boldsymbol{\eta}_{\mathbf{kin}},\boldsymbol{\eta}_{\mathbf{lens}}|\mathbf{d},\mathbf{R}\right)=\frac{P\left(\mathbf{d}|\lambda,\boldsymbol{\eta}_{\mathbf{lens}},\boldsymbol{\eta}_{\mathbf{kin}},\mathbf{R}\right)P\left(\lambda,\boldsymbol{\eta}_{\mathbf{kin}},\boldsymbol{\eta}_{\mathbf{lens}}\right)}{P\left(\mathbf{d}|\mathbf{R}\right)}. \tag{2.11}$$

Assuming a prior which is flat in $\log\lambda$, $\boldsymbol{\eta}_{\mathbf{lens}}$ and $\boldsymbol{\eta}_{\mathbf{kin}}$, equation (2.11) can be expressed as

$$P\left(\mathbf{d}|\lambda, \boldsymbol{\eta}_{\mathbf{lens}}, \boldsymbol{\eta}_{\mathbf{kin}}, \mathbf{R}\right) = \int P\left(\mathbf{d}|\mathbf{s}, \boldsymbol{\eta}_{\mathbf{lens}}\right) P\left(\mathbf{s}|\lambda, \boldsymbol{\eta}_{\mathbf{kin}}, \mathbf{R}\right)\, d\mathbf{s}. \tag{2.12}$$

If we assume a Gaussian noise and a quadratic form of regularization, equation (2.12) can be written as

$$\begin{aligned} P\left(\mathbf{d}|\lambda, \boldsymbol{\eta}_{\mathbf{lens}}, \boldsymbol{\eta}_{\mathbf{kin}}, \mathbf{R}\right) = -E\left(\mathbf{s}_{\mathbf{MP}}\right) - \frac{\mathrm{N_{ch}}}{2}\log\det\mathbf{H}_{\mathrm{E}} + \frac{\mathrm{N_s N_{ch}}}{2}\log\lambda \\ +\lambda E_{\mathrm{R}}\left(\mathbf{s}_{\mathbf{kin}}\right) + \frac{\mathrm{N_{ch}}}{2}\log\det\mathbf{H}_{\mathrm{R}} - \frac{\mathrm{N_d N_{ch}}}{2}\log 2\pi - \frac{1}{2}\sum_{\mathrm{i}=1}^{\mathrm{Nch}}\log\det\mathbf{C}_{\mathrm{d\,i}}. \end{aligned} \tag{2.13}$$

In the above equation, $E = E_{\mathrm{D}} + \lambda E_{\mathrm{R}}$, $\mathbf{H}_{\mathrm{E}}$ is its Hessian and $\mathbf{s}_{\mathbf{MP}}$ is the most probable solution that maximizes the posterior, $\nabla E\left(\mathbf{s}_{\mathbf{MP}}\right) = 0$.
The expression for the posterior probability, equation (2.13), differs from that derived by Suyu et al. (2006) and Vegetti & Koopmans (2009) for the multiplications/summation by/over $\mathrm{N_{ch}}$ and the presence of the term $E_{\mathrm{R}}\left(\mathbf{s}_{\mathbf{kin}}\right)$, which is the main novelty of our approach. This allows us to derive the kinematic parameters of the source, while retaining the flexibility of a pixelated source surface brightness distribution, simultaneously infer the lens-mass distribution, and take advantage of the extra constraints provided by the velocity channels.

Third level of inference - Model comparison

At the third level of inference, to compare and rank different models, we calculate the marginalized Bayesian evidence, which is a measure of the probability of the data given the model. In our case, this marginalized evidence can be expressed as the integral of the normalization factor in equation (2.4) over the lens parameters $\boldsymbol{\eta}_{\mathbf{lens}}$, the kinematic parameters $\boldsymbol{\eta}_{\mathbf{kin}}$ and the source regularization λ, such that

$$P\left(\mathbf{d}|\mathbf{R}\right) = \int P\left(\mathbf{d}|\lambda, \boldsymbol{\eta}_{\mathbf{lens}}, \boldsymbol{\eta}_{\mathbf{kin}}, \mathbf{R}\right) \times P\left(\lambda, \boldsymbol{\eta}_{\mathbf{lens}}, \boldsymbol{\eta}_{\mathbf{kin}}\right)\, d\lambda\, d\boldsymbol{\eta}_{\mathbf{lens}}\, d\boldsymbol{\eta}_{\mathbf{kin}}. \tag{2.14}$$

This integral is calculated numerically with MultiNest (Feroz et al. 2009, 2013), which is a Nested Sampling-based method improving on the original idea by Skilling (2004). As a by-product of this evidence calculation, we also obtain the posterior distributions of the model parameters, allowing us to estimate their statistical uncertainties and degeneracies (see Section 2.4).

2.1.2 Lens mass model

The lens parameters $\boldsymbol{\eta}_{\mathbf{lens}}$ that define the lensing operator $\mathbf{L}$ are: κ_0, q, γ, x_0, y_0, θ, Γ_{sh}, θ_{sh}. These parameters describe a projected mass density profile as a cored elliptical power-law

distribution with the contribution of an external shear component of strength $\Gamma_{\rm sh}$ and position angle $\theta_{\rm sh}$. The dimensionless projected mass density profile is defined as

$$\kappa\left(x,y\right)=\frac{\kappa_0\left(2-\frac{\gamma}{2}\right)q^{\gamma-\frac{3}{2}}}{2\left[q^2\left(x^2+r_{\rm c}^2\right)+y^2\right]^{\frac{\gamma-1}{2}}}\,. \tag{2.15}$$

κ_0 is the surface mass-density normalization, q is the projected flattening, γ is the density slope, x_0 and y_0 define the center of the mass distribution, $r_{\rm c}$ is the core radius, and θ is the position angle of the major axis. The Einstein radius for this density profile is defined as

$$R_{\rm ein}=\left[\frac{\kappa_0\left(2-\frac{\gamma}{2}\right)q^{\frac{\gamma-2}{2}}}{3-\gamma}\right]^{\frac{1}{\gamma-1}}\,. \tag{2.16}$$

In the following sections, we assume that the mass distribution has a negligible core radius of 10^{-4} arcsec.

2.1.3 Source kinematic model

We build the kinematic model using a modified version of the building-model function of $^{\rm 3D}$BAROLO (Di Teodoro & Fraternali 2015). To simulate the gas emission from a rotating galaxy the $^{\rm 3D}$BAROLO algorithm uses a stochastic function that populates a 6D domain (three spatial and three spectral dimensions) with emitting gas clouds, which allow us to build the line profiles. The rotating galaxy is modeled as a series of concentric circular rings using the so-called tilted-ring model (Rogstad et al. 1974). On each ring, the positions of the clouds are chosen randomly in such a way that, on average, the clouds become uniformly distributed over its surface. Each ring is described by the following parameters:

1. the coordinates of the center $x_{\rm s}, y_{\rm s}$;
2. the inclination angle i, defined such that $i = 90°$ for an edge-on galaxy and $i = 0°$ for a face-on one;
3. the position angle PA, defined as the angle between the north direction of the sky and the projected major axis of the receding half of the rings measured counterclockwise;
4. the gas column density Σ;
5. the systemic velocity $V_{\rm sys}$;
6. the rotation velocity $V_{\rm rot}$;
7. the velocity dispersion $\sigma_{\rm gas}$.

The projected velocity along the line of sight $V_{\rm los}$ at a particular radius R is defined by

$$V_{\rm los}\,(R) = V_{\rm sys} + V_{\rm rot}\,(R)\cos\phi\sin i\,, \tag{2.17}$$

where ϕ is the azimuthal angle in the plane of the galaxy. To build the 3D model, at each radius, the positions of the clouds are then rotated and projected into the plane of the sky with an orientation with respect to the observer defined by both the position and the inclination angles at that radius. As in ^{3D}BAROLO, to obtain the velocity profile at each location, the clouds are divided into sub-clouds. Each of these sub-clouds has a velocity which is drawn from a Gaussian distribution with a dispersion of $\sigma^2 = \sigma^2_{\rm gas} + \sigma^2_{\rm instr}$. Here, $\sigma_{\rm instr}$ takes into account the instrumental broadening.
Unlike ^{3D}BAROLO, our implementation does not allow for a variation of all these parameters ring by ring. Instead, we make the following assumptions: (i) all the rings have the same center coordinates and systemic velocity (in Section 2.4.10, we explicitly test the effects of this assumption); (ii) the radial variation of the inclination and position angles are described by a polynomial of degree from 0 to 3; (iii) the radial variation of the rotation velocity and velocity dispersion are described by functional forms. The use of functional forms for the rotation velocity and velocity dispersion allows us to reduce the number of free parameters. Our kinematic model $\mathbf{s_{kin}}$ is, therefore, defined by the following set of parameters $\boldsymbol{\eta}_{\mathbf{kin}} = \{R_{\rm ext}, \Sigma, x_{\rm s}, y_{\rm s}, V_{\rm sys}, i, PA, V_{\rm rot}, \sigma_{\rm gas}\}$. $R_{\rm ext}$ is the radial extension and is a fixed parameter chosen by the user. In Section 2.3, we describe the assumptions made to estimate $R_{\rm ext}$ for the simulated data analyzed in this chapter. Following ^{3D}BAROLO, the surface density of the gas Σ is also not a free parameter; instead, we impose a pixel-by-pixel normalization, which is given by the surface brightness distribution obtained from the lens modeling of the zeroth-moment map. The advantage of using a spatially-changing normalization is that it allows us to take into account for possible asymmetries in the ionized or molecular gas distribution, as it is typical for high-z galaxies given the presence of massive star-forming regions (e.g. Genzel et al. 2011, Swinbank et al. 2012a, Livermore et al. 2015). Therefore, the presence of clumpy emissions or holes should not affect the derived kinematics, because this normalization ensures that the kinematics is independent of the gas distribution (e.g., Lelli et al. 2012, Di Teodoro & Fraternali 2015).
By construction, the kinematic model is built on a cartesian grid, defined by a pixel scale and dimensions chosen by the user. Since the source reconstruction is determined on a Delaunay tessellation (see Section 2.1.1), we then map this model at the positions of the triangle vertices.

Rotation velocity and velocity dispersion curves

We have implemented three empirical functions to describe the rotation curves: the arctangent function (Courteau 1997), the hyperbolic tangent function (Andersen et al. 2001) and a multi-parameter function (Rix et al. 1997). These are expressed by the following three expressions, respectively:

$$V_{\rm rot}\,(R) = \frac{2}{\pi}\,V_{\rm t}\,\arctan\left(\frac{R}{R_{\rm t}}\right), \tag{2.18}$$

$$V_{\rm rot}\,(R) = V_{\rm t}\,\tanh\left(\frac{R}{R_{\rm t}}\right), \tag{2.19}$$

$$V_{\rm rot}\,(R) = V_{\rm t}\frac{\left(1+\frac{R_{\rm t}}{R}\right)^{\beta}}{\left[1+\left(\frac{R_{\rm t}}{R}\right)^{\xi}\right]^{1/\xi}}. \tag{2.20}$$

$R_{\rm t}$ is the turnover radius between the inner rising and outer part of the curve. $V_{\rm t}$ is the asymptotic velocity for the arctangent and hyperbolic tangent functions, and the velocity scale for the multi-parameter one. ξ defines the sharpness of the turnover while β specifies the power-law behavior of the curve at large radii. The arctangent function has mainly been used to model the kinematics of high-z galaxies (e.g. Swinbank et al. 2012b, Leethochawalit et al. 2016). However, it is not flexible enough to reproduce the different kinds of observed rotation curves, especially in the inner regions where a bump can be present. For this reason, we prefer the multi-parameter function, which is, by definition, more flexible.
To describe the velocity dispersion profile, the user can choose from a power-law, a linear or an exponential function:

$$\sigma_{\rm gas}\,(R) = \sigma_0\left(\frac{R}{R_\sigma}\right)^{\zeta}, \tag{2.21}$$

$$\sigma_{\rm gas}\,(R) = \sigma_0 + \zeta\,R, \tag{2.22}$$

$$\sigma_{\rm gas}\,(R) = \sigma_0\,e^{-\frac{R}{R_\sigma}} + \sigma_1. \tag{2.23}$$

2.1.4 Optimization scheme

We infer the unknown parameters $\boldsymbol{\eta}_{\rm lens}$, λ, $\boldsymbol{\eta}_{\rm kin}$ and the source $\mathbf{s}$ with an optimization scheme, which is divided in the following four stages (see also Figure 2.2 for a schematic view):

1. To find a good initial guess for the lens model parameters, $\boldsymbol{\eta}_{\rm lens}$, we start by modeling the zeroth-moment map of the data. This optimization is performed in three separate sub-steps. First, λ is kept fixed at a relatively large value, such that the source model remains relatively smooth, and $P\,(\boldsymbol{\eta}_{\rm lens}|\lambda, \mathbf{d}, \mathbf{R})$ is maximized relatively to $\boldsymbol{\eta}_{\rm lens}$. Secondly, the lens parameters are kept fixed at the most probable values found at the previous step, while $P\,(\lambda|\boldsymbol{\eta}_{\rm lens}, \mathbf{d}, \mathbf{R})$ is optimized for the source regularization level λ. Finally, $P\,(\boldsymbol{\eta}_{\rm lens}|\lambda, \mathbf{d}, \mathbf{R})$ is maximized again for the lens parameters with a source regularization level fixed to the most probable value determined in the previous stage. At every point of the non-linear mass-model optimization, the corresponding most probable source surface brightness distribution $\mathbf{s}_{\rm MP}$ is obtained by solving the linear system (2.10) with $\mathbf{s}_{\rm kin} = 0$.

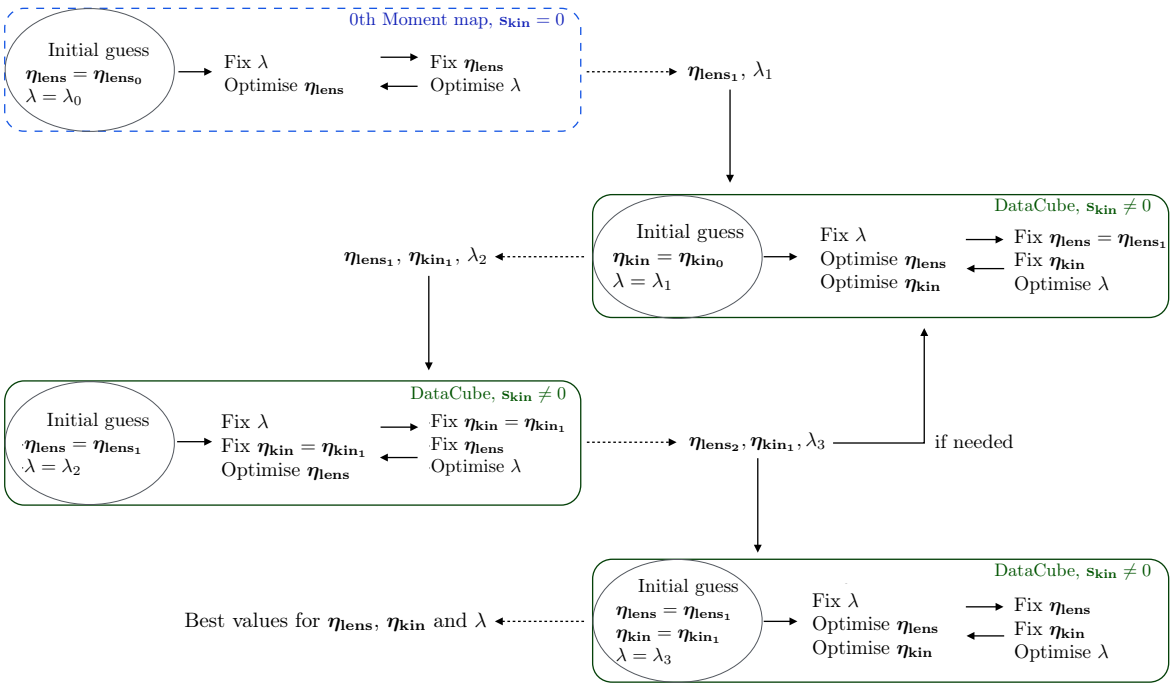

Figure 2.2: **A schematic overview of the four-step optimization scheme used to infer the unknown parameters $\boldsymbol{\eta}_{\mathbf{lens}}$, λ, $\boldsymbol{\eta}_{\mathbf{kin}}$.** The four boxes represent the points 1 - 4 in Section 2.1.4. An initial estimate of the lens parameters is obtained by fitting the zeroth-moment map, while for the successive steps the full 3D data cube is used.

2. We now model the entire 3D data cube. Assuming the values of $\boldsymbol{\eta}_{\mathbf{lens}}$ found in step 1, we infer the optimal regularization constant λ and $\boldsymbol{\eta}_{\mathbf{kin}}$, maximizing equation (2.13) by varying first the kinematic parameters that define $\mathbf{s}_{\mathbf{kin}}$, then the source regularization level λ and finally the kinematic parameters again. At this stage, the user can choose between a value of the regularization level λ which is the same for all of the spectral channels or a value that varies channel by channel.

3. We repeat the process described in 1, using equations (2.11) and (2.10) with $\boldsymbol{\eta}_{\mathbf{kin}}$ equal to the value found in 2.

4. Finally, the lens parameters, λ and only the kinematic parameters that describe the rotation velocity and velocity dispersion, i.e., $V_{\rm rot}$, $\sigma_{\rm gas}$, are simultaneously left free to vary, starting from the values of the parameters found at the previous steps. As for the last two, at this stage, we focus on the 3D data cube.

The analysis described at the points 2 and 3 are repeated if a visual inspection of the residuals reveals a mismatch between the model and the data. All of the optimization steps described above are done with a non-linear optimizer (i.e., a Downhill-Simplex with Simulated Annealing, Press et al. 1992). As discussed in Section 2.1.1, the calculation of the Bayesian

evidence with MULTINEST allows us to explore the parameter space and obtain the posterior distributions of the parameters. In this case, both the kinematic and lens parameters are simultaneously changed.

2.2 IFU mock data

To investigate the ability of our new modeling technique to recover reliable lens and kinematic parameters, we simulate nine observations of Hα emission from star-forming lensed galaxies at redshifts between 1 and 2. In particular, we use the technical features of the OSIRIS spectrograph (Larkin et al. 2006). We have chosen to focus on OSIRIS because it has the typical characteristics of a NIR IFU mounted on an 8 - 10m telescope in terms of spatial resolution, AO performances, and spectral resolution, with a typical channel width of 30 - 40 km s^{-1}. To simulate the lensed data, we first build a cube from a rotating galaxy (Section 2.2.1); we then lens it forward using the lens mass model described in Section 2.1.2. Finally, we convolve the lensed cube with a spatial PSF and add the noise (Section 2.2.2).

2.2.1 Simulated sources

The lensed sources have redshifts between 1.3 and 2.4 (column 2 in Table 2.1) which results in their Hα emission line falling in the H or K filters (column 4 in Table 2.1). The total Hα fluxes (column 7 in Table 2.1) have values typical of star-forming galaxies at $z \sim 1$ - 2 (Förster Schreiber et al. 2006, Livermore et al. 2015). The average resolving power is $\sim$ 3400 corresponding to $\sim$ 6 Å in these bands. The cube of the rotating galaxy is built using ^{3D}BAROLO (Di Teodoro & Fraternali 2015). Input values for the geometrical and kinematic parameters that define the inclination i and position angle PA and the rotation velocity $V_{\rm rot}$ and dispersion $\sigma_{\rm gas}$ are listed in Table 2.2. The sources have an extension of $\sim$ 5 - 8 kpc along the major axis, as typical of $z \sim 1$ - 2 galaxies (e.g., Wisnioski et al. 2015, Leethochawalit et al. 2016, Patrício et al. 2018).

In the sections below, we provide more details on each model. In general, to check whether the functional forms in equations (2.18) - (2.23) are flexible enough to reproduce a variety of realistic kinematic scenarios, we have considered different input rotation curves of varying complexity and different shapes. In particular, the mock data M1 and M2 are created and modeled with the same functional forms implemented in our code (Sections 2.4.1 - 2.4.2). The mock data M3 is created with a different functional form (Section 2.4.3), while the simulated data M4, M5, and M6 have rotation curves derived from real observed galaxies (Sections 2.4.4 - 2.4.6). The rotation curves of M1 and M4 are typical of dwarf galaxies, the rotation curves of M2 and M5 are prototypes of spirals, while those of M3 and M6 are typical of massive spirals with a prominent bulge. We have included dwarf galaxy kinematics to test if our code is able to recover the shape of the rotation curve when the turning point is not reached, and only the increasing part is observable. Finally, the mock data M7, M8, and M9 are used to

test the limits of our modeling technique. The aim is to quantify the minimum and maximum inclination angles that allow us to recover the kinematics reliably (M7 and M8, Sections 2.4.7 - 2.4.8), as well as the minimum warp in the position angle that can be detected given the angular resolution of the data (M9, Sections 2.4.9).

2.2.2 Simulated observations

We generate the simulated lensed data using a set of lens parameters (see Table 2.2), $\boldsymbol{\eta}_{\mathbf{lens}}$, that we have derived from the lens modeling of a set of real lenses from the SLACS (Bolton et al. 2006) and SHARP (Lagattuta et al. 2012) surveys. This choice is motivated by the fact that in this thesis, we are only focusing on galaxy-scale lenses. For the analysis of galaxy-cluster lenses, more complicated mass distributions would have to be considered. Using the lens equation, we lens forward the source surface brightness to the image plane for each spectral channel of the source cube. The simulated datasets have a spatial pixel scale in the image plane of 0.1 arcsec. Taking the OSIRIS characteristics, the field of view (FoV, column 5 in Table 2.1) varies between 3.6×6.4 arcsec^2 and 4.8×6.4 arcsec^2 depending on the filter (column 4 in Table 2.1). We convolve the lensed cube with a spatial PSF, g, which is described by the combination of two Gaussians

$$g = S\, g_{\rm dif} + (1 - S)\; g_{\rm seeing}. \tag{2.24}$$

This assumption allows us to take into account for the effects of the AO system, in the sense that the light of the source is divided between a diffraction limited-core, $g_{\rm dif}$, and a seeing-limited halo, $g_{\rm seeing}$, for a given strehl of the AO correction S (Law et al. 2006). In particular, M1 to M3 and M8 are simulated using a Full Width at Half Maximum (FWHM) of about 0.17 arcsec for $g_{\rm dif}$, a FWHM of about 0.95 arcsec for $g_{\rm seeing}$, and $S = 0.2$; for M4 to M7 and M9 we use a FWHM equal to 0.2 arcsec and 0.6 arcsec for $g_{\rm dif}$ and $g_{\rm seeing}$, respectively, and $S = 0.24$. All values of the PSF parameters are typical of OSIRIS observations (e.g. Stark et al. 2008, Jones et al. 2010b, Wisnioski et al. 2011). The effect of the spectral resolution is included on the plane of the source, as described in Section 2.1.3.
To simulate a realistic noise distribution, we create the sky-subtracted data, $\mathbf{d}$, using the simulation method by Law et al. (2006), which was specifically designed for OSIRIS observations. The value of $\mathbf{d}$ is then obtained as

$$\mathbf{d} = \mathbf{n} + \mathbf{t} \tag{2.25}$$

where the noise $\mathbf{n}$ is a value extracted from a Gaussian distribution with a dispersion given by the sum in quadrature of the counts from the observed target, $\mathbf{t}$, and the background $\mathbf{t}_{\rm BG}$. For our mock observations $\mathbf{t} = \sum_{\rm i}^{\rm Nch} \mathbf{M} s_{\rm i}$.
As explained in detail by Law et al. (2006), the background count rate $\mathbf{t}_{\rm BG}$ is a function of the wavelength and takes into account the Mauna Kea NIR sky brightness spectrum, the telescope emissivity, and the AO system emissivity. We have taken into account the updated characteristics of the telescope and OSIRIS spectrograph relatively to those used by Law et al. (2006): improved grating efficiency (~0.78, Mieda et al. 2014) and the halved read-out noise

Table 2.1: **Observational properties for the nine mock systems.** Column 1: name of the mock data. Column 2: redshift of the source. Column 3: redshift of the lens. Column 4 and 5: OSIRIS filter and the corresponding FoV. Column 6: FWHM for the core+halo PSF (see Section 2.2.1). Column 7: intrinsic Hα flux for the simulated galaxies. Column 8: exposure time of the mock observations.

			Observation set-up				
Mock ID	$z_{\rm source}$	$z_{\rm lens}$	Filter	FOV arcsec	FWHM arcsec	F(Hα)/10^{-18} erg s^{-1} cm^{-2}	$t_{\rm exp}$ ks
M1	2.05	0.881	Kn1	3.6×6.4	0.17+0.95	15	14.4
M2	2.19	0.191	Kn2	4.5×6.4	0.17+0.95	20	14.4
M3	2.15	0.722	Kn2	4.5×6.4	0.17+0.95	33	14.4
M4	2.26	0.191	Kn3	4.8×6.4	0.20+0.60	15	12.6
M5	1.34	0.410	Hn2	4.5×6.4	0.20+0.60	6	10.8
M6	2.36	0.881	Kn3	4.8×6.4	0.20+0.60	6	12.6
M7	1.34	0.410	Hn2	4.5×6.4	0.20+0.60	9	10.8
M8	2.19	0.191	Kn2	4.5×6.4	0.17+0.95	20	14.4
M9	1.34	0.410	Hn2	4.5×6.4	0.20+0.60	10	12.4

given by the installation of a new detector (T. Jones, private communications). The exposure times used for the simulated datasets M1 – M9 are listed in column 8 of Table 2.1 and are typical of data containing star-forming lensed galaxies (Livermore et al. 2015, Leethochawalit et al. 2016). The resulting mock data have a median SNR of $\sim$ 14 (see Figure 2.10 in the Supplementary Material Section 2.6).

2.3 Modeling strategy

In this section, we describe how we build the kinematic prior $\mathbf{s_{kin}}$ and derive the best kinematic parameters $\boldsymbol{\eta}_{\mathbf{kin}}$ (we refer to Section 2.1.3 for a definition). In particular, we discuss the assumptions made to define the radial extension $R_{\rm ext}$, the center, the systemic velocity, and the initial conditions for the geometrical and kinematic parameters for the specific data analyzed in this chapter. These assumptions can change depending on, e.g., the data quality of the observations, previous estimates of the kinematic and/or geometric parameters, the accuracy of the redshift of the source.

The first step is to define the radial extension and the effective resolution on which $\mathbf{s_{kin}}$ is sampled. From the reconstruction of the zeroth moment, we first derive an SNR map on the reconstructed source, by propagating the observational noise of the data. We then define the radial extension $R_{\rm ext}$ of the kinematic model as the radius along the apparent major axis of the galaxy at which the SNR $\sim$ 3. The kinematic models are built using a ring width that

Table 2.2: **Physical properties for the nine mock systems.** Top Table: Kinematic parameters used to create the source. Bottom Table: Lens parameters used to lens the source and to create the observed mock data.

	Input kinematic parameters							
Mock ID	i °	PA °	V_t km s^{-1}	R_t kpc	β	ξ	σ_0/σ_1 km s^{-1}	R_σ kpc
M1	72.0	265.0	120.0	2.0	_	_	30.0	-1.5
M2	52.0	100.0	223.0	1.0	_	_	15.0/25.0	1.2
M3	64.0	23.0	157.2	27.4	1.13	93.7	29.0	_
M4	59.0	145.0	73.7	5.52	0.24	50.1	46.0	-1.19
M5	68.0	280.0	151.4	2.17	_	_	34.0	26.0
M6	65.0	45.0	219.7	0.65	0.56	5.6	38.0	_
M7	40.0	280.0	151.4	2.17	_	_	34.0	26.0
M8	80.0	100.0	223.0	1.0	_	_	15.0/25.0	1.2
M9	68.0	280.0/-3.75	151.4	2.17	_	_	34.0	26.0

	Input lens parameters					
Mock ID	κ_0 arcsec	θ °	q	γ	Γ_{sh}	θ_{sh} °
M1	1.44	-12.72	0.82	2.06	-0.039	13.33
M2	1.33	157.95	0.93	2.28	0.050	174.45
M3	1.00	0.00	0.99	2.00	0.240	38.00
M4	1.33	157.95	0.93	2.28	0.050	174.45
M5	0.81	71.20	0.84	2.00	0.096	34.40
M6	1.44	-12.72	0.82	2.06	-0.039	13.33
M7	0.81	71.20	0.84	2.00	0.096	34.40
M8	1.33	157.95	0.93	2.28	0.050	174.45
M9	0.81	71.20	0.84	2.00	0.096	34.40

is half the pixel size on the image plane. We have explicitly verified that these choices do not influence the recovered kinematic parameters. The cartesian grid is then mapped onto a triangular adaptive grid, with triangles of average dimensions between $\sim 10^{-3}$ arcsec to $\sim 10^{-1}$ arcsec (this is set by a combination of the pixel scale on the image plane and the lensing magnification).

To reduce the number of free kinematic parameters during the optimization, we chose to keep the center of the source galaxy fixed at the flux-weighted average position of the zeroth-moment map (these differ by at most by 1 percent from the correct values). The systemic

velocity is also kept fixed at 0 km s^{-1}. When dealing with real data, one will be able to estimate its value from the global velocity profile, where the latter is obtained from the source intensity in each spectral channel of the data cube or other independent estimations. In Section 2.4.10, we discuss the results obtained by changing the center and systemic velocity from the true values. The free kinematic parameters are then $\boldsymbol{\eta}_{\mathbf{kin}} = \{i, PA, V_{\rm rot}, \sigma_{\rm gas}\}$.
Since the geometrical and kinematic parameters are coupled and degenerate, see equation (2.17), they need to be initialized with educated guess values. In this chapter, we estimate the geometrical parameters (i and PA) by applying ^{3D}BAROLO to the 3D source derived from the lens parameters inferred at point 1 of Section 2.1.1. We set the initial values for $V_{\rm t}$ and $R_{\rm t}$ that define the rotation curve to the arbitrary, but observationally motivated, values of 100 km s^{-1} and 1 kpc respectively (e.g. Livermore et al. 2015, Jones et al. 2010b). For the multi-parameter function, we set $\beta = 0.2$ and $\xi = 10.0$ as initial guesses. The choice of the functional form is arbitrary, but it should be noted that the multi-parameter function is the most flexible one, and it reproduces the arctangent function for $\xi = 1.1$. Furthermore, as demonstrated in Section 2.4.2, a wrong choice of the functional form for the rotation curve leads to systematic image residuals, indicating that a different choice should be made. The initial value for σ_0 is set to 30 km s^{-1}, while initial guesses for the other parameters that define the velocity dispersion functions, are chosen such that $\sigma\,(R_{\rm ext}) - \sigma_0$ is not larger than 20 km s^{-1}, as it is typical for the ionized gas of star-forming galaxies (e.g. Epinat et al. 2010, Di Teodoro et al. 2016, Mason et al. 2017).

2.3.1 Functional forms for the rotation velocity

Here, we briefly summarize the functional forms used to create and model the rotation velocities that define $\mathbf{s}_{\mathbf{kin}}$ (see columns 2 and 3 in Table 2.3). For the background galaxy of the simulated data M1, we assume a hyperbolic tangent function for the rotation velocity (blue squares in Figure 2.3). The data are then modeled assuming the same parametric form that we have used to create them. These simulated data represent, therefore, a zeroth-order test of our modeling technique.
The mock data M2 were built assuming an arctangent function for the rotation velocity (blue squares in Figure 2.3). The data are modeled twice, once with the same functional form used as input and once with a hyperbolic tangent function.
We have created the simulated data M3 using the following functional form for the rotation velocity (blue squares in Figure 2.3):

$$V_{\rm rot}\,(R) = \sqrt{V_1^2 + V_2^2}, \tag{2.26}$$

where V_1 is the contribution from an isothermal dark matter halo while V_2 represents the contribution from a Sérsic profile with a Sérsic index $n = 1$ (Freeman 1970). Since our lens modeling code does not include the functional form expressed by equation (2.26), we model these mock data using the flexible multi-parameter function (dashed red line in Figure 2.3). After checking that the input rotation curve is well reproduced (see discussion in Section 2.4.3

for further details), we fit the input 1D rotation curve with the multi-parameter function (solid blue line in Figure 2.3)[1]. By comparing the results of this fit with the kinematic parameters derived by the 3D lens modeling code, we can then quantify the accuracy of our technique and study the systematic errors that may derive from the choice of the kinematic functional forms.
We have created the mock datasets M4, M5, and M6 using the rotation curves measured for three low-z galaxies: NGC 2976, NGC 3198, and NGC 6674 from Lelli et al. (2016). For these sources the values of the rotation parameters listed in Table 2.2 are obtained by fitting the input data points (blue squares in Figure 2.3) with one of the functional forms implemented in our code (blue solid line in Figure 2.3). As for M2, this fitting allows us to evaluate the accuracy of the inferred kinematic parameters, which is independent of the choice of the parametrization. As discussed in Sections 2.4.4 to 2.4.6 these mock data are then modeled assuming the multi-parameter function for M4 and M6 and the hyperbolic tangent function for M5.
The simulated data M7, M8, and M9 are built to test the limits of our method. M7 and M8 have the same kinematics of M5 and M2 but an inclination angle of 40° and 80°, respectively. M9 has the same kinematics of M5, but it has a strong warp, which causes a change of 30° of its position angle across the galaxy.

2.4 Results

To test the ability of our method to recover the input lens and kinematic parameters, we model the nine mock datasets introduced in Section 2.2.2 with the new modeling technique described in Section 2.1.1. All assumptions made during the modeling procedure were discussed in Section 2.3 and summarized in Table 2.3.

We obtain the uncertainties on the inferred parameters using MultiNest (see Section 2.1.4). For each parameter we adopt priors which are flat in the intervals $[\overline{\eta}_{\mathbf{lens/kin}} - 0.2\overline{\eta}_{\mathbf{lens/kin}}, \overline{\eta}_{\mathbf{lens/kin}} + 0.2\overline{\eta}_{\mathbf{lens/kin}}]$, where $\overline{\eta}_{\mathbf{lens/kin}}$ are the best-fit parameters, inferred from the non-linear optimization (see Section 2.1.1). To be conservative, we report as errors in the parameters the sum in quadrature of the following two contributions: the 1-σ uncertainties on the posterior distributions derived by MultiNest and the difference between the maximum a posteriori parameter values obtained by MultiNest, and the non-linear optimizer. This difference arises because, as discussed above, the geometrical parameters that describe the source, i.e., PA and i, are kept fixed during the optimization, while they are left free to vary during the MultiNest exploration of the parameters space. In most cases, the discrepancy is smaller than 5 percent, while it reaches a level of 20 percent in one case that will be discussed separately (see Section 2.4.6). For the mock data M1, M2 and M8, for which we have used the same functional forms to create and model the data, these errors only account for the statistical uncertainties, while for the other models they also provide an estimate of the systematic errors, related to

[1]The fitting of the input rotation curves for M3 to M6 was done using the Python package Scipy.optimize.

Table 2.3: **Summary on the assumptions.** For each mock data in column 1, we show the assumptions on the input (column 2) and recovered (column 3) shapes for the rotation curves. Columns 4 and 5 show the median uncertainties on the lens and kinematic parameters. Columns 6 and 7 show the relative median accuracies for the lens and kinematic parameters respectively.

Mock dataset	Input RC	Model RC	Uncertainty on $\boldsymbol{\eta_{\rm lens}}$ %	Uncertainty on $\boldsymbol{\eta_{\rm kin}}$ %	Accuracy on $\boldsymbol{\eta_{\rm lens}}$ %	Accuracy on $\boldsymbol{\eta_{\rm kin}}$ %
M1	Arctangent	Arctangent	2	7	3.6	2.3
M2	Hyperbolic	Hyperbolic	5	13	1.3	2.8
M3	Equation (2.26)	Multi-parameter	5	3	2.8	1.7
M4	NGC 2976	Multi-parameter	5	9	1.5	3.0
M5	NGC 3198	Hyperbolic	3	8	0.5	0.5
M6	NGC 6674	Multi-parameter	6	9	1.0	1.1
M7	NGC 3198 +low inclination	Hyperbolic	8	6	2.4	3.1
M8	Hyperbolic +large inclination	Hyperbolic	3	7	0.7	2.0
M9	NGC 3198 +warp	Hyperbolic	6	7	1.9	0.5

the choice of parametrization. The median relative uncertainties on $\boldsymbol{\eta}_{\mathbf{lens}}$ and $\boldsymbol{\eta}_{\mathbf{kin}}$ for each model are listed in Table 2.3 (columns 4 and 5, respectively), while columns 6 and 7 in Table 2.3 list the relative accuracies[2].

Figures 2.5 (for M1) and 2.12 - 2.19 in the Supplementary Material Section 2.6 (for M2 - M8) show the comparison between mock observations and best-fit models. We plot the contour levels of the input source (column 1), the simulated lensed data (column 2), the inferred lensed model (column 3), the normalized image residuals (column 4), the reconstructed source (column 5) and the contour levels of the kinematic model (column 6), for a selected number of spectral channels. We present the input and recovered rotation curves and velocity dispersion profiles with blue squares and dashed red lines, respectively, in Figure 2.3. The orange band for the rotation velocities denotes the uncertainties $\epsilon_{\rm p}$, obtained after propagating the uncertainties on the parameters that describe the profiles (see Table 2.4). To take into account the contribution to the velocity dispersion uncertainties due to the spectral resolution, we compute the uncertainties on the values of $\sigma(R)$ as $\sqrt{\epsilon_{\rm p}^2 + \epsilon_{\rm cw}^2}$ (light-orange bands in Figure 2.3). $\epsilon_{\rm p}$ (orange bands in Figure 2.3) has the same meaning defined above for $V_{\rm rot}(R)$, while $\epsilon_{\rm cw}$ is obtained as the FWHM of the channel width divided by 3×2.355. The factor of 3 is obtained after testing the effect of the spectral resolution on the recovered velocity dispersion with mock data. We list the inferred lens and kinematic parameters in Table 2.4. These values should be compared with those reported in Table 2.2.

In Figure 2.4, we show the comparison between the input and recovered flat velocities $V_{\rm flat}$ and average velocity dispersions $\sigma_{\rm gas}$. The values of $V_{\rm flat}$ are obtained as the average of the rotation velocities at large radii, while the $\sigma_{\rm gas}$ values are obtained by averaging the values of $\sigma_{\rm gas}(R)$ starting from $R = 0$ kpc. The error bars in Figure 2.4 take into account the contribution of both the uncertainties on the values of $V_{\rm rot}$ and $\sigma_{\rm gas}$ at each radius, as shown by the orange and light-orange bands in Figure 2.3, and the standard deviation. The flat part of the rotation curves is correctly reproduced for all mock dataset. In particular, with our technique, we are able to recover $V_{\rm flat}$ not only for the galaxies for which the input rotation curves are described by functional forms but also for the rotation curves taken from real galaxies. This test ensures that the functional forms implemented in our code are flexible enough to reproduce the variety of observed rotation curves (from dwarf to massive galaxies). Even if the details in the inner region could be lost (see Section 2.4.3), the physical parameters that depend on $V_{\rm flat}$ can be exactly recovered. The values of $\sigma_{\rm gas}$ are recovered with great accuracy, even if they are more affected by the spectral resolution.

Below, we provide a detailed discussion on the modeling results for each of the nine simulated datasets. The reader not interested in the details can skip to Section 2.4.10, where we address some key issues related to radial motions, SNR and changes in the center coordinates and systemic velocities and Section 2.5 where we summarize the results of our tests.

[2]The median accuracies on $\boldsymbol{\eta}_{\mathbf{kin}}$ are calculated taking into account the relative difference between the input (Table 2.2) and recovered parameters (Table 2.4) as (input-recovered)/input.

Table 2.4: Top Table: Recovered kinematic parameters that best describe the kinematic model for the nine sources. Bottom Table: Recovered lens parameters for the nine mock datasets. The uncertainties are derived using a MultiNest method, as explained in Section 2.4.

	Recovered kinematic parameters							
Mock ID	i $^\circ$	PA $^\circ$	V_t km s^{-1}	R_t kpc	β	ξ	σ_0/σ_1 km s^{-1}	R_σ kpc
M1	74.0±1.6	260.0±3.2	115.0±4.8	1.86±0.23	_	_	28.9±3.7	-1.1±0.23
M2	54.4±0.1	102.6±2.7	219.3±2.2	0.97±0.09	_	_	13.4±2.6/ 28.5±4.6	1.15±0.21
M3	63.2±0.4	24.6±1.5	155.4±4.2	27.1±5.2	1.09±0.02	95.8±13.1	25.9±0.25	_
M4	60.0±1.8	150.0±5.6	72.9±5.6	5.23±0.53	0.25±0.03	51.4±5.3	43.9±6.8	-1.13±0.20
M5	70.7±5.9	282.9±2.5	151.2±13.9	2.07±0.18	_	_	31.8±3.2	26.2±2.1
M6	62.0±3.3	45.0±4.2	220.9±1.2	0.75±0.13	0.57±0.03	4.80±1.70	42.6±8.5	_
M7	40.2±0.5	281.4±2.7	151.2±11.4	2.09±0.13	_	_	41.1±4.6	24.9±1.8
M8	81.2±2.5	97.5±3.8	219.7±2.4	1.07±0.09	_	_	13.9±1.0/ 27.8±2.8	1.12±0.12
M9	67.6±6.3	277.8±2.7/ -3.3±1.9	152.4±7.8	2.23±0.18	_	_	38.2±5.8	25.9±2.6

	Recovered lens parameters					
Mock ID	κ_0 arcsec	θ $^\circ$	q	γ	Γ_{sh}	θ_{sh} $^\circ$
M1	1.43±0.01	-15.6±0.5	0.79±0.02	2.05±0.01	-0.044±0.004	10.2±0.8
M2	1.34±0.05	155.8±4.9	0.95±0.06	2.25±0.10	0.056±0.011	173.38±0.11
M3	0.97±0.04	-0.08±0.01	0.98±0.01	2.04±0.06	0.257±0.025	39.1±0.07
M4	1.31±0.09	160.50±6.5	0.95±0.01	2.31±0.16	0.051±0.009	173.8±6.8
M5	0.78±0.03	69.6±0.4	0.83±0.06	2.03±0.04	0.096±0.002	34.3±3.2
M6	1.43±0.01	-15.65±2.7	0.82±0.03	2.08±0.12	-0.037±0.001	14.76±1.19
M7	0.83±0.04	72.1±6.2	0.81±0.07	1.96±0.09	0.093± 0.002	33.3±3.1
M8	1.32±0.02	153.7±4.5	0.96±0.03	2.28±0.02	0.056±0.004	173.2±4.1
M9	0.82±0.07	72.6±4.4	0.82±0.02	1.99±0.13	0.101±0.004	33.9±1.7

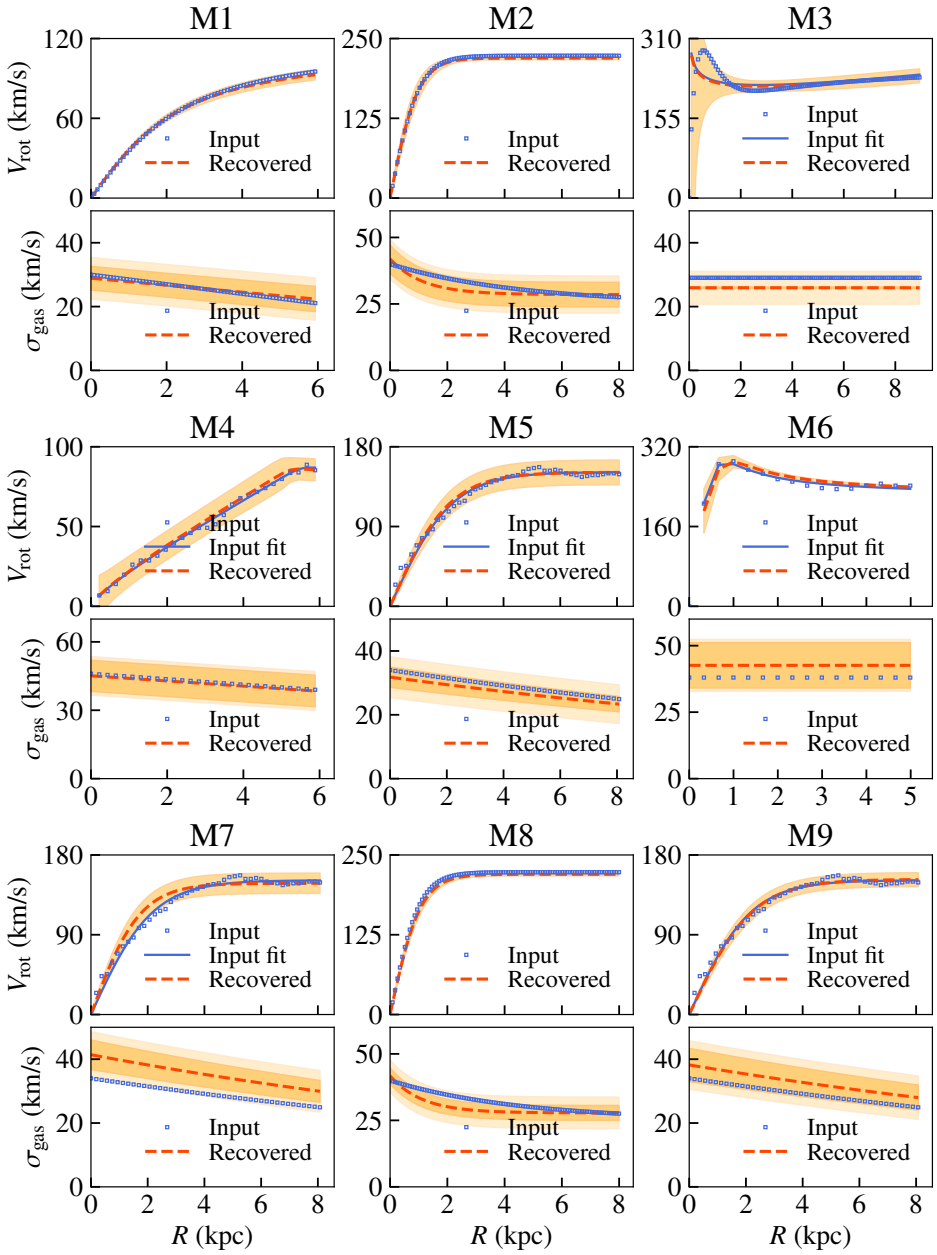

Figure 2.3: **Rotation curves and velocity dispersions for the mock dataset M1- M9.** The blue squares are the input data, the dashed red lines are the functional forms that best describe the kinematic priors, while the solid blue line for M3 - M7 and M9 show the fit to the input data using the same functional forms as those used for the kinematic priors at the 3D lens modeling stage. The orange bands for V_{rot} and σ_{gas} are obtained by error propagation from the uncertainties of the parameters that defined the rotation curves and velocity dispersion profiles, while the light-orange bands for σ_{gas} take into account also the contribution from the spectral resolution (see Section 2.4 for further details). In the velocity dispersion profile of M3, the orange band is too thin (0.25 km s^{-1}) to be visible, see discussion in Section 2.4.3 for further details.

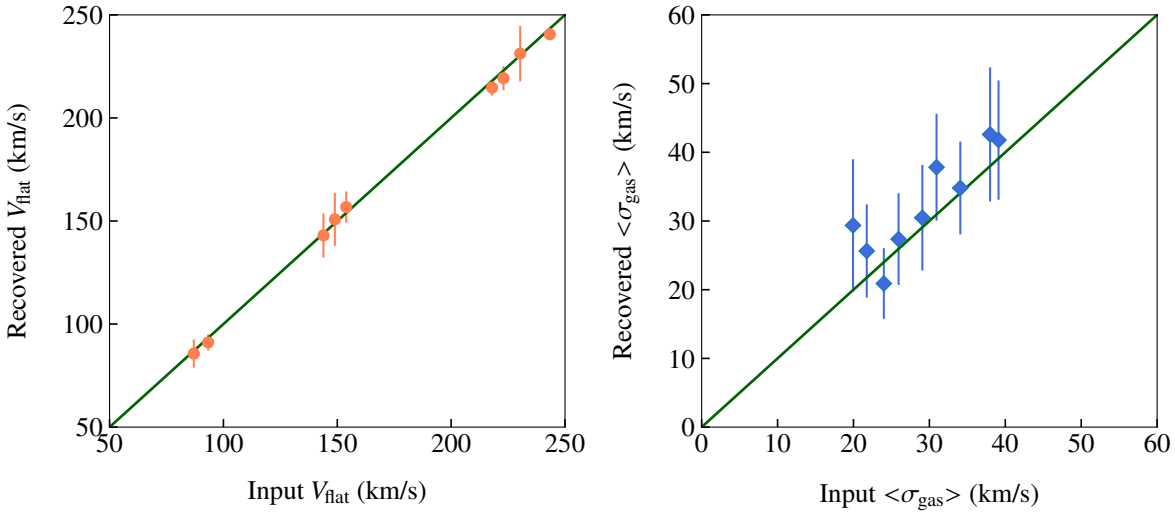

Figure 2.4: **Recovered versus input kinematic parameters.** Left: Recovered versus input values of V_{flat} for the nine mock datasets. Some points are shifted both on x- and y-axis by the same quantity for a better visualization of all the points. The green line represents a 1:1 relation between quantities on x- and y-axis. Right: same as in the left panel, but for σ_{gas}. The errors bars take into account both the standard uncertainties due to error propagation and the standard deviation due to fact that these are averaged quantities.

2.4.1 Mock dataset M1

The simulated data M1 were created assuming an arctangent function for the rotation velocity and a dispersion curve which is linearly declining from a value of 30 km s^{-1} at $R = 0$ kpc to 21 km s^{-1} at $R = 5.9$ kpc. The source position angle also changes linearly from 270° in the inner regions to 260° in the outer areas.
We model the simulated data with the same functional forms used to create them. Since the small change in the position angle is not detectable by a visual analysis of the zeroth-moment map, resulting from the first step of the optimization scheme (see Section 2.1.4), we decided to keep it fixed to the constant value of 260° during the following steps. We have found that this assumption does not significantly influence the derived kinematics. The inferred parameters that define the rotation velocity and the velocity dispersion have median relative uncertainties of 7 percent and are within 2-σ from the input values. The inferred lens parameters, characterized by median relative uncertainties of 2 percent, are within 1-σ from the input values, with the only exceptions of the lens and external-shear position angles θ and θ_{sh} which differ by 5.7-σ and 3.9-σ, respectively, from the input values. This result is related to the fact that the lens is very close to being spherical, and the shear strength almost negligible.

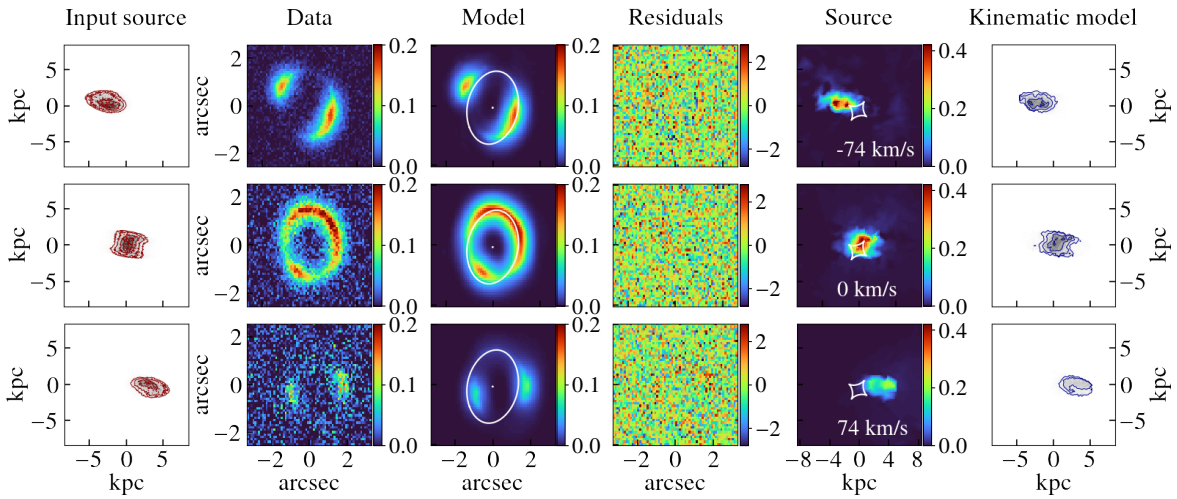

Figure 2.5: **Channel maps for the simulated dataset M1.** The rows show some representative channel maps for M1. Column 1: Input source. Column 3: Mock lensed data. Column 3: Lensed model and the corresponding critical curves. Column 4: Normalized residuals obtained as the ratio between the difference of the data and the model and the corresponding noise. Column 5: Reconstructed source and caustics. Column 6: Kinematic prior used to constrain the source reconstruction. The contour levels in the first and sixth columns are set at n = 0.1, 0.2, 0.4, 0.6, 0.8 times the value of the maximum flux.

2.4.2 Mock dataset M2

We have created the simulated data M2 using a hyperbolic tangent function for the source rotation curve and an exponential function for its velocity dispersion.
First, we model this dataset assuming the same functional forms used as input. This choice produces normalized residuals that are of the order of 0.5 percent (see column 4 in Figure 2.12). The inferred lens parameters have a median relative uncertainty of 5 percent, while the recovered kinematic parameters have median relative uncertainties of 13 percent (Table 2.4). The largest contribution to the kinematic uncertainties comes from the velocity dispersion parameters, due to the limited spectral resolution (channel width of $\sim 36.8\,\mathrm{km\,s^{-1}}$) of these data (see the orange band in Figure 2.3). The input lens and the kinematic parameters are within the 1-σ uncertainties from the recovered values. To test our capability to distinguish between different forms of parametrization, we have also modeled this dataset with an arctangent function. We have found that under this assumption, the residuals get worse (see column 3 in Figure 2.6), reaching a maximum value of $\sim$ 6-σ. We have then computed the marginalized Bayesian evidence to compare and rank these two models. As anticipated in Section 2.1.4, the marginalized evidence in equation (2.14), allows us to quantify how well a model $\mathrm{m_i}$ is supported by the data against another model $\mathrm{m_j}$. This quantification is expressed in terms of the Bayes factor, $\Delta \log E_{\mathrm{ij}} = \log E_{\mathrm{i}} - \log E_{\mathrm{j}}$. We find that the Bayes factor is of the order of 1400 against the arctangent model, meaning that the hyperbolic tangent function for the

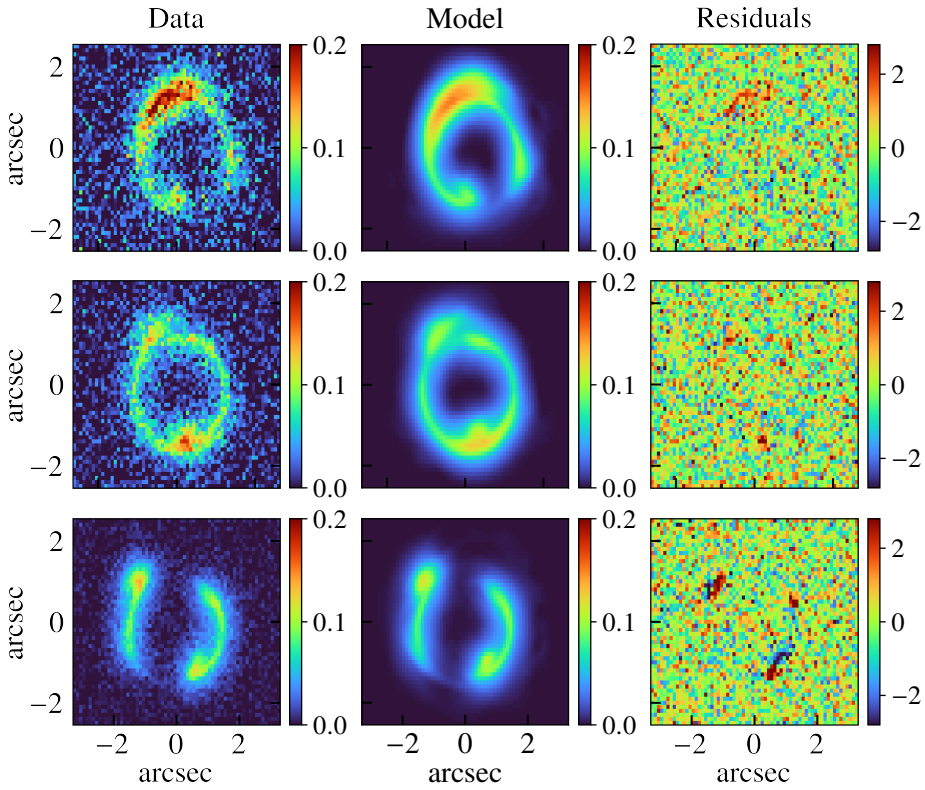

Figure 2.6: **Tests on the rotation curve parametrization.** Same as Figure 2.12, for a rotation velocity described by an arctangent function.

rotation curve is largely supported by the data. We can conclude, therefore, that the data contain enough information to infer the most suitable shape.

2.4.3 Mock dataset M3

The lens system M3 was created assuming a rotation curve for the background galaxy described by the functional form in equation (2.26). This function is not implemented in our code. The velocity dispersion was assumed to be constant.
We model these simulated data using the multi-parameter function given by equation (2.20), which is the most flexible function that we have implemented. We find that the lens parameters are recovered with a median relative uncertainty of 5 percent and are within 1-σ from the input values. Our constraints on the lens mass model are, therefore, not significantly influenced by our assumptions on the source prior. The inferred parameters that define the rotation curve (V_t, R_t, β, ξ) in Table 2.4 should be compared with those reported in Table 2.2, obtained by fitting the input 1D rotation curve (blue squares in Figure 2.3) using the multi-parameter function (solid blue line in Figure 2.3). The inferred kinematic parameters have median uncertainties of 3 percent, and they are within 2-σ from the fitted values. The only exception is the recovered

velocity dispersion, which is more than 3-σ away. However, this discrepancy is due to an underestimation of the uncertainties that do not include the systematic errors introduced by the spectral resolution. If we take into account the uncertainties due to spectral resolution, $\epsilon_{\rm cw}$ in Section 2.4, the recovered dispersion profile is in agreement within 1-σ with the input profile (see the light-orange band in Figure 2.3). We find that both the fit to the input rotation curve (solid blue line in Figure 2.3) and the rotation curve derived from our lens modeling technique (red dashed line in Figure 2.3) are a poor description of the inner regions of the real curve (see the blue squares in Figure 2.3). Despite its flexibility, the multi-parameter function does not allow us to correctly reproduce the peculiarity of the data in the central regions. Correspondingly, we find that the overall fit to the data has systematic residuals that reach maximum values of $\sim$ 5-σ (see column 3 in Figure 2.13). However, the rotation velocity at the outer regions is well reproduced, ensuring that even if the details of the inner regions are lost, the physical parameters that depend on the asymptotic velocity (e.g., angular momentum and dynamical mass) can still be recovered with good accuracy (see Figure 2.4).

2.4.4 Mock dataset M4

The input values of the rotation velocity for this system are taken from the rotation curve of the nearby dwarf galaxy NGC 2976 (Lelli et al. 2016). This choice allows us to test whether the assumed functional forms are good enough to reproduce real rotational curves. A linear equation describes the velocity dispersion curve.
During the modeling phase, we use the multi-parameter function, equation (2.20), to describe the rotation velocity, while for the velocity dispersion, we use the same functional form used as input. As for the simulated data M3, to have a quantitative estimate of the accuracy on the derived kinematics, we first fit the input 1D rotation curve with the same functional form used in the 3D lens modeling process (solid blue line in Figure 2.3). The recovered kinematic parameters have a median relative uncertainty of 9 percent, while the lens parameters have a median relative uncertainty of 5 percent (Table 2.3). The inferred lens parameters are within the 2-σ errors from the input values. The kinematic parameters are within 1-σ from the values derived by fitting the 1D rotation curve.

2.4.5 Mock dataset M5

As for the simulated dataset M4, we create M5 using the rotation curve of a real galaxy as input, in this case, NGC 3198 (Lelli et al. 2016). The input functional form for the velocity dispersion is an exponential function, equation (2.23), with $\sigma_1 = 0.0$ km s^{-1}.
At the modeling stage, we use the hyperbolic tangent function for the rotation curve and an exponential function with σ_1 fixed at 0 km s^{-1} for the velocity dispersion. As for the simulated data M3 and M4, we start by fitting the 1D rotation curve with the same functional form used for the 3D lens modelling. We find that the hyperbolic tangent function provides a good enough description of the data. The normalized residuals (column 4 in Figure 2.15), indeed, do not show any systematic features, usually indicative of wrong assumptions in the building

of the prior (e.g., see the model M2 and M3 in Sections 2.4.2, 2.4.3). The recovered lens and kinematic parameters have median relative uncertainties of 3 and 8 percent, respectively, and they are within 1-σ from the input values.

2.4.6 Mock dataset M6

The simulated data M6 were created using the rotation curve of the nearby galaxy NGC 6674 (Lelli et al. 2016), while for the velocity dispersion curve, we have used a constant value of 38 km s^{-1}. When modeling the data, the prior is built assuming the multi-parameter function for the rotation curve, while the dispersion is assumed to be constant.
The input lens parameters (Table 2.2) are within the 1-σ uncertainties from the recovered values (Table 2.4). The kinematic parameters inferred by the 3D lens modeling technique are within 1-σ from the values derived by fitting the 1D rotation curve directly. We find that the inferred lens and kinematic parameters have a median relative uncertainty of 6 and 9 percent, respectively. In particular, the velocity dispersion, σ_0, has an uncertainty of 20 percent. The major contribution to this error is the difference between the maximum a posteriori parameter value of 51.1 km s^{-1} obtained by MultiNest and the corresponding value of 42.6 km s^{-1} obtained by the non-linear optimizer (see Section 2.4). However, given the channel width of 33.9 km s^{-1} for this system, we believe the discrepancy not to be significant.

2.4.7 Mock dataset M7

The derivation of the rotation curve for low-inclination galaxies is challenging for any kinematic-fitting algorithm. For example, for $i = 40°$ an error as small as $\pm 5°$ in the estimation of the inclination angle can lead to a significant underestimation/overestimation of the rotation velocity as large as 10 percent. To test the reliability of our modeling technique when the background source is a low-inclination galaxy, we have created the mock data M7 with the same lens and kinematic parameters of M5, but with an inclination angle for the source of 40°, instead of 68°.
As described above, we first model the zeroth-moment map and then use the recovered lens model parameters to derive a 3D model of the source. The latter is then analyzed with ^{3D}BAROLO to obtain initial guesses for the source geometrical parameters. For the mock data M7, this results in a value of $i = 41.5°$, in close agreement with the input value. Subsequently, by applying our 3D lens modeling analysis to the full lensed data cube, we derive an inclination angle of 40.2°. The inferred lens and kinematic parameters have median relative uncertainties of 8 and 6 percent, respectively, differing by 1-σ and 2-σ from the input values. We can conclude, therefore, that the accurate reconstruction of the zeroth-moment map allows one to obtain a reasonable initial estimate of the inclination, and, as a consequence, the kinematic properties of the galaxy are correctly recovered.

2.4.8 Mock dataset M8

Di Teodoro & Fraternali (2015) have shown that for large inclinations, $i \gtrsim 75°$, the inner points of the rotation curve can be underestimated and that this effect can be more significant for a flat rather than for a solid-body rotation curve. This is due to the fact that ^{3D}BAROLO works ring by ring. However, we note that for a value of the inclination angle $\gtrsim 75°$, the errors on the inclination have little impact on the derived rotation curve, due to the sinusoidal dependence between the line-of-sight velocity and the inclination, see equation (2.17).
These mock data were built to study how an extreme value of the inclination angle affects the reconstruction of the source kinematics. For this reason, we have built the mock data M8 using the same lens and kinematic models as those used for M2 but assuming an inclination angle of 80°. In particular, we focus on M2 because it has a flat rotation curve.
The inferred values that describe the rotation velocity differ by ~ 4 percent from the input values, reproducing very well also the inner regions of the curve (see the red dashed line in Figure 2.3). We can conclude, therefore, that the use of functional forms for the rotation velocity allows us to reproduce the inner regions of an edge-on galaxy better than a ring by ring method. Moreover, the inferred lens and kinematic parameters are characterized by a median relative uncertainty of 3 and 7 percent, and they are within 2-σ from the input values.

2.4.9 Mock dataset M9

The input lens and kinematic models are the same as those used to create the simulated data M5, but the input geometry of the source is different. In particular, the position angle has a strong warp, and it decreases linearly from a value of 280° at $R = 0$ kpc to 250° at the outermost radius.
Interestingly, we find that the presence of the warp is already revealed at the first step of our optimization strategy (Figure 2.7), where we focus on the lens modeling of the zeroth moment (i.e., point 1, Section 2.1.4). From a ^{3D}BAROLO analysis of the derived source cube, we then obtain a position angle that changes linearly with a slope of 2.6 $^\circ$ kpc^{-1} from an inner value of 278°. We then apply our 3D lens modeling technique with a position angle which changes linearly. The two parameters that describe this change are left free to vary, starting from the initial guesses found by ^{3D}BAROLO. The best-fit slope that describes the variation of the PA is 3.3 $^\circ$ kpc^{-1}, which differs by ∼6 percent from the input value of 3.5 $^\circ$ kpc^{-1}. The inferred value of PA at $R = 0$ kpc is 277.8°, differing by ~ 1 percent from the input value of 280.0°. The inferred kinematic parameters have a median uncertainty of 7 percent, while the lens parameters have a median uncertainty of 6 percent. Both the lens and the kinematic parameters are within 1-σ from the input values.

2.4.10 Further tests

Observational evidence seems to indicate that physical processes such as disk turbulence, gas accretion, and subsequent disk instabilities are more prevalent at high-z (e.g. Wisnioski et al.

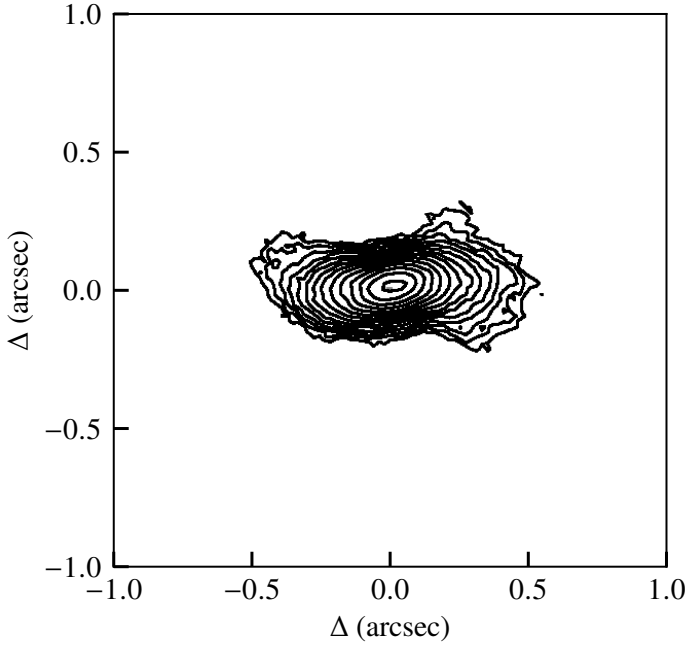

Figure 2.7: **Mock galaxy with a warp.** Zeroth-moment map for the reconstructed source M9, resulting after the first step (i.e., point 1, Section 2.1.4) of our optimization strategy.

2015, Übler et al. 2019, Turner et al. 2017). As a consequence, the contribution of non-rotational components could have a significant impact on the kinematic of high-z galaxies. The presence of significant radial motions, which are not included in the current analysis, could, in principle, limit the applicability of our technique to high-z galaxies. To quantify this issue, we have created a simulated dataset which has the same lens and kinematic models as M1 but includes radial motions of 25 km s^{-1}. We note that this value is larger than what is typically observed at low-z (i.e., $\lesssim$ 10 km s^{-1}, Trachternach et al. 2008), while, to date, there are no studies of radial motion in high-z galaxies. We have compared the lensed images of these simulated data with those of M1 for different values of angular resolution. Even in the ideal case of no observational noise, we have found no significant discrepancy, with a relative difference between the two lensed images of the order of $\sim$ 2 percent, for the highest angular resolution case. We can conclude that, although non-circular motions could contribute to the overall kinematics, they are mostly not detectable at the current angular and spectral resolution.

To test how the SNR of the data affects the accuracy with which the lens-mass and source-kinematics parameters are recovered, we have re-simulated the mock data M1 with five different noise levels, obtained using different exposure times (see Figure 2.11 in the Supplementary Material Section 2.6). As shown in the left panel of Figure 2.8, for an SNR[3] below $\sim$ 3, the relative difference between the input and the recovered values is higher than

[3]The values of the SNR are calculated as the median of the SNR$_i$ for each spectral channel i of the data cube.

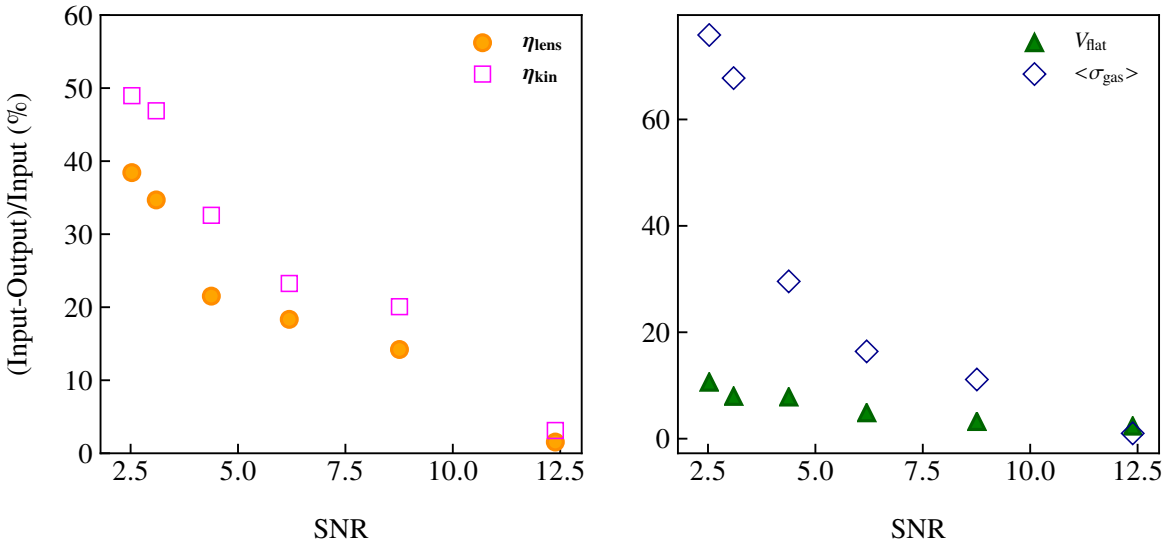

Figure 2.8: **Signal-to-noise ratio tests.** Left: Relative difference between the input and the recovered lens (orange circles) and kinematic (magenta empty squares) parameters as a function of the SNR for different data-quality realizations of M1 mock dateset. Right: same as in the left panel but for $V_{\rm flat}$ (green triangles) and $\sigma_{\rm gas}$ (blue empty diamonds).

30 percent both for the lens (orange circles) and for the kinematic parameters (magenta empty squares). If we focus on the relative difference between the input and the output $V_{\rm flat}$ (green triangles on the right panel of Figure 2.8), we conclude that we are still able to recover it with an accuracy of the order of 90 percent even for the mock dataset with the lowest SNR. The relative differences between the input and the recovered values of $\sigma_{\rm gas}$ (empty blue diamonds on the right panel of Figure 2.8) are smaller than $\sim$ 30 percent for SNR larger than 3.

So far, we have modeled all the simulated datasets with a fixed systemic velocity of 0 km s^{-1} and the center of the kinematic prior set at the flux-weighted average position of the zeroth-moment map. However, for high-z galaxies, one expects error on the center of the order of 5 to 10 percent and on the systemic velocity of the order of the channel width. We have, therefore, repeated the analysis of M1 by fixing the coordinates of the center to values that are offset from the real ones by 10 percent and with values of the systemic velocity, which are offset by the channel width velocity from the real value. We have found that an incorrect choice of the systemic velocity does not affect our results significantly, while changes in the center have a significant effect only if both coordinates are shifted by 10 percent relative to the real values in the same direction.

Because of the small FoV of many IFU instruments, complete imaging of the lensed emission is often not possible, instead only a limited part of the arc is observed. Here, we show how

The latter is calculated as $\mathrm{SNR_i} = \sum_k S_{\rm ki}/\sqrt{N_{\rm ki}^2}$, where the sum is over the pixels of the ith channel, $S_{\rm ki}$ is the signal at kth pixel, and $N_{\rm ki}$ is its noise.

this observational limitation can strongly affect the reconstruction of the source morphology. The first row of Figure 2.9 shows the emission of a background disk galaxy as lensed by a power-law mass distribution. In the same figure, we present the source that is reconstructed by considering an increasingly smaller part of the data. In particular, on the second row, we have modeled the entire set of images, on the third one we have excluded the counter image, on the fourth we have modeled only a small region of the main arc and the counter image, while on the fifth one only a small region of the main arc was taken into account. We find that one can safely ignore the counter image only if all images are modeled (see row 3 of Figure 2.9). However, failure to observe the entire main arc leads to an incorrect source reconstruction and a wrong estimate of both the center of the galaxy and its extension, strongly affecting the derived kinematics (see row 5 of Figure 2.9). In this case, including the counter image is fundamental for a better reconstruction of the source (see row 4 in Figure 2.9). This result is due to the extension of the source, such that different regions of the galaxy are lensed into different regions and/or number of the images, depending on the lens system configuration. We conclude, therefore, that the analysis of the full set of lensed images (obtainable for example with mosaic observations) is crucial for a reliable derivation of the source properties.

2.5 Summary

In this chapter, we have presented a new method to model the kinematics of strong gravitationally lensed galaxies from 3D emission line observations. The technique is entirely Bayesian: a Bayesian penalty function allows us to simultaneously infer the lens-mass and the source-kinematics properties from the same 3D data cube, while the Bayesian marginalized evidence enables us to rank and compare different lens and kinematic models. This new approach is also grid-based and hierarchical. The source is reconstructed on a magnification-dependent Delaunay tessellation, and its kinematics represent the hyper-parameter of the source prior. The primary focus of this method is to provide a robust approach for studying the resolved kinematic properties of high-z lensed galaxies. In this respect, it represents a significant improvement over past and recent approaches. Indeed, since the kinematic model is a hyper-parameter of the reconstructed source, the inferred kinematic properties are not influenced by the poor understanding of the errors and spatial resolution on the unlensed plane. Furthermore, the lens mass distribution is derived consistently from the same 3D data cube.

To test the capabilities of this new method in inferring the correct model parameters, we have studied a sample of nine simulated lensed galaxies as they would be observed with the OSIRIS spectrograph. These galaxies are characterized by a variety of rotation curves and geometries. In particular, we have focused on rotation curves that are described either by different functional forms (i.e., simulated data M1 - M3) or derived from real galaxies (i.e., datasets M4 - M6). We have found that this variety of shapes for the input rotation curves (from solid-body to flat rotation curves) is robustly recovered. In particular, the median relative accuracy on the inferred lens and kinematic parameters are at the level of ~ 1 and $\sim$

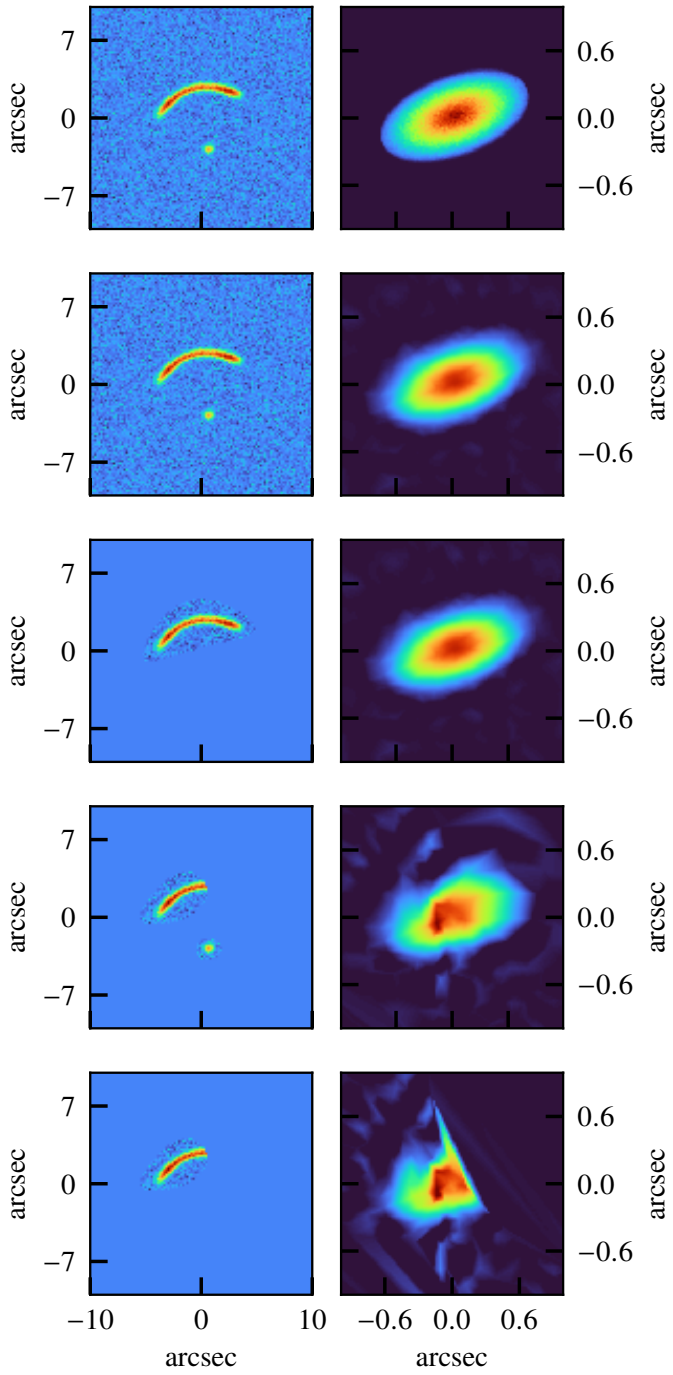

Figure 2.9: **Tests with different FoV.** Row 1: on the left side the input lensed data obtained by lensing forward the disk galaxy on the right side. From row 2 ro 5: reconstruction of the source (right panels) obtained by modeling different parts of the mock lensed data (left panels). Row 2: all data are considered for the source reconstruction. Row 3: the counter image is excluded. Row 4: the counter image and only part of the arc are modeled . Row 5: only part of the arc is modeled to reconstruct the source.

2 percent, respectively.
Focusing on the extreme cases of a low-inclination (40°, M7) and edge-on (80°, M8) galaxy, we have also studied how the inclination of the source affects the accuracy of the reconstructions. We have found that the kinematic parameters can be recovered with a median accuracy of 1 and 2 percent, respectively, if a reasonable initial estimate of the inclination can be obtained from the analysis of the zeroth-moment map. We have then tested the capability of our code to identify the presence of a warp. We have concluded that warps as large as 30° can significantly affect the lensed data. However, we are still able to recover the kinematic parameters with an accuracy of 3 percent. The rotation curves in all cases are accurately reconstructed; therefore, the most important physical parameters of the source galaxy (e.g., the dynamical mass and the angular momentum) can be correctly inferred.

We have also investigated the effect of increasing noise and concluded that the parameters are recovered with an accuracy better than 30 percent whenever the SNR is higher than ~ 3. The flat part of the rotation velocity is recovered with an accuracy of the order of 90 percent, even when the SNR is ~ 3. Finally, we have examined the effect of strong radial motions and found it to be irrelevant for the typical angular and spectral resolution of IFU observations. From these extensive tests, we can conclude that the method presented in this chapter offers a novel and robust way to study the gas kinematics of high-z lensed galaxies using data from the last generation of IFUs. Taking advantage of strong gravitational lensing, we can study the kinematic properties of galaxies at $z \sim 2$ - 3 with spatial resolutions and SNR not achievable for unlensed galaxies, even with current observational technique. Moreover, gravitational lensing offers the unique opportunity to study galaxies in the low stellar-mass range, which is almost impossible for studies targeting unlensed galaxies.

In this thesis, we have focused on galaxy-scale lenses. The formalism of our method is also applicable to cluster lenses, although with a more complex parametrization of the lensing potential. However, as the mass distribution of galaxy clusters is more complicated, we expect, in this case, larger uncertainties on both the lens parameters and the source kinematics. In this chapter, we have also only focused on NIR observations. However, as demonstrated in the rest of this thesis, our technique can also be used for probing the kinematics of galaxies using emission lines in the radio/sub-mm range (e.g., CO, [CI], [CII], see Appendix A.2). In the following chapters, we will show how the high spatial and spectral resolution achievable with ALMA, combined with the magnification effect from strong gravitational lensing, allows us to study the kinematic and dynamical properties of galaxies up to $z \sim 5$.

2.6 Supplementary material

2.6.1 Signal-to-noise ratio

In Figure 2.10, we show the SNR map for the same spectral channels shown in Figures 2.5 and 2.12 - 2.19. For each spectral channels the noise is added considering the procedure described in Section 2.2.2 and the exposure time listed in Table 2.1.
In Figure 2.11, we show the SNR maps for the same spectral channels shown in Figures 2.5

and for the different values of data quality, as described in Section 2.4.10 and summarized in Figure 2.8. The six different noise levels are obtained by considering six values of the exposure times for M1: 14.4 ks, 7.2 ks, 3.6 ks, 1.8 ks, 900 s, and 600 s.

2.6.2 Mock dataset M2 - M9

As for Figure 2.5 (for M1), we show in Figures 2.12 - 2.19 the input and best-fit models for M2 - M8. For a selected number of spectral channels, we plot in the first column the contour levels of the input source, in the second column the simulated lensed data, in the third column the inferred lensed model, in the fourth column the normalized image residuals, in the fifth the reconstructed source and in the sixth column the contour levels of the kinematic model.

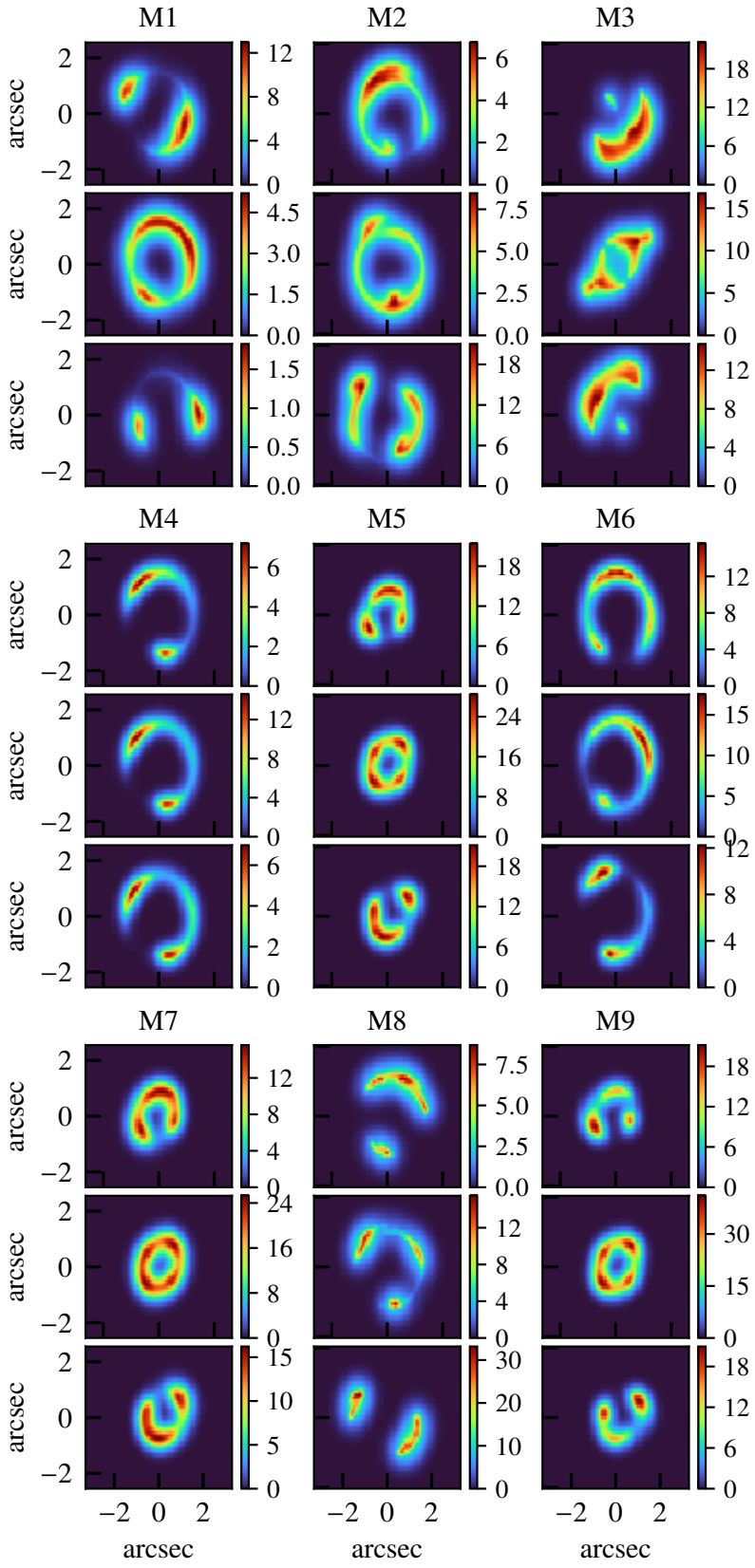

Figure 2.10: **SNR maps for M1 - M9.** The color bars show the SNR for the representative spectral channels shown in Figure 2.5 for M1 and 2.12-2.19 for M2 - M9.

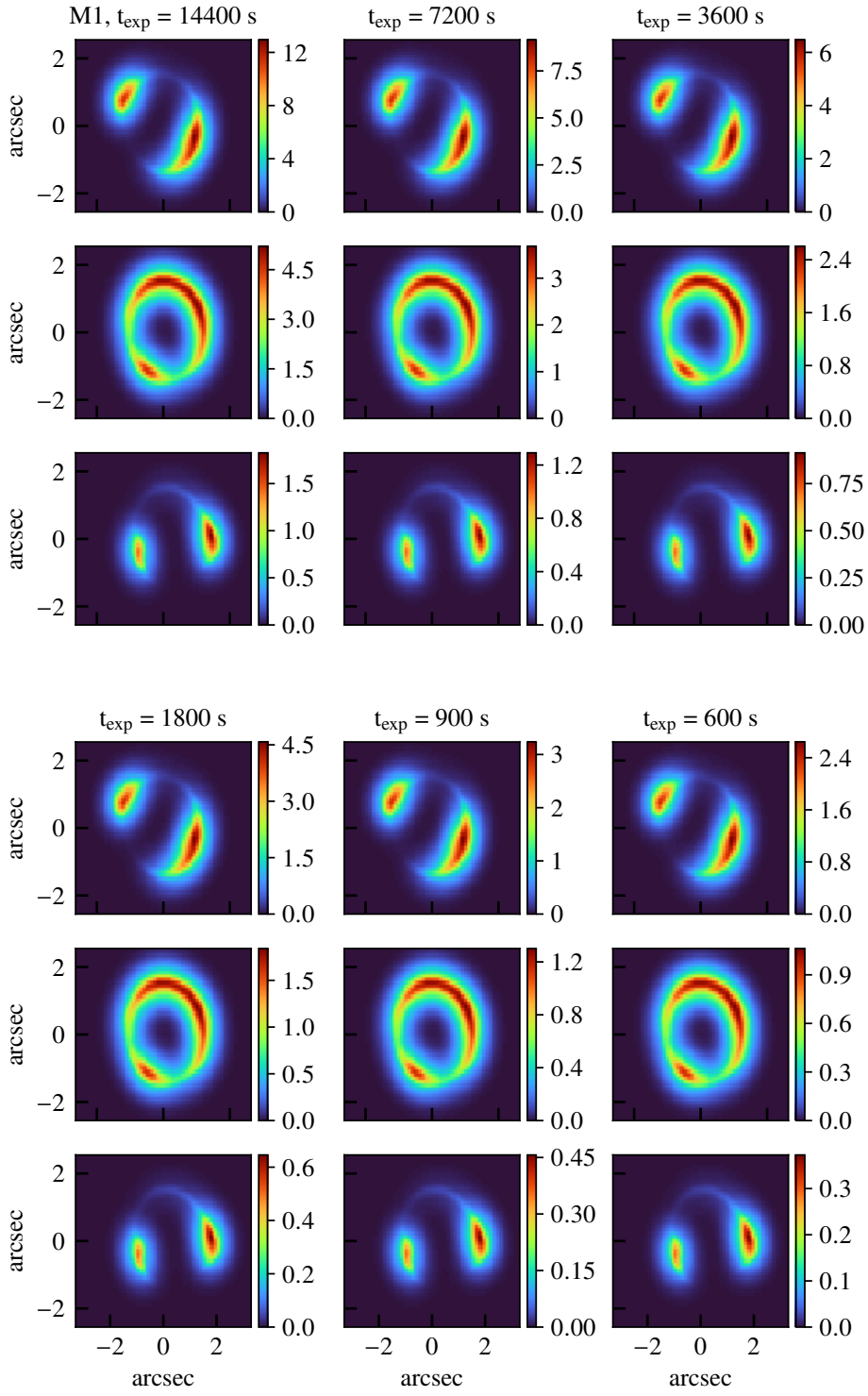

Figure 2.11: **SNR maps for data-quality tests.** The color bars show the SNR for the same representative spectral channels shown in Figure 2.5 but for the mock data described in Section 2.4.10 and in Figure 2.8. The different qualities of the data are obtained by using different exposure times, as indicated in the titles. Note the change in the scales of the color bars.

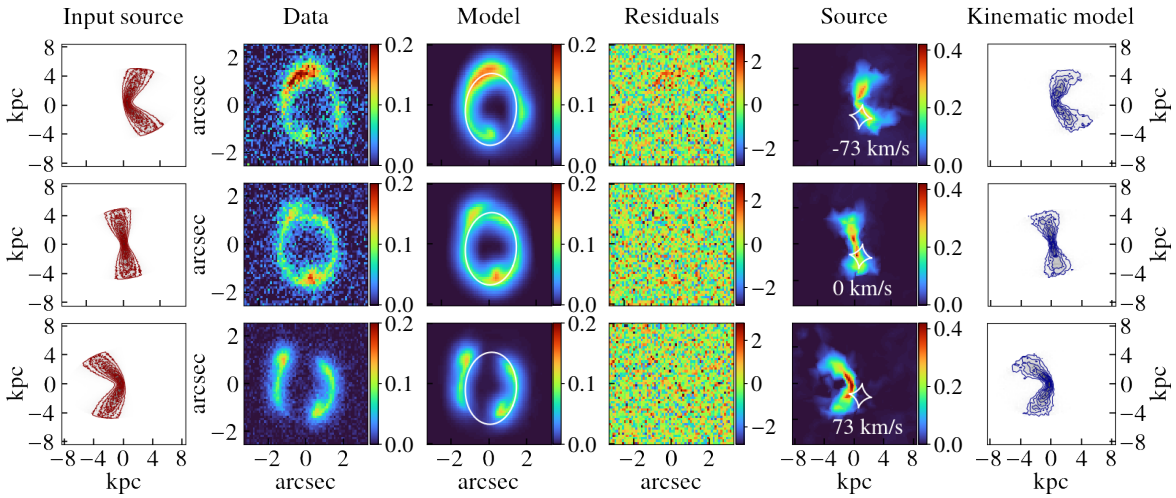

Figure 2.12: **Channel maps for the simulated dataset M2.** Same as Figure 2.5, with n = 0.1, 0.2, 0.3, 0.4, 0.5, 0.6, 0.7, 0.8.

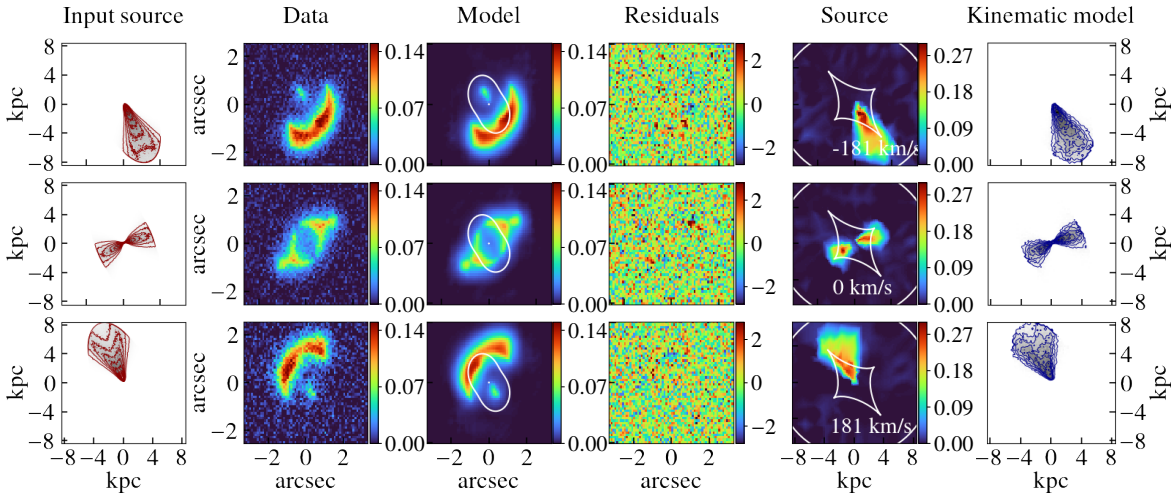

Figure 2.13: **Channel maps for the simulated dataset M3.** Same as Figure 2.5, with n = 0.1, 0.2, 0.4, 0.6, 0.8.

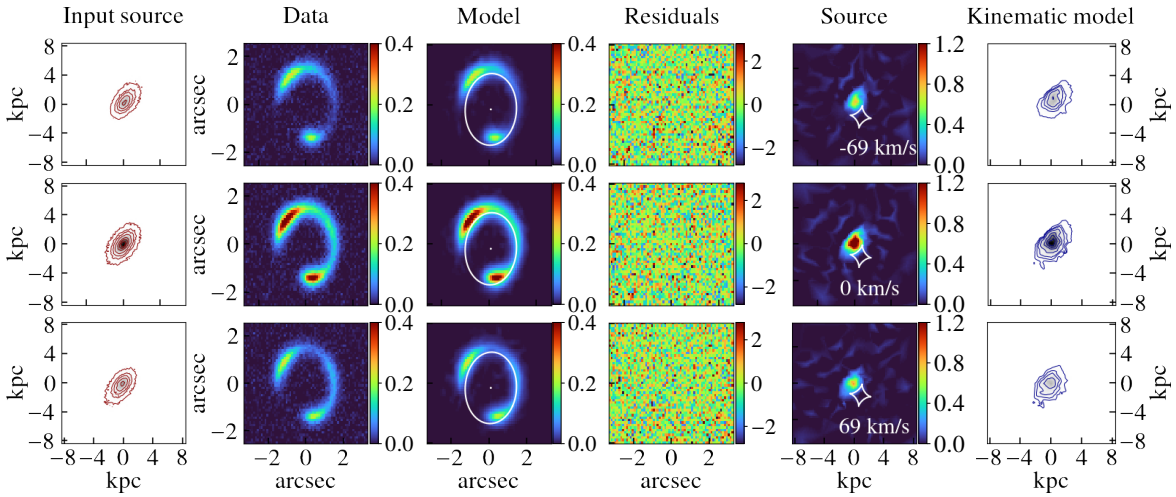

Figure 2.14: **Channel maps for the simulated dataset M4.** Same as Figure 2.5, with n = 0.01, 0.05, 0.1, 0.2, 0.4, 0.6, 0.8.

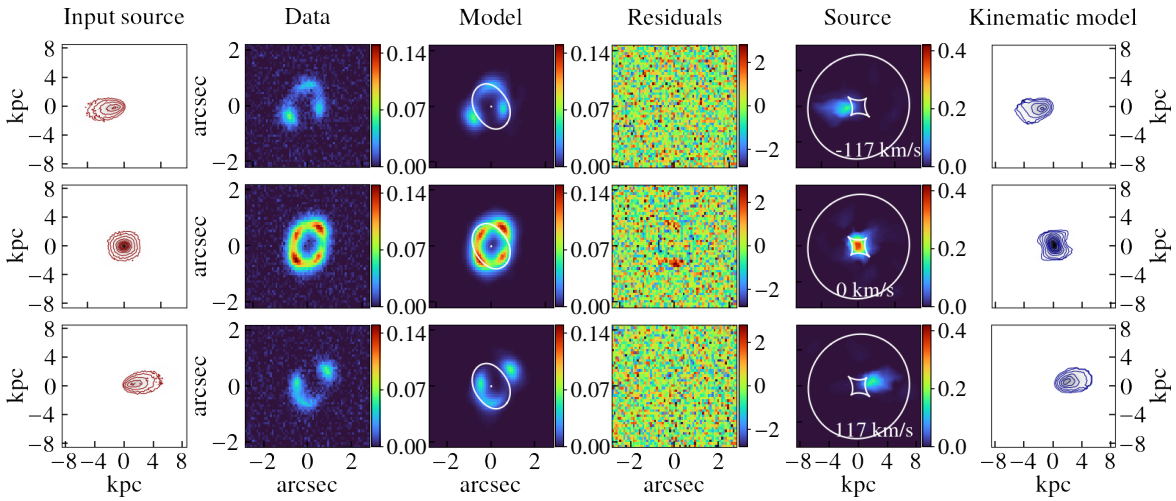

Figure 2.15: **Channel maps for the simulated dataset M5.** Same as Figure 2.5, with n = 0.025, 0.05, 0.1, 0.2, 0.3, 0.4, 0.6, 0.8.

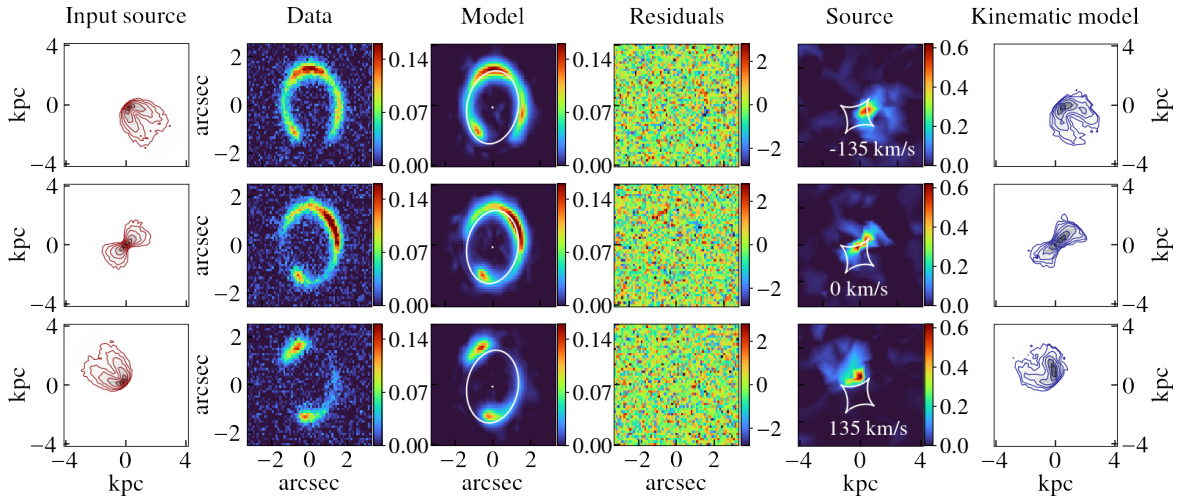

Figure 2.16: **Channel maps for the simulated dataset M6.** Same as Figure 2.5, with n = 0.025, 0.05, 0.1, 0.2, 0.4, 0.6, 0.8.

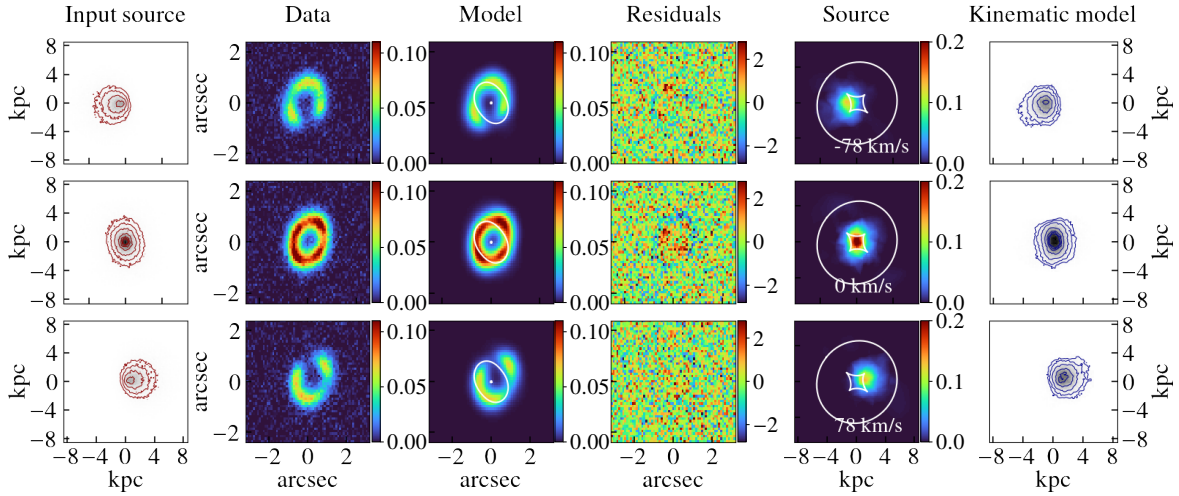

Figure 2.17: **Channel maps for the simulated dataset M7.** Same as Figure 2.5, with n = 0.09, 0.18, 0.36, 0.54, 0.64, 0.72.

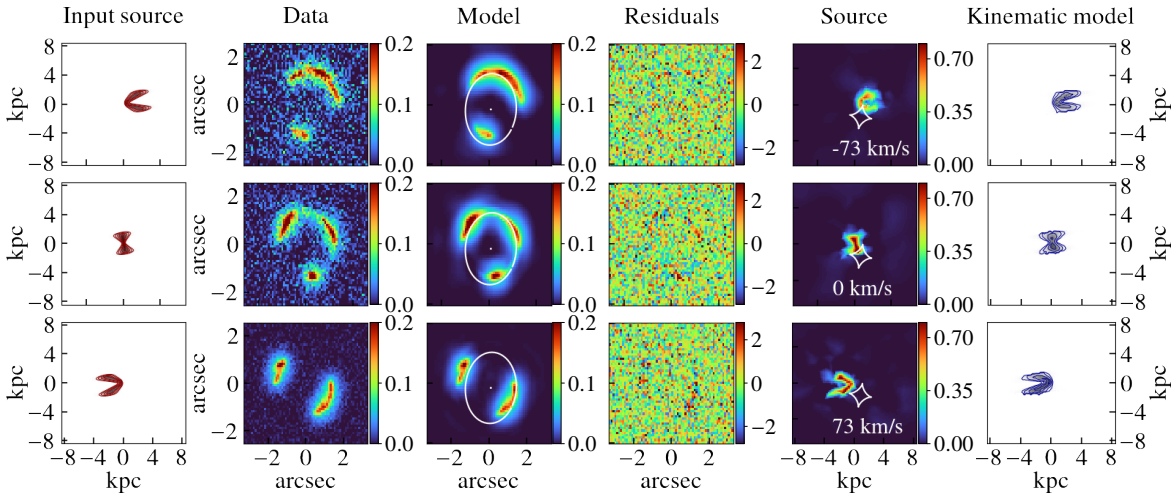

Figure 2.18: **Channel maps for the simulated dataset M8.** Same as Figure 2.5, with n = 0.1, 0.2, 0.4, 0.6, 0.8.

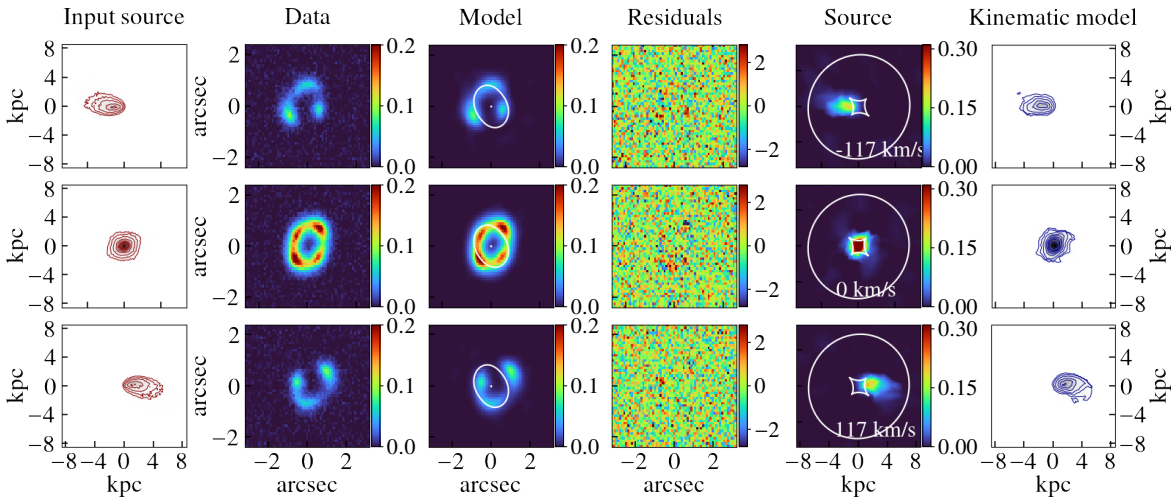

Figure 2.19: **Channel maps for the simulated dataset M9.** Same as Figure 2.5, with n = 0.1, 0.2, 0.4, 0.6, 0.8.

Chapter 3

A dynamically cold disk galaxy in the early Universe

The content of this chapter is based on the work originally published as ***Rizzo, F.****, Vegetti, S., Powell, D., Fraternali, F., McKean, J. P., Stacey, H. R., White S. D. M., 2020, Nature, 584, 201-204*

Within the framework of current galaxy formation end evolutionary models, galaxies grow by acquiring material through gas accretion and mergers (e.g., Dekel et al. 2009a, Rodriguez-Gomez et al. 2016, Naab & Ostriker 2017, see also Section 1.1). Feedback processes driven by AGN or star formation are, instead, able to temper the growth of galaxies through the heating or expulsion of gas (Hopkins et al. 2012, Silk 2013, Nelson et al. 2019). While this scenario seems comprehensive, observational evidence able to give a consistent and quantitative picture is still lacking. For example, the importance of mergers in driving the stellar mass growth, as well as in determining the resulting kinematic and chemical properties of galaxies, is still a matter of debate (e.g. Oesch et al. 2010, Satyapal et al. 2014, Eliche-Moral et al. 2018). The influence of feedback processes (e.g., outflows) in regulating the growth of stellar mass is observationally challenging to evaluate since complex physical mechanisms operating at different scales (from 10^{-5} pc to $\sim$ 10s kpc) need to be identified and constrained (Chisholm et al. 2017, Perna et al. 2017, McQuinn et al. 2019). Observations of galaxies, particularly during the early cosmic epochs, when the primary phase of mass assembly is underway, are thus fundamental to understand the relative contributions of these processes.

In the past six years, ALMA has opened up a new frontier for detailed studies of galaxies in the redshift range $z \sim 4$ - 6, which so far had been almost unexplored. Observations of the FIR emission lines and continuum are providing insights into the ISM properties of young galaxies (e.g., De Breuck et al. 2014, Jones et al. 2017, Smit et al. 2018, Rybak et al. 2019, 2020). In particular, the $^2P_{3/2} \rightarrow ^2 P_{1/2}$ transition at 1900.5469 GHz (157.74 μm, [CII]) of the ionized carbon C+ is a powerful tool to investigate the gas physical conditions in the distant Universe:

it is typically the brightest fine-structure line emitted in star-forming galaxies, representing $\sim$ 0.1 - 1 percent of the total FIR luminosity in the most active systems (Stacey et al. 2010a, Sargsyan et al. 2014). Due to the lower ionization potential of 11.3 eV of the atomic carbon with respect to HI, the [CII] emission line can trace multiple phases of the ISM, including the warm ionized, the warm and cold neutral atomic, and the dense molecular medium (Stacey et al. 2010b). However, several studies (Rigopoulou et al. 2014, Cormier et al. 2015, De Breuck et al. 2019) have argued that more than 60 percent of the [CII] emission originates in the photodissociation regions, the external layers of molecular clouds heated by the far-UV photons emitted from OB stars. In these regions, both atomic and molecular hydrogen, as well as electrons, can collisionally excite the ground state of C+ ions producing the [CII] emission line. Furthermore, there are observational and theoretical studies (Pineda et al. 2013, Nordon & Sternberg 2016, Glover & Smith 2016) suggesting that [CII] is also a good tracer of the "CO-dark" gas. In low-metallicity environments or the outer regions of molecular clouds, the presence of H_2 can be missed by CO observations: whereas H_2 self-shields and survives, CO can easily photodissociate into C and C+. Under this condition, the molecular gas is thus an efficient emitter of [CII] rather than CO. This wide range of physical conditions makes [CII] an excellent tracer of the kinematics of high-z star-forming galaxies over large areas of their disks.

The study of the dynamical properties of $z \gtrsim 4$ galaxies through [CII] allows one to probe galaxy evolution models. In particular, state-of-the-art theoretical studies (Pillepich et al. 2019, Dekel & Burkert 2014, Zolotov et al. 2015, Krumholz et al. 2018, Hayward & Hopkins 2017) have argued that the extreme astrophysical processes and conditions that characterize the early Universe are expected to result in galaxies that are dynamically different from those observed today. This is because the strong effects associated with galaxy mergers and supernova explosions would lead to the majority of young star-forming galaxies being dynamically hot, chaotic, and strongly unstable (Pillepich et al. 2019, Dekel & Burkert 2014).

In this chapter, we present ALMA observations of the [CII] emission line from a gravitationally lensed galaxy at $z = 4.2$. The exquisite angular resolution allows us to study its kinematic and dynamical properties on $\sim$ 60 pc scale for the first time at this redshift. This analysis enables us to test the predictions from theoretical studies and set constraints on galaxy formation models on sub-kpc scales at cosmologically important epochs.
This chapter is organized as follows. In Section 3.1, we describe the observations and the reduction process. Section 3.2 describes our gravitational lens modeling and source reconstruction technique, as well as our dynamical analysis. In Sections 3.3 and 3.4, we present the results and discuss their implications. Finally, Section 3.5 presents a summary of our main findings. Throughout this and the following chapter, we assumed a ΛCDM cosmology, with Hubble constant $H_0 = 67.8$ km s^{-1}Mpc^{-1}, matter density $\Omega_m = 0.308$, and vacuum energy density $\Omega_\Lambda = 0.691$ from Planck Collaboration et al. (2016).

3.1 Data and observations

SPT–S J041839–4751.9 (hereafter SPT0418-47) was identified by the South Pole Telescope Survey (SPT, Carlstrom et al. 2011) as a far-infrared luminous source with dust-like spectral indices at 1.4 and 2.0 mm (Vieira et al. 2013). Follow-up observations (Vieira et al. 2013) with ALMA confirmed SPT0418–47 to be a DSFG at $z = 4.2248$ (Weiß et al. 2013) that is strongly gravitationally lensed by a foreground galaxy at $z = 0.263$.
The data used in this chapter were taken from the ALMA Archive. In particular, SPT0418-47 was observed with ALMA on 5 July 2017 under project code 2016.1.01499.S (PI: Litke). The observations were taken at a central frequency of 358 GHz with an antenna configuration with a maximum baseline of 1400 m. The data were correlated with both linear polarizations (XX and YY), with a visibility integration time of 6 s, in four spectral windows, each with 240 channels and 1.875 GHz bandwidth. The spectral windows were centered on 350.8, 352.7, 362.8, and 364.6 GHz, where the last spectral window covers the redshifted rest frequency of the [CII] line. J0519−4546 was observed to calibrate the flux density scale, and J0522−3627 was used to correct the spectral bandpass. J0428−5005 was observed as a secondary check source. Phase switching to J0439−4522 was carried out at 7-minute intervals to calibrate the complex gains resulting from atmosphere-induced phase and amplitude fluctuations. The total on-source integration time was 21 minutes.

We calibrated the raw visibility data using the ALMA pipeline in the Common Astronomy Software Applications (CASA) package (McMullin et al. 2007). The data were then inspected to confirm the quality of the pipeline calibration and that no further flagging was required. Phase-only self-calibration was performed on the continuum with a solution interval of 100 s to correct for residual phase errors. The complex gain corrections from the continuum were applied to the line spectral window. The line data were prepared by fitting a model to the line-free spectral windows and subtracting it from the visibilities, to produce a dataset with only the spectral line emission. To improve the SNR, we averaged the data into groups of 4 velocity channels resulting in 28 independent channels each with a width of 25.7 km s^{-1}.
SPT0418-47 was imaged on a pixel scale of 0.03 arcsec pixel^{-1} with natural weighting of the visibilities and deconvolved using CLEAN (Högbom 1974). The zeroth, first, and second-moment maps of the [CII] emission are shown in panels a - c of Figure 3.1: note that these images are intended only for visualization, as all the modeling and analysis is performed on the visibility data directly (see Section 3.2 and Appendix A.2).

3.2 Analysis overview

In this section, we provide an overview of the lens-kinematic modeling technique with which we derive the gas surface brightness distribution in each spectral channel, as well as the kinematic and dynamical properties of the lensed galaxy. In addition, we also reconstruct the FIR surface brightness distribution of the heated dust emission from the interferometric continuum dataset.

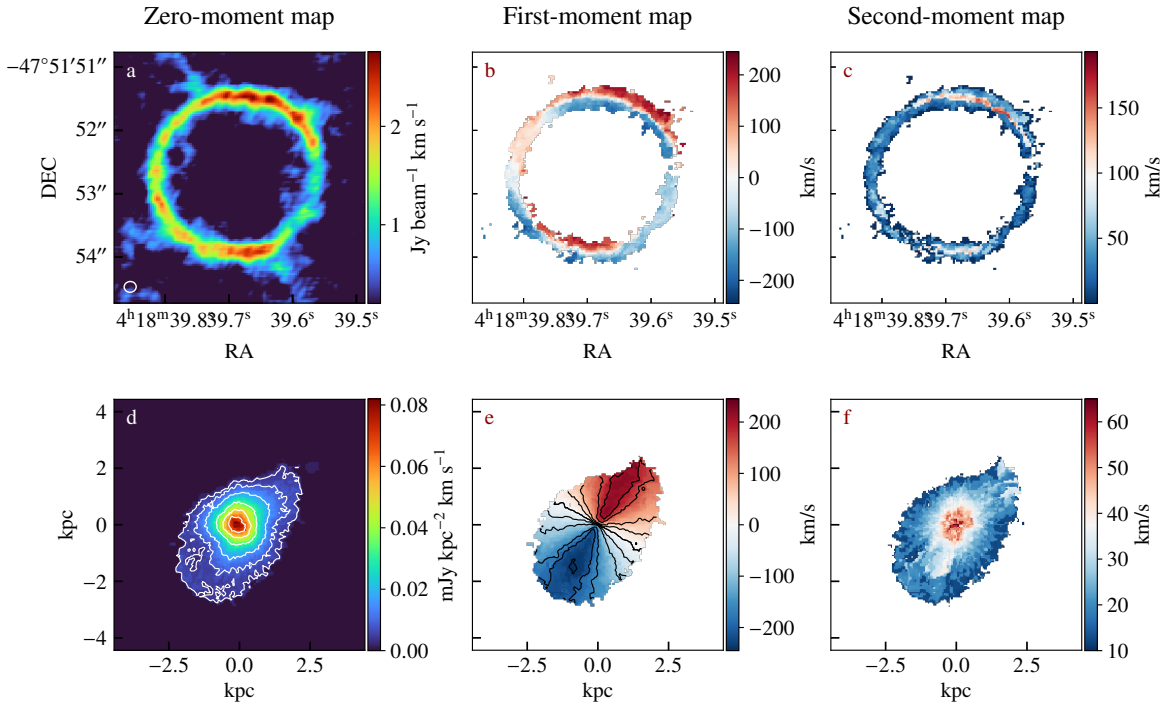

Figure 3.1: **[CII] emission from the lensed galaxy SPT0418-47 and source plane reconstruction.** Panel a: Emission of the 158-μm fine-structure line of ionized carbon [CII] integrated across a velocity range of 721 km s^{-1} (zeroth-moment map). The beam size, shown as a white ellipse on the lower left corner, is 0.19×0.17 arcsec^2 at a position angle of 85.22°. Panels b and c: as in a, but the emission is colour-coded by the flux-weighted velocity (b) and velocity dispersion (c) (first- and second-moment maps). Panels d - f: zeroth-, first- and second moment-maps of the reconstructed source. In d the white contours are set at n = 0.05, 0.1, 0.2, 0.4, 0.6, 0.8 times the value of the maximum flux of the zeroth-moment map. In e the black solid contours are at $V_{\rm sys} \pm \Delta V$, where $V_{\rm sys}$ is the systemic velocity $V_{\rm sys} = 0$ km s^{-1} and $\Delta V = 40$ km s^{-1}. We note that the scales of the second-moment maps (c and f) are different because c shows the observed values, whereas f shows the intrinsic ones (beam-smearing corrected). These six maps are intended only for visualization; the source reconstruction and its kinematic modeling are performed using the full 3D information of the data cube containing the [CII] emission line.

3.2.1 Lens and kinematic model

We model the data cube containing the [CII] emission line using a 3D Bayesian lens-kinematic modeling technique that fits the data directly in their native space (Figure 3.2, see Chapter 2, Appendix A.2, and Powell et al. 2020, for a more detailed description of the modeling approach). In the case of interferometric observations, the data **d** are the visibilities, that is, the Fourier transform of the sky brightness distribution from the observed target (see Appendix A.1). As a consequence, in the response operator **M**, equations (2.3), (2.5), (2.4), the Discrete

Fourier transform operator **D** takes the place of the PSF operator **B**.

The method used to model the source is grid-based (see Section 2.1): the surface brightness distribution of the background source is reconstructed on a triangular adaptive grid (Vegetti & Koopmans 2009) that has a high pixel-density in the high-magnification regions. For this system, the resulting spatial resolution is ~ 40 pc in the inner regions and ~ 90 pc in the outer regions. As extensively described in Section 2.1.3, the kinematics of the background galaxy is obtained by fitting the lensed data directly in a hierarchical Bayesian fashion, where the 3D kinematic model, $\mathbf{s_{kin}}$, that describes a rotating disk is used as a regularizing prior for the pixelated source reconstruction.

As commonly done when modeling galaxy-galaxy strong lensing observations, the lens is described by a projected mass density profile with a cored elliptical power-law distribution plus the contribution of an external shear component of strength $\Gamma_{\rm sh}$ and position angle $\theta_{\rm sh}$, see equation (2.15). This assumption has been shown to provide a good fit to large samples of known lenses, as discussed, for example, by Koopmans et al. (2006) and Barnabè et al. (2009). The best-fit lens mass model parameters (Table 3.1) are in agreement within 2-σ with those derived from modeling the dust continuum (Spilker et al. 2016).

The kinematic model $\mathbf{s_{kin}}$ is defined by the parameters describing the rotation velocity, the velocity dispersion profile, and the geometry of the galaxy (see Section 2.1.3). We choose the multi-parameter function as the functional form for the rotation velocity, see equation (2.20), because it is flexible enough to reproduce the large variety of observed rotation curves, and allows, therefore, for much more freedom than other typically used functions, for example, the arctangent.

The velocity dispersion profile, $\sigma(R)$, is described by an exponential function, which is more flexible than the more common choice of a constant value (Wisnioski et al. 2015, Turner et al. 2017). We also tested a linear function, but found it to be significantly less favored by the data, with a Bayes factor of 1.8 relative to the exponential model.
For the geometry of the kinematic model, defined by the inclination (i) and position angle (PA), we assume that there is no radial variation. The surface density of the gas is not a free parameter; instead, we impose a pixel-by-pixel normalization, which is given by the surface brightness distribution obtained from the lens modeling of the zeroth-moment map. The advantage of using this normalization is that it allows us to account for possible asymmetries in the gas distribution. The maximum a posteriori parameters describing the kinematics of the source are listed in Table 3.1.

The derivation of the lens mass model and the source kinematics is done using a four-step optimization scheme (see Section 2.1.4 in Chapter 2), while the uncertainties on the parameters are obtained from the posterior distributions calculated with MultiNest (Feroz et al. 2009, 2013), by adopting the user-defined tolerance, sampling efficiency and live points of 0.5, 0.8 and 200. We have then verified that the evidences estimated by MultiNest flatten as a

Table 3.1: **Lens and source kinematic parameters.** Left: the lens parameters describe a projected mass density profile with a cored elliptical power-law distribution, equation (2.15), plus the contribution of an external shear component (Γ_{sh}, θ_{sh}). Right: the kinematic parameters describe a rotating disk with a rotation curve defined by a multi-parameter function, equation (2.20), a velocity dispersion profile defined by an exponential function (σ_0, R_σ), and a geometry defined by the inclination (i) and the position angles (PA).

Lens parameters		Kinematic parameters	
κ_0 (arcsec)	1.22±0.04	i (°)	54± 2
θ (°)	22.6±1.6	PA (°)	-27±3
q	0.91±0.02	V_t (km s^{-1})	245.1±0.8
γ	2.05±0.09	R_t (kpc)	0.14±0.03
Γ_{sh}	0.0082±0.0003	β	0.80±0.02
θ_{sh} (°)	29.9±3.0	ξ	2.0±0.4
		σ_0 (km s^{-1})	58.1±1.8
		R_σ (kpc)	1.7±0.1

function of the prior volume. As described in Chapter 2, for each parameter, we adopt priors that are flat in the intervals $[\overline{\eta}_{\mathbf{lens/kin}} - 0.2\overline{\eta}_{\mathbf{lens/kin}}, \overline{\eta}_{\mathbf{lens/kin}} + 0.2\overline{\eta}_{\mathbf{lens/kin}}]$, where $\overline{\eta}_{\mathbf{lens/kin}}$ are the best-fitting parameters, inferred from the non-linear optimization. To be conservative, we report as errors in the parameters the sum in quadrature of the following two contributions: the 1-σ uncertainty on the posterior distributions derived by MultiNest and the difference between the maximum a posteriori parameter values obtained by MultiNest and by the non-linear optimizer. These values of the uncertainties are in line with what is expected from the tests presented in Chapter 2, where we applied our methodology to data characterized by spatial and spectral resolutions of at least a factor of ~ 3 worse than those analyzed in this chapter.

3.2.2 Dynamical model and Toomre parameter

Under the assumption that the total galactic gravitational potential Φ is axisymmetric, the rotation velocity $V_{rot}(R)$ of the gas, in cylindric coordinates (R, ϕ, z), is related to Φ by the equation:

$$R\left(\frac{\partial\Phi}{\partial R}\right)_{z=0} = V_c^2 = V_{rot}^2 + V_A^2, \tag{3.1}$$

where V_c is the circular velocity, and V_A is the asymmetric-drift correction that accounts for the pressure support due to the random motions. Under the assumptions that the gas of the rotating disk has a thickness independent of the radius (Iorio et al. 2017), that it is thin and

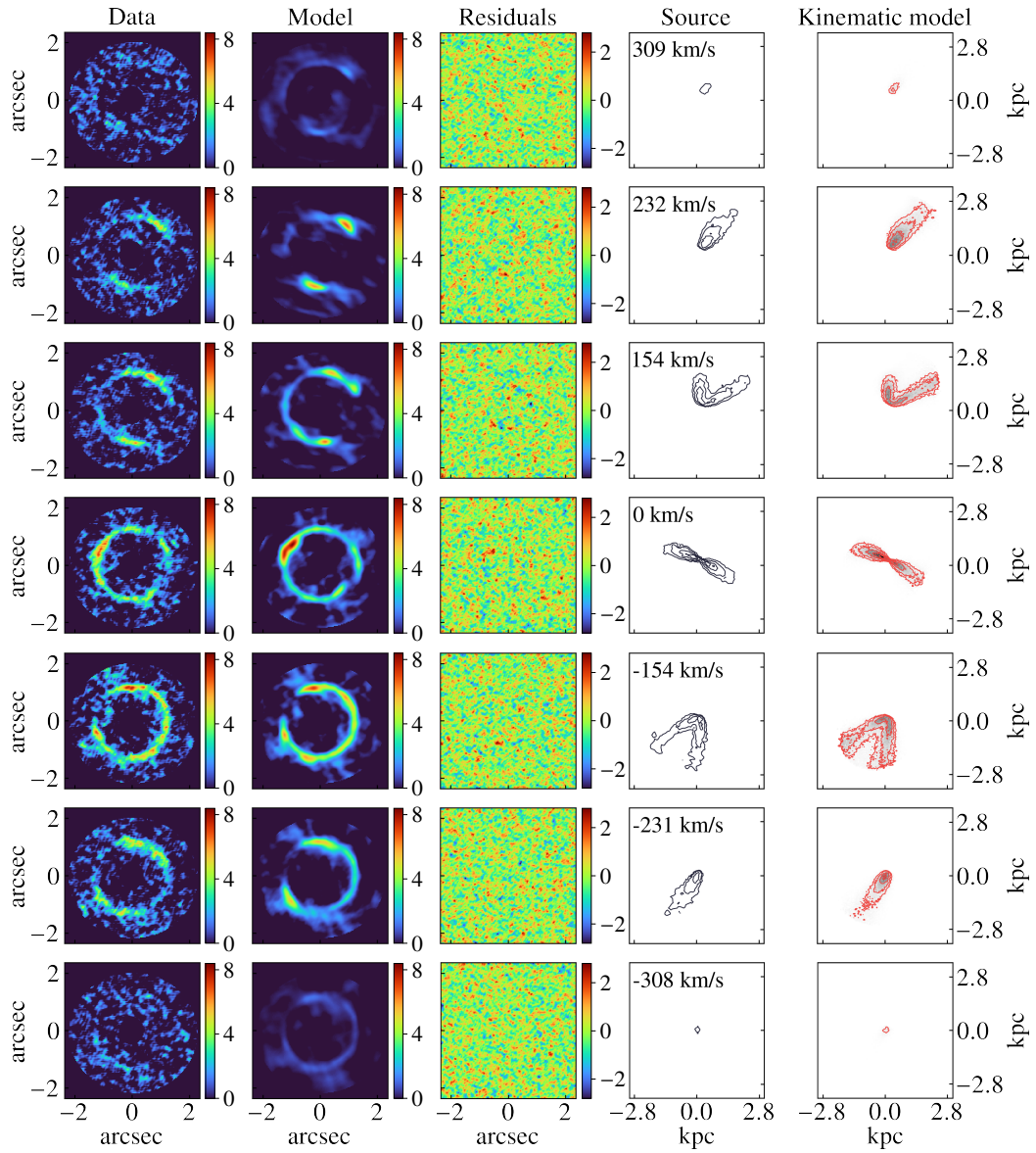

Figure 3.2: **Reconstruction of the [CII] emission and kinematic model.** The rows show some representative channel maps at the velocity shown on the upper left corner of column 4. Columns 1 and 2 show the dirty image (see Appenedix A.1) of the data and the model respectively, colour-coded by the flux in units of mJy/beam. Column 3 shows the residuals (data - model) normalised to the noise. Column 4 and 5 show the contours of the reconstructed source and of the kinematic model used to constrain the source reconstruction. The contour levels in the last two columns are set at n = 0.1, 0.2, 0.4, 0.6, 0.8 times the value of the maximum flux of the kinematic model.

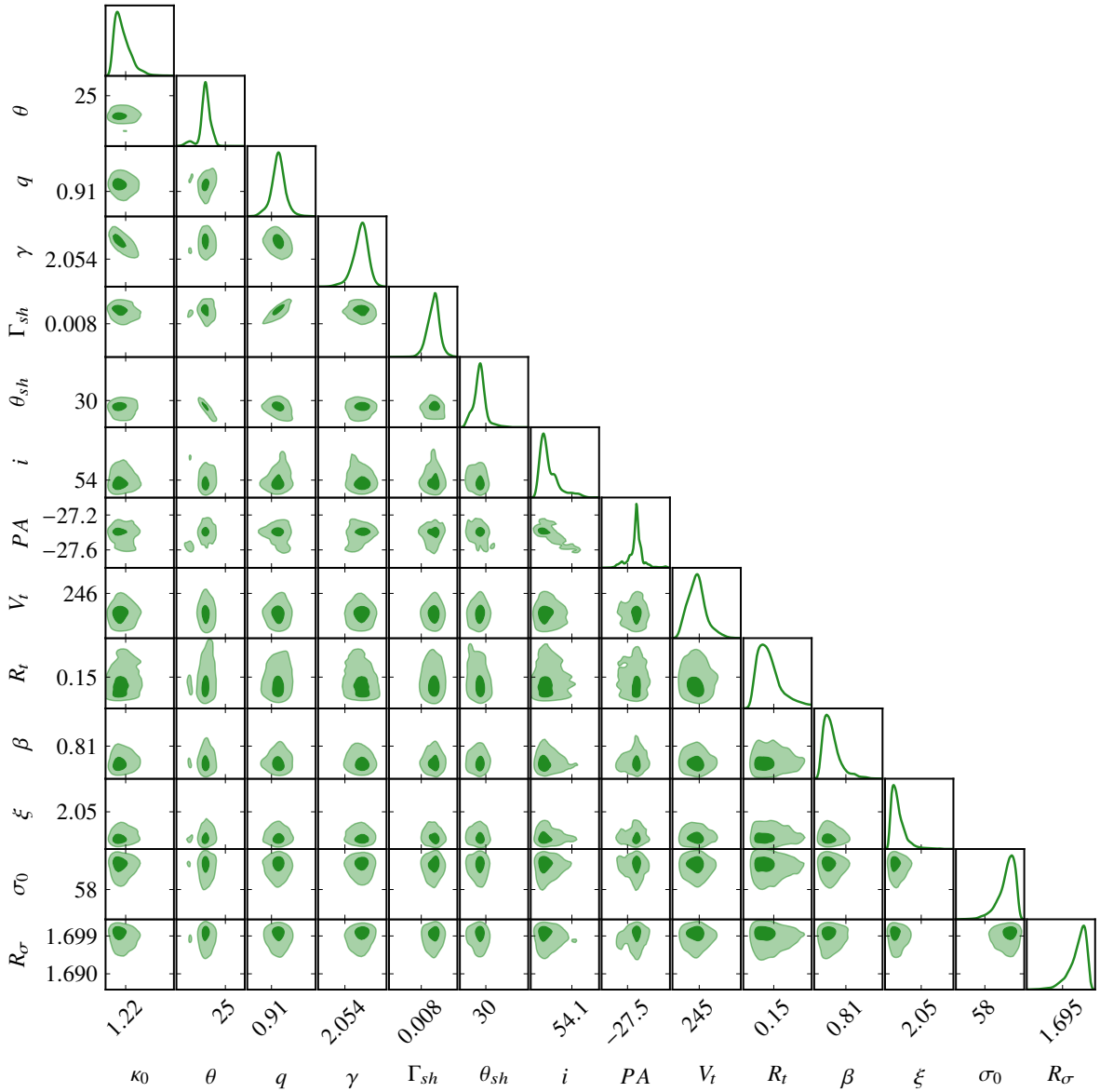

Figure 3.3: **Corner plot showing the posterior distributions of the lens and kinematic parameters.** The dark and light areas in the two-dimensional distributions show the 39 percent and 86 percent confidence levels, corresponding to 1-σ and 2-σ, respectively, obtained with the methodology described in Chapter 2. From left to right, the first 6 panels show the lens parameters, and the other panels show the source kinematic parameters.

that it has a spatial distribution described by an exponential profile,

$$\Sigma_{\rm gas} = \Sigma_0 \exp\left(-\frac{R}{R_{\rm gas}}\right), \tag{3.2}$$

the expression for V_A is given by

$$V_A^2 = -R\sigma^2 \frac{\partial \ln(\sigma^2 \Sigma_{gas})}{\partial R} = -R\sigma^2 \frac{\partial \ln(\sigma^2 \exp(-R/R_{gas}))}{\partial R}. \quad (3.3)$$

To measure the scale radius R_{gas} we divide the zeroth-moment map of the reconstructed source (Figure 4.1, panel d) in rings having centers, PA and i defined by the values of the kinematic model (Table 3.1) and we calculate the surface density at a certain radius as the azimuthal average inside that ring. The surface density profile obtained in this way is then fitted using the exponential profile, resulting in a value of $R_{gas} = 0.9$ kpc. The resulting asymmetric-drift correction, equation (3.3), gives a small contribution ($\lesssim 1$ percent) with respect to $V_{rot}(R)$.

To derive the contribution of the gas, stellar and dark matter components to the total gravitational potential, we model the circular velocity as

$$V_c = \sqrt{V_{star}^2 + V_{gas}^2 + V_{DM}^2}. \quad (3.4)$$

In particular, to fit V_{star}, V_{gas}, V_{DM}, we make the following assumptions:

- V_{star} is the stellar contribution under the assumption that this component is described by a Sérsic profile (Lima Neto et al. 1999, Terzić & Graham 2005), defined by the total stellar mass M_{star}, the effective radius R_{eff} and the Sérsic index n. The lack of spatially resolved data from the rest-frame optical/UV emission prevent the fitting of two stellar components (i.e., bulge and disk), due to the strong degeneracies between the two. The single Sérsic component employed in the dynamical fitting should be, therefore, considered as a global description of the stellar distribution (see Section 3.4 for further discussion).

- V_{gas} is the gas contribution, under the assumption that the gas in this galaxy has a distribution described by an exponential profile, as traced by the [CII] emission line. The scale length that enters in V_{gas} is fixed at the value R_{gas} found above, and the only free parameter of the fit for V_{gas} is the conversion factor ($\alpha_{[CII]}$) between the total [CII] luminosity and the total gas mass. A number of recent studies have found that [CII] is a good tracer of the total gas mass (Zanella et al. 2018, Gullberg et al. 2018). For SPT0418-47 the [CII] luminosity is 1.8×10^9 $L_\odot$, obtained by computing the zeroth-moment map of the [CII] emission as the signal integrated along the spectral axis at each pixel of the reconstructed source.

- The dark matter contribution V_{DM} is modeled as a Navarro-Frenk-White (NFW Navarro et al. 1996) spherical halo, with a concentration parameter of $c = 3.06$. The latter is obtained by averaging the values of c at $z = 4.22$ for dark matter haloes with masses between $10^{10} M_\odot$ and $10^{13} M_\odot$, assuming the mass-concentration relation estimated in N-body cosmological simulations (Dutton & Macciò 2014). We notice that at this redshift, c is almost independent of the dark-matter halo mass varying by just 6 percent

Table 3.2: **Assumptions for the dynamical fit.**

Component	Density profile	Free parameters	Priors
Stars	Sérsic	$M_{\rm star}$	$[10^7, 10^{11}]\ M_\odot$
		$R_{\rm e}$	[0.04, 2.0] kpc
		n	[0.5, 10]
Gas	Exponential	$\alpha_{\rm [CII]}$	$[3.8, 238.0]\ M_\odot/L_\odot$
DM	NFW	$M_{\rm DM}$	$[10^{10}, 10^{13}]\ M_\odot$

for a variation of 3 orders of magnitude in the halo mass. To test the effect of our assumption of a constant concentration, we repeated the analysis with a concentration c free to vary according to either a uniform prior or a Gaussian prior centered on the predicted mass-concentration relation, finding that all inferred dynamical parameters do not change significantly with c.

We summarize all our assumptions for the dynamical model in the second column of Table 3.2, while the corresponding free parameters are shown in the third column of the same table. We compute the Bayesian posterior distribution of these parameters using DYNESTY, a python implementation of the Dynamic Nested Sampling algorithm (Speagle 2019, see Figure 3.5). We use log uniform priors for the mass parameters and uniform priors for the scale radii (column 4 of Table 3.2). For $\alpha_{\rm [CII]}$, we employ a uniform prior in the range corresponding to ± 3 standard deviations around the mean value of 30 $M_\odot/L_\odot$, derived from a large sample of low- and high-z galaxies (Zanella et al. 2018).

The inferred dynamical parameters are shown in Table 3.3. We note that the derived $M_{\rm star} = 1.2^{+0.2}_{-0.1} \times 10^{10}\ M_\odot$ is in excellent agreement with the value of $(9.5 \pm 3.0) \times 10^9\ M_\odot$ found in a recent independent study (De Breuck et al. 2019) by fitting the spectral energy distribution of this galaxy. For the conversion factor $\alpha_{\rm [CII]}$, we infer a value of $\alpha_{\rm [CII]} = 7.3^{+1.0}_{-1.2}\ M_\odot/L_\odot$, in agreement with other studies of z $\sim$ 4 DSFGs (Gullberg et al. 2018). In Table 3.3, we show some relevant physical quantities (see also Figure 3.4, panel d), that are derived from our dynamical analysis. In particular, for each of these we quote the 16th, 50th and 84th percentile, which were obtained from the full posterior sample points returned by DYNESTY. We also calculate the Toomre parameter (Toomre 1964) using the general definition

$$Q(R) = \frac{\sigma \kappa}{\pi G \Sigma_{\rm gas}}, \tag{3.5}$$

where κ is the epicycle frequency defined as $\kappa = \sqrt{R d\Omega^2/dR + 4\Omega^2}$, where Ω is the angular frequency, defined as $V_{\rm rot}/R$. The Toomre parameter profile is shown in Figure 3.4, panel d.

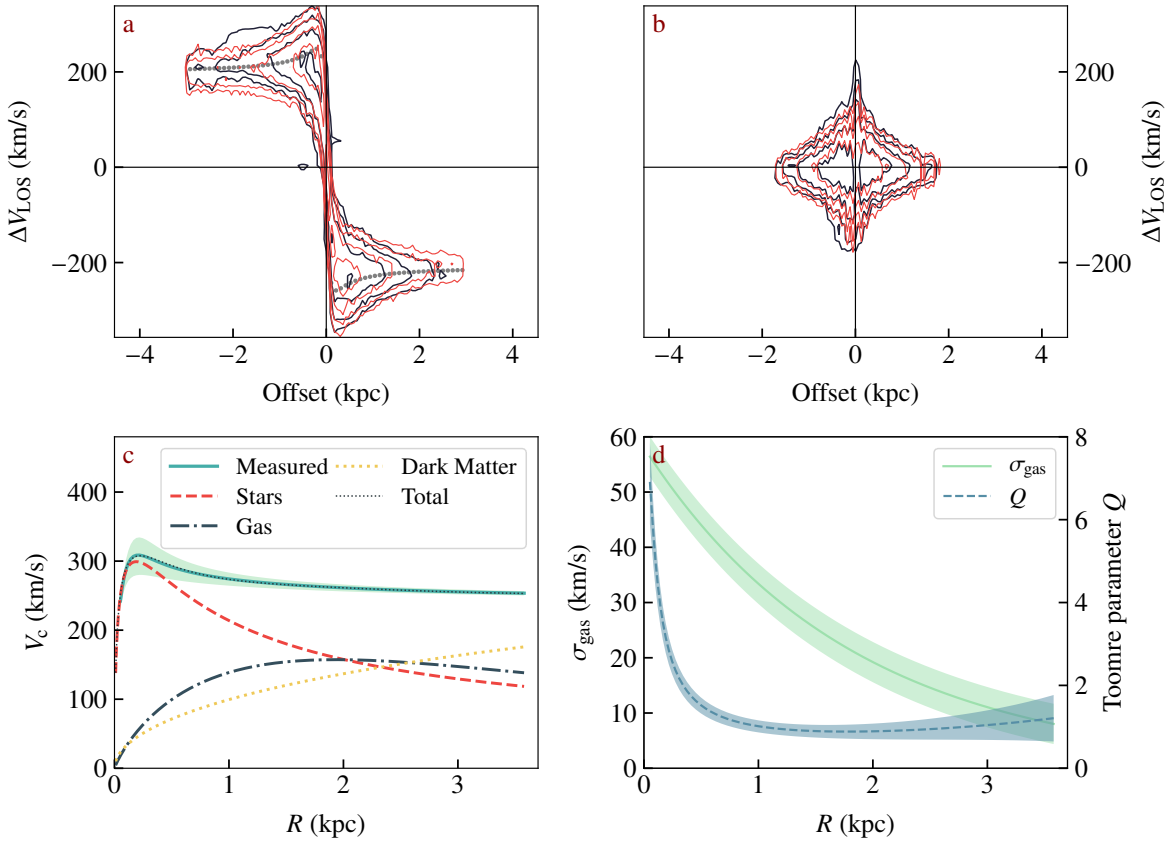

Figure 3.4: **Kinematic and dynamical properties of SPT0418-47.** Panels a, b: [CII] emission in the position–velocity diagrams along the major (a) and minor (b) axis. These diagrams show slices, the equivalent of putting long slits along the two axes. The x axis shows the offset from the galaxy center along the major and minor axis, and the y axis represents the line-of-sight velocity ($\Delta V_{\rm LOS}$) centered at the systemic velocity of the galaxy. The dark-blue contours show the reconstructed source, and the red contours show the best kinematic model. The contour levels are set at n = 0.1, 0.2, 0.4, 0.8 times the value of the maximum flux in the major-axis position–velocity diagram. The gray circles show the rotation velocities derived using our 3D lens–kinematic methodology. Panel c: rotation curve decomposition. The green solid line shows the circular velocity profile. The black dotted line is the best dynamical model, obtained by fitting the different mass components contributing to the total gravitational potential, as shown in the key. Panel d: velocity dispersion profile (solid green line) and Toomre parameter profile (dotted blue line). The colored bands in c and d represent uncertainties obtained by error propagation from the 1-σ uncertainties of the parameters that define the respective profiles.

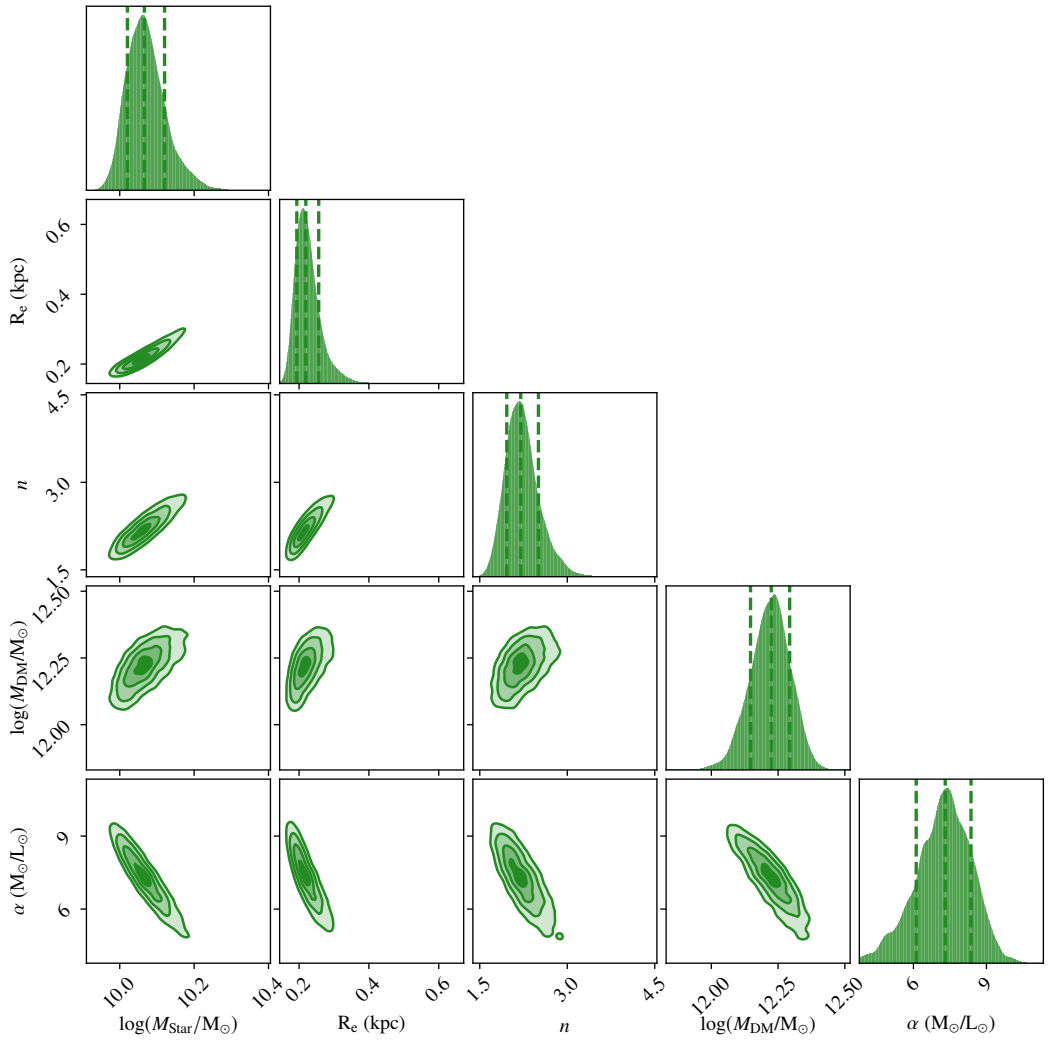

Figure 3.5: **Corner plot for the posterior distributions of the dynamical parameters.** The posterior distributions are the results of the decomposition of the circular velocity (Figure 3.4, panel c) into the physical components contributing to the total gravitational potential: the stars, the gas disks, and the dark matter halo. The fitted parameters are the stellar mass $M_{\rm star}$, the effective radius $R_{\rm e}$ and the Sérsic index n (Sérsic profile), the mass of an NFW dark-matter halo $M_{\rm DM}$ and the conversion factor between the [CII] luminosity and the gas mass $\alpha_{\rm [CII]}$. The dashed lines in the 1D histograms show the 16th, 50th and 84th percentiles (see Table 3.3).

Table 3.3: **Physical quantities of SPT0418-47 derived from the kinematic and dynamical modeling.** Left: parameters inferred from a dynamical fit to the circular velocity. The stellar component is described by a Sérsic profile, the gas disk by an exponential profile, while the dark matter is defined by an NFW profile. Right: the quantities in square brackets are calculated considering the gas component, under the assumption that all the gas that we observe today will be converted into stars, preserving the disk configuration. [a]Total gas mass, computed as $M_{\rm gas} = \alpha_{\rm [CII]} L_{\rm [CII]}$. [b]Total baryonic mass, computed as $M_{\rm bar} = M_{\rm star} + M_{\rm gas}$. [c]Baryonic half mass radius. [d]Dark matter fraction within the half mass radius. [e]Stellar-to-halo-mass ratio: $M_{\rm star}/M_{\rm DM}$ $[(M_{\rm star} + M_{\rm gas})/M_{\rm DM}]$. [f]Gas fraction: $M_{\rm gas}/(M_{\rm star} + M_{\rm gas})$. [g]Virial velocity of the dark matter halo. [h]Virial radius of the dark matter halo. [i]Maximum velocity for an NFW halo, computed as $V_{200}\sqrt{0.216\,c/(\ln(1+c) - c/(1+c))}$.

Parameters of the dynamical model		Derived parameters	
$M_{\rm star}$ $(10^{10} M_\odot)$	$1.2^{+0.2}_{-0.1}$	[a] $M_{\rm gas}$ $(10^{10} M_\odot)$	$1.3^{+0.2}_{-0.2}$
$R_{\rm e}$ (kpc)	$0.22^{+0.04}_{-0.02}$	[b] $M_{\rm bar}$ $(10^{10} M_\odot)$	$2.5^{+0.2}_{-0.1}$
n	$2.2^{+0.3}_{-0.2}$	[c] $R_{\rm e,bar}$ (kpc)	$[0.75^{+0.06}_{-0.06}]$
$M_{\rm DM}$ $(10^{12} M_\odot)$	$1.7^{+0.3}_{-0.3}$	[d] $f_{\rm DM}(< R_{\rm e})$	$0.018^{+0.005}_{-0.003}$ $[0.095^{+0.008}_{-0.007}]$
$\alpha_{\rm [CII]}$ $(M_\odot/L_\odot)$	$7.3^{+1.0}_{-1.2}$	[e] $f_\star$ (10^{-3})	$7.1^{+1.0}_{-0.8}$ $[14.9^{+3.7}_{-2.6}]$
		[f] $f_{\rm gas}$	$0.53^{+0.06}_{-0.08}$
		[g] V_{200} (km s^{-1})	320^{+17}_{-18}
		[h] R_{200} (kpc)	70^{+4}_{-4}
		[i] $V_{\rm max}$ (km s^{-1})	323^{+18}_{-19}

3.2.3 Dust continuum and SFR

Using the parameters of the lens mass model shown in Table 3.1, we perform a pixelated source reconstruction of the dust continuum at 160 μm (rest frame), which allows us to calculate a total magnification factor μ of 32.3±2.5. SPT0418-47 has an observed (unlensed) infrared luminosity, $L_{\rm IR,obs}$, of $(7.7 \pm 1.3) \times 10^{13}$ L$_\odot$ (Aravena et al. 2016). This value was obtained from a spectral energy distribution fitting of seven photometric data points in the wavelength rest frame range between 48 and 574 μm. Under the assumption that the morphology of the source is the same for all photometric points in the infrared band, we can use the magnification factor estimated from the emission at 160 μm to estimate an intrinsic luminosity of $L_{\rm IR} = L_{\rm IR,obs}/\mu = (2.4 \pm 0.4) \times 10^{12}$ L$_\odot$. By assuming that the IR emission comes from the thermal emission of dust, heated by the radiation field coming from young stars, we compute an SFR of 352 ± 65 M$_\odot$ yr^{-1}. This last value is derived from $L_{\rm IR}$, by applying a conversion factor of 1.48×10^{-10} M$_\odot$ (yr L$_\odot$)$^{-1}$, valid for a Kroupa Initial Mass Function (Kennicutt & Evans 2012). The gas depletion timescale is $M_{\rm gas}$/SFR = 38 ± 9 Myr.

3.3 Dynamical properties of SPT0418-47

As described in Section 1.4, for galaxies at $z \gtrsim 4$, there have been very few attempts to go beyond the fitting of the integrated line profile (Jones et al. 2017, Smit et al. 2018). Furthermore, marginally resolved observations and low SNRs have prevented the measurement of robust dynamical parameters, such as beam-smearing-corrected V/σ ratios at this high-z. The combination of the high SNR and the spatial resolution achievable thanks to gravitational lensing joined with an intrinsically beam-smearing corrected kinematic analysis has allowed us to probe the intrinsic V/σ ratio for the first time at $z \sim 4$. In this section, we describe the global kinematic properties of SPT0418-47, and we compare them with both observational and theoretical studies from the literature.

The kinematic analysis described in Section 3.2 reveals that the rotation curve of SPT0418-47 has the typical shape of a bulge-dominated spiral galaxy in the local Universe (Lelli et al. 2016): it has a bump at 0.2 kpc from the galaxy center and then declines before flattening at radii larger than 1.5 kpc (Figure 3.4, panels a and c, see Section 3.4 for further discussions on the morphology). The velocity dispersion σ, described by an exponential profile, has average values of ~ 45 km s^{-1} in the inner regions ($\lesssim 1$ kpc) and $\sim$18 km s^{-1} in the outer disk ($\gtrsim 1$ kpc, Figure 3.4, panels b and d). Since different definitions of the V/σ ratio can be found in literature (see Table 3.4), we make use of the two most popular ones (Table 3.5). We obtain $V/\sigma = 9.7 \pm 0.4$, calculated as the ratio between the maximum rotation velocity $V_{\rm max}$ and the mean velocity dispersion $\sigma_{\rm m}$; while we obtain $V/\sigma = 13.7 \pm 0.7$, when calculated as the ratio between the flat part of the rotation velocity $V_{\rm flat}$ and the velocity dispersion $\sigma_{\rm ext}$ at outer radii ($R > 1$ kpc).

3.3.1 Comparison with galaxy evolution models

There is consensus (Hung et al. 2019, Teklu et al. 2018, Bird et al. 2013, Martizzi 2020) that galaxy disks at high-z are much more turbulent than their local counterparts in all components (stars, warm and cold gas).
In Figure 3.6 we show the V/σ predicted (or assumed) by current galaxy evolution models:

- The light-blue area shows the predicted evolution of V/σ in the TNG50 simulation (Pillepich et al. 2019) for galaxies with stellar masses of 10^9 to $10^{10.5}$ $M_\odot$ where the gas kinematics is derived from Hα emitting gas. However, since, by construction, the ionized and molecular gas of TNG50 galaxies have the same dynamics, we can compare these estimations with our measurement coming from the [CII] emission line. TNG50 galaxies at $z \sim 4$ have median $V_{\rm max}/\sigma_{\rm m} \sim 3$, with a standard deviation of 1.5, meaning that SPT0418-47 is 4.5 standard deviations away from the median value.

- By using an analytic approach and a cosmological mesh refinement simulation, two recent studies (Dekel & Burkert 2014, Zolotov et al. 2015) found that galaxies at $z \gtrsim$

3 are dominated by violent disk instabilities, which lead to V/σ values $\lesssim 2$ in all components (gray area in Figure 3.6).

- By using an analytic model that combines stellar feedback and gravitational instabilities, Krumholz et al. (2018) derived a prediction for the correlation between cold gas velocity dispersion and SFR, such that SFR = $(0.42 f_{\rm eff,gas} V^2 \sigma)/(\pi G Q_{\rm min})$ (their equation 60), where we have used the constants appropriate for high-redshift galaxies (Übler et al. 2019). By using $f_{\rm eff,gas} = f_{\rm gas} \times 1.5 = 0.53 \times 1.5$, SFR = 352 $M_\odot$ yr^{-1}, V = 259 km s^{-1}, $Q_{\rm min}$ = 0.88, we derived a value of $\sigma = 183^{+53}_{-42}$ km s^{-1}, which is a factor of ~ 6 higher than our measured value of 32 km s^{-1}, and implies a $V/\sigma = 1.4^{+0.4}_{-0.3}$ (black band in Figure 3.6).

- Hayward & Hopkins (2017) used an analytic model to study the effects of stellar feedback in regulating star formation and driving outflow. In this case, the gas velocity dispersion is not a predicted quantity, but it is derived by assuming the following relation between σ and the circular velocity: $\sigma \sim f_{\rm gas} V_{\rm c}/\sqrt{2}$. For the values of the gas fraction and $V_{\rm c}$ measured for SPT0418-47, this analytical model implies a value of σ = 120 km s^{-1}, which is a factor of ~ 4 higher than the measured value, resulting in a $V/\sigma = 2.6$. In Figure 3.6 (green band), we show the predictions of V/σ for this model, obtained by using their relations for velocity versus stellar mass, and the redshift evolution of velocity dispersion with respect to gas fraction.

Overall, the V/σ found for SPT0418-47 is significantly larger than what is predicted by numerical (Pillepich et al. 2019, Zolotov et al. 2015) and analytical (Dekel & Burkert 2014, Krumholz et al. 2018, Hayward & Hopkins 2017) models. For example, the majority of star-forming galaxies at $z \sim 4$, from the TNG50 simulation (Pillepich et al. 2019) have $V/\sigma \lesssim 3$ (light-blue band in Figure 3.6). Even though such simulated galaxies have rotationally-supported gas-rich disks, they are dynamically hotter than their low-z counterparts. Complex astrophysical processes (e.g., stellar feedback, galaxy mergers, gas inflows, and outflows) are expected to have a significant impact on the gas kinematics within galaxies at this early epoch and are predicted to be responsible for a progressive increase of chaotic, random motions with redshift (Pillepich et al. 2019, Krumholz et al. 2018, Hayward & Hopkins 2017). However, the dynamical properties of SPT0418-47 seem to rule out models in which high star-formation feedback and a high gas fraction necessarily produce large turbulent motions (Pillepich et al. 2019, Krumholz et al. 2018, light-blue, green, and black bands in Figure 3.6) and violent disk instabilities (Zolotov et al. 2015, Dekel & Burkert 2014), resulting in dispersion dominated systems with $V/\sigma \lesssim 2$ at these redshifts (gray band in Figure 3.6). Our result requires galaxy evolution models to produce dynamically cold galaxies, not characterized by large turbulent motions (Pillepich et al. 2019, Krumholz et al. 2018) and violent instabilities (Dekel & Burkert 2014, Zolotov et al. 2015), already at early times.

Table 3.4: **Kinematic measurements of the comparison samples.** [a]The value of σ are not provided, but we assume a value of 10 km s^{-1}, typical of HI in local spiral galaxies (Lelli et al. 2016). [b] $V_{\rm PV,max}$ and $V_{\rm PV,min}$ are the maximum and minimum velocity along the position-velocity diagram.

Study	Tracer	V	σ
Lelli et al. (2016)	HI	$V_{\rm flat}$	[a]10 km/s
Swinbank et al. (2017)	Hα, [OII]	Extracted at $3R_{\rm disk}$	Average ($\sigma_{\rm m}$)
Harrison et al. (2017)	Hα	Extracted at $3.4R_{\rm disk}$	Median value at $R > 3.4\,R_{\rm disk}$
Di Teodoro et al. (2016)	Hα	$V_{\rm flat}$	$\sigma_{\rm m}$
Wisnioski et al. (2015)	Hα	$(V_{\rm PV,max} - V_{\rm PV,min})/2$[b]	$\sigma_{\rm ext}$
Lelli et al. (2018)	[CI]	$V_{\rm flat}$	$\sigma_{\rm m}$
Turner et al. (2017)	[OIII]	Extracted at $3.4R_{\rm disk}$	Median

Table 3.5: **Kinematic properties of SPT0418-47 derived under different assumptions.** Parameters representing the rotation velocities and velocity dispersion profile, as well as the rotation support for this galaxy, calculated under different definitions. [a]Maximum rotation velocity. [b]Mean velocity dispersion. [c]Rotation-to-random-motions ratio calculated from $V_{\rm max}$ and $\sigma_{\rm m}$. [d]Flat rotation velocity, calculated by using the flat part of the rotation curve (R > 2 kpc, see Figure 4.2, panel c). [e]Velocity dispersion at outer radii (R > 1 kpc). [f]Rotation-to-random-motion ratio, calculated from $V_{\rm flat}$ and $\sigma_{\rm ext}$.

Global kinematic properties			
[a]$V_{\rm max}$ (km s^{-1})	308±4	[d]$V_{\rm flat}$ (km s^{-1})	259±1
[b]$\sigma_{\rm m}$ (km s^{-1})	32±1	[e]$\sigma_{\rm ext}$ (km s^{-1})	18±1
[c]$V_{\rm max}/\sigma_{\rm m}$	9.7±0.4	[f]$V_{\rm flat}/\sigma_{\rm ext}$	13.5±0.7

3.3.2 Comparison with observations at lower redshifts

Our high-resolution 3D kinematic analysis shows that SPT0418-47 has a ratio $V/\sigma = 9.7\pm0.4$, which is similar to spiral galaxies in the local Universe (Lelli et al. 2016, see Figure 3.6). The comparison with the intermediate-z star-forming galaxies is, instead, challenging, due to different gas tracers and different extraction methods used in the literature (see Table 3.4) to determine the evolution of the dynamical properties of galaxies across cosmic time (see also discussion in Section 1.4). While it is firmly established that the kinematics of the molecular gas traces the galaxy kinematics, there is an open debate on the validity of this assumption for the ionized gas tracers (Übler et al. 2018, Levy et al. 2018). For example, by comparing the kinematics of the ionized and molecular gas, recent studies (Übler et al. 2018, Girard et al. 2018) found that they are consistent with each other and that the ionized gas kinematics reflects the cold gas motions of galaxies. Since the [CII] emission line can be considered a

tracer of both the warm and cold gas, we can compare the dynamic properties of SPT0418-47 directly with those found for intermediate-z galaxies from ionized gas tracers, finding that the V/σ is, on average, larger than the V/σ values measured from the ionized gas. The difference may be ascribed to a combination of the following reasons:

- the velocity dispersions measured from the ionized tracers is, on average, higher than those measured from the molecular and neutral media tracers both at low- (Varidel et al. 2020) and high-z (Girard et al. 2018). For example, a recent study (Übler et al. 2019) found that velocity dispersions measured from ionized tracers tend to be $\sim$ 10 - 15 km s^{-1} higher than those measured from molecular tracers. However, if we add this 15 km s^{-1} to our inferred [CII] velocity dispersions, we find $V_{\rm max}/\sigma_{\rm m}$ = 6.6 and $V_{\rm flat}/\sigma_{\rm ext}$ = 7.8, which are still much higher than most observations at $z \lesssim 3$. We also stress that while the above analysis mostly compared the molecular and the ionized gas tracers, in this chapter, we focus on the [CII] emission, which traces both cold and warm gas.

- the Hα, [OIII], and [OII] emission lines are not good tracers of the galaxy dynamics. A recent study (Levy et al. 2018) on a sample of local galaxies showed, for example, that the kinematics of the molecular and ionized gas are different (Levy et al. 2018) and that the difference may be ascribed to stellar feedback processes. In particular, the measured ionized gas kinematics is affected by the presence of gas in outflows or in extraplanar layers. Unfortunately, the lack of good quality data for large samples of galaxies at $1 \lesssim z \lesssim 3$ prevents an accurate comparison with the kinematics traced by the molecular or neutral gas.

- the measured V/σ values are biased towards low values due to the beam-smearing effect (see Section 1.8).

We note, also, that the V/σ ratio of SPT0418-47 is similar to that measured (Lelli et al. 2018) for a galaxy at z = 2.6 from the [CI] emission line (violet cross in Figure 3.6). Overall, the comparison of the dynamical properties of galaxies at different redshifts from similar tracers (i.e., HI, [CI], [CII]) seems to indicate that there is no decrease of V/σ with time. However, larger samples will be needed to confirm this trend.

3.3.3 Toomre parameters and instabilities

Our kinematic analysis also allows the level of axisymmetric disk instabilities to be measured within SPT0418-47 via the Toomre parameter Q (see equation (3.5), Toomre 1964). A value of $Q > 1$ ensures that no instabilities will develop as a large-scale collapse is prevented by differential rotation, while $Q \lesssim 1$ indicates that instabilities will be able to grow and lead to the formation of gas and star-formation clumps within the disk. For SPT0418-47, we find an average value of $Q = 0.97 \pm 0.06$ at $R > 1$ kpc (Figure 3.4, panel d), where the gas component is dominant (Figure 3.4, panel c), indicating a potentially unstable disk, prone to form clumpy star-forming regions. This result supports the hypothesis (Carilli & Walter 2013)

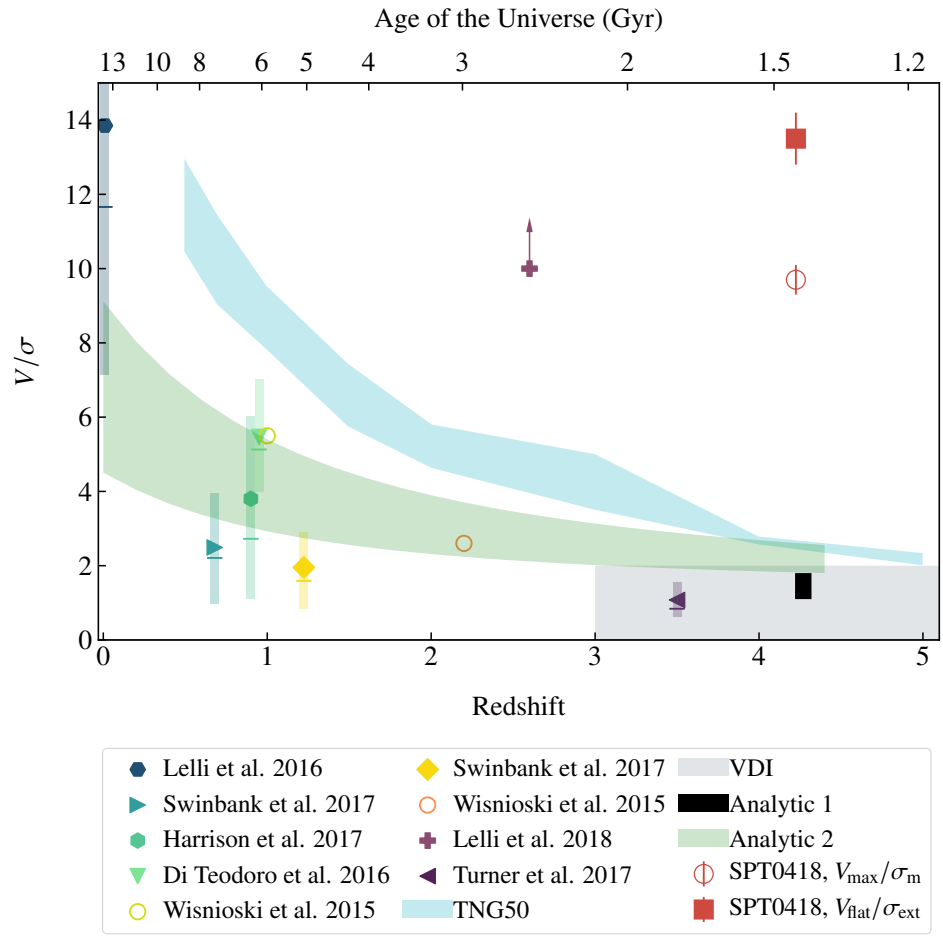

Figure 3.6: **Comparison between SPT0418-47 and samples of observed and simulated galaxies.** Mean ratio of the rotational to random motion (V/σ) versus redshift for the comparison samples of observed star-forming galaxies indicated in the legend and for SPT0418-47 (red square and empty circle). The gas tracers are shown in Table 3.4. For the comparison samples, the shaded regions show the area between the 16th and 84th percentiles of the distributions, and the horizontal bars show the median values (where available). For the empty markers, the V/σ values were calculated using for each galaxy a proxy for the maximum rotation velocity, V_{max}. The V/σ values shown by the full markers were calculated using the flat or the outer part of the rotation curve, V_{flat} (see Table 3.4 for details). The violet cross is a lower limit for a single galaxy. The light-blue band shows V/σ for simulated galaxies from TNG50 (Pillepich et al. 2019) in the mass range $10^9 - 10^{11} M_\odot$. For these simulated galaxies, V/σ is calculated as the ratio between V_{max}, and the mean velocity dispersion, σ_m. The gray area shows the expected V/σ for galaxies dominated by violent disk instabilities (VDI) (Zolotov et al. 2015, Dekel & Burkert 2014). The black and green areas show a prediction and an assumption, respectively, from two different analytical models, Analytic 1 (Krumholz et al. 2018) and Analytic 2 (Hayward & Hopkins 2017). The red square and and the empty red circle show the positions of V_{max}/σ_m and V_{flat}/σ_{ext} for SPT0418-47, respectively (see Table 3.5).

that the irregular morphologies found for DSFGs in the optical/UV rest-frame wavelengths (Chen et al. 2015) are poorly resolved clumpy star-forming regions and not objects that are undergoing or have recently experienced a merging event.

3.4 Morphology and evolutionary connection with quiescent systems

Thanks to our rotation curve decomposition (Section 3.2), we find that a Sérsic profile well describes the stellar component of SPT0418-47 with a Sérsic index of $2.2^{+0.3}_{-0.2}$ and a stellar mass of $1.2^{+0.2}_{-0.1} \times 10^{10}$ $M_{\odot}$. Several observational studies of the structural properties (Lang et al. 2014, van der Wel et al. 2014) of galaxies have confirmed that the Hubble sequence is already in place at $z \sim 2.5$, with galaxies showing a large variety of morphologies. However, at $z \gtrsim 3$, the lack of spatially resolved data in the rest-frame optical emission for these galaxies has prevented the study of their structure and morphologies. The unprecedented spatial resolution of 60 pc of the dataset for SPT0418-47 allows us to study for the first time the morphological properties of a $z \sim 4$ galaxy. The bump in the inner region of the rotation curve clearly indicates that a bulge is already in place at $z \sim 4$, while the Sérsic index of ~ 2 is a signature of either a disky bulge (Krajnović et al. 2013) or an embedded disk-like component.

DSFGs are believed to be the progenitors of ETGs, which are the most massive galaxies observed today, dominated by old stellar populations. The most popular evolutionary track for this transformation (e.g., Toft et al. 2012, Zolotov et al. 2015, Dekel & Burkert 2014) predicts that the dusty-star-forming phase is followed by a quenching phase, during which AGN feedback leads to gas consumption and heating with the consequent formation of a population of compact quiescent galaxies (Barro et al. 2014) at $z \sim 2$. In the final phase, dry minor mergers are expected to be responsible for a growth in galaxy size and the transformation into present-day ETGs.

In Figure 3.7 (panels a-d), we compare the main physical quantities of SPT0418-47 as inferred from our dynamical model, with the corresponding quantities for the sample of local ETGs from the ATLAS^{3D} survey (Cappellari et al. 2011). We consider only those local ETGs with estimated stellar ages $\gtrsim 12$ Gyr (McDermid et al. 2015), which is the lookback time corresponding to $z \sim 4$. The thin orange diamond in each panel shows the values derived for SPT0418-47 as observed today, while the red diamond shows the corresponding baryonic values (gas + stars), under the assumption that all the gas that we observe today will be converted into stars, preserving the disk configuration. Given the SFR estimated for SPT0418-47, this conversion will happen in ~ 38 Myr.

The comparison between the ETGs and the stellar/baryonic quantities for SPT0418-47 in the size–mass plane (Figure 3.7, panel a) indicates that this starburst galaxy should increase its stellar mass by a factor of 6 (3 for the red diamond) and its effective radius by a factor of 11 (3 for the red diamond), in order to evolve into an average ETG (yellow cross). This result is in agreement with a simple toy model (Naab et al. 2009) for mergers, where a single

dry major merger event would be responsible for an increase in both the size and stellar mass of SPT0418-47 by a factor of 3. On the same panel, the gray stars show the populations of compact galaxies (Barro et al. 2014) at $2 < z < 3$. Interestingly, the median size for this population is comparable to the size of SPT0418-47 (red diamond), but its median stellar mass is a factor of 3 larger. Also, the position of SPT0418-47 on the mass-size plane is compatible with the low-mass end of both ETGs and $z \sim 2$ compact galaxies. This result implies that either this galaxy will evolve smoothly into a low-mass ETG after the consumption and heating of the cold gas reservoir or, as predicted by the merger scenario, it will reach the bulk of the ETG population in the size-mass plane. Figure 3.7 panel c, shows that a potential progenitor of an ETG has already at $z \sim 4$ a disky stellar component, a feature that is very common especially amongst local fast-rotator ETGs (Krajnović et al. 2013). Finally, we have derived the fraction of mass in dark matter within the effective radius and found that with a value of $f_{\rm DM}(< R_{\rm e}) = 0.095^{+0.004}_{-0.004}$ (red diamond), the central regions of SPT0418-47 are dominated by baryons. As shown in Figure 3.7 panel c, such a low fraction of dark matter is compatible with observations of local ETGs (Cappellari et al. 2013a), implying that the physical mechanisms responsible for the mass and size growth of this galaxy with cosmic time, should preserve the dark matter contribution within the inner $\sim$ 1 kpc.

3.5 Summary

In this chapter, we use our novel 3D lens technique (see Chapter 2 and Appendix A.2) to reconstruct the intrinsic properties of a lensed galaxy at $z = 4.2$ and derive its kinematic and star-formation properties. From a rotation curve decomposition, we derive the relative contribution of the different mass components to the total galactic gravitational potential: the stellar component, the gaseous disk, and the dark matter halo.

We found that SPT0418-47 has global physical properties, e.g., total stellar mass $M_{\rm star}$, dark matter mass $M_{\rm DM}$ and gas fraction ($f_{\rm gas}$), that are in agreement with the predictions from the most recent theoretical models (McAlpine et al. 2019), as well as observations of the population of DSFGs at this redshift (Hodge et al. 2015). Also, from the de-lensed dust emission, we derive an SFR and gas depletion timescale, which are typical of DSFGs (Hodge et al. 2015). However, our kinematic analysis on ~60 pc scales reveals a ratio of rotational-to-random motions V/σ of 9.7 ± 0.4, which is at least 4 times larger than expected from any galaxy evolution model at this epoch (Pillepich et al. 2019, Dekel & Burkert 2014, Zolotov et al. 2015, Krumholz et al. 2018, Hayward & Hopkins 2017), but similar to spiral galaxies in the local Universe (Lelli et al. 2016). Also, the rotation curve of SPT0418-47 has the typical shape of nearby massive spiral galaxies, which demonstrates that at least some young galaxies are dynamically akin to those observed in the local Universe, and only weakly affected by extreme physical processes.

In the next chapter, we will extend this analysis to a sample of six DSFGs at $z \sim 4$. This study will allow us to test whether the unexpected properties found for SPT0418-47 are unique or common amongst the DSFG population.

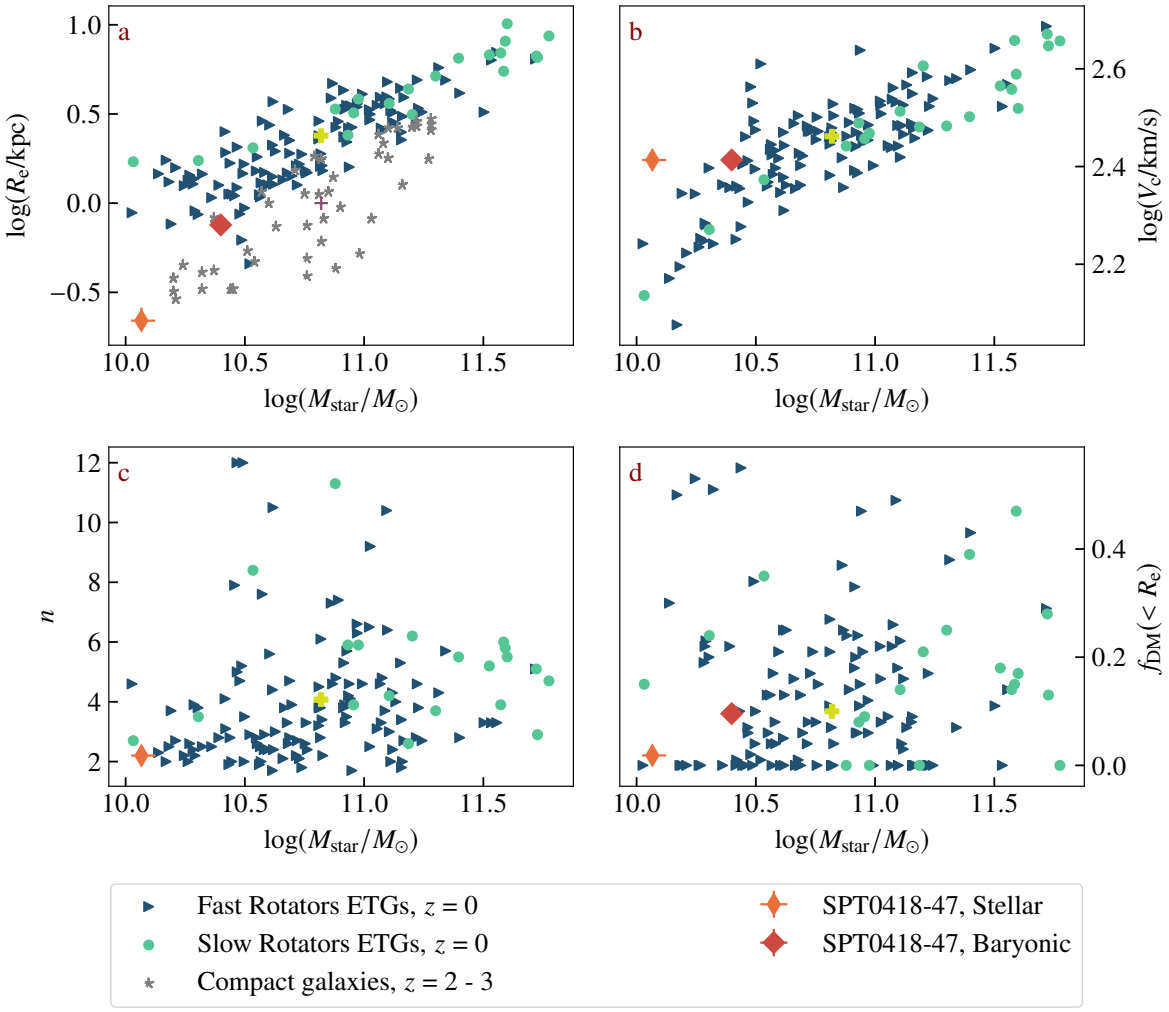

Figure 3.7: **Comparison between SPT0418-47 and samples of its plausible descendants.** In all panels the orange thin diamond shows the position of SPT0418-47, and the red diamond shows the baryonic quantities (gas + stars), under the assumption that all the gas that we observe today will be converted into stars, preserving the disk configuration. The $z \sim 0$ ETGs from ATLAS^{3D} survey (Cappellari et al. 2011, McDermid et al. 2015, Krajnović et al. 2013, Cappellari et al. 2013b,a), the plausible descendants of SPT0418-47, are shown according to their kinematic classification: blue triangles show fast rotators, green circles show the slow rotators (Emsellem et al. 2011) and yellow crosses show the median values. Panel a: size-stellar mass plane. The gray stars show the compact galaxies (Barro et al. 2014) at $z \sim$ 2 - 3 and the violet cross shows the median values for this sample. Panel b: circular velocity versus stellar mass. Panel c: Sérsic index versus stellar mass. Panel d: fraction of dark matter within the effective radius versus stellar mass.

This chapter makes use of the following ALMA data: 2016.1.01499.S. ALMA is a partnership of ESO (representing its member states), NSF (USA) and NINS (Japan), together with NRC (Canada), NSC and ASIAA (Taiwan), and KASI (Republic of Korea), in cooperation with the Republic of Chile. The Joint ALMA Observatory is operated by ESO, AUI/NRAO and NAOJ.

Chapter 4

A pilot study on the kinematics of galaxies at $z \sim 4$

The content of this chapter is based on results that will be submitted for publication to the Monthly Notices of the Royal Astronomical Society as ***Rizzo F.*** *et al.*

Current galaxy formation and evolution models (e.g., Schaye et al. 2015, Grand et al. 2017, Pillepich et al. 2019) predict that the structural and kinematic properties of galaxies are affected by numerous processes: gas accretion, galaxy mergers, feedback from star formation and supermassive black holes. However, feedback processes operate on physical scales that are not resolved by numerical simulations, and are, therefore, usually parametrized using simple sub-grid prescriptions (Kim & Ostriker 2018, Nelson et al. 2019), which are mostly calibrated to match observations in the local Universe.
In Chapter 3, we found that the $z \sim 4$ DSFG, SPT0418-47, has dynamical properties similar to those of local spiral galaxies: it is rotationally supported, dynamically cold and with a flat-rotation curve. Recently, Neeleman et al. (2020) obtained a similar result for the non-lensed galaxy, DLA0817g. While SPT0418-47 was selected based on its high sub-mm fluxes (Vieira et al. 2013), DLA0817g was identified as an absorption-selected galaxy, that is, it lies in front of a bright background source. The global SFR and ISM properties of SPT0418-47 and DLA0817g are typical of the corresponding samples of DSFGs (Hodge et al. 2015, Aravena et al. 2016) and absorption-selected galaxies (Neeleman et al. 2019) at $z \sim 4$. Together with the fact that these galaxies were selected with two different methods, this could suggest that such systems are common among star-forming galaxies at these redshifts. However, reproducing the existence of galaxies with such a large rotational velocity and significant content of cold gas remains challenging for most of the numerical simulations and semi-analytic models (e.g. Pillepich et al. 2019, Dekel & Burkert 2014, Zolotov et al. 2015, Krumholz et al. 2018). Robust observational constraints on the properties of star-forming galaxies at these epochs are thus necessary to inform us about how galaxies acquire their mass and how they are affected by different physical processes.

By studying the structural properties of star-forming galaxies at $z \sim 3$ - 4, we also gain insights into the formation of massive quiescent galaxies at lower redshift. Stellar population studies of both local ETGs (Thomas et al. 2010, McDermid et al. 2015) and quiescent galaxies at $z \lesssim 2.5$ (e.g. Kriek et al. 2009, Toft et al. 2012, Stockmann et al. 2020) indicate that the majority of their stars were formed at $z \gtrsim 3$. The common structural feature of these quiescent systems is the presence of a spheroidal component, i.e., a bulge (Krajnović et al. 2013, Lang et al. 2014, van der Wel et al. 2014, Belli et al. 2017, see Section 1.3 for further details). Despite several theories and scenarios have been proposed so far (e.g. Dekel & Burkert 2014, Zolotov et al. 2015, Tacchella et al. 2016), it is still unclear when and how these bulges formed and whether they are the main drivers behind the quenching of these galaxies (Martig et al. 2009).
Robust measurements of the kinematic and structural properties of $z \sim 3$ - 4 galaxies require high spatial resolution observations, which nowadays can be achieved by targeting strongly gravitationally lensed galaxies with ALMA. In this chapter, we present the results of a pilot project based on a small sample of lensed DSFGs. Using the 3D kinematic-lens modeling technique described in Chapter 2 and applied to the interferometric data, we reconstruct the dust and [CII] emission in these galaxies on ~100 pc scales. In Section 4.1, we describe the targets, observations, and data reduction process. In Section 4.2 we summarize our lens modeling and source reconstruction technique. In particular, the dynamical analysis and the measurement of the SFR properties of the sample are reported in Sections 4.2.3 and 4.2.4, respectively. In Section 4.3 we present the results and we discuss the implications of our findings in the context of galaxy evolution models. The main conclusions of this chapter are summarized in Section 4.4.

4.1 Sample and observations

The targets in this work are six gravitationally lensed DSFGs (Table 4.1). We collected the sample by selecting from the ALMA public archive DSFGs at $z \sim 3-5$ which are lensed by a galaxy or a galaxy group and with data of angular ($\lesssim 0.3$ arcsec) and spectral ($\lesssim 40$ km/s) resolutions high enough to resolve the size and structure of the [CII] emission line.
The observations for each target have one spectral window covering the redshifted rest frequency of the [CII] line and three spectral windows for the continuum. Each spectral window has 240 channels and a 1.875 GHz bandwidth. The raw visibility data were calibrated using the ALMA pipeline in the CASA package (McMullin et al. 2007). These data were then inspected to confirm the quality of the pipeline calibration and that no further flagging was required. The continuum was subtracted from the line spectral window using UVCONTSUB. The data were averaged into groups of between 4 (e.g., SPT0345-47, SPT2132-58) and 8 (e.g., SDP.81) channels in order to increase the overall SNR. This procedure results in channels with a typical velocity width of ~ 35 km s^{-1}.
The targets were imaged with natural weighting of the visibilities and deconvolved using CLEAN (Högbom 1974, see Appendix A.1). In the panels a to c of Figure 4.1 and Figures

Table 4.1: **Summary of the observed targets.** Columns 1 and 2: IAU and short name. Column 3: lens redshifts from Negrello et al. (2010) and Spilker et al. (2016). Column 4: source redshifts from Negrello et al. (2010), Weiß et al. (2013) and Strandet et al. (2016). Column 5: total on-source integration time. Column 6: ALMA project code.

IAU Name	Short Name	$z_{\rm lens}$	$z_{\rm source}$	$t_{\rm s}$ (min)	Project code
HATLAS J090311.6+003906	SDP.81	0.299	3.042	35.8	2016.1.01093.S
SPT-S J011308-4617.7	SPT0113-46	n.a.	4.2328	13.9	2016.1.01499.S
SPT-S J034510-4725.7	SPT0345-47	0.364	4.2958	29.2	2016.1.01499.S
SPT-S J044143-4605.5	SPT0441-46	0.882	4.4771	28.0	2016.1.01499.S
SPT-S J214654-5507.9	SPT2146-56	n.a.	4.5672	23.8	2016.1.01499.S
SPT-S J213244-5803.1	SPT2132-58	n.a.	4.7677	24.4	2016.1.01499.S

4.9 to 4.15 in the Supplementary Material Section 4.5, we show the spectral line moment maps of the lensed galaxies. As described in Section 3.2 and Appendix A.2, these images are intended only for visualization, as the analysis is performed on the visibility data directly.

4.2 Analysis overview

To infer the lens mass models, the sources, and their kinematic properties, we make use of the 3D Bayesian pixellated technique developed by Rizzo et al. (2018, see Chapter 2) and further extended by Powell et al. (2020). We refer the readers to Chapters 2 and Appendix A.2 for a detailed description of the methodology. Here, we provide a summary and emphasize that our modeling technique enables us to simultaneously reconstruct the lensing mass distribution and the kinematics of the source from the same 3D data, by fitting directly in the visibility space (see Appendix A.1).
The results of this analysis can be visualized in three sets of figures for each system. The first set shows the zeroth-, first- and second-moment maps for the data, the reconstructed source and the source kinematic model (Figure 4.1 and Figures 4.9 to 4.15). The second set displays the data, the model, the reconstructed source and the kinematic model for some representative channel maps (Figure 4.3 and Figures 4.11 to 4.23). The third set of images shows the position-velocity diagrams for the reconstructed sources and their kinematic models (4.2 and Figures 4.10 to 4.22).

4.2.1 Lens modeling

We assumed that the lens mass distribution is described by an elliptical power-law profile (see equation (2.15) in Chapter 2) with an external shear component. The parameters defining the power-law profile are the surface mass density normalization κ_0, the position angle θ, the axis ratio q and the slope γ. The parameters defining the shear component are its strength $\Gamma_{\rm sh}$ and

positional angle θ_{sh}. The lens mass model parameters for each system are listed in Table 4.2. Five out of six sources are lensed by a galaxy, while SPT0113-46 is lensed by a group of galaxies (Spilker et al. 2016). When modeling SPT0113-46, we therefore also included the contribution to the lensing potential of the three closest galaxies in the form of three elliptical power-law components. We found that this was sufficient to fit the data to the noise level (see column 3 in Figure 4.19).

4.2.2 Source kinematic properties

We used our 3D kinematic model that describes a rotating disk as a regularizing prior to the pixellated source reconstruction (see Chapter 2). The kinematic model is defined by the geometrical parameters (inclination i and position angle PA) and the parameters describing the rotation and velocity dispersion curves. In particular, for all but one of the sources in the sample, we adopted a multi-parameter function, equation (2.20), for their rotation curve. In contrast, we found that for SPT2132-58 a simpler arctangent function, equation (2.18), was sufficient to fit the data to the noise level. We believe this to be related to the small Einstein ring $\sim$ 0.3 arcsec of this system that results in a lower spatial resolution and, therefore, in fewer constraints. For all of the galaxies in the sample, we assume the velocity dispersion curve to have an exponential profile, equation (2.23).
The most probable a posteriori kinematic parameters are listed in Table 4.3. In Figure 4.2 and Figures 4.10-4.22 in the Supplementary Material Section 4.5, we plot the position-velocity diagrams along the major and minor axis for the reconstructed sources (black contours) and the corresponding kinematic models (red contours).

4.2.3 Source dynamical properties

To quantify how the different matter components contribute to the total galactic gravitational potential, we performed a rotation curve decomposition, by applying the same assumptions used in Chapter 3. This method (see Section 3.2.2 for further details) allowed us to derive not only the gas (yellow dotted lines in Figure 4.4), star (red dashed lines in Figure 4.4) and dark matter halo (blue dotted-dashed lines in Figure 4.4) masses, but also to infer the stellar structural properties, in terms of a Sérsic index and effective radius (Table 4.4). As in Section 3.2.2, to obtain the gas mass, we assume that the gas has the same distribution of the [CII] emission line and the free parameter of the dynamical fitting is, therefore, the conversion factor between the [CII] luminosity and the gas mass, $\alpha_{[CII]}$. We note that the inferred values of M_{gas} are consistent, within the 2-σ uncertainties, with the values found by Aravena et al. (2016) from the CO luminosities and the dust masses.
In Table 4.5 we also list other derived physical quantities, which are relevant to gain insight into the physical mechanisms driving galaxy evolution at the early epochs, as the gas fraction f_{gas} and the total baryonic mass M_{bar}.

Table 4.2: **The mass model parameters of the gravitational lens galaxies.** From left to right we list the mass density profile normalization, position angle, axis ratio, slope, the external shear strength and its position angle (see Section 2.1.2 for further details).

Name	κ_0 arcsec	θ $^\circ$	q	γ	$\Gamma_{\rm sh}$	$\theta_{\rm sh}$ $^\circ$
SDP.81	1.61±0.01	8.7±0.6	0.83±0.04	2.02±0.12	0.037±0.002	1.68±0.22
SPT0113-46	1.20±0.02	90.9±1.7	0.72± 0.02	1.99±0.02	0.0013±0.0002	13.7±1.8
	0.43±0.02	177.7±6.2	0.89±0.10	2.1±0.2		
	0.15±0.02	37.2±1.9	0.82±0.11	2.0±0.1		
SPT0345-47	0.36±0.05	128.0±0.3	0.71±0.04	1.9±0.2	-0.027±0.004	-6±1
SPT0441-46	0.63±0.05	82.4±1.6	0.61±0.07	2.04±0.23	0.00011±0.00001	37.2±4.7
SPT2146-56	0.89±0.07	106±15	0.95±0.01	2.02±0.14	0.0136±0.0007	-23.6±2.8
SPT2132-58	0.30±0.01	105±8	0.64±0.07	2.03±0.14	-0.0610±0.003	-11.4±0.8

Table 4.3: **Kinematic parameters of the sources.** The kinematic model is defined by the geometrical parameters (i and PA) and the parameters defining the rotation curve and velocity dispersion profile (see Section 2.1.3 for further details).

Name	i	PA	V_t	R_t	β	ξ	σ_0	R_σ
	$^\circ$	$^\circ$	km s^{-1}	kpc		km s^{-1}	kpc	
SDP.81	50±7	10±3	329±17	0.63±0.10	0.30±0.03	2.28±0.35	85±8	1.33±0.19
SPT0113-46	70±1	240±3	352±8	0.0104±0.0009	0.79±0.09	2.3±0.2	145±12	1.5±0.2
SPT0345-47	53±5	303±6	200±25	0.68±0.09	1.17±0.14	2.85±0.26	123±13	2.2±0.3
SPT0441-46	57±8	10±2	293±7	0.17±0.02	1.1±0.1	2.9±0.3	151±23	0.68±0.09
SPT2146-56	47±5	302±6	176±18	0.34±0.03	0.68±0.05	2.1±0.3	76±10	2.0±0.3
SPT2132-58	52±7	65±8	219±22	0.48±0.03			50±7	2.6±0.3

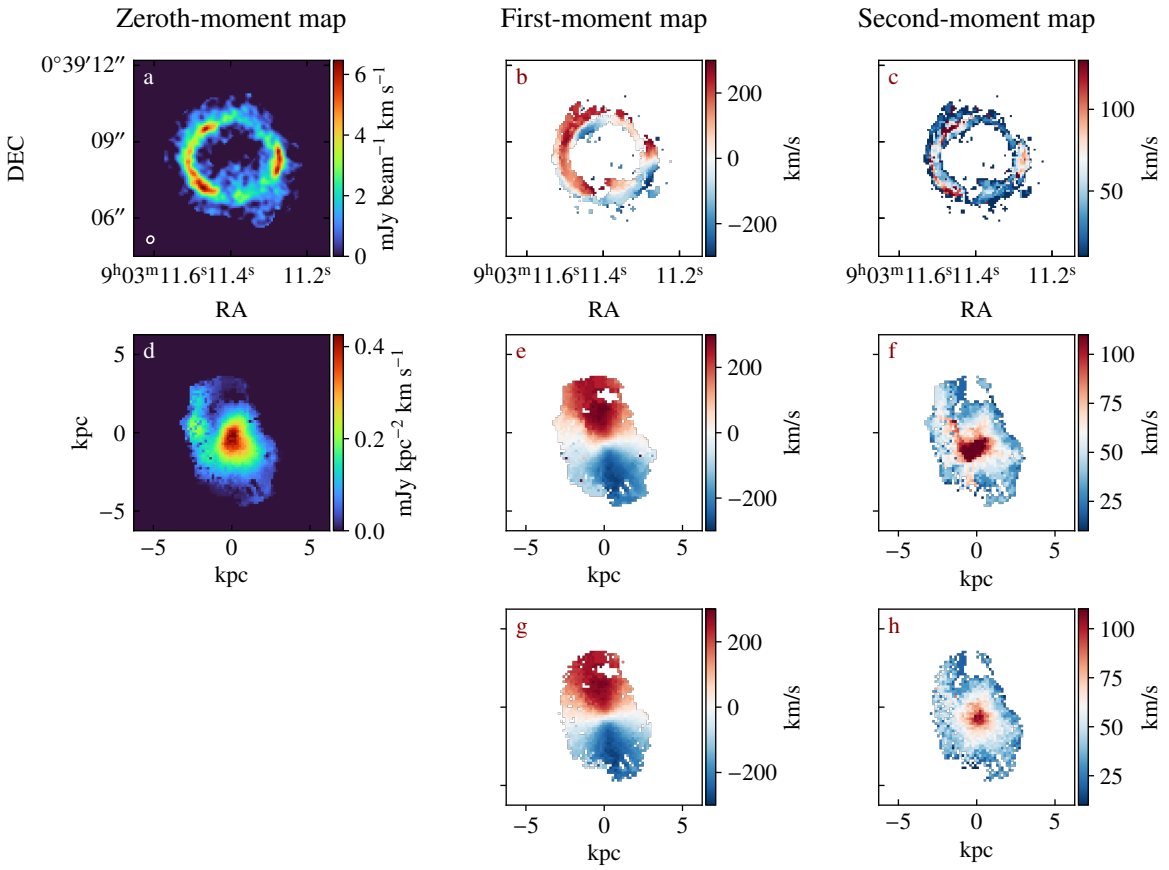

Figure 4.1: **Moment maps for SDP.81.** Panels a, b and c: the observed [CII] zeroth-, first- and second-moment maps. The beam size, shown as a white ellipse on the lower left corner of panel a, is 0.29×0.26 arcsec^2 at a position angle of -32.3°. Panels d, e and f: zeroth-, first- and second-moment maps of the reconstructed source. Panels g and h: first- and second-moment maps of the kinematic prior. These maps are intended only for visualization as the full analysis is performed on the data cube.

4.2.4 Source continuum properties and SFR

In order to derive the star formation properties of the sources we modeled their continuum emission in a narrow spectral range close to the redshifted [CII] emission and used the strong lensing magnification factor (Table 4.6) to compute the intrinsic infrared luminosity from the observed one (Aravena et al. 2016, column 2 of Table 4.6). By applying the Kroupa IMF conversion factor of 1.48×10^{-10} M$_\odot$ yr^{-1} L$_\odot^{-1}$(Kennicutt & Evans 2012), we then derived the SFR for each source (column 4 of Table 4.6).

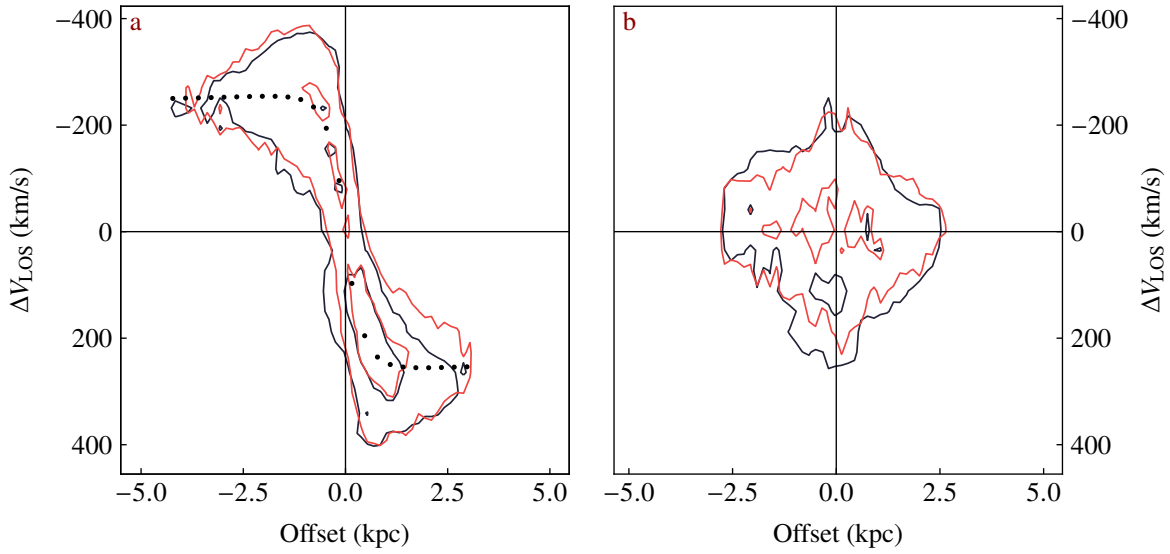

Figure 4.2: **Position-velocity diagrams for SDP.81.** The x-axes show the offset along the major (panel a) and minor axes (panel b) from the galaxy center. The y-axes show the line-of-sight velocity centered at the systemic velocity of the galaxy. The reconstructed source is shown in black, the kinematic prior in red. The black dots show the derived rotation curve.

Table 4.4: **Dynamical parameters of the sources.** All parameters were inferred from the rotation curve decomposition assuming a Sérsic profile for the stellar component, an exponential profile for the gas disk and an NFW profile for the dark matter halo. From left to right: the stellar mass, the stellar effective radius and Sérsic index, the dark matter mass and the conversion factor between the [CII] luminosities and the gas mass.

Name	$M_{\rm star}$ 10^{10} M$_\odot$	$R_{\rm e}$ kpc	n	$M_{\rm DM}$ 10^{11} M$_\odot$	$\alpha_{\rm [CII]}$ M$_\odot$/L$_\odot$
SDP.81	$3.1^{+0.4}_{-0.4}$	$0.61^{+0.06}_{-0.05}$	$0.95^{+0.07}_{-0.07}$	$45.6^{+20.4}_{-15.6}$	$10.6^{+1.8}_{-1.7}$
SPT0113-46	$11.2^{+4.4}_{-3.3}$	$2.6^{+1.6}_{-1.0}$	$5.76^{+0.73}_{-0.78}$	$20.3^{+10.7}_{-7.9}$	$9.0^{+4.3}_{-3.3}$
SPT0345-47	$2.3^{0.4}_{-0.3}$	$0.30^{+0.06}_{-0.04}$	$1.49^{+0.48}_{-0.33}$	$1.8^{+1.7}_{-1.0}$	$7.3^{+1.5}_{-1.5}$
SPT0441-46	$1.8^{+0.2}_{-0.2}$	$0.11^{+0.02}_{-0.02}$	$2.0^{+0.9}_{-0.6}$	$71.7^{+8.2}_{-8.1}$	$7.9^{+1.0}_{-1.1}$
SPT2146-56	$0.96^{+0.15}_{-0.13}$	$0.38^{+0.07}_{-0.05}$	$1.59^{+0.25}_{-0.21}$	$1.0^{+0.5}_{-0.5}$	$4.9^{+1.4}_{-0.8}$
SPT2132-58	$1.9^{+0.3}_{-0.3}$	$1.4^{+0.1}_{-0.1}$	$0.94^{+0.05}_{-0.04}$	$0.32^{+0.23}_{-0.09}$	$7.2^{+0.9}_{-0.9}$

4.3 Results

In this section, we investigate the physical properties of the reconstructed sources and discuss the implications of our findings in the broader context of galaxy evolution. For the rest of this chapter, we also include SPT0418-47 (see Chapter 3) in the sample.

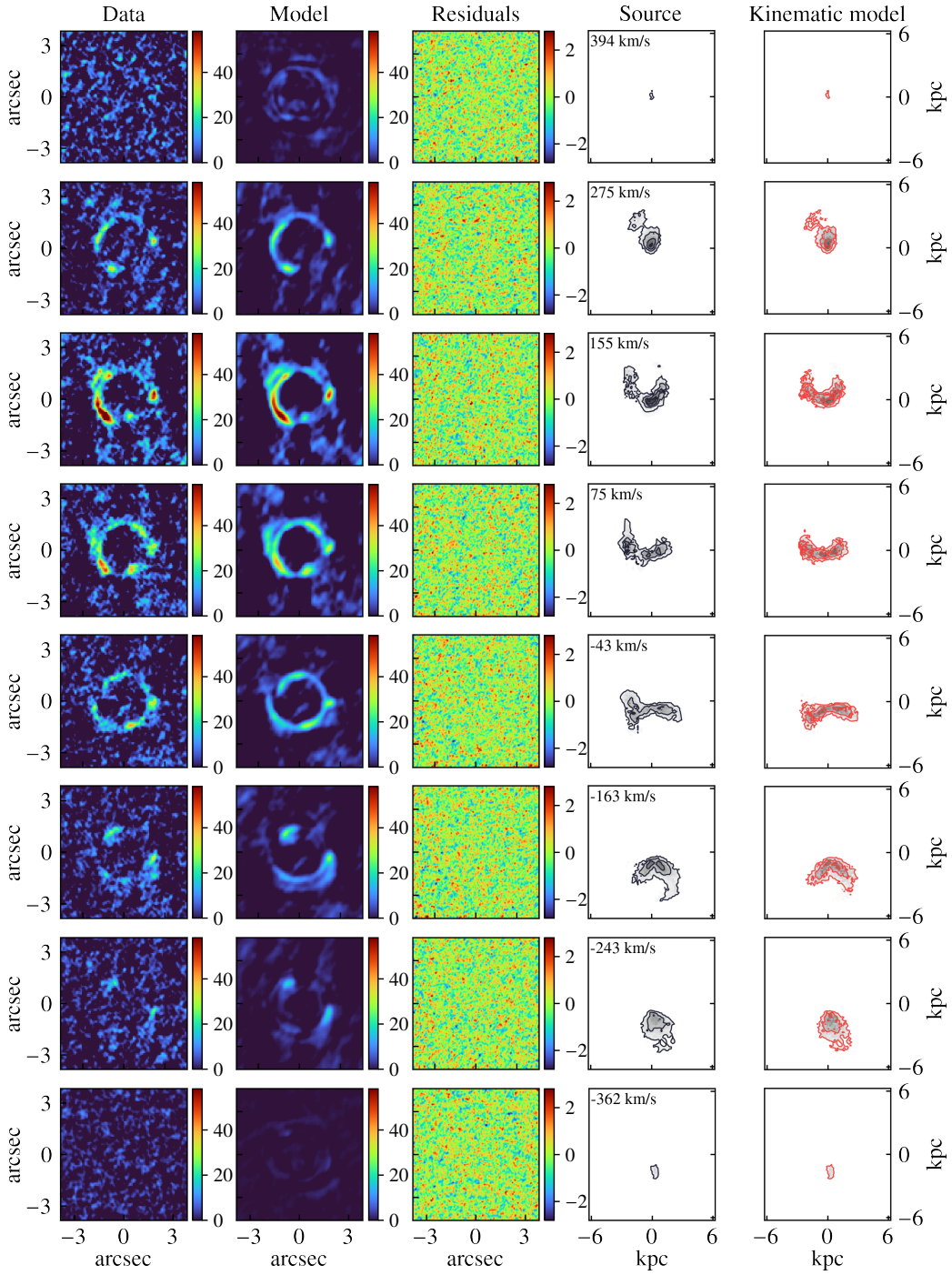

Figure 4.3: **Channel maps for SDP.81.** From left to right the dirty image (see Appendix A.1) of the data, the dirty image of the model, the dirty image residuals, the reconstructed source and the kinematic model.

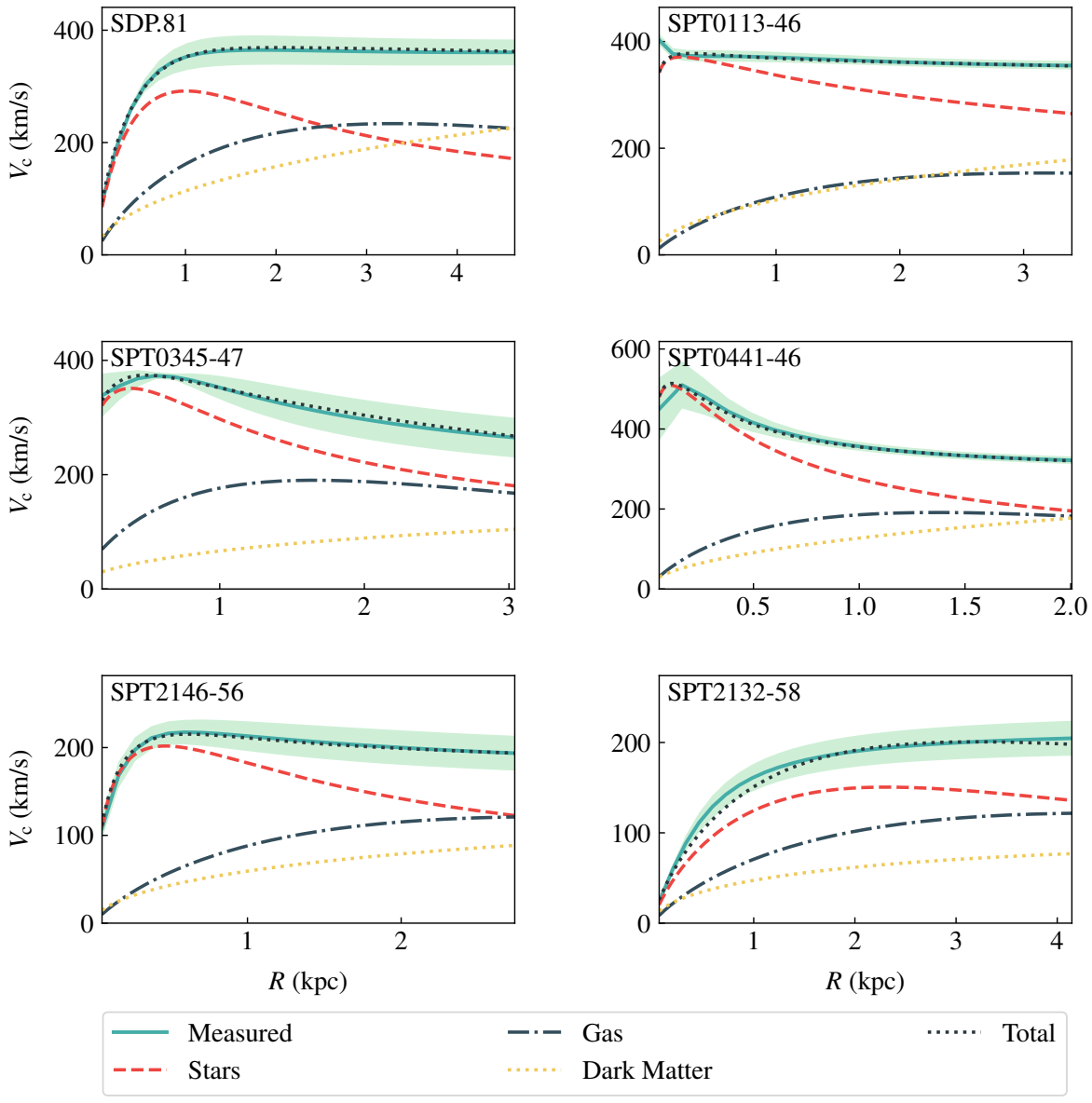

Figure 4.4: **Rotation curve decomposition.** The green solid lines show the circular velocity profiles. The black dotted lines show the best dynamical models, and the contribution from the different mass components as indicated by the legend and listed in Tables 4.4 and 4.5.

Table 4.5: **Derived physical properties of the sources.** From left to right the gas mass, the fraction of total baryonic mass in gas, the total baryonic mass, the baryonic effective radius and the gas depletion time (see Section 3.2.2 for details).

Name	M_{gas} 10^{10} M$_\odot$	f_{gas}	M_{bar} 10^{10} M$_\odot$	R_{bar} kpc	t_{dep} Myr
SDP.81	$4.7^{+1.9}_{-1.6}$	$0.60^{+0.13}_{-0.16}$	$7.9^{+1.3}_{-1.0}$	$1.5^{+0.1}_{-0.1}$	77±28
SPT0113-46	$2.1^{+1.0}_{-0.8}$	$0.15^{+0.11}_{-0.07}$	$13.4^{+3.9}_{-2.8}$	$3.8^{+1.8}_{-1.2}$	173±35
SPT0345-47	$1.7^{+0.4}_{-0.4}$	$0.42^{+0.08}_{-0.09}$	$4.0^{+0.3}_{-0.3}$	$0.64^{+0.07}_{-0.05}$	12±2
SPT0441-46	$1.4^{+0.2}_{-0.2}$	$0.45^{+0.05}_{-0.06}$	$3.2^{+0.2}_{-0.2}$	$0.35^{+0.06}_{-0.05}$	22±4
SPT2146-56	$1.3^{+0.4}_{-0.2}$	$0.57^{+0.09}_{-0.07}$	$2.3^{+0.3}_{-0.2}$	$1.3^{+0.2}_{-0.2}$	19±4
SPT2132-58	$1.9^{+0.3}_{-0.3}$	$0.50^{+0.07}_{-0.07}$	$3.9^{+0.4}_{-0.3}$	$2.47^{+0.13}_{-0.12}$	20±4

Table 4.6: **SFR and [CII] luminosities of the sources.** Column 2: the observed infrared luminosity from Frayer et al. (2011) and from Aravena et al. (2016). Column 3: the magnification factor of the continuum in the infrared bands. Column 4: SFR derived for a Kroupa IMF. Column 5: intrinsic [CII] luminosities.

Name	$L_{IR,obs}$ 10^{13} L$_\odot$	μ	SFR 10^2M$_\odot$/yr	$L_{[CII]}$ 10^9 L$_\odot$
SDP.81	5.2±1.8	13.6±1.2	5.6±2.0	4.2±0.7
SPT0113-46	3.0±0.5	36.5±4.3	1.2±0.3	2.3±0.1
SPT0345-47	13.0±2.4	14.5±1.2	13.3±2.6	2.3±0.2
SPT0441-46	4.8±0.9	10.8±0.5	6.6±1.3	1.8±0.1
SPT2146-56	3.6±0.8	7.8±0.2	6.8±1.5	2.6±0.2
SPT2132-58	4.2±0.7	6.3±0.4	9.8±1.7	3.7±0.7

4.3.1 Position in the SFR - M_{star} plane

As described in Section 1.2, for most star-forming galaxies, there is a tight correlation between their SFR and their stellar mass (Brinchmann et al. 2004), the so-called MS. Several studies (e.g., Noeske et al. 2007, Whitaker et al. 2012, Steinhardt et al. 2014, Tasca et al. 2015) showed that the MS hold from $z = 0$ out to $z \sim 6$, with a redshift evolution of its normalization. Also, there are starbursts galaxies, characterized by significantly higher SFR than normal MS galaxies. While starburst galaxies are rare in the local Universe (Renzini et al. 2015), they constitute a significant percentage (~15%, Bisigello et al. 2018, Caputi et al. 2017) of all galaxies at $z \gtrsim 2$, contributing up to 50% of the cosmic SFR density at $z \sim 4$ (Caputi et al. 2017).

Starting from the physical properties derived in the previous section, we now explore the

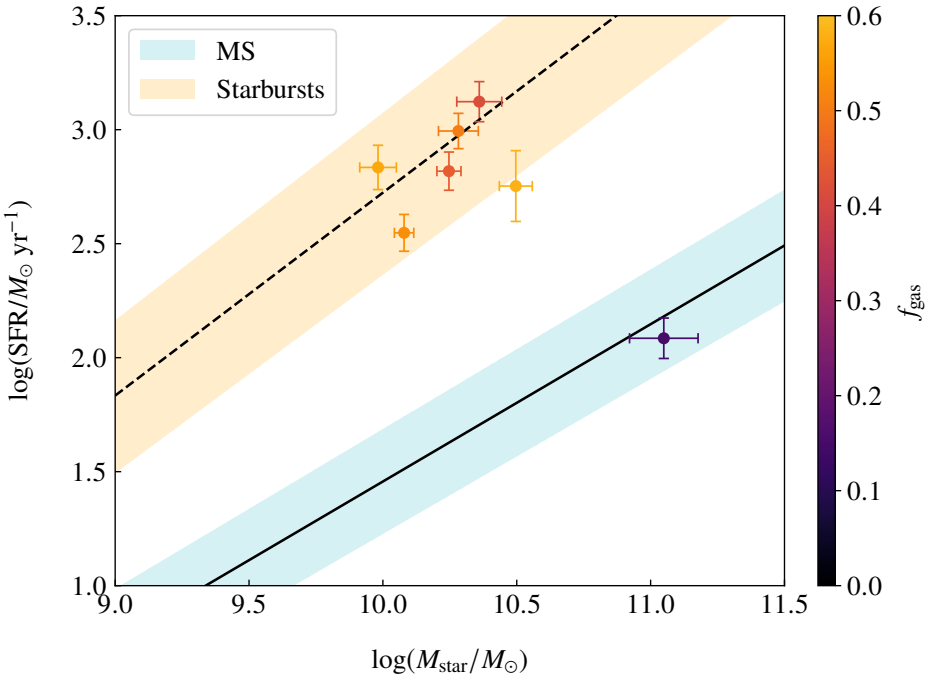

Figure 4.5: **SFR - $M_{\rm star}$ plane.** Location on the SFR - $M_{\rm star}$ of the source galaxies in our sample (circles), with symbols color-coded according to their gas fraction. The solid black line and the blue area show the best-fit and the 1-σ scatter for main-sequence galaxies at $z \sim 4$ - 5 from Caputi et al. (2017), respectively. The dotted black line and the orange area show the starburst sequence (Caputi et al. 2017).

location of the source galaxies in the SFR - $M_{\rm star}$ diagram. We find that six out of seven galaxies in our sample are consistent with the starburst sequence, while SPT0113-46 is an MS galaxy. These findings are not surprising, given that the selection criteria used for the identification of DSFGs are based on the observed flux (Vieira et al. 2013) rather than the intrinsic one. SPT0113-46 has, indeed, an observed infrared luminosity of $L_{\rm IR,obs}$, which is similar to the rest of the sample (see column 2 in Table 4.6). However, the large magnification factor of $\sim$ 36 leads to an intrinsic luminosity $L_{\rm IR}$ and SFR which are on average a factor of $\sim$ 5 below the other galaxies in the sample.

From the SFR - $M_{\rm star}$ diagram (Figure 4.5) a clear trend becomes visible: lower SFRs correspond to lower gas fractions. Our results confirm, therefore, a known trend that is present at all redshifts (e.g., Saintonge et al. 2018, Scoville et al. 2017, Boogaard et al. 2019) and that is consistent with a scenario in which large gas reservoirs fuel a strong starburst phase.

4.3.2 Evolutionary path: from DSFGs to ETGs

In this section, we extended the comparison of the physical properties of the DSFGs and their plausible descendants, local ETGs, to our larger sample of objects (see also Sections 1.3 and 3.4). In particular, we focus on the position of our galaxies in the size-stellar mass plane (R_e - M_{star}). The relation between the size and stellar mass of galaxies, and how it evolves with cosmic time, provides, indeed, important insights onto the assembly history of galaxies (van der Wel et al. 2014, Lang et al. 2014).

In Figure 4.6, local ETGs (Cappellari et al. 2013b) and $z \sim 2$ cSFG (Barro et al. 2014) are shown with green squares and gray stars, respectively. The cSFG have been proposed as a transition population between the star-forming and quiescent systems (e.g., Barro et al. 2014, van Dokkum et al. 2015). In panels a and b, we show the position of our sample in the size-mass plane, color-coded according to the gas fraction and depletion time (M_{gas}/SFR, respectively (see columns 3 and 6 of Table 4.5).

Interestingly, SPT0113-46, the only main-sequence galaxy in our sample (see Section 4.3.1 and Figure 4.5), is consistent with the size-mass relation of local ETGs (panel a of Figure 4.6). Its depletion time of $\sim$ 173 Myr suggests that it can rapidly consume all of its gas and become a quiescent system. There is, indeed, growing evidence of the existence of a population of quiescent galaxies at $z \gtrsim 3$ (e.g., Glazebrook et al. 2017, Simpson et al. 2017, D'Eugenio et al. 2020). Moreover, three galaxies in our sample have Sérsic index $n \sim 1$, indicative of a disky stellar component, three others have $n \sim 2$, typical of disky bulges, while SPT0113-46 has the largest Sérsic index, $n \sim 5$. Unfortunately, it is not possible to establish a direct causal correlation; however, we can speculate that by stabilizing the gas disk against fragmentation, the massive stellar bulge of SPT0113-46 may be slowing down its star formation rate, via the so-called morphological quenching process (Martig et al. 2009, see Section 1.3). Furthermore, the Sérsic indices derived from our analysis suggest that the spheroidal components visible in $z \lesssim 2$ galaxies were already in place when the Universe was about 10 percent of its current age.

In Figure 4.6 panel b, we show how the stellar mass and size of the galaxies in our sample will evolve if all of their observed gas were to be converted into stars while preserving the disk configuration. This scenario is not an impossible one: while some of the gas may be expelled by galactic outflows (Nelson et al. 2019), more could also be accreted (e.g., Bouché et al. 2010, Dekel et al. 2009a). On the other hand, the sizes calculated under this assumption should be considered only as upper limits: dissipative processes lead to an accumulation of gas mainly in the central regions of galaxies, effectively shrinking the sizes of their bulges (Dekel & Burkert 2014, Zolotov et al. 2015, Tacchella et al. 2016). Panel b of Figure 4.6 shows that all galaxies in our sample will end up with a stellar mass typical of the local ETGs or cSFGs already at $z \sim 4$. This finding allows us to put some constraints on the physical processes (e.g., mergers, accretion, Naab et al. 2014, Bouché et al. 2010) that will be acting on these galaxies in the following $\sim$ 12 Gyr: they should either preserve the stellar mass or be responsible only for a mild growth in size.

We note that the depletion times for our sample go from ~ 170 to 10 Myr (see column 6 of Table 4.5), with a median value of 20 Myr. Except for SDP.81, all galaxies in the sample are at $z > 4$, meaning that potentially they could be the progenitors of the recently discovered quiescent systems at $3 \lesssim z \lesssim 3.7$ (e.g., Glazebrook et al. 2017, Simpson et al. 2017, D'Eugenio et al. 2020). Unfortunately, due to the lack of size measurements for this quiescent population, a comparison with our DSFGs on the size-stellar mass plane is currently not possible. The next generation of instruments, such as the James Webb Space Telescope (Gardner et al. 2009, JWST,), will allow one to measure the structural (e.g., sizes) and the stellar-population properties (age, metallicity) of these high-z populations, facilitating further investigations of the evolutionary connection between the DSFGs and the $z \sim 3$ quiescent galaxies.

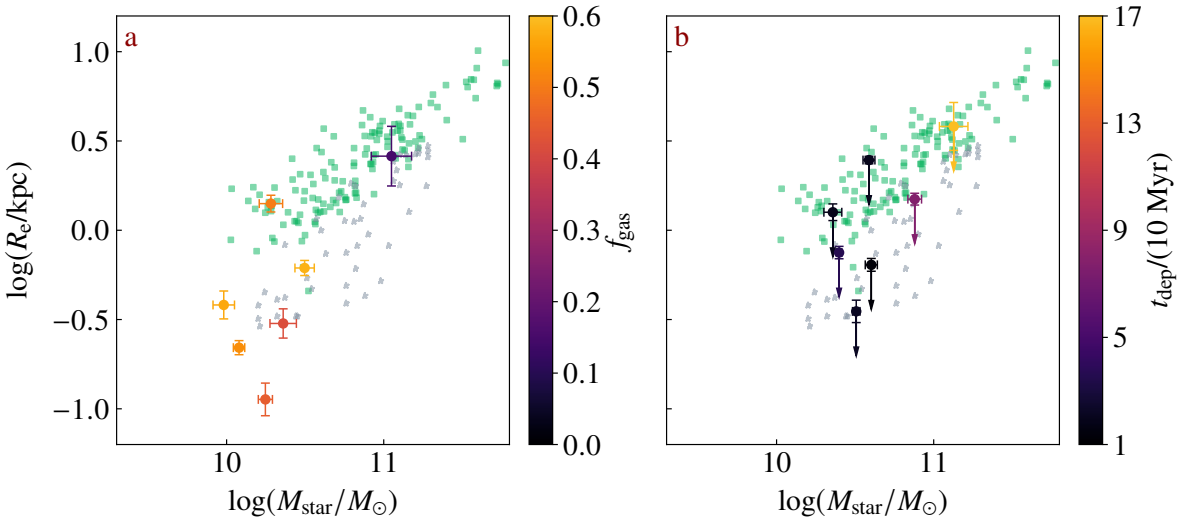

Figure 4.6: R_e-M_{Star} **plane.** Location on the size versus stellar mass plane for the source galaxies in our sample color-coded according to their gas fraction (panel a, see column 3 of Table 4.5) and depletion time (panel b, see column 6 of Table 4.5). In panel b, the stellar masses and sizes are obtained under the assumption that all the observed gas will be converted into stars, preserving the disk configuration (see the baryonic quantities in columns 4 and 5 of Table 4.5). Under this assumption, the sizes should be considered as upper limits. The green squares correspond to local ETGs from the ATLAS^{3D} survey (Cappellari et al. 2013b), while the gray stars are the cSFG at z ~ 2, taken from Barro et al. (2014).

4.3.3 Turbulence in high-z galaxies

Recent studies (e.g., Übler et al. 2019, Turner et al. 2017, Pillepich et al. 2019) showed that many high-z galaxies, despite being rotationally supported systems, have intrinsic velocity dispersions which are higher than those of local galaxies. These results imply a significant level of turbulence in the ISM of these galaxies, which is most plausibly (e.g. Übler et al.

2019, Krumholz et al. 2018, Varidel et al. 2020) related to either star-formation feedback (e.g., momentum injection by supernova explosions, stellar winds, and expansion of HII regions) or gravitational phenomena (e.g., gas accretion, gravitational interactions, and gravitational instabilities). Both mechanisms may play an important role in driving turbulent motions also in nearby galaxies (Bacchini et al. 2020). However, due to the high level of star-formation and the significant gas fraction, it is expected that both feedback and gravity-driven turbulence are more significant for high-z galaxies (Varidel et al. 2020, Krumholz et al. 2018).
The level of rotational support relative to the amount of turbulence in a galaxy is generally quantified with the ratio between the rotation velocity and the velocity dispersion, V/σ. As in Section 3.3, we compute the V/σ ratios for our sample using the two most popular definitions: $V_{\rm max}/\sigma_{\rm m}$, the ratio between the maximum rotation velocity and the median velocity dispersion and $V_{\rm flat}/\sigma_{\rm ext}$, the ratio between the flat part of the rotation velocity and the velocity dispersion at outer radii.
In Table 4.7, we listed the V/σ calculated with these two definitions for each galaxy of our sample. In Figure 4.7, the V/σ ratios are plotted as a function of redshift and compared with theoretical predictions (Pillepich et al. 2019, Dekel & Burkert 2014, Zolotov et al. 2015, Krumholz et al. 2018, Hayward & Hopkins 2017, see also Section 3.3.1). We find that the six galaxies analyzed in this chapter have a V/σ ratio that is significantly larger than any current theoretical prediction. In particular, the median V/σ ratio of the sample is 12, which is at least 6-σ away from the highest value of 3 predicted by TNG50 (Pillepich et al. 2019). This result confirms the findings presented in Chapter 3 that star-forming galaxies at these high redshifts may be significantly less turbulent than expected.

To investigate the influence of feedback by star-formation on the gas dynamics, we plot our sample in the SFR versus V/σ and σ planes. We find that there is a weak anti-correlation between the SFR and the V/σ (Figure 4.8, panel a), suggesting that stellar feedback can potentially lead to a high-velocity dispersion. However, given the observed trend between the SFR and the $f_{\rm gas}$ for our sample (Figure 4.5), it is not possible to clearly disentangle between the effect of feedback and gravity.

In Figure 4.8 panel b, we show the position of our sample in the SFR versus σ plane. In particular, the red square and circle show the median values for the two definitions of velocity dispersion, $\sigma_{\rm ext}$ and $\sigma_{\rm m}$, respectively. In the same plot, we also show the position of local MS (Leroy et al. 2008, Varidel et al. 2020) and dwarf starburst galaxies (Lelli et al. 2014). These samples, together with ours, span more than five orders of magnitude in SFR. By comparing the different samples, it is evident that only a very weak trend of increasing velocity dispersion with increasing SFR is present: a change of three orders of magnitude in SFR corresponds to a change of only a factor of two in the velocity dispersion. Previous studies focusing on lower-z galaxies with typical SFR of $\lesssim 100\ M_{\odot}\ {\rm yr}^{-1}$ found a similar result (Di Teodoro et al. 2016, Moiseev et al. 2015). Our analysis shows that the weak correlation between SFR and turbulence is present even in the starburst regime, and it implies that turbulence in the gas is only mildly related to supernova explosions. If confirmed with a larger sample of galaxies, this finding will provide observational evidence in support of the so-called 'self-regulated-system'

Table 4.7: **Global kinematic parameters of the sources.** Column 2: the maximum rotation velocity. Column 3: the median velocity dispersion. Column 4: the ratio between $V_{\rm max}$ and $\sigma_{\rm m}$. Column 5: the rotation velocity in the flat part of the rotation curve. Column 6: the velocity dispersion in the external regions ($R \gtrsim R_{\rm e}$). Column 7: the ratio between $V_{\rm flat}$ and $\sigma_{\rm ext}$.

Name	$V_{\rm max}$ km s^{-1}	$\sigma_{\rm m}$ km s^{-1}	$V_{\rm max}/\sigma_{\rm m}$	$V_{\rm flat}$ km s^{-1}	$\sigma_{\rm ext}$ km s^{-1}	$V_{\rm flat}/\sigma_{\rm ext}$
SDP.81	364±26	49±12	7.4±1.9	362±7	46±2	7.8±0.4
SPT0113-46	382±9	41±22	9.2±4.8	358±3	27±1	13.2±0.6
SPT0345-47	373±5	66±15	5.6±1.2	280±25	40±7	6.9±1.4
SPT0441-46	489±67	31±21	15.8±10.8	342±4	23±4	14.9±2.6
SPT2146-56	217±13	31±11	7.0±2.6	194±7	20±2	9.8±1.2
SPT2132-58	199±18	27±6	7.2±1.7	196±14	16±3	12±2

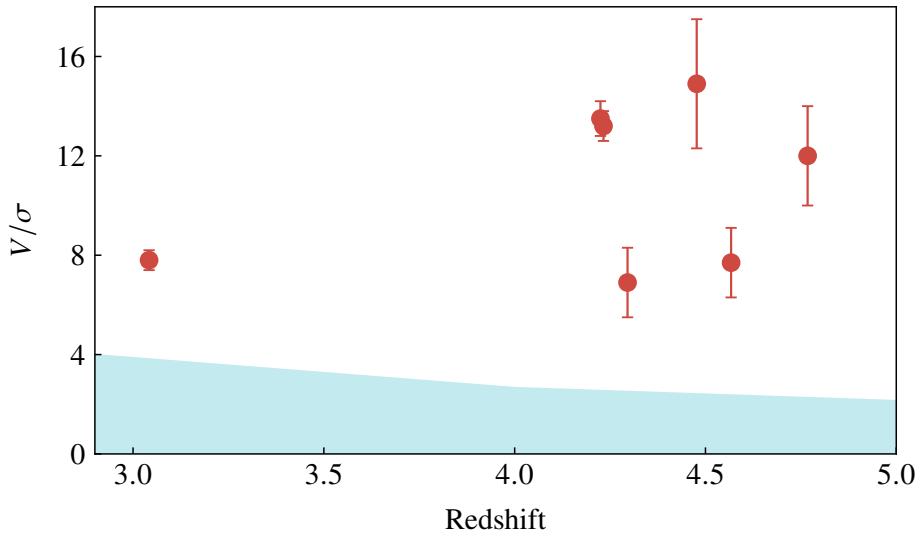

Figure 4.7: V/σ **versus redshift.** The V/σ for our sample (red circles), defined as $V_{\rm flat}/\sigma_{\rm ext}$. The light-blue area shows the region covered by theoretical studies (Pillepich et al. 2019, Dekel & Burkert 2014, Zolotov et al. 2015, Krumholz et al. 2018, Hayward & Hopkins 2017).

model (Ostriker & Shetty 2011, Bacchini et al. 2020, Sun et al. 2020). According to this model, star formation is part of a self-regulating cycle where the momentum injected to the ISM by star formation balances the gravitational force confining the ISM gas in the disk. In particular, Ostriker & Shetty (2011) have shown that this self-regulated-system model leads to a relatively small velocity dispersion, of the order of ~10 km s $^{-1}$, with little variation as a function of SFR.

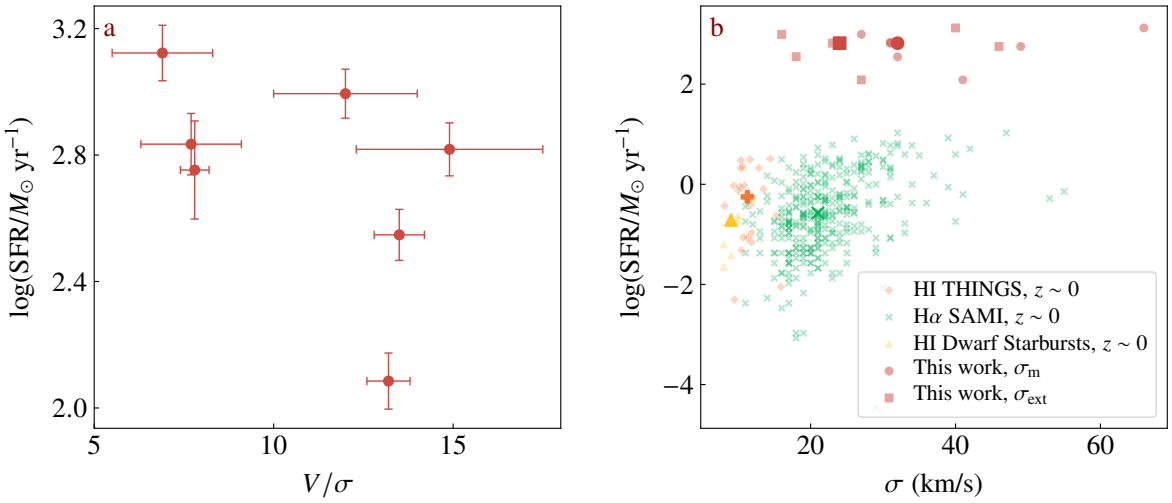

Figure 4.8: **SFR and dynamical properties.** Panel a: SFR versus V/σ. Panel b: SFR versus σ for our sample and for $z = 0$ samples from Leroy et al. (2008), Varidel et al. (2020), Lelli et al. (2014), as indicated in the legend. For each sample, the small markers show the position of each galaxy, while the big markers show the corresponding median value.

Gravitational instabilities and Toomre parameter

To account for the presence of gravitational instabilities in the rotating disks of our sample, we compute the Toomre parameter profiles, equation (3.5). The median and the corresponding 16th and 84th percentiles of Q computed at $R \gtrsim 1$, where the gas dominates the total gravitational potential over the other components (see Figure 4.4), are listed in Table 4.8. The values of $Q \sim 1$ - 2 for these galaxies indicate that they are stable or only marginally unstable, that is, their gas disks might fragment and form clumps of star formation.
Several studies (e.g., Dekel et al. 2009b, Ceverino et al. 2010, Zolotov et al. 2015) showed that angular-momentum transfer, clump-clump interactions and dynamical friction cause the migration of the gaseous clumps into the central regions of galaxies, causing the formation of a bulge at high redshift. However, there is a time requirement for the formation of a bulge through this channel: the timescale for clump migration, t_{mig}, should be shorter than the timescale for star formation, t_{dep}, otherwise the gas turns into stars before reaching the central regions. In Table 3.5, we list the migration times (Dekel et al. 2009b) for the galaxies analyzed here, computed as

$$t_{mig} = 2\frac{Q^2}{\delta^2}t_d, \tag{4.1}$$

where $\delta = M_{gas}/[M_{gas}(< R_{gas}) + M_{star}(< R_{gas}) + M_{DM}(< R_{gas})]$ and $t_d = R_{gas}/V_{flat}$ is the dynamical time. For the galaxies studied in this chapter, the star-formation timescales t_{dep} (see column 6 in Table 4.5) are at most an order of magnitude larger than t_{mig} (see column 4 in Table 4.8) and in all cases the ratios t_{dep}/t_{mig} are consistent with values $\lesssim 1$ within the 1-σ uncertainties. Overall, the stability of the disks of our sample prevents a rapid migration

Table 4.8: **Toomre parameters and dynamical times.** Column 2: median Toomre parameter computed using equation (3.5) at $R \gtrsim 1$ kpc. Column 3: migration timescale computed using equation (4.1). Column 4: ratio between the gas depletion time shown in Table 4.5 and the migration timescale.

Name	Q	$t_{\rm mig}$ Myr	$t_{\rm dep}/t_{\rm mig}$
SDP.81	$1.7^{+0.5}_{-0.3}$	$4.9^{+3.0}_{-2.0}$	15^{+11}_{-9}
SPT0113-46	$2.3^{+1.2}_{-0.7}$	$33.9^{+48.7}_{-50.6}$	5^{+8}_{-8}
SPT0345-47	$1.5^{+0.7}_{-0.6}$	$2.6^{+2.6}_{-2.2}$	5^{+5}_{-5}
SPT0441-46	$0.6^{+0.3}_{-0.3}$	$0.8^{+0.8}_{-0.7}$	29^{+31}_{-31}
SPT2146-56	$1.5^{+0.5}_{-0.4}$	$8.8^{+6.4}_{-5.2}$	2^{+2}_{-1}
SPT2132-58	$0.8^{+0.2}_{-0.2}$	$2.0^{+1.1}_{-1.0}$	10^{+6}_{-6}

of clumps into the inner regions. The comparison between the migration timescale and the star-formation timescale indicates that the formation of bulge through gaseous clumps can not be completely ruled out, but can not be considered as the main formation channel of high-z spheroidal components.

4.4 Summary

In this chapter, we have presented ALMA observations of the [CII] emission line for six gravitationally lensed dusty star-forming galaxies at redshift between 3 and 5. Using our lens modeling technique, we reconstructed the background sources and inferred their kinematic and dynamical properties on $\sim$ 100 pc scales. By combining these observations and analysis with those from Chapter 3 for the lensed galaxy SPT0418-47, we have thus built a sample of seven DSFGs. Due to instrumental limitations, this is the largest sample of $z \sim 4$ galaxies with such high-quality data and spatial resolutions of their [CII] line emission to date.

The rotation curves of the galaxies analyzed here have shapes similar to those of local spirals: they flatten at large radii and show a variety of behaviors in the inner regions, from smooth to steeply rising. This similarity implies that the dynamical structures of local galaxies were already in place at higher redshifts. On the other hand, the individuality of the observed rotation curves can be explained by the difference in the dynamical parameters defining the stellar, gas, and dark matter halo distributions.
The lack of spatially-resolved optical/NIR data prevented us from making sophisticated assumptions on the stellar distribution. We thus decomposed the rotation curve of our galaxies using a single Sérsic profile for the stellar component, an NFW for the dark matter halo, and an exponential disk for the gas, as traced by the [CII] line emission. From the dynamical

fitting, we found that the galaxies in our sample have a stellar-mass between $\sim 1 \times 10^{10} M_{\odot}$ and $10^{11} M_{\odot}$. Their gas fraction ranges between 0.15 and 0.6. Furthermore, four out of seven galaxies have a stellar component which is well described by a Sérsic index of $n \gtrsim 2$.
This analysis allowed us to put constraints on the mechanisms responsible for the transformation of these galaxies into their most plausible descendants, the quiescent systems observed at $z \lesssim 3$. In particular, by comparing our sample with local ETGs and $z \sim 2$ cSFGs in the size-stellar mass plane, we found that two galaxies in our sample, SPT0113-46 and SPT2132-58, have sizes and stellar masses consistent with the low-z samples, two galaxies are consistent with the low-mass end of the cSFGs, while the others cover the low-mass, small-size region. Interestingly, SPT0113-46 has the lowest gas fraction within our sample and it is the only galaxy on the MS. All these properties seem to indicate that SPT0113-46 is in the process of consuming its residual gas, quenching its star formation, and transforming into a typical ETG. We also found that the baryonic masses in our sample are all consistent with those of local ETGs. This result allowed us to set constraints on the small amount of baryonic matter that can be accreted in the following $\sim$ 12 Gyr of the lifetime of these galaxies.

Dynamical studies of DSFGs in the barely known redshift regime ($z \sim 3$ - 5) allowed us to gain insights on how the extreme astrophysical processes and conditions characterizing the early Universe affect the properties of young galaxies at sub-kpc scales. In particular, the sample studied in this chapter allowed us to confirm our previous finding (see Chapter 3): DSFGs have V/σ in the range 6 to 15 and median velocity dispersion in the range between $\sim$ 30 and $\sim$ 50 km s^{-1}. To date, such dynamically cold galaxies are not predicted by any theoretical studies. The weak anti-correlation between the SFR and the corresponding V/σ and velocity dispersion confirms that stellar feedback processes play a minor role in driving high-levels of turbulence within young galaxies.

Our results are based on just seven galaxies. While statistically significant conclusions can not be drawn, these first results are promising. In the current observing cycle of ALMA, we should obtain data for six lensed sources (Project number: 2019.1.01673.S, PI: Rizzo F.), which will further probe the dynamical and structural properties of this class of galaxies. Furthermore, in the near future, the thousands of strong gravitationally lensed galaxies discovered by Euclid, combined with the capability of ALMA, NOEMA, and JWST will provide us with the opportunity to fully characterize the dynamical properties of galaxies at $z \gtrsim 4$ (see Chapter 5).

This chapter makes use of the following ALMA data: 2016.1.01499.S and 2016.1.01093.S. ALMA is a partnership of ESO (representing its member states), NSF (USA) and NINS (Japan), together with NRC (Canada), NSC and ASIAA (Taiwan), and KASI (Republic of Korea), in cooperation with the Republic of Chile. The Joint ALMA Observatory is operated by ESO, AUI/NRAO and NAOJ.

4.5 Supplementary material

In this section, we show the outputs of the lens and kinematic modeling for each galaxy of the sample. As for SDP.81 in Section 4.2.2 (Figures 4.1 - 4.3), we show three sets of figures: the moment map of the lensed galaxies, the corresponding reconstructed source, and kinematic model; the position-velocity diagrams along the minor and major axes; some representative channel maps from the cubes containing the data, the model, the residuals, the source, and the kinematic model.

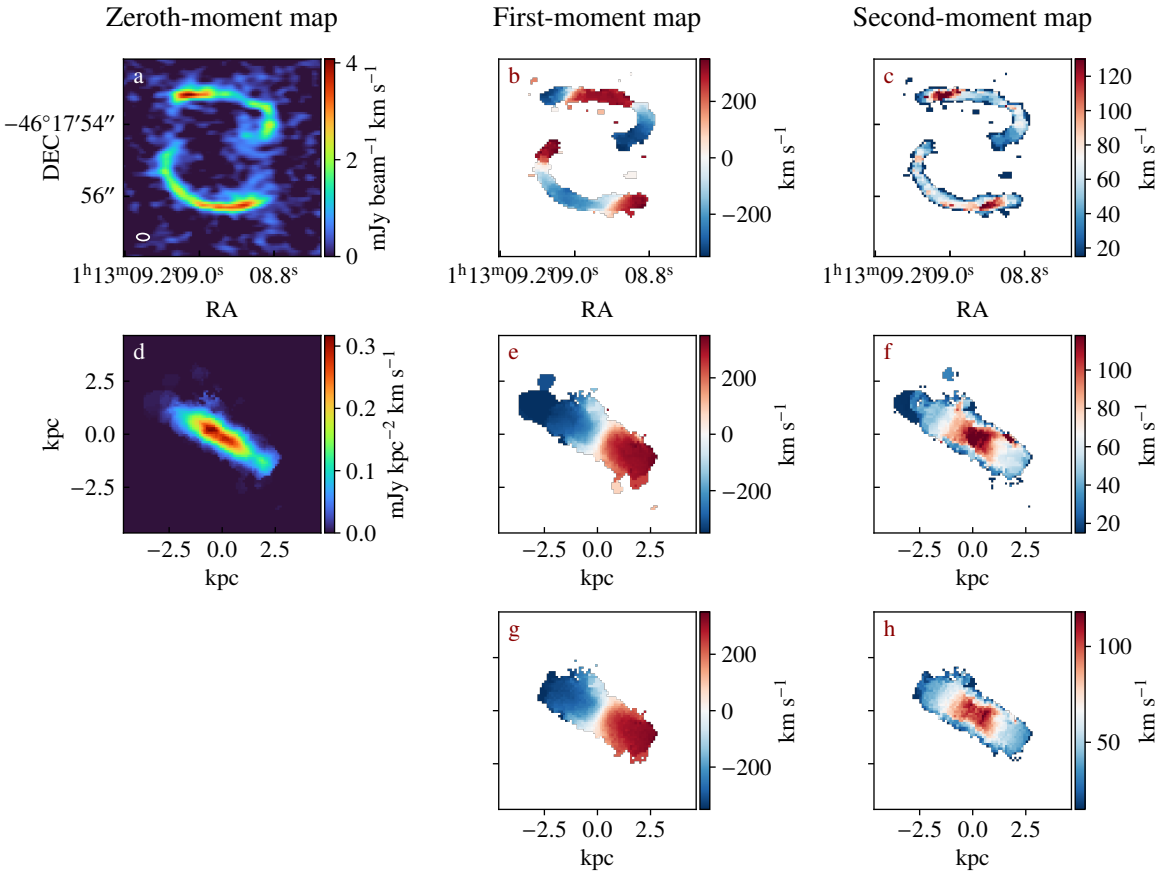

Figure 4.9: **Moment maps for SPT0113-46.** Same as in Figure 4.1. The beam size, shown as a white ellipse on the lower left corner of panel a, is 0.35×0.19 arcsec^2 at a position angle of 87.0°.

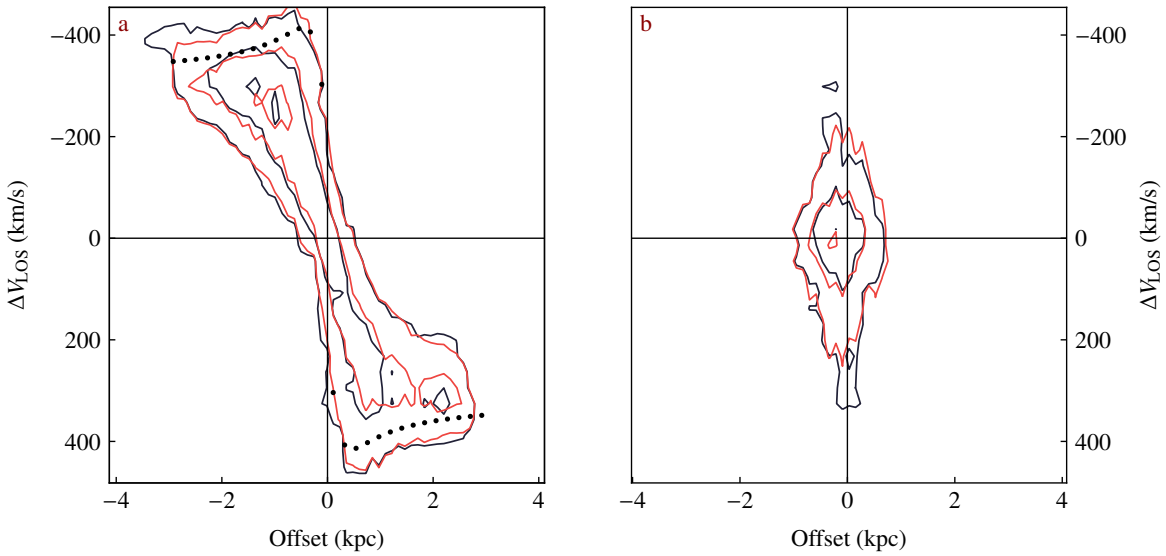

Figure 4.10: **Position-velocity diagrams for SPT0113-46.** Same as in Figure 4.2.

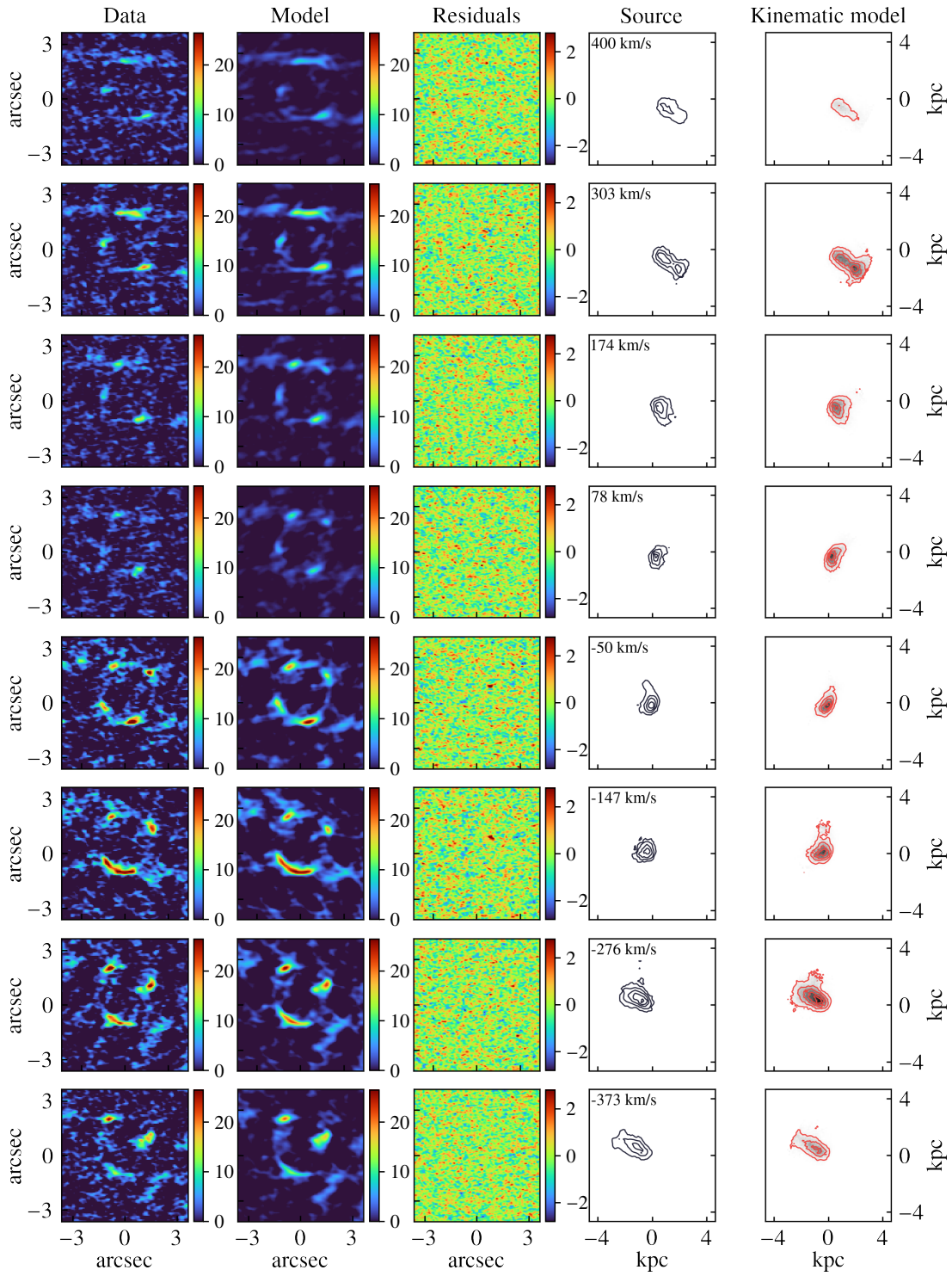

Figure 4.11: **Channel maps for SPT0113-46.** Same as in Figure 4.3.

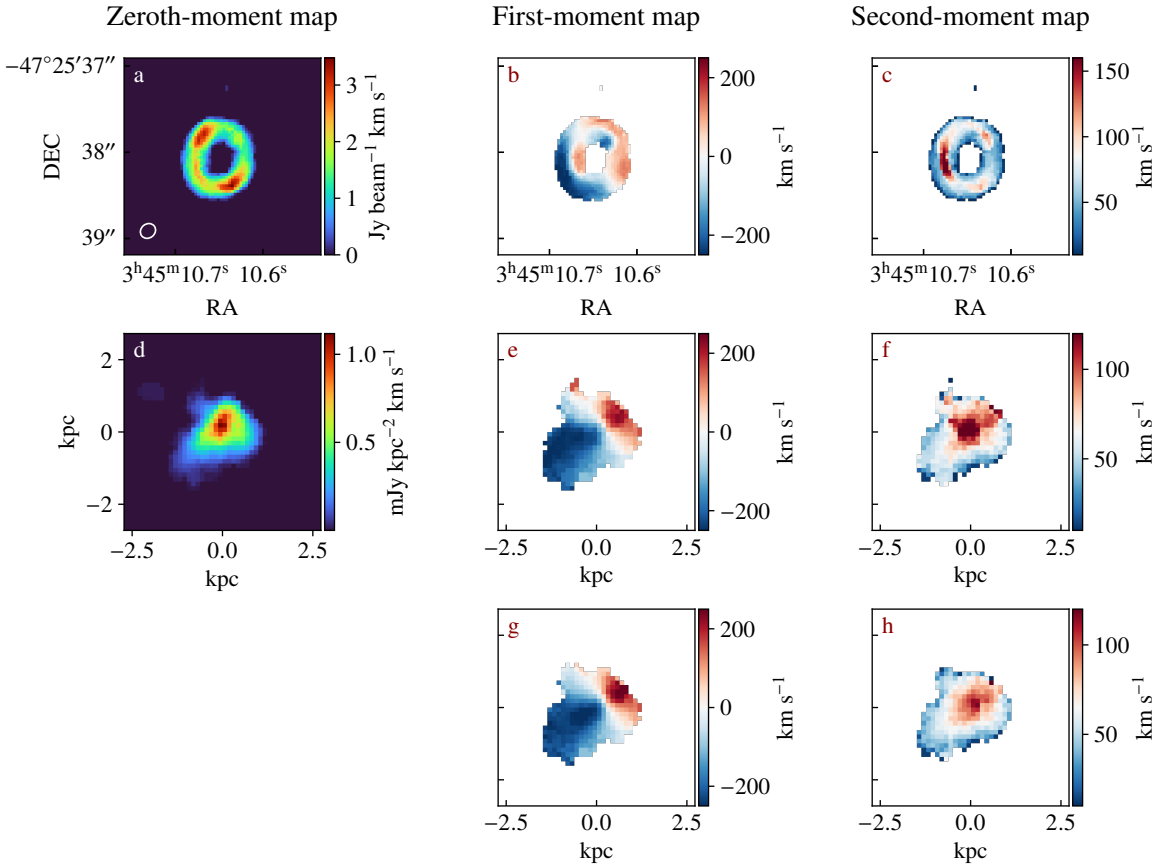

Figure 4.12: **Moment maps for SPT0345-47.** Same as in Figure 4.1. The beam size, shown as a white ellipse on the lower left corner of panel a, is 0.18×0.16 arcsec^2 at a position angle of -50.6°.

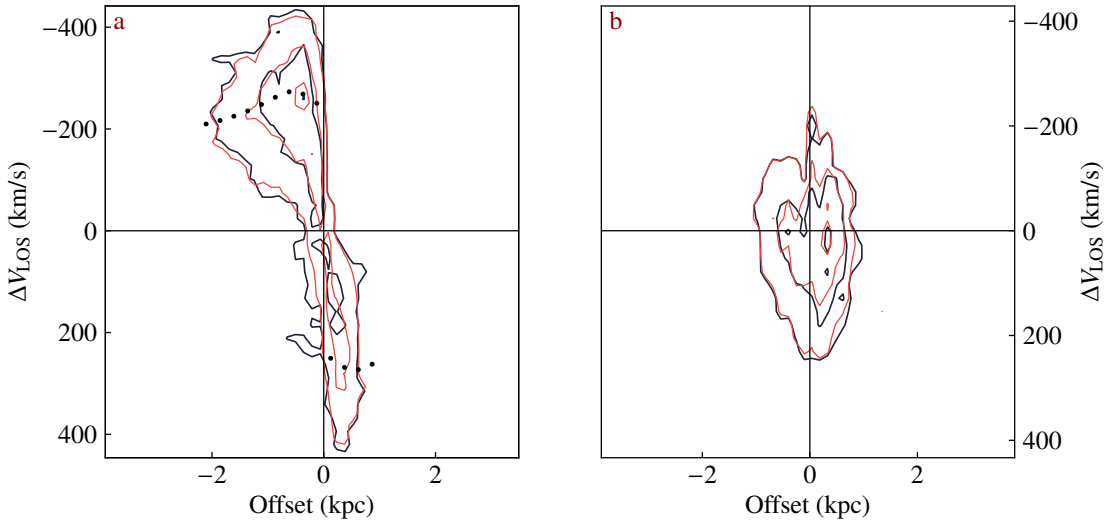

Figure 4.13: **Position-velocity diagrams for SPT0345-47.** Same as in Figure 4.2.

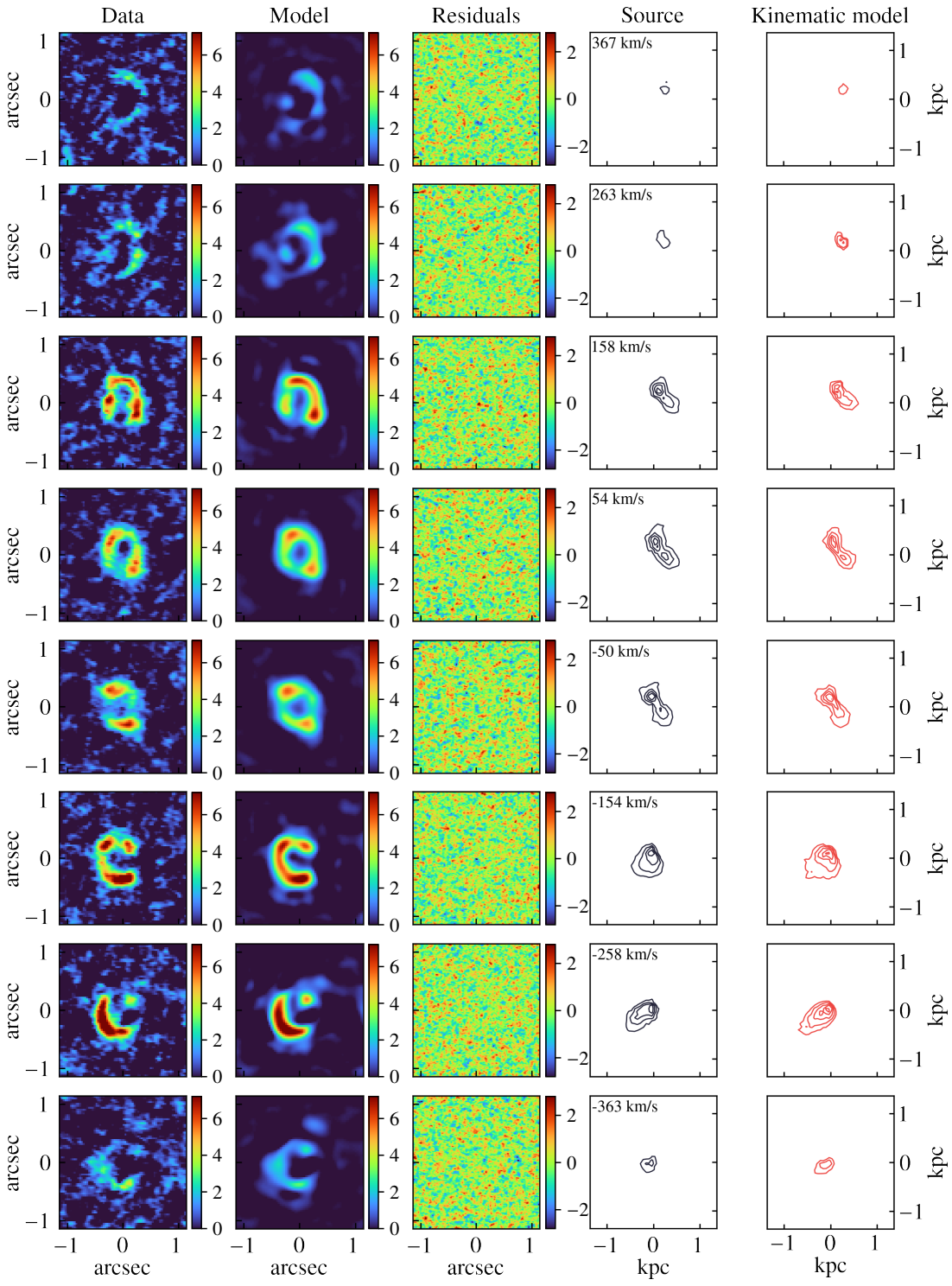

Figure 4.14: **Channel maps for SPT0345-47.** Same as in Figure 4.3.

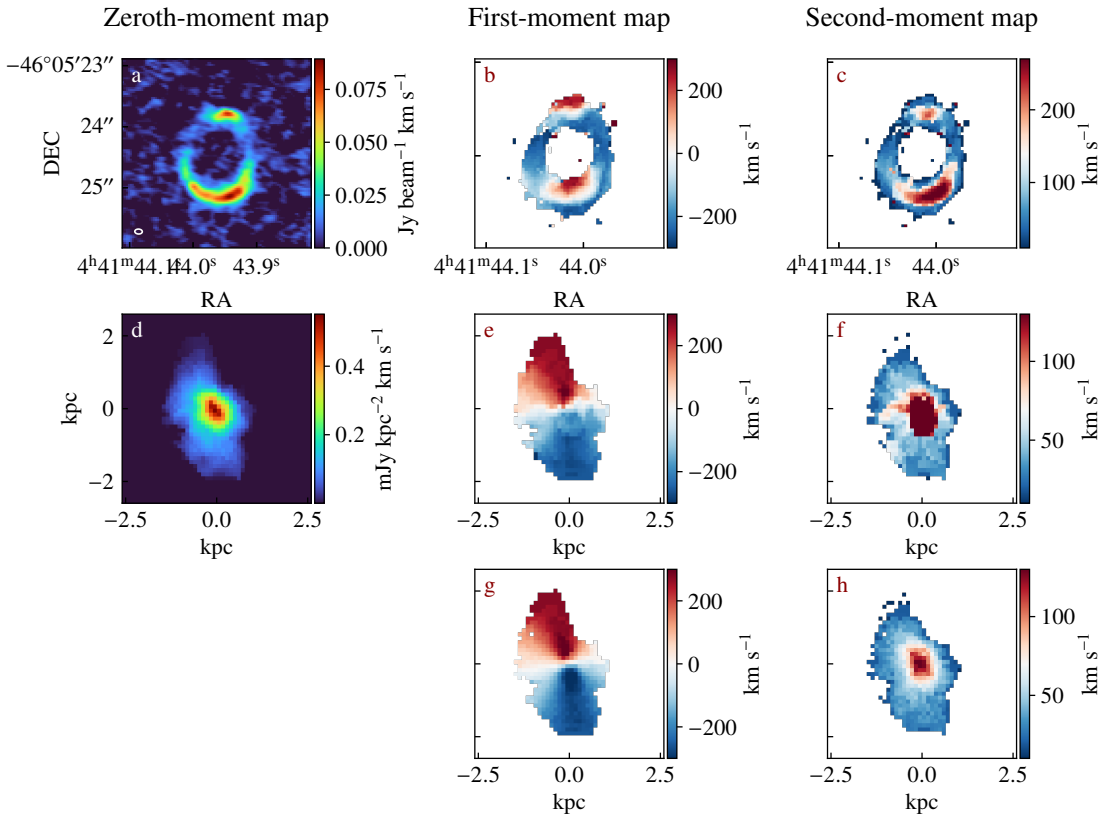

Figure 4.15: **Moment maps for SPT0441-46.** Same as in Figure 4.1. The beam size, shown as a white ellipse on the lower left corner of panel a, is 0.23×0.19 arcsec^2 at a position angle of -46.6°.

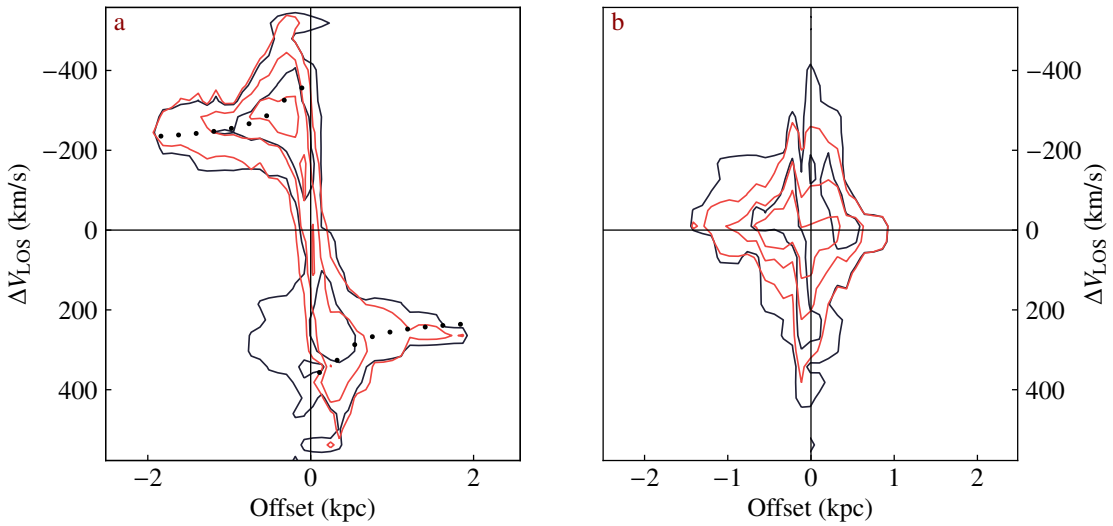

Figure 4.16: **Position-velocity diagrams for SPT0441-46.** Same as in Figure 4.2.

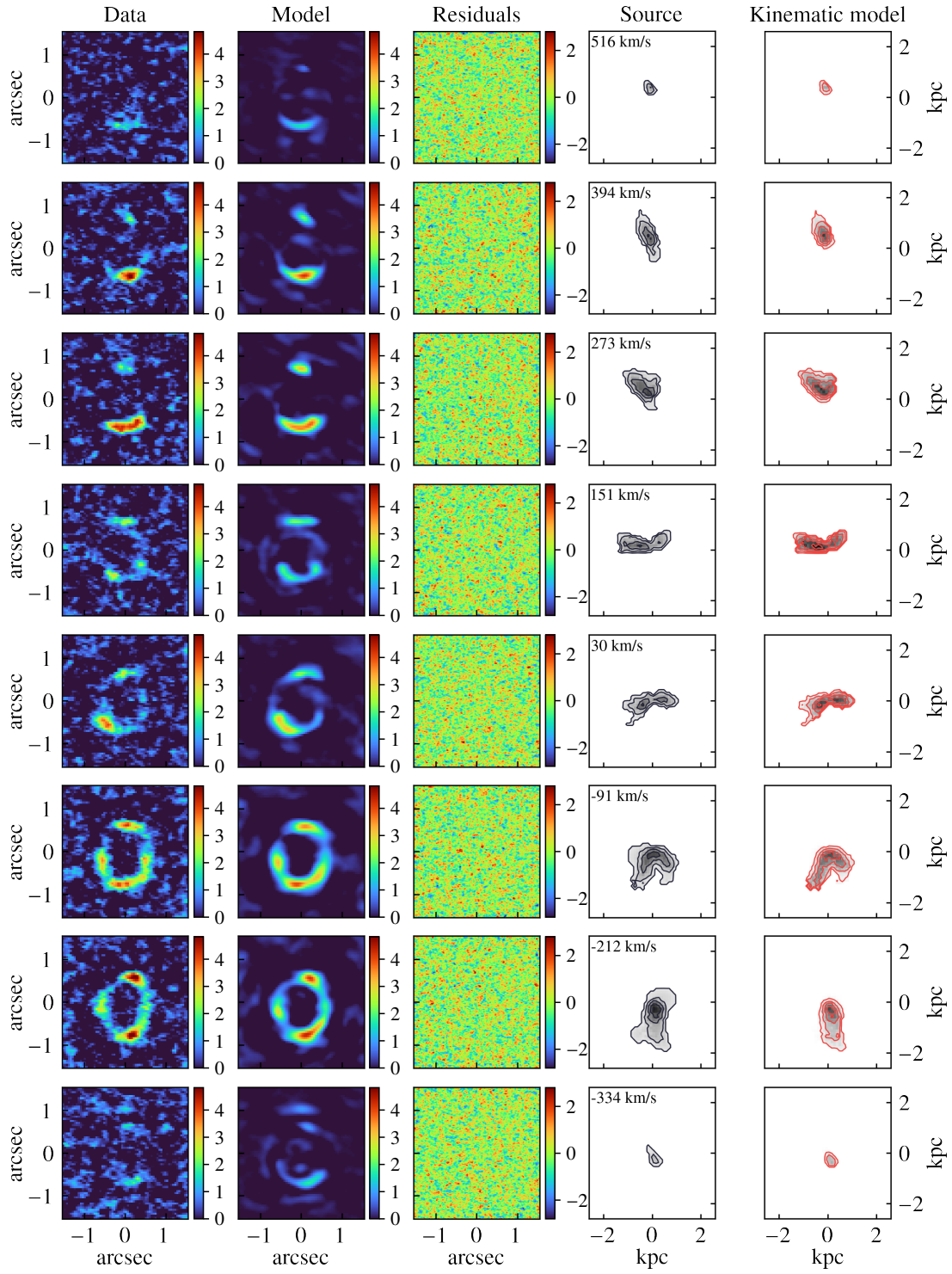

Figure 4.17: **Channel maps for SPT0441-46.** Same as in Figure 4.3.

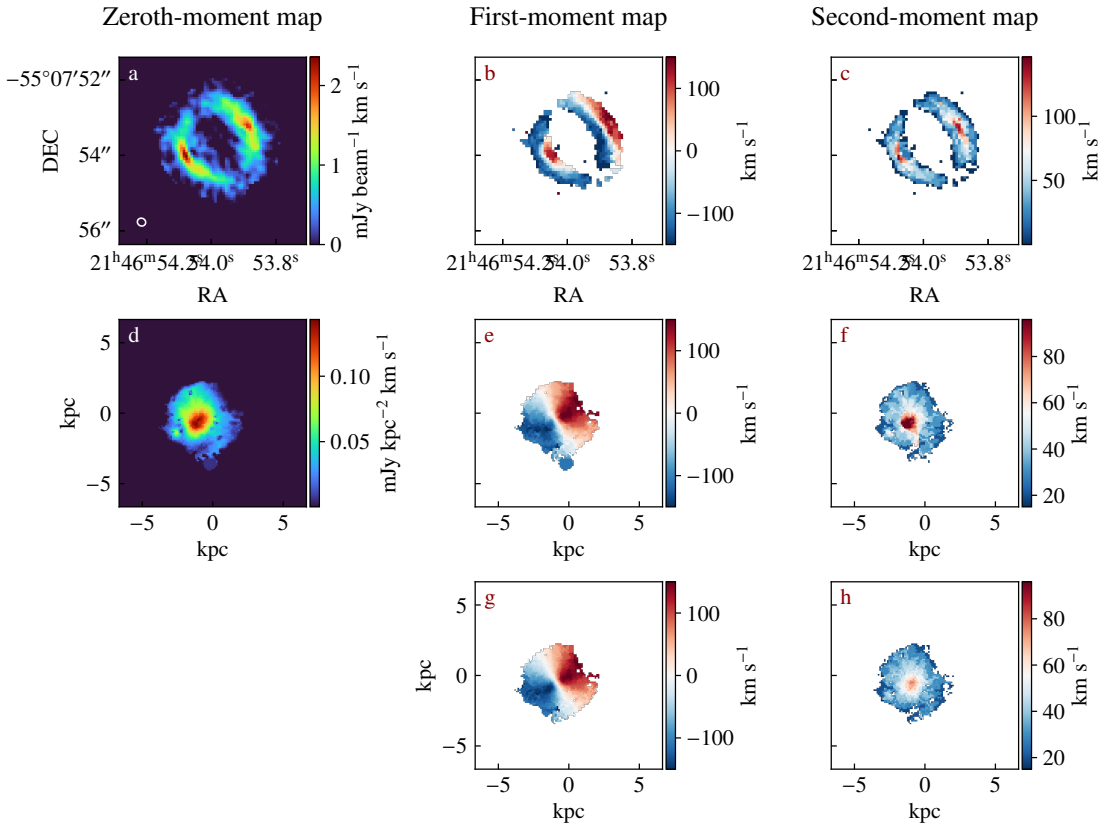

Figure 4.18: **Moment maps for SPT2146-56.** Same as in Figure 4.1. The beam size, shown as a white ellipse on the lower left corner of panel a, is 0.23×0.20 arcsec^2 at a position angle of -64.1°.

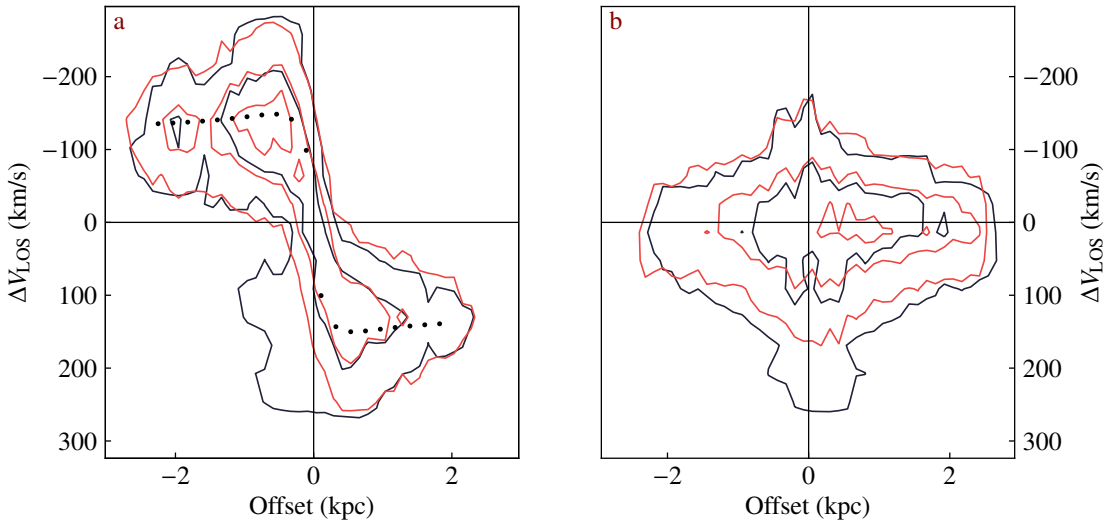

Figure 4.19: **Position-velocity diagrams for SPT2146-56.** Same as in Figure 4.2.

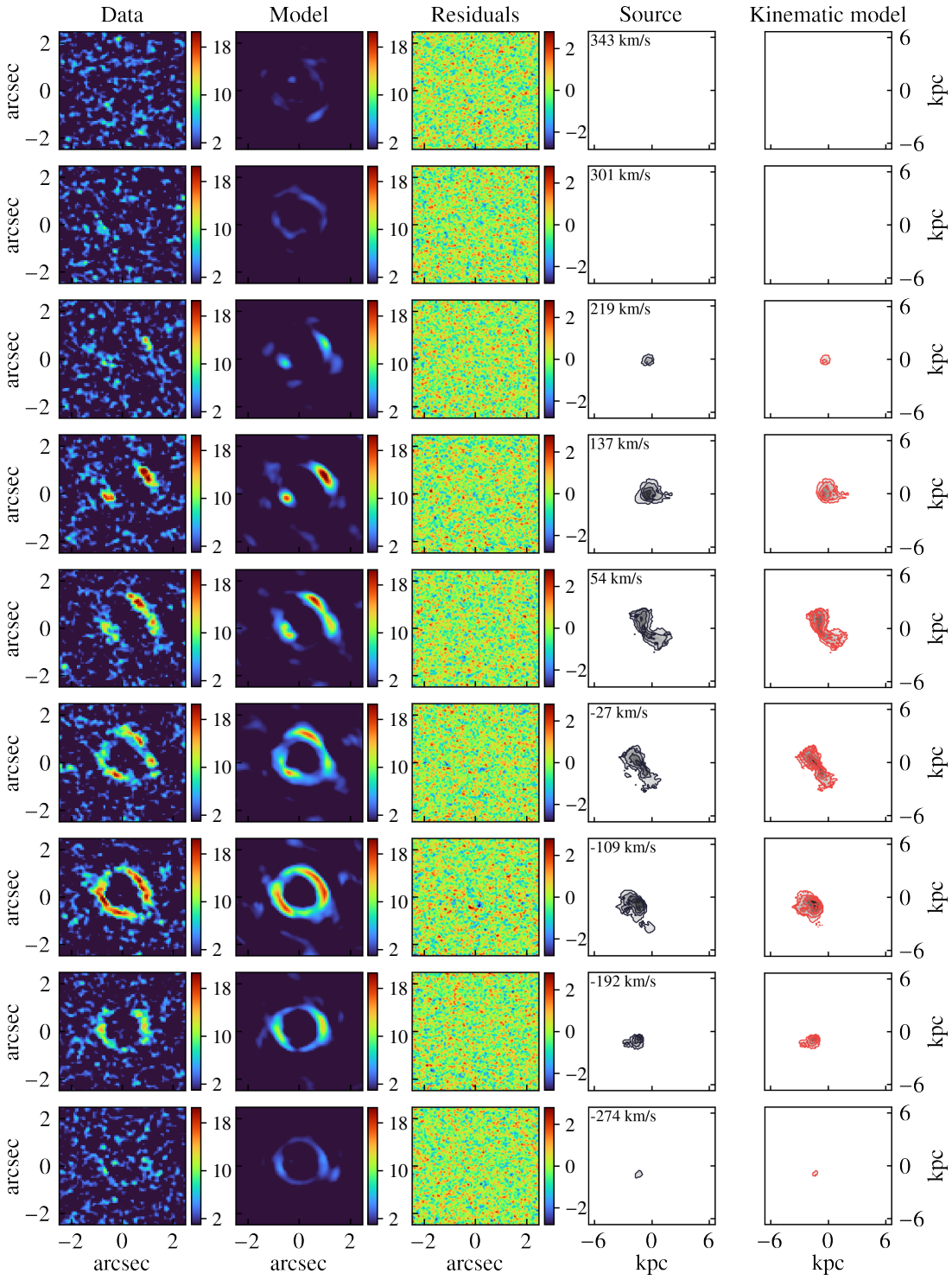

Figure 4.20: **Channel maps for SPT2146-56.** Same as in Figure 4.3.

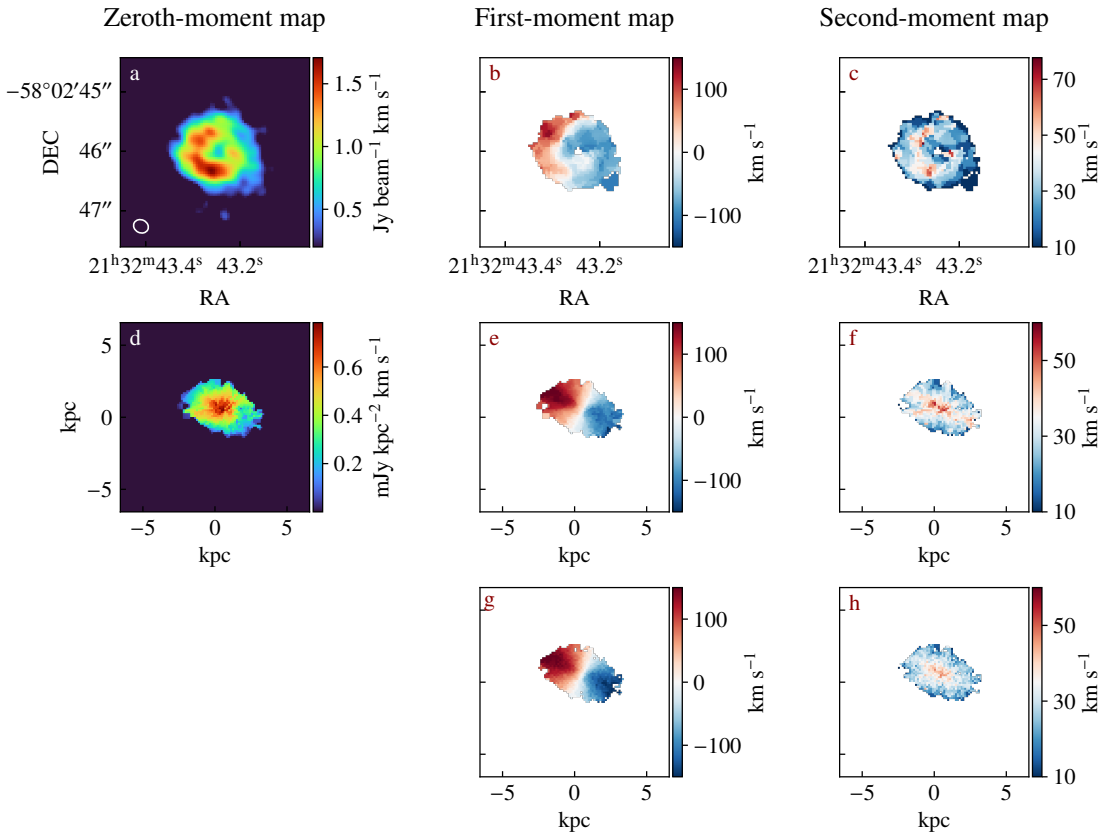

Figure 4.21: **Moment maps for SPT2132-58.** Same as in Figure 4.1. The beam size, shown as a white ellipse on the lower left corner of panel a, is 0.25×0.22 arcsec^2 at a position angle of 63.3°.

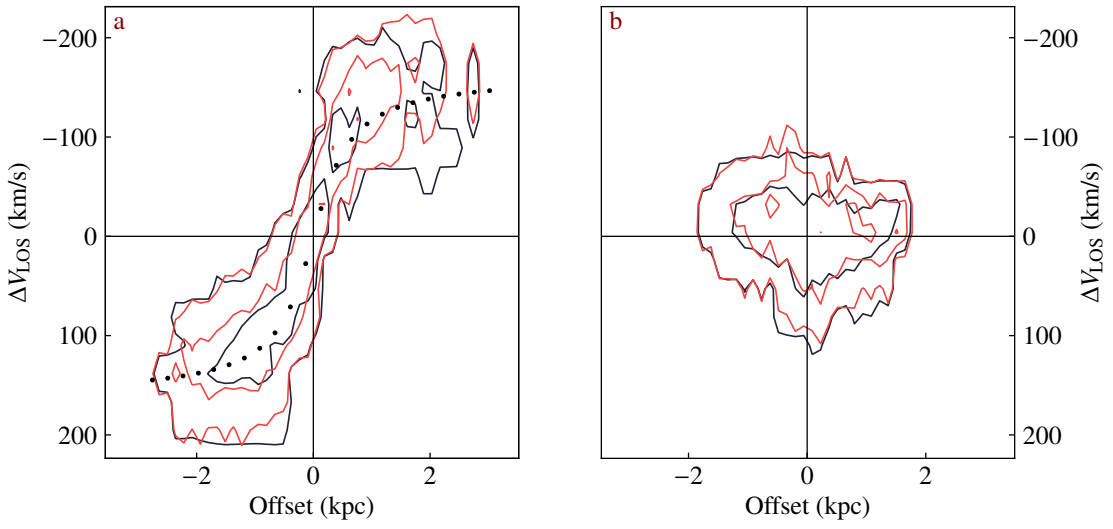

Figure 4.22: **Position-velocity diagrams for SPT2132-58.** Same as in Figure 4.2.

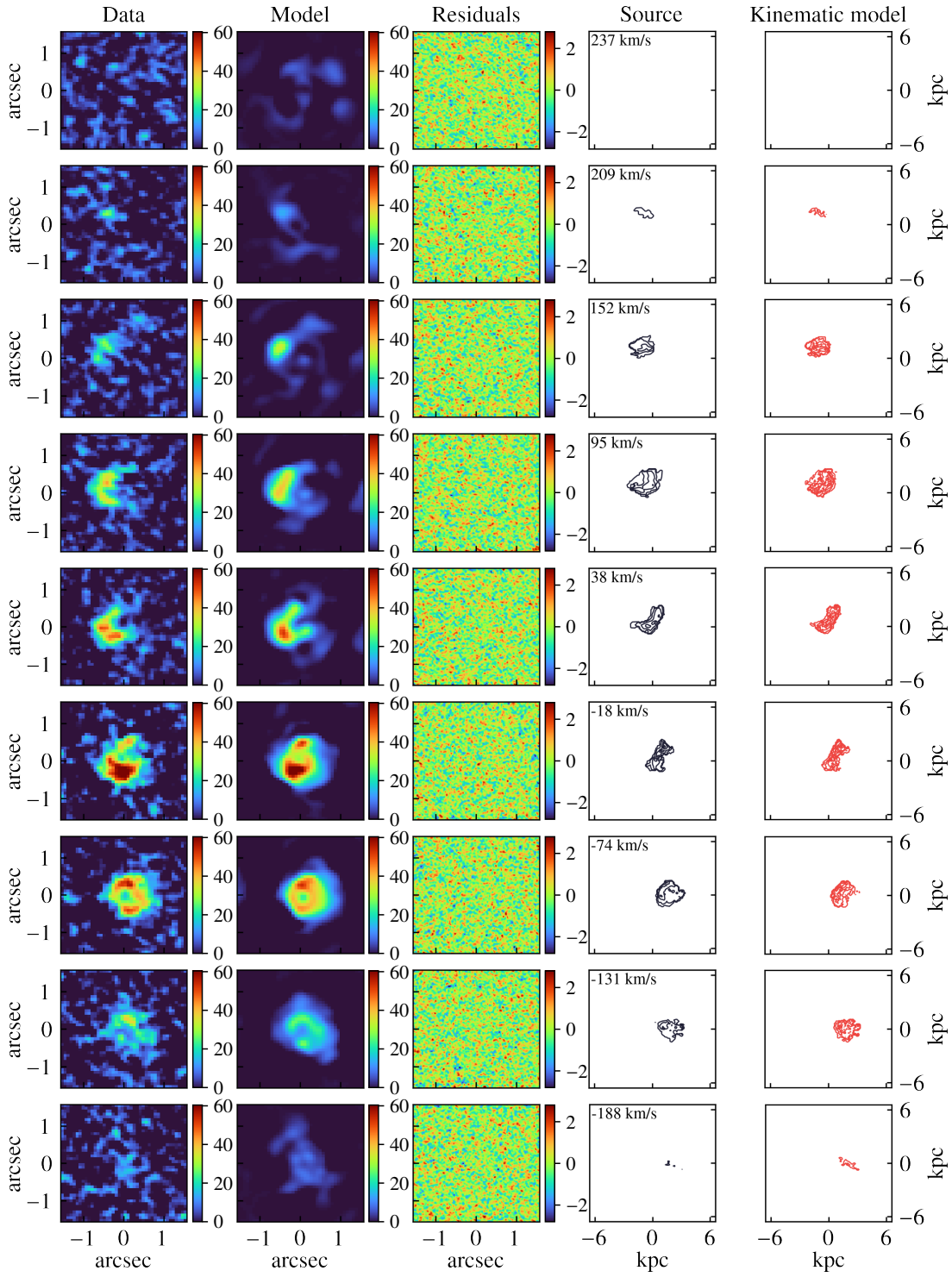

Figure 4.23: **Channel maps for SPT2132-58.** Same as in Figure 4.3.

Chapter 5

Conclusions

The study of galactic dynamics across cosmic time represents a unique opportunity to reach a comprehensive view of the formation and evolution of galaxies and gain insight into the main physical mechanisms shaping their properties at different epochs. In particular, rotation curves are a powerful tool, allowing the derivation of the gravitational potential of galaxies and the relative distribution of baryonic and dark matter. Velocity dispersion measurements provide, instead, information on the turbulence within galaxies and the evolution of the stability of disks.

In the last decade, astronomers have extensively investigated the dynamics of star-forming galaxies at increasingly higher redshift using spectroscopic observations of gas emission lines. In general, the relative importance of rotation and random motions can be easily derived from high spatial resolution observations. However, the rotation velocity and the velocity dispersion become increasingly degenerate with each other as the spatial resolution of the observations decreases, because of the so-called beam-smearing effect (see Section 1.5 for details). Observations of high-z galaxies are thus still challenging, and limited SNRs and spatial resolution might be the leading cause of biased dynamical measurements. In this thesis, we have partly overcome these limitations by targeting strongly gravitationally lensed sources. Gravitational lensing offers a unique opportunity to efficiently observe high-z sources thanks to the effect of the lensing magnification. Below, we summarize the key results presented in this thesis (Section 5.1), while an overview of future projects is presented in Section 5.2.

5.1 Summary of this thesis

In this section, we report a summary of the main results presented in the previous chapters, and we address the two questions posed in Section 1.7.

In Chapter 2, we have presented a novel method that derives the kinematic properties of gravitationally lensed galaxies. To date, most of the analyses aimed at studying the kinematics of lensed sources have been suboptimal because they have been performed on the reconstructed source, where the pixels are correlated, the noise properties are not fully characterized, and there is a change of the spatial resolution with the lensing magnification. As a result, one introduces systematic errors in the derivation of the kinematics of these sources, which may be difficult to quantify and correct a posteriori. Instead, with our new approach, it is possible to derive the lens-mass distribution and the source kinematics simultaneously from the same 3D data. By using a rotating disk as a hyper-prior for the source reconstruction, the inferred kinematic properties are not influenced by the poor understanding of the errors and spatial resolution on the source plane. Our technique offers, therefore, the opportunity to exploit the great spatial resolution and SNR achievable with gravitational lensing and perform a robust analysis of the kinematic properties of high-z lensed galaxies.

In Chapter 3, we applied our kinematic-lens modeling code to ALMA observations of the [CII] line from a DSFG at $z = 4.2$, SPT0418-47. The spatial resolution of just 60-parsec allowed us to study the dynamical properties with unprecedented details at these high redshifts. We found that SPT0418-47 is dynamically cold, with a ratio of rotational-to-random motions of ~ 10, which is four times larger than expected from numerical simulations at this epoch, but similar to spiral galaxies in the local Universe. In particular, the high V/σ in a galaxy with an SFR of ~ 300 $M_\odot$ yr^{-1} and a gas fraction of ~ 0.5 rules out theoretical models in which high star-formation feedback and a high gas fraction produce large turbulent motions and violent disk instabilities, resulting in dispersion dominated systems with $V/\sigma \lesssim 1$ at these redshifts.

Chapter 4 deals with ALMA observations of the [CII] emission line from six gravitationally lensed DSFGs at redshifts between ~ 3 and ~ 5. We have combined the dynamical measurements obtained for these galaxies with those obtained for SPT0418-47 to build the largest sample of $z \sim 4$ galaxies with high-quality data and spatial resolutions of ~ 100 pc, so far. All galaxies in the sample are dynamically cold, with V/σ between 6 to 15, confirming that SPT0418-47 is not an outlier for this galaxy population. We then investigated whether there is any correlation between the SFR and the dynamical properties, as predicted by theoretical studies. The weak trend between the SFR and the corresponding V/σ and velocity dispersion indicates that stellar feedback processes play only a minor role in driving high-levels of turbulence within these young galaxies. By considering some measurements from the literature for local star-forming galaxies, we found that a change of three orders of magnitude in SFR corresponds to a change of only a factor of two in the velocity dispersion. In addition, we perform a rotation curve decomposition to infer the relative contribution of the baryonic (gas, stars) and dark matter components to the total gravitational potentials. This analysis allowed us to compare the structural properties of the studied DSFGs with those of their descendants, the local ETGs. In particular, we found that the baryonic mass of the high-z DSFGs is similar to that measured for local ETGs, implying that the physical mechanisms acting on these galaxies in the following ~ 12 Gyr should accrete only a small amount of baryonic matter.

As a result of our dynamical analysis on a sample of DSFGs at $z \sim 4$, we can now give the first answers to the two questions posed at the beginning of this thesis:

- *Is there any observational signature of the extreme physical processes that are assumed to be the main drivers of galaxy evolution in the early Universe?* No, our analysis indicates that high-z galaxies are only weakly affected by highly perturbing mechanisms. For example, the high rate of star formation and, as a consequence, the expected high level of stellar feedback weakly affect the dynamical properties of the studied galaxies, challenging any prediction from state-of-the-art numerical simulations. This tension suggests that the role of baryonic physics in shaping some observed galaxy properties is more complicated than currently captured in simulations. Despite most properties of the local galaxy population are well reproduced by simulations, it may be possible that details of feedback implementations and potentially the lack of relevant physical processes with a compensating effect are responsible for the observed mismatch at high redshifts.

- *When and how do the morphological and structural properties of the local ETGs form and evolve?* Our studies on the baryonic masses of DSFGs, as well as on their morphologies, allowed us to investigate a temporal fragment of the evolutionary history of quiescent galaxies. We found that already at $z \sim 4$, DSFGs have baryonic masses similar to their descendants. Also, for some of them, there is evidence of a spheroidal component, suggesting that the bulge growth has started before the quenching of their star formation. The physical properties observed for our sample provide strong constraints on the successive growth of mass, size, and bulge that is driven by the physical processes responsible for the transformation of DSGFs into massive quiescent galaxies.

5.2 Future prospects

In this section, we introduce future avenues of research that are a natural evolution of the work presented in this thesis. The main focus of these upcoming projects is to quantify the impact of stellar feedback on galactic dynamics as well as gain insight into the ISM properties of star-forming galaxies at almost unexplored cosmological epochs. In particular, we will exploit state-of-the-art facilities such as ALMA, VLT, and JWST to target different dynamical tracers within a broad range of redshift.

5.2.1 A large sample of DSFGs at $z \sim 4$

In this thesis, we inspected the properties of seven DSFGs at z $\sim$ 4. Although the galaxies in our sample have physical properties (e.g., SFR, dust sizes, dust temperatures) typical of their population, a larger sample is needed to corroborate our results statistically. Observations of six DSFGs are underway within the current observing cycle of ALMA (Project number:

2019.1.01673.S, PI: Rizzo F.). Furthermore, we are planning a large campaign for the next observing cycle of ALMA to obtain [CII] observations for $\sim$ 30 gravitationally lensed DSFGs in the redshift range between 3 and 5. Thanks to the broad SFR range covered by this sample, we will be able to target the heterogeneous population of the DSFG population, consisting of both MS and starburst galaxies (Michałowski et al. 2017, Hodge & da Cunha 2020). Our analysis of galactic dynamics, gas fraction, and SFR properties will allow us to reach a comprehensive view of the turbulence on sub-kpc scales and its driving mechanisms in the early Universe. This campaign will, therefore, set significant constraints on galaxy formation models during the early phase of galaxy formation.

5.2.2 SPT0418-47: a test case with the JWST

The JWST is expected to revolutionize the study of high-z galaxies. The 6.5-meter diameter mirror combined with the Near-Infrared Camera (NIRCam, Rieke et al. 2005) and Spectrograph (NIRSpec, Posselt et al. 2004) as well as the Mid-Infrared instruments (MIRI, Rieke et al. 2015), will open up the possibility to observe spatially-resolved rest-frame NIR and optical emission of galaxies at $z \gtrsim 3$ (see discussion in Section 1.3 and Figure 1.3). Starting from JWST observations of the lensed galaxy SPT0418-47, as part of the Early Release Science data output[1][2], we will efficiently plan a JWST observing campaign to follow-up DSFGs with existing and upcoming ALMA observations. Combining the information provided by ALMA with that from the JWST we will address the following outstanding puzzles of extragalactic astrophysics:

- Bulge and disk formation. The results presented in this thesis show that DSFGs at high redshift may already display the dynamical signature of a spheroidal component. However, due to a combination of degeneracies and lack of constraints, we could not establish whether a stellar disk is also already in place at $z \sim 4$. For example, a rotation curve that is well fitted by a Sérsic component with $n \sim 2$, i.e., a disky bulge, could be explained by the combination of a classical bulge with $n \sim 4$ and a stellar disk, instead. Observations in the optical frequency range will provide the necessary information to break this degeneracy. By linking morphological studies with spatially-resolved constraints on the age and metallicities of their stellar populations, we will provide invaluable constraints on the formation epochs of these structures, as well as on the physical processes contributing to shaping them.

- Initial Mass Function (IMF). The IMF is the distribution of masses for a population of stars at the time of their formation (Cimatti et al. 2019), and it is a fundamental ingredient for observational and theoretical astrophysics: it allows the computation of a galaxy stellar mass and SFR and their evolution with cosmic time (Bastian et al. 2010).

[1] https://www.stsci.edu/jwst

[2] The Early Release Science observations will take place during the first five months of JWST science operations and will be available to the scientific community.

Despite its importance, the IMF is to these days poorly constrained. In particular, astronomers are still debating whether the IMF is universal (Casey et al. 2014), i.e., the same for every galaxy in the Universe, or whether it varies with the physical properties of each galaxy. For example, several studies showed that a variation of the IMF is necessary to reproduce the observed properties of local ETGs (Cappellari et al. 2012) and the number counts of DSFGs at high-z (Baugh et al. 2005, Lacey et al. 2016). However, Lagos et al. (2019) and Lovell et al. (2020) showed, recently, that a universal IMF is sufficient to reproduce both observations. Since different IMFs result in different values of the mass-to-light ratio, by combining the results of our dynamical analysis with measurements of the luminosity from JWST observations, we will be able to investigate the nature of the IMF.

- Galaxy dynamics as a cosmological probe. The dynamical analysis presented in this thesis assumes that the dark-matter halo has a mass density profile given by CDM simulations (see discussion in Section 3.2.2). This choice was necessary because of the limited amount of constraints that were available to us. However, several studies have shown that the dark-matter distribution can be significantly affected by changes to the dark matter particles (e.g., warm and self-interacting dark matter versus CDM Ludlow et al. 2016, Vogelsberger et al. 2016), and galaxy formation (e.g., different implementation of feedback) models (e.g., Despali & Vegetti 2017, Di Cintio et al. 2017, Lovell et al. 2020). Observations of the stellar distribution with the JWST will provide us with enough constraints to relax this assumption. By allowing the dark-matter profile to have more freedom, we will then be able to test the predictions from different dark-matter models and their interplay with the physics of baryons.

5.2.3 Stellar feedback at $z \sim 1$ - 2: comparison between different tracers

According to current galaxy formation models, galaxies with low stellar masses (i.e., $\lesssim 10^{10}$ $M_\odot$) are the most influenced by stellar feedback. Their shallow potential wells may not be able to retain the gas that is instead expelled in the form of outflows driven by supernova explosions (Nelson et al. 2019, Vogelsberger et al. 2020). Unfortunately, observations of these low-mass systems are still challenging even at intermediate-z. Once more, our strategy is to take advantage of the magnifying power of strong gravitational lensing to push the limits of current observational facilities. We are thus planning a pilot multiwavelength campaign on a small sample of ~ 10 low-stellar masses MS galaxies at $z \sim 1-2$. In particular, we will exploit ALMA observations of the CO and [CII] emission lines to study their gas fraction and the dynamics of the molecular and neutral gas components, respectively. By targeting the Hα emission line with the Enhanced Resolution Imager and Spectrograph (Kenworthy et al. 2018), the new IFU instrument on the VLT, we will, instead, probe the warm phase of the ISM (see Section 1.2). Comparing the dynamical properties of the different phases of the ISM is fundamental to investigate the impact of stellar feedback in driving the evolution of these low-mass galaxies. While it is firmly established that the kinematics of the molecular and ionized gas traces the galaxy kinematics, there is an open debate on the validity of this

assumption for the Hα emission line (Übler et al. 2018, Girard et al. 2018, Levy et al. 2018). Some studies have shown, indeed, that the kinematics of the molecular and ionized gas are different (Girard et al. 2018, Levy et al. 2018), while others found consistency between the two tracers (Übler et al. 2018). In the first case, the difference is explained as due to gas in outflows or in extraplanar layers because of mild stellar feedback processes (Levy et al. 2018, Olivares et al. 2016). The synergy between our multiwavelength pilot projects will, therefore, allow us to investigate this tension and constrain the effect of stellar feedback in driving ionized gas out of the galaxy.

5.2.4 Final remarks

As we have extensively shown in this thesis, the magnifying power of strong gravitational lensing allows one to study high-z galaxies with a precision that will only be possible, for unlensed objects, with the next generation of ground-based Extremely Large Telescopes (ELTs, e.g., the European Extremely Large Telescope[3]). Studies of lensed galaxies are thus pioneering the field of galaxy evolution, allowing the development of efficient observational strategies for the next-generation of large surveys targeting unlensed galaxies. Above, we have outlined a series of pilot projects that can be undertaken now with the limited number of known strongly lensed galaxies, and that will provide essential clues on the evolution of galaxies across cosmic time. To date, the number of known galaxy-galaxy lens systems is less than a thousand. Moreover, only a minority of them are usually suitable for a specific astrophysical application (e.g., studies of distant sources, studies of the dark matter distribution). However, the field of strong gravitational lensing is about to change dramatically as the Euclid space telescope[4], the Rubin Observatory[5] and the Square Kilometer Array[6] will soon increase the number of known gravitationally lensed systems by several orders of magnitude (Oguri & Marshall 2010, Collett 2015, McKean et al. 2015). These large samples coupled with high-resolution follow-up observations with the JWST and the ELTs will open up a new avenue for detailed investigations of lensed galaxies during the epoch of reionization (i.e., the first Gyr of the history of the Universe) and significant progress in our understanding of how galaxies evolve in time.

[3] https://www.eso.org/sci/facilities/eelt/
[4] https://www.euclid-ec.org
[5] https://www.lsst.org
[6] https://www.skatelescope.org

Appendix A

A.1 Interferometric data

A radio interferometer is an array of antennas, dishes or dipoles. The relative distances between different pairs of antennae are called baselines. Given a source with surface brightness distribution I at coordinates in the plane of the sky (l, m) and at an observed frequency ν, an interferometer measures the so-called visibility function (Thompson et al. 1986)

$$V(u, v, w, \nu) = \int A(l, m, \nu) I(l, m) e^{-2\pi i [ul + vm + w(\sqrt{1-l^2-m^2}-1)]} \frac{dl dm}{\sqrt{1 - l^2 - m^2}}. \tag{A.1}$$

In equation (A.1), $A(l, m, \nu)$ is the attenuation function of the sky map induced by the beam of the antenna, (u, v) and w are the coordinates in the Fourier plane, corresponding to the projection of the baselines on the plane of the sky and parallel to the line of sight, respectively. Since for typical galaxy-galaxy lensing observations, the accuracy of the pointing is within a few arcseconds, the coordinate w, measured respect to the phase center[1] can be discarded, $w \approx 0$, and the following inequality $l^2 + m^2 << 1$ is valid. In such case, equation (A.1) becomes

$$V(u, v, \nu) = \int A(l, m, \nu) I(l, m) e^{-2\pi i (ul + vm)} dl dm, \tag{A.2}$$

that is, the visibility function is the Fourier transform of the sky surface brightness $I(l, m)$. In reality, the visibility function is not continuous, because the uv-plane is sampled only discretely at the positions of the baselines. The inversion of the sampled visibility function results in the so-called dirty image

$$I_{\mathrm{D}}(l, m, \nu) = A(l, m, \nu)^{-1} \int S(u, v, \nu) V(u, v) e^{2\pi i (ul + vm)} du dv, \tag{A.3}$$

where $S(u, v)$ is the sampling function, equal to 1 for sampled u, v positions and 0 otherwise. By applying the convolution theorem, it can be shown that the dirty image is the result of the convolution of the intrinsic sky brightness distribution $I(l, m)$ with the dirty beam

$$B_{\mathrm{D}}(l, m, \nu) = \int S(u, v, \nu) e^{2\pi i (ul + vm)} du dv, \tag{A.4}$$

[1]The phase center is the reference position of the observation on the sky, usually corresponding to the center or nominal position of the target source.

that is, the inverse Fourier Transform of the sampling function. As a consequence of the incomplete sampling of the uv-plane, the pattern of the dirty beam may have large positive or negative side-lobe structures. Deconvolution algorithms (e.g., CLEAN, Högbom 1974) are, therefore, employed to mitigate the effects of the side lobes and recover the sky surface brightness distribution, that is, the so-called clean image.

Despite the success of the deconvolution algorithms, the study of the astrophysical sources from the clean images presents a few major limitations. The non-linear deconvolution processes introduce, indeed, non-trivial correlations between the signal and the noise over the entire image constructed by the cleaning algorithms. As a consequence, it is unclear how to properly propagate the Gaussian noise of the visibilities to the clean image. Moreover, deconvolution algorithms do not guarantee the conservation of the surface brightness, which is a fundamental feature of gravitational lensing.

A.2 Visibility-space modeling

In Chapters 3 and 4, we use a kinematic-lens modeling technique that fits the data directly in the native visibility-space, overcoming the limitations of the deconvolution algorithms described in the previous section (Powell et al. 2020). As mentioned in Section 3.2, in case of interferometric data, the Discrete Fourier Transform operator $\mathbf{D}$ takes the place of the PSF operator $\mathbf{B}$, while the data $\mathbf{d}$ correspond to the complex visibilities V. However, due to the large number of visibilities N_{vis}, the solution of the linear system (2.10) becomes computationally expensive. This is because the Discrete Fourier Transform operator $\mathbf{D}$ that enters both on the left and right-hand side of the linear system (2.10) would require huge amount of memory storage ($2N_{vis} \times N_d$) and a matrix-vector multiplication by $\mathbf{D}$ would demand $\sim 10^{11}$ floating point sine and cosine evaluations. For this reason, we substituted the Discrete Fourier Transform operator with a non-uniform Fast Fourier Transform operator (NUFFT, $\tilde{\mathbf{D}}$, Greengard & Lee 2004, Beatty et al. 2005). This NUFFT operator takes the following form

$$\tilde{\mathbf{D}} = \mathbf{GFW}, \tag{A.5}$$

where $\mathbf{W}$ represents an apodization correction that allows the mapping of the model onto the Fourier Transform of the original uv-sampling; $\mathbf{F}$ is the Fast Fourier Transform operator and $\mathbf{G}$ interpolates the visibilities from a regular gridded uv-plane onto the observed arbitrarily-spaced uv-plane.

Because NUFFT does not have an explicit matrix representation, the source, equation (2.10), is obtained using an iterative linear solver that applies an operator repeatedly, subtracting residuals from a trial solution until the desired tolerance is reached. In particular, we have adopted a preconditioned conjugate gradient solver, with a convergence tolerance of 10^{-8}, resulting in typical accuracies of 10^{-6} for the source inversions.

Bibliography

Andersen, D. R., Bershady, M. A., Sparke, L. S., Gallagher, III, J. S., & Wilcots, E. M. 2001, ApJ, 551, L131

Aravena, M., Spilker, J. S., Bethermin, M., et al. 2016, Mon. Not. R. Astron. Soc., 457, 4406

Bacchini, C., Fraternali, F., Iorio, G., & Pezzulli, G. 2019, A&A, 622, A64

Bacchini, C., Fraternali, F., Iorio, G., et al. 2020, arXiv e-prints, arXiv:2006.10764

Barnabè, M., Czoske, O., Koopmans, L. V. E., et al. 2009, Mon. Not. R. Astron. Soc., 399, 21

Barro, G., Faber, S. M., Pérez-González, P. G., et al. 2014, Astrophys. J., 791, 52

Bastian, N., Covey, K. R., & Meyer, M. R. 2010, ARA&A, 48, 339

Baugh, C. M., Lacey, C. G., Frenk, C. S., et al. 2005, MNRAS, 356, 1191

Beatty, P. J., Nishimura, D. G., & Pauly, J. M. 2005, IEEE Transactions on Medical Imaging, 24, 799

Begeman, K. G. 1987, PhD thesis, -

Belli, S., Newman, A. B., & Ellis, R. S. 2017, ApJ, 834, 18

Benson, A. J. 2010, Phys. Rep., 495, 33

Bessell, M. S. 2005, ARA&A, 43, 293

Bird, J. C., Kazantzidis, S., Weinberg, D. H., et al. 2013, Astrophys. J., 773, 43

Bisigello, L., Caputi, K. I., Grogin, N., & Koekemoer, A. 2018, A&A, 609, A82

Bolton, A. S., Burles, S., Koopmans, L. V. E., Treu, T., & Moustakas, L. A. 2006, ApJ, 638, 703

Boogaard, L. A., Decarli, R., González-López, J., et al. 2019, ApJ, 882, 140

Boomsma, R., Oosterloo, T. A., Fraternali, F., van der Hulst, J. M., & Sancisi, R. 2008, A&A, 490, 555

Bosma, A. 1978, PhD thesis, -

Bosma, A. 1981, AJ, 86, 1825

Bouché, N., Carfantan, H., Schroetter, I., Michel-Dansac, L., & Contini, T. 2015, AJ, 150, 92

Bouché, N., Dekel, A., Genzel, R., et al. 2010, ApJ, 718, 1001

Brinchmann, J., Charlot, S., White, S. D. M., et al. 2004, MNRAS, 351, 1151

Burkert, A., Förster Schreiber, N. M., Genzel, R., et al. 2016, ApJ, 826, 214

Caminha, G. B., Rosati, P., Grillo, C., et al. 2019, A&A, 632, A36

Cappellari, M., Emsellem, E., Krajnović, D., et al. 2011, Mon. Not. R. Astron. Soc., 413, 813

Cappellari, M., McDermid, R. M., Alatalo, K., et al. 2012, Nature, 484, 485

Cappellari, M., McDermid, R. M., Alatalo, K., et al. 2013a, Mon. Not. R. Astron. Soc., 432, 1862

Cappellari, M., Scott, N., Alatalo, K., et al. 2013b, Mon. Not. R. Astron. Soc., 432, 1709

Caputi, K. I., Deshmukh, S., Ashby, M. L. N., et al. 2017, ApJ, 849, 45

Carilli, C. L. & Walter, F. 2013, Annu. Rev. Astron. Astr., 51, 105

Carlstrom, J. E., Ade, P. A. R., Aird, K. A., et al. 2011, Publ. Astron. Soc. Pac., 123, 568

Casey, C. M., Narayanan, D., & Cooray, A. 2014, Phys. Rep., 541, 45

Ceverino, D., Dekel, A., & Bournaud, F. 2010, MNRAS, 404, 2151

Chen, C.-C., Smail, I., Swinbank, A. M., et al. 2015, Astrophys. J., 799, 194

Chisholm, J., Tremonti, C. A., Leitherer, C., & Chen, Y. 2017, MNRAS, 469, 4831

Cimatti, A., Fraternali, F., & Nipoti, C. 2019, Introduction to Galaxy Formation and Evolution: From Primordial Gas to Present-Day Galaxies

Collett, T. E. 2015, ApJ, 811, 20

Cook, R. H. W., Cortese, L., Catinella, B., & Robotham, A. 2020, MNRAS, 493, 5596

Cormier, D., Madden, S. C., Lebouteiller, V., et al. 2015, A&A, 578, A53

Courteau, S. 1997, AJ, 114, 2402

Davies, R., Förster Schreiber, N. M., Cresci, G., et al. 2011, ApJ, 741, 69

de Blok, W. J. G., McGaugh, S. S., & Rubin, V. C. 2001, AJ, 122, 2396

De Breuck, C., Weiß, A., Béthermin, M., et al. 2019, A&A, 631, A167

De Breuck, C., Williams, R. J., Swinbank, M., et al. 2014, A&A, 565, A59

Decarli, R., Walter, F., Aravena, M., et al. 2016, ApJ, 833, 69

Decarli, R., Walter, F., Gónzalez-López, J., et al. 2019, ApJ, 882, 138

Dekel, A., Birnboim, Y., Engel, G., et al. 2009a, Nature, 457, 451

Dekel, A. & Burkert, A. 2014, Mon. Not. R. Astron. Soc., 438, 1870

Dekel, A., Sari, R., & Ceverino, D. 2009b, ApJ, 703, 785

Despali, G. & Vegetti, S. 2017, MNRAS, 469, 1997

D'Eugenio, C., Daddi, E., Gobat, R., et al. 2020, ApJ, 892, L2

Di Cintio, A., Tremmel, M., Governato, F., et al. 2017, MNRAS, 469, 2845

Di Teodoro, E. M. & Fraternali, F. 2015, MNRAS, 451, 3021

Di Teodoro, E. M., Fraternali, F., & Miller, S. H. 2016, Astron. Astrophys., 594, A77

Di Teodoro, E. M., Grillo, C., Fraternali, F., et al. 2018, MNRAS, 476, 804

Dutton, A. A. & Macciò, A. V. 2014, Mon. Not. R. Astron. Soc., 441, 3359

Dye, S., Furlanetto, C., Swinbank, A. M., et al. 2015, MNRAS, 452, 2258

Dziourkevitch, N., Elstner, D., & Rüdiger, G. 2004, A&A, 423, L29

Eliche-Moral, M. C., Rodríguez-Pérez, C., Borlaff, A., Querejeta, M., & Tapia, T. 2018, A&A, 617, A113

Emsellem, E., Cappellari, M., Krajnović, D., et al. 2011, Mon. Not. R. Astron. Soc., 414, 888

Epinat, B., Amram, P., Balkowski, C., & Marcelin, M. 2010, MNRAS, 401, 2113

Feroz, F., Hobson, M. P., & Bridges, M. 2009, MNRAS, 398, 1601

Feroz, F., Hobson, M. P., Cameron, E., & Pettitt, A. N. 2013, ArXiv e-prints [[arXiv]1306.2144]

Förster Schreiber, N. M., Genzel, R., Bouché, N., et al. 2009, ApJ, 706, 1364

Förster Schreiber, N. M., Genzel, R., Lehnert, M. D., et al. 2006, ApJ, 645, 1062

Förster Schreiber, N. M., Renzini, A., Mancini, C., et al. 2018, ArXiv e-prints [[arXiv]1802.07276]

Frayer, D. T., Harris, A. I., Baker, A. J., et al. 2011, ApJ, 726, L22

Freeman, K. C. 1970, ApJ, 160, 811

Gardner, J. P., Mather, J. C., Clampin, M., et al. 2009, Astrophysics and Space Science Proceedings, 10, 1

Genzel, R., Newman, S., Jones, T., et al. 2011, ApJ, 733, 101

Genzel, R., Schreiber, N. M. F., Übler, H., et al. 2017, Nature, 543, 397

Girard, M., Dessauges-Zavadsky, M., Schaerer, D., et al. 2018, A&A, 613, A72

Glazebrook, K., Schreiber, C., Labbé, I., et al. 2017, Nature, 544, 71

Glover, S. C. O. & Smith, R. J. 2016, MNRAS, 462, 3011

Grand, R. J. J., Gómez, F. A., Marinacci, F., et al. 2017, MNRAS, 467, 179

Greengard, L. & Lee, J.-Y. 2004, SIAM Review, 46, 443

Gullberg, B., Swinbank, A. M., Smail, I., et al. 2018, Astrophys. J., 859, 12

Harrison, C. M. 2017, Nature Astronomy, 1, 0165

Harrison, C. M., Johnson, H. L., Swinbank, A. M., et al. 2017, Mon. Not. R. Astron. Soc., 467, 1965

Hayward, C. C. & Hopkins, P. F. 2017, Mon. Not. R. Astron. Soc., 465, 1682

Hodge, J. A. & da Cunha, E. 2020, arXiv e-prints, arXiv:2004.00934

Hodge, J. A., Riechers, D., Decarli, R., et al. 2015, Astrophys. J. Lett., 798, L18

Högbom, J. A. 1974, Astron. Astrophys. Sup., 15, 417

Hopkins, P. F., Quataert, E., & Murray, N. 2012, MNRAS, 421, 3522

Hung, C.-L., Hayward, C. C., Yuan, T., et al. 2019, Mon. Not. R. Astron. Soc., 482, 5125

Iorio, G., Fraternali, F., Nipoti, C., et al. 2017, Mon. Not. R. Astron. Soc., 466, 4159

Johnson, H. L., Harrison, C. M., Swinbank, A. M., et al. 2018, MNRAS, 474, 5076

Jones, G. C., Carilli, C. L., Shao, Y., et al. 2017, ApJ, 850, 180

Jones, T., Ellis, R., Jullo, E., & Richard, J. 2010a, ApJ, 725, L176

Jones, T., Ellis, R. S., Richard, J., & Jullo, E. 2013, ApJ, 765, 48

Jones, T. A., Swinbank, A. M., Ellis, R. S., Richard, J., & Stark, D. P. 2010b, MNRAS, 404, 1247

Joung, M. K. R. & Mac Low, M.-M. 2006, ApJ, 653, 1266

Kennicutt, R. C. & Evans, N. J. 2012, Annu. Rev. Astron. Astr., 50, 531

Kenworthy, M. A., Snik, F., Keller, C. U., et al. 2018, in Society of Photo-Optical Instrumentation Engineers (SPIE) Conference Series, Vol. 10702, Ground-based and Airborne Instrumentation for Astronomy VII, 1070246

Kereš, D., Katz, N., Weinberg, D. H., & Davé, R. 2005, MNRAS, 363, 2

Kim, C.-G. & Ostriker, E. C. 2018, ApJ, 853, 173

Kleiner, D., Koribalski, B. S., Serra, P., et al. 2019, MNRAS, 488, 5352

Koopmans, L. V. E. 2005, MNRAS, 363, 1136

Koopmans, L. V. E., Treu, T., Bolton, A. S., Burles, S., & Moustakas, L. A. 2006, Astrophys. J., 649, 599

Koprowski, M. P., Dunlop, J. S., Michałowski, M. J., et al. 2016, MNRAS, 458, 4321

Krajnović, D., Alatalo, K., Blitz, L., et al. 2013, Mon. Not. R. Astron. Soc., 432, 1768

Krajnović, D., Cappellari, M., de Zeeuw, P. T., & Copin, Y. 2006, MNRAS, 366, 787

Kriek, M., van Dokkum, P. G., Labbé, I., et al. 2009, ApJ, 700, 221

Krumholz, M. R. & Burkhart, B. 2016, MNRAS, 458, 1671

Krumholz, M. R., Burkhart, B., Forbes, J. C., & Crocker, R. M. 2018, Mon. Not. R. Astron. Soc., 477, 2716

Lacey, C. G., Baugh, C. M., Frenk, C. S., et al. 2016, MNRAS, 462, 3854

Lagattuta, D. J., Vegetti, S., Fassnacht, C. D., et al. 2012, MNRAS, 424, 2800

Lagos, C. d. P., Robotham, A. S. G., Trayford, J. W., et al. 2019, MNRAS, 489, 4196

Lagos, C. d. P., Theuns, T., Stevens, A. R. H., et al. 2017, MNRAS, 464, 3850

Lang, P., Förster Schreiber, N. M., Genzel, R., et al. 2017, ApJ, 840, 92

Lang, P., Wuyts, S., Somerville, R. S., et al. 2014, Astrophys. J., 788, 11

Larkin, J., Barczys, M., Krabbe, A., et al. 2006, in Proc. SPIE, Vol. 6269, Society of Photo-Optical Instrumentation Engineers (SPIE) Conference Series, 62691A

Law, D. R., Steidel, C. C., & Erb, D. K. 2006, AJ, 131, 70

Leethochawalit, N., Jones, T. A., Ellis, R. S., et al. 2016, ApJ, 820, 84

Lelli, F., De Breuck, C., Falkendal, T., et al. 2018, Mon. Not. R. Astron. Soc., 479, 5440

Lelli, F., McGaugh, S. S., & Schombert, J. M. 2016, AJ, 152, 157

Lelli, F., Verheijen, M., & Fraternali, F. 2014, Astron. Astrophys., 566, A71

Lelli, F., Verheijen, M., Fraternali, F., & Sancisi, R. 2012, A&A, 537, A72

Leroy, A. K., Walter, F., Brinks, E., et al. 2008, AJ, 136, 2782

Levy, R. C., Bolatto, A. D., Teuben, P., et al. 2018, ApJ, 860, 92

Lima Neto, G. B., Gerbal, D., & Márquez, I. 1999, Mon. Not. R. Astron. Soc., 309, 481

Litke, K. C., Marrone, D. P., Spilker, J. S., et al. 2019, ApJ, 870, 80

Livermore, R. C., Jones, T. A., Richard, J., et al. 2015, MNRAS, 450, 1812

Lovell, C. C., Geach, J. E., Davé, R., Narayanan, D., & Li, Q. 2020, arXiv e-prints, arXiv:2006.15156

Ludlow, A. D., Bose, S., Angulo, R. E., et al. 2016, MNRAS, 460, 1214

Mac Low, M.-M., Klessen, R. S., Burkert, A., & Smith, M. D. 1998, Phys. Rev. Lett., 80, 2754

Madau, P. & Dickinson, M. 2014, ARA&A, 52, 415

Man, A. & Belli, S. 2018, Nature Astronomy, 2, 695

Martig, M., Bournaud, F., Teyssier, R., & Dekel, A. 2009, ApJ, 707, 250

Martizzi, D. 2020, Mon. Not. R. Astron. Soc., 492, 79

Mason, C. A., Treu, T., Fontana, A., et al. 2017, ApJ, 838, 14

McAlpine, S., Smail, I., Bower, R. G., et al. 2019, Mon. Not. R. Astron. Soc., 1653

McDermid, R. M., Alatalo, K., Blitz, L., et al. 2015, Mon. Not. R. Astron. Soc., 448, 3484

McKean, J., Jackson, N., Vegetti, S., et al. 2015, in Advancing Astrophysics with the Square Kilometre Array (AASKA14), 84

McMullin, J. P., Waters, B., Schiebel, D., Young, W., & Golap, K. 2007, in Astronomical Society of the Pacific Conference Series, Vol. 376, Astr. Soc. P., ed. R. A. Shaw, F. Hill, & D. J. Bell, 127

McQuinn, K. B. W., van Zee, L., & Skillman, E. D. 2019, ApJ, 886, 74

Michałowski, M. J., Dunlop, J. S., Koprowski, M. P., et al. 2017, MNRAS, 469, 492

Michałowski, M. J., Hayward, C. C., Dunlop, J. S., et al. 2014, A&A, 571, A75

Mieda, E., Wright, S. A., Larkin, J. E., et al. 2014, PASP, 126, 250

Mogotsi, K. M., de Blok, W. J. G., Caldú-Primo, A., et al. 2016, AJ, 151, 15

Moiseev, A. V., Tikhonov, A. V., & Klypin, A. 2015, MNRAS, 449, 3568

Molina, J., Ibar, E., Swinbank, A. M., et al. 2017, MNRAS, 466, 892

Morselli, L., Popesso, P., Erfanianfar, G., & Concas, A. 2017, A&A, 597, A97

Naab, T., Johansson, P. H., & Ostriker, J. P. 2009, Astrophys. J. Lett., 699, L178

Naab, T., Oser, L., Emsellem, E., et al. 2014, MNRAS, 444, 3357

Naab, T. & Ostriker, J. P. 2017, ARA&A, 55, 59

Navarro, J. F., Frenk, C. S., & White, S. D. M. 1996, Astrophys. J., 462, 563

Neeleman, M., Kanekar, N., Prochaska, J. X., Rafelski, M. A., & Carilli, C. L. 2019, ApJ, 870, L19

Neeleman, M., Prochaska, J. X., Kanekar, N., & Rafelski, M. 2020, Nature, 581, 269

Negrello, M., Hopwood, R., De Zotti, G., et al. 2010, Science, 330, 800

Nelson, D., Genel, S., Vogelsberger, M., et al. 2015, MNRAS, 448, 59

Nelson, D., Pillepich, A., Springel, V., et al. 2019, MNRAS, 490, 3234

Nesvadba, N. P. H., Lehnert, M. D., Eisenhauer, F., et al. 2006, ApJ, 650, 661

Newman, S. F., Genzel, R., Förster Schreiber, N. M., et al. 2013, ApJ, 767, 104

Noeske, K. G., Weiner, B. J., Faber, S. M., et al. 2007, ApJ, 660, L43

Nordon, R. & Sternberg, A. 2016, MNRAS, 462, 2804

Oesch, P. A., Carollo, C. M., Feldmann, R., et al. 2010, ApJ, 714, L47

Oguri, M. & Marshall, P. J. 2010, MNRAS, 405, 2579

Olivares, V., Treister, E., Privon, G. C., et al. 2016, ApJ, 827, 57

Ostriker, E. C. & Shetty, R. 2011, ApJ, 731, 41

Papovich, C., Labbé, I., Quadri, R., et al. 2015, ApJ, 803, 26

Patrício, V., Richard, J., Carton, D., et al. 2018, MNRAS[[arXiv]1802.08451]

Perna, M., Lanzuisi, G., Brusa, M., Mignoli, M., & Cresci, G. 2017, A&A, 603, A99

Pillepich, A., Nelson, D., Springel, V., et al. 2019, arXiv e-prints, arXiv:1902.05553

Pineda, J. L., Langer, W. D., Velusamy, T., & Goldsmith, P. F. 2013, A&A, 554, A103

Planck Collaboration, Ade, P. A. R., Aghanim, N., et al. 2016, A&A, 594, A13

Posselt, W., Holota, W., Kulinyak, E., et al. 2004, in Society of Photo-Optical Instrumentation Engineers (SPIE) Conference Series, Vol. 5487, Optical, Infrared, and Millimeter Space Telescopes, ed. J. C. Mather, 688–697

Powell, D., Vegetti, S., McKean, J. P., & Spingola, C. 2020, arXiv e-prints, arXiv:2005.03609

Press, W. H., Teukolsky, S. A., Vetterling, W. T., & Flannery, B. P. 1992, Numerical recipes in C. The art of scientific computing

Rees, M. J. & Ostriker, J. P. 1977, MNRAS, 179, 541

Renzini, A., D'Antona, F., Cassisi, S., et al. 2015, MNRAS, 454, 4197

Rescigno, U., Grillo, C., Lombardi, M., et al. 2020, A&A, 635, A98

Riechers, D. A., Pavesi, R., Sharon, C. E., et al. 2019, ApJ, 872, 7

Rieke, G. H., Wright, G. S., Böker, T., et al. 2015, PASP, 127, 584

Rieke, M. J., Kelly, D., & Horner, S. 2005, in Society of Photo-Optical Instrumentation Engineers (SPIE) Conference Series, Vol. 5904, Cryogenic Optical Systems and Instruments XI, ed. J. B. Heaney & L. G. Burriesci, 1–8

Rigopoulou, D., Hopwood, R., Magdis, G. E., et al. 2014, ApJ, 781, L15

Rix, H.-W., Guhathakurta, P., Colless, M., & Ing, K. 1997, MNRAS, 285, 779

Rizzo, F., Vegetti, S., Fraternali, F., & Di Teodoro, E. 2018, Mon. Not. R. Astron. Soc., 481, 5606

Rodighiero, G., Brusa, M., Daddi, E., et al. 2015, ApJ, 800, L10

Rodriguez-Gomez, V., Pillepich, A., Sales, L. V., et al. 2016, MNRAS, 458, 2371

Rogstad, D. H., Lockhart, I. A., & Wright, M. C. H. 1974, ApJ, 193, 309

Rubin, V. C., Ford, W. K., J., & Thonnard, N. 1978, ApJ, 225, L107

Rybak, M., Calistro Rivera, G., Hodge, J. A., et al. 2019, ApJ, 876, 112

Rybak, M., Vegetti, S., McKean, J. P., Andreani, P., & White, S. D. M. 2015, MNRAS, 453, L26

Rybak, M., Zavala, J. A., Hodge, J. A., Casey, C. M., & Werf, P. v. d. 2020, ApJ, 889, L11

Saintonge, A., Wilson, C. D., Xiao, T., et al. 2018, MNRAS, 481, 3497

Sargent, M. T., Daddi, E., Béthermin, M., et al. 2014, ApJ, 793, 19

Sargsyan, L., Samsonyan, A., Lebouteiller, V., et al. 2014, ApJ, 790, 15

Satyapal, S., Ellison, S. L., McAlpine, W., et al. 2014, MNRAS, 441, 1297

Schaye, J., Crain, R. A., Bower, R. G., et al. 2015, MNRAS, 446, 521

Schneider, P. 2006, in Saas-Fee Advanced Course 33: Gravitational Lensing: Strong, Weak and Micro, ed. G. Meylan, P. Jetzer, P. North, P. Schneider, C. S. Kochanek, & J. Wambsganss, 1–89

Schreiber, C., Pannella, M., Elbaz, D., et al. 2015, A&A, 575, A74

Scoville, N., Lee, N., Vanden Bout, P., et al. 2017, ApJ, 837, 150

Sharples, R., Bender, R., Agudo Berbel, A., et al. 2013, The Messenger, 151, 21

Shirazi, M., Vegetti, S., Nesvadba, N., et al. 2014, MNRAS, 440, 2201

Silk, J. 2013, ApJ, 772, 112

Simpson, J. M., Smail, I., Wang, W.-H., et al. 2017, ApJ, 844, L10

Skilling, J. 2004, in American Institute of Physics Conference Series, Vol. 735, American Institute of Physics Conference Series, ed. R. Fischer, R. Preuss, & U. V. Toussaint, 395–405

Smit, R., Bouwens, R. J., Carniani, S., et al. 2018, Nature, 553, 178

Sofue, Y. & Rubin, V. 2001, ARA&A, 39, 137

Speagle, J. S. 2019, arXiv e-prints, arXiv:1904.02180

Spilker, J. S., Marrone, D. P., Aravena, M., et al. 2016, Astrophys. J., 826, 112

Stacey, G. J., Hailey-Dunsheath, S., Ferkinhoff, C., et al. 2010a, ApJ, 724, 957

Stacey, G. J., Hailey-Dunsheath, S., Ferkinhoff, C., et al. 2010b, Astrophys. J., 724, 957

Stark, D. P., Swinbank, A. M., Ellis, R. S., et al. 2008, Nature, 455, 775

Steinhardt, C. L., Speagle, J. S., Capak, P., et al. 2014, ApJ, 791, L25

Stilp, A. M., Dalcanton, J. J., Skillman, E., et al. 2013, ApJ, 773, 88

Stockmann, M., Toft, S., Gallazzi, A., et al. 2020, ApJ, 888, 4

Stone, J. M., Ostriker, E. C., & Gammie, C. F. 1998, ApJ, 508, L99

Strandet, M. L., Weiss, A., Vieira, J. D., et al. 2016, ApJ, 822, 80

Sun, J., Leroy, A. K., Ostriker, E. C., et al. 2020, ApJ, 892, 148

Suyu, S. H., Marshall, P. J., Hobson, M. P., & Blandford, R. D. 2006, MNRAS, 371, 983

Swinbank, A. M., Bower, R. G., Smith, G. P., et al. 2007, MNRAS, 376, 479

Swinbank, A. M., Dye, S., Nightingale, J. W., et al. 2015, ApJ, 806, L17

Swinbank, A. M., Harrison, C. M., Trayford, J., et al. 2017, MNRAS, 467, 3140

Swinbank, A. M., Smail, I., Sobral, D., et al. 2012a, ApJ, 760, 130

Swinbank, A. M., Sobral, D., Smail, I., et al. 2012b, MNRAS, 426, 935

Tacchella, S., Dekel, A., Carollo, C. M., et al. 2016, MNRAS, 458, 242

Tacchella, S., Diemer, B., Hernquist, L., et al. 2019, MNRAS, 487, 5416

Tacconi, L. J., Genzel, R., & Sternberg, A. 2020, arXiv e-prints, arXiv:2003.06245

Tasca, L. A. M., Le Fèvre, O., Hathi, N. P., et al. 2015, A&A, 581, A54

Teklu, A. F., Remus, R.-S., Dolag, K., et al. 2018, Astrophys. J. Lett., 854, L28

Terzić, B. & Graham, A. W. 2005, Mon. Not. R. Astron. Soc., 362, 197

Thomas, D., Maraston, C., Schawinski, K., Sarzi, M., & Silk, J. 2010, MNRAS, 404, 1775

Thompson, A. R., Moran, J. M., & Swenson, G. W. 1986, Interferometry and synthesis in radio astronomy

Tielens, A. G. G. M. 2005, The Physics and Chemistry of the Interstellar Medium

Tiley, A. L., Swinbank, A. M., Harrison, C. M., et al. 2019, MNRAS, 485, 934

Toft, S., Gallazzi, A., Zirm, A., et al. 2012, ApJ, 754, 3

Toomre, A. 1964, Astrophys. J., 139, 1217

Trachternach, C., de Blok, W. J. G., Walter, F., Brinks, E., & Kennicutt, Jr., R. C. 2008, AJ, 136, 2720

Turner, O. J., Cirasuolo, M., Harrison, C. M., et al. 2017, Mon. Not. R. Astron. Soc., 471, 1280

Übler, H., Genzel, R., Tacconi, L. J., et al. 2018, Astrophys. J. Lett., 854, L24

Übler, H., Genzel, R., Wisnioski, E., et al. 2019, Astrophys. J., 880, 48

Utomo, D., Blitz, L., & Falgarone, E. 2019, ApJ, 871, 17

Valentino, F., Tanaka, M., Davidzon, I., et al. 2020, ApJ, 889, 93

van Albada, T. S., Bahcall, J. N., Begeman, K., & Sancisi, R. 1985, ApJ, 295, 305

van de Voort, F., Schaye, J., Booth, C. M., Haas, M. R., & Dalla Vecchia, C. 2011, MNRAS, 414, 2458

van den Bosch, F. C. & Swaters, R. A. 2001, MNRAS, 325, 1017

van der Wel, A., Franx, M., van Dokkum, P. G., et al. 2014, Astrophys. J., 788, 28

van Dokkum, P. G., Nelson, E. J., Franx, M., et al. 2015, ApJ, 813, 23

Varidel, M. R., Croom, S. M., Lewis, G. F., et al. 2020, MNRAS, 495, 2265

Vegetti, S. & Koopmans, L. V. E. 2009, Mon. Not. R. Astron. Soc., 392, 945

Vieira, J. D., Marrone, D. P., Chapman, S. C., et al. 2013, Nature, 495, 344

Vogelsberger, M., Marinacci, F., Torrey, P., & Puchwein, E. 2020, Nature Reviews Physics, 2, 42

Vogelsberger, M., Zavala, J., Cyr-Racine, F.-Y., et al. 2016, MNRAS, 460, 1399

Walker, M. G. & Peñarrubia, J. 2011, ApJ, 742, 20

Walter, F., Brinks, E., de Blok, W. J. G., et al. 2008, AJ, 136, 2563

Walter, F., Decarli, R., Aravena, M., et al. 2016, ApJ, 833, 67

Walter, F., Decarli, R., Sargent, M., et al. 2014, ApJ, 782, 79

Weiß, A., De Breuck, C., Marrone, D. P., et al. 2013, Astrophys. J., 767, 88

Werner, M. W., Roellig, T. L., Low, F. J., et al. 2004, ApJS, 154, 1

Whitaker, K. E., van Dokkum, P. G., Brammer, G., & Franx, M. 2012, ApJ, 754, L29

White, S. D. M. & Rees, M. J. 1978, MNRAS, 183, 341

Wisnioski, E., Förster Schreiber, N. M., Fossati, M., et al. 2019, ApJ, 886, 124

Wisnioski, E., Förster Schreiber, N. M., Wuyts, S., et al. 2015, ApJ, 799, 209

Wisnioski, E., Glazebrook, K., Blake, C., et al. 2011, MNRAS, 417, 2601

Wootten, A. & Thompson, A. R. 2009, IEEE Proceedings, 97, 1463

Wright, S. A., Larkin, J. E., Law, D. R., et al. 2009, ApJ, 699, 421

Wuyts, S., Förster Schreiber, N. M., Wisnioski, E., et al. 2016, ApJ, 831, 149

Yuan, T., Richard, J., Gupta, A., et al. 2017, ApJ, 850, 61

Zanella, A., Daddi, E., Magdis, G., et al. 2018, Mon. Not. R. Astron. Soc., 481, 1976

Zolotov, A., Dekel, A., Mandelker, N., et al. 2015, Mon. Not. R. Astron. Soc., 450, 2327